CONVECTIVE HEAT AND MASS TRANSFER IN A NANOFLUID FLOW OVER FRUSTUM OF A CONE

A THESIS SUBMITTED TO
NATIONAL INSTITUTE OF TECHNOLOGY WARANGAL, (T.S.)
FOR THE AWARD OF THE DEGREE OF
DOCTOR OF PHILOSOPHY
IN
MATHEMATICS

BY
VENKATARAO CHUKKA
(Roll No. 714158)

UNDER THE SUPERVISION OF
Dr. CH. RAMREDDY

DEPARTMENT OF MATHEMATICS
NATIONAL INSTITUTE OF TECHNOLOGY
WARANGAL-506004, INDIA

JUNE 2018

CERTIFICATE

This is to certify that the thesis entitled “ **Convective Heat and Mass Transfer in a Nanofluid Flow over Frustum of a Cone** ” submitted to National Institute of Technology Warangal, for the award of the degree of ***Doctor of Philosophy***, is the bonafide research work done by **Mr. VENKATARAO CHUKKA** under my supervision. The contents of this thesis have not been submitted elsewhere for the award of any degree.

Dr. Ch. Ramreddy
Assistant Professor
Department of Mathematics
National Institute of Technology Warangal
Telangana State, INDIA

.

DECLARATION

This is to certify that the work presented in the thesis entitled **“Convective Heat and Mass Transfer in a Nanofluid Flow over Frustum of a Cone”**, is a bonafide work done by me under the supervision of **Dr. CH. RAMREDDY** and has not been submitted elsewhere for the award of any degree.

I declare that this written submission represents my ideas in my own words and where others’ ideas or words have been included, I have adequately cited and referenced the original sources. I also declare that I have adhered to all principles of academic honesty and integrity and have not misrepresented or fabricated or falsified any idea / data / fact /source in my submission. I understand that any violation of the above will be a cause for disciplinary action by the Institute and can also evoke penal action from the sources which have thus not been properly cited or from whom proper permission has not been taken when needed.

Venkatarao Chukka
Roll No. 714158
Date:____________

Dedicated to

My Parents, Wife

&

Lord Shiva

ACKNOWLEDGEMENTS

It is a rare privilege and boon that I could associate myself for pursuing my research work with Dr. Ch. Ramreddy, Assistant Professor of Mathematics, National Institute of Technology, Warangal, India. I sincerely record my gratitude for his invaluable guidance and constant encouragement throughout the preparation of this thesis and his involvement and meticulous supervision while my work was in progress. With his inimitable qualities as a good teacher, he chiseled my path towards perfection. Ever since I met him, he has been a perpetual source of motivation, inspiration, encouragement and enlightenment. He is responsible for making the period of my research work as an educative and enjoyable learning experience. The thesis would not have seen the light of the day without his unrelenting support and cooperation. I deem it a privilege to have worked under his amiable guidance. My vocabulary is inadequate to express my gratitude.

I am greatly indebted to the dynamic personality Prof. D. Srinivasacharya, Head, Department of Mathematics for his affectionate support, encouragement and for sparing his valuable time in bringing a proper form for presentation of the results in the thesis. It is not an exaggeration to state that without his assistance and suggestions, this thesis would not have taken this form.

I am grateful to Prof. T.K.V. Iyengar (Late), Prof. G. Radhakrishnamacharya (Retd.), Prof. Y. N. Reddy, Prof. K.N.S. Kasi Viswanadham and Prof. Debashis Dutta, Department of Mathematics for their help and support throughout my research period.

I thank the members of the Doctoral Scrutiny Committee, Prof. J. V. Ramana Murthy, Prof. D. Srinivasacharya, Department of Mathematics and Prof. Deva Pratap, Department of Civil Engineering for their valuable suggestions, moral support and encouragement while my work was in progress.

I place on record my gratitude to Dr. J. Pranitha and all other faculty members of the Department of Mathematics, for their constant encouragement. Also, I thank the office staff.

I express my sincere thanks to Prof. N.V. Ramana Rao, Director, National Institute of Technology, Warangal for awarding me Institute Fellowship (MHRD, GoI) to carry out my research work. I thank him for his kind support and encouragement at every stage of this endeavor.

I express my sincere thanks and gratitude to Sri. P. Ashok Gajapathi Raju (Chairman), Dr. K. V. L. Raju (Principal), Dr. D. R. K. Raju (Correspondent-MANSAS), Dr.

Ch. Purna Chandra Rao (Asst. Principal-Academics), Dr. P. GovindaRao (Head) and all other faculty members of the Department of Mathematics, MVGR College of Engineering, Vizianagaram, Andhra Pradesh for their valuable support and encouragement at every stage of this endeavor.

My sincere thanks to Prof. V. Ramachandra Raju, Vice Chancellor, RGUKT, Andhra Pradesh for his constant support and encouragement throughout my career.

I owe my special thanks to Dr. K. Kaladhar, Dr. M. Krishna Prasad, Dr. M. Upendar, Dr. O. Surender, Dr. P. Vijay Kumar, Dr. G. Madhava Rao, Dr. K. Hima Bindu, Dr. Md. Shafeeurrahaman, Dr. T. Pradeepa for their support. I thank Mr. G. Venkata Suman, Mr. P. Jagadeeshwar, Mr. P. Naveen, Mr. I. Sreenath, Mr. M. Varun Kumar, Mr. G. Nithish Kumar and all other research colleagues in the Department of mathematics and my friends, who helped me during my Ph.D for being cooperative and also for making my stay in the NITW campus fruitful and enjoyable every moment.

My deepest gratitude to my Parents, Ch. Apparao and Ch. Satyaveni, brother, Ch. Prasad, and other family members for their continuous support and constant encouragement over the years. All of their love and affection have been motivating force behind what I am today.

Finally, and most importantly, I would like to thank my better half, K. Vahini for her support, patience and understanding. Without her help and encouragement, I would not have been finished this thesis.

. Venkatarao Chukka

ABSTRACT

Mathematical modeling and analysis of the convective flow of nanofluids is an emerging field of research due to their high thermal conductivity properties and large number of industrial applications. Nanofluids are prepared by the uniform dispersion and suspension of nanometer sized metallic particles into the conventional heat transfer fluids such as water, oil, or ethylene glycol. Moreover, the problems on natural/mixed convective flow of a nanofluid over the vertical frustum of a cone under various physical conditions become slightly more complicated, and leading to the complex interactions of the fluid flow, heat and mass transfer mechanisms. The main aim of the thesis is to investigate the natural and mixed convective flow of a nanofluid in the presence of Soret and viscous dissipation, double stratification, non-Darcy porous medium, Arrhenius activation energy, thermal radiation, double dispersion, nonlinear convection, amplitude and angle of the wavy frustum of a cone. The problems considered deal with the vertical frustum of a cone, rotating frustum of a cone and wavy frustum of a cone.

The thesis consists of EIGHT chapters. Chapter–1 provides an introduction to the concepts in nanofluid, porous medium, convective boundary condition and a review of the pertinent literature. Chapter–2 deals with the effects of Soret and viscous dissipation on the convective flow of a nanofluid over the vertical frustum of a cone, whereas Chapter–3 explores the convective heat and mass transport over the frustum of a cone embedded in a non-Darcy porous medium saturated by a doubly stratified nanofluid. Chapter–4 considers the combined effects of Arrhenius activation energy with binary chemical reaction and thermal radiation on the convective nanofluid flow over the frustum of a cone subject to the convective boundary condition. Chapter–5 investigates the thermal and solutal dispersion effects on the convective flows over the vertical frustum of a cone in a nanofluid saturated non-Darcy porous medium subject to the convective boundary condition. Chapter–6 reports the convective flow of a nanofluid due to the vertically rotating permeable frustum of a cone under the influence of convective boundary condition. The nonlinear convective flow of a nanofluid over the permeable wavy frustum of a cone in the presence of convective boundary condition, is discussed in Chapter–7.

In all the above chapters, the non-linear governing equations and their associated boundary conditions are initially cast into dimensionless form by using a suitable set of non-similarity transformations. The resulting system of equations is solved using the *Bivariate Pseudo-Spectral Local Linearization Method (BPSLLM)*. The influence of pertinent parameters on the non-dimensional velocity, temperature, nanoparticle volume fraction, and regular

concentration are presented graphically. Moreover, the skin friction, local heat transfer rate, local nanoparticle and regular mass transfer rates are studied quantitatively and qualitatively.

The last chapter (Chapter–8) gives a summary and overall conclusions and scope for future work.

NOMENCLATURE

A	Half angle of the frustum of a cone
a	Amplitude of the wavy surface
Bi	Biot number
b	Forchheimer constant
C	Regular concentration
C_w	Regular concentration at the wall
C_∞	Regular concentration at the ambient medium
C_p	Specific heat capacity
C_f	Local skin-friction coefficient
D_B	Brownian diffusion coefficient
D_T	Thermophoretic diffusion coefficient
D_S	Solutal diffusivity
D_{CT}	Soret type diffusivity
Da	Darcy number
D_y	Effective solutal diffusivity
Ds	Thermal dispersion parameter
Dc	Solutal dispersion parameter
E	Arrhenius activation energy parameter
Ec	Eckert number
f_w	Suction/Injection parameter
f	Reduced stream function
g	Gravitational acceleration
$Gr_{\overline{x}}$	Local Grashof number
h_f	Convective heat transfer coefficient
k	Thermal conductivity
K_p	Permeability of the medium
k^*	Mean absorption coefficient
L	Characteristic length
Le	Lewis number
Nc	Regular buoyancy ratio
Nr	Nanoparticle buoyancy ratio
Nt	Thermophoresis parameter
Nb	Brownian motion parameter
$Nu_{\overline{x}}$	Local Nusselt number
$NSh_{\overline{x}}$	Local nanoparticle Sherwood number
Pr	Prandtl number
q_w	Surface heat flux
q_n	Nanoparticle mass flux
q_m	Regular mass flux
$Re_{\overline{x}}$	Local Reynolds number
Rd	Radiation parameter

r	Radius of a frustum of a cone
S	Dimensionless regular concentration
$Sh_{\overline{x}}$	Local regular Sherwood number
Sc	Schmidt number
S_T	Soret number
T	Temperature
T_w	Temperature at the wall
T_f	Convective wall temperature
T_∞	Temperature at the ambient medium
U_∞	Reference velocity
x_0	Leading edge distance of a frustum of a cone

Greek Symbols

α_m	Thermal diffusivity
ρ_{f_∞}	Density of the base fluid
ρ_p	Density of the nanoparticles
μ	Viscosity of the base fluid
ϕ	Nanoparticle volume fraction
ϕ_∞	Nanoparticle volume fraction at the ambient medium
β_T, β_{TT}	First and second order thermal expansion coefficients
β_C, β_{CC}	First and second order solutal expansion coefficients
ψ	Stream function
ξ	Streamwise coordinate
η	Similarity variable
ν	Kinematic viscosity
θ	Dimensionless temperature
γ	Dimensionless nanoparticle volume fraction
ε	Porosity
τ_w	Surface shear stress
α_y	Effective thermal diffusivity
λ	Mixed convection parameter
σ^*	Stefan-Boltzmann constant
$\varepsilon_1, \varepsilon_2$	Thermal and solutal stratification parameters

Operators

∇^2	Laplacian operator

Subscripts

w	Wall condition
∞	Ambient condition

Superscript

$'$	Differentiation with respect to η

Contents

---

[1] Case(a): Published in "**Journal of Nanofluids**" 6(3) (2017) 530–540, Case(b): Published in "**Journal**

---

of Mechanics" 33(5) (2017) 687–702

[2] Case(a): Published in "**International Journal of Applied and Computational Mathematics**" 3 (2017) 99–113, Case(b): Published in "**Journal of Nanofluids**" 6 (2017) 971–981

[3] Case(a): Published in "**International Journal of Chemical Reactor Engineering**" 16(3) (2017) DOI: 10.1515/ijcre-2016-0188, Case(b): Accepted in "**Advanced Science, Engineering and Medicine**"

[4] Case(a): Published in "**Nonlinear Engineering**" 6(4) (2017) 277–292, Case(b): Published in "**Heat Transfer Research**" DOI: 10.1615/HeatTransRes.2018018754

---

[5] Case(a): Communicated to "**Sadhana–Academy Proceedings in Eng. Sci.**", Case(b): Communicated to "**Indian Journal of Physics**"

[6] Case(a): Published in "**Journal of Nanofluids**" 7 (2018) 1258–1271, Case(b): Communicated to "**International Journal of Numerical Methods for Heat & Fluid Flow**"

Chapter 1

Preliminaries and Review

1.1 Introduction

The science of fluid dynamics encompasses the motion of gases and liquids, the forces those are responsible for this motion, and the interaction of the fluid with solids. This field stands to various branches of science and engineering, and touches almost every aspect of our daily life. From predicting the aerodynamic behavior of moving vehicles, to the movement of biological fluids in the human body, weather predictions, cooling of electronic components, performance of microfluidic devices, all demand a detailed understanding of the subject of fluid dynamics and substantial research, thereof.

Due to the complexity of the subject and breadth of its applications, fluid dynamics is proven to be a highly exciting and challenging subject of modern sciences. The quest for more profound understanding of the subject has not only inspired the development of the subject itself but has also led to the progress in the supporting areas, such as applied mathematics, numerical computing, and experimental techniques. A large number of problems in fluid dynamics have claimed the attention of mathematicians, physicists, and engineers for many years. As a result, an enormous body of established results has accumulated steadily but remains scattered in the literature.

The mechanism of heat transfer is the passage of thermal energy from a hot to a cold body. It occurs through conduction, convection, radiation or any combination of these. The combined process of heat transfer by conduction and convection is referred to as the convective heat transfer. The convective mode of heat transfer is generally divided into two basic processes: free (or natural) convection and forced convection. If the fluid motion is set up by buoyancy effects resulting from density differences, which is caused by temperature variations in the fluid, then the heat transfer is said to be free convection. On the other hand, if the motion of the fluid arises from an external agent, then the process is termed as forced convection. When both free and forced convection effects are significant, and neither of these can be neglected, then the process is termed as mixed convection. Both free and mixed convection processes may be divided into external flows over immersed bodies (such as flat plates, cones, cylinders and wires, spheres or other bodies), free boundary flows (such as plumes, jets, and wakes), and internal flow in ducts (such as pipes, channels and enclosures).

The transport of a component in a mixture, from a region of high concentration to a region of low concentration, is called mass transfer. The involvement and applications of mass transfer process have gained much attention, and it goes to a greater length in multiple fields such as the industrial, biological, physical and chemical engineering processes. Mass transfer is divided into two modes: Diffusive mass transfer and Convective mass transfer. The convective mass transfer is analogous to the convective heat transfer, it occurs between a moving mixture of fluid species and an exposed solid surface. Coupled heat and mass transport constitute a significant area of research in modern fluid dynamics such as an electronic cooling, drying processes, manufacture of electric cable insulations, curing of plastics, solar energy system, purification processes, etc.

In the recent past, the nanofluids have gained considerable interest for their potential to enhance the heat transfer rate in several engineering systems, while reducing or possibly eliminating, sedimentation and clogging that plagued earlier solid-liquid mixtures with larger particles. Nanofluids can be used in a wide variety of engineering applications ranging from the automotive industry to the medical arena, power plant cooling systems as well as computers. The convection due to heated/cooled objects of various shapes in a nanofluid saturated porous medium yields one of the most critical scenarios for heat and mass transfer theory, and thus is of considerable theoretical and practical interest.

1.2 Nanofluids

Conventional heat transfer fluids like water, ethylene glycol, and oil have relatively low thermal conductivities when compared to the thermal conductivity of solids. Hence, an innovative way of improving the thermal conductivity of fluid is that, by suspending small solid particles, such as millimeter or micrometer-sized particles into the conventional fluids. In 1904, Maxwell added millimeter or micrometer-sized solid particles into the conventional fluids to enhance their thermal conductivity. However, they have not been of interest for practical applications as they include sedimentation, erosion, fouling and increased pressure drop of the flow. These situations are highly undesirable for many practical applications in cooling process. The recent advances in material technology has made it possible to produce nanometer-sized particles that can overcome the above said difficulties.

A base fluid with suspended solid nanoparticles is named as a nanofluid, which is initially introduced by Choi [21]. The thermal conductivity of nanometer-sized particles is typically in the order of magnitude higher than those of the base fluids. The addition of nanoparticles to the base fluid even at low volume concentrations, results in significant increase of the thermal performance. The goal of nanofluids is to achieve the highest possible thermal properties at the smallest possible concentrations (preferably $< 1\%$ by volume) by uniform dispersion and stable suspension of nanoparticles (preferably < 10nm) in host fluids. During the past decade, the study of nanofluids has attracted immense enthusiasm from researchers, because of its exceptional applications in electronics, communication, computing technologies, high power X-rays, medicine, lasers, optical devices, scientific measurement, material processing, material synthesis, etc. The detailed introduction and applications of nanofluids can be seen in the textbook by Das *et al.* [24].

Currently, two different models being investigated: (i) Tiwari-Das model [118], and (ii) Buongiorno model [13]. These models have been used frequently by several researchers to investigate the heat transfer enhancement by very fine particles suspended in a host fluid.

Tiwari-Das model

Tiwari and Das [118] developed a model to analyze the behaviour of nanofluids by taking the volumetric fraction of nanparticles into the consideration. In this model, the basic governing equations for laminar, incompressible flow of a nanofluid can be written as

$$\nabla \cdot \overline{u} = 0 \tag{1.1}$$

$$\frac{\partial \overline{u}}{\partial t} + \overline{u} \cdot \nabla \overline{u} = -\frac{1}{\rho_{nf}} \nabla p + \frac{\mu_{nf}}{\rho_{nf}} \nabla^2 \overline{u} + \frac{\phi \rho_s \beta_s (1-\phi) \rho_f \beta_f}{\rho_{nf}} g (T - T_\infty) \tag{1.2}$$

$$\frac{\partial T}{\partial t} + \overline{u} \cdot \nabla T = \alpha_{nf} \nabla^2 T \tag{1.3}$$

where $\overline{u}$ is the velocity vector, T is the fluid temperature, ϕ is the volume fraction of the nanoparticle, g is the acceleration due to gravity, β_f and β_s are the thermal expansion coefficients of the base fluid and nanoparticles, respectively. Further, μ_{nf} is the viscosity of the nanofluid, α_{nf} is the thermal diffusivity of the nanofluid and ρ_{nf} is the density of the nanofluid, which are given by

$$\begin{gathered} \mu_{nf} = \frac{\mu_f}{(1-\phi)^{2.5}},\ \rho_{nf} = (1-\phi)\rho_f + \phi\rho_s,\ \alpha_{nf} = \frac{k_{nf}}{\rho C_{pnf}}, \\ \rho C_{pnf} = (1-\phi)\rho C_{pf} + \phi \rho C_{ps},\ \frac{k_{nf}}{k_f} = \frac{(k_s + 2k_f) - 2\phi(k_f - k_s)}{(k_s + 2k_f) + \phi(k_f - k_s)} \end{gathered} \tag{1.4}$$

where ρ_f is the density of the base fluid, ρ_s is the density of the solid particle, μ_f is the viscosity of the base fluid, k_{nf} is the effective thermal conductivity of the nanofluid, k_f and k_s are the thermal conductivities of the base fluid and nanoparticle, respectively.

Buongiorno model

Buongiorno [13] proposed an analytical model for convective transport in nanofluids, which incorporates the effects of Brownian diffusion and thermophoresis. Contrary to the Tiwari-Das model [118], that focuses on volumetric fraction of nanoparticles, Buongiorno model [13] pays more attention to Brownian motion and thermophoresis effects. The arbitrary motion of nanoparticles within the base fluid is called Brownian motion, and this results from continuous collisions between nanoparticles and molecules of the base fluid. Particles can diffuse under the influence of a temperature gradient. This phenomenon is called thermophoresis, and is the particle equivalent of the renowned Soret effect for gaseous or liquid mixtures. This Buongiorno's model has been used in many recent works such as those of, Nield and Kuznetsov ([81], [82], [83]), Kuznetsov and Nield ([52], [53]) and Khan and Aziz [50], among others.

The basic governing equations of Buongiorno's nanofluid model are given by

$$\nabla \cdot \overline{u} = 0 \tag{1.5}$$

$$\frac{\partial \overline{u}}{\partial t} + \overline{u} \cdot \nabla \overline{u} = -\frac{1}{\rho_{f\infty}} \nabla p + \nu \nabla^2 \overline{u} + g\,(1-\phi_\infty)\beta_T\,(T - T_\infty) - (\rho_p - \rho_{f\infty})\, g\,(\phi - \phi_\infty) \tag{1.6}$$

$$\frac{\partial T}{\partial t} + \overline{u} \cdot \nabla T = \alpha \nabla^2 T + \frac{(\rho c)_p}{(\rho c)_f}\left[D_B \nabla \phi \cdot \nabla T + \frac{D_T}{T_\infty} \nabla T \cdot \nabla T\right] \tag{1.7}$$

$$\frac{\partial \phi}{\partial t} + \overline{u} \cdot \nabla \phi = D_B \nabla^2 \phi + \frac{D_T}{T_\infty} \nabla^2 T \tag{1.8}$$

where β_T is the thermal expansion coefficient, ν is the kinematic viscosity of the nanofluid. Further, ρ_p is the density of nanoparticle, $\rho_{f\infty}$ is the density of the base fluid, α is the thermal diffusivity of the nanofluid, D_B is the Brownian diffusion coefficient and D_T is the thermophoretic diffusion coefficient. Finally, $(\rho c)_f$ and $(\rho c)_p$ are the heat capacity of the nanofluid and the effective heat capacity of the nanoparticle material, respectively.

1.3 Porous Medium

A porous medium may be defined as a solid matrix containing holes either connected or non-connected, dispersed within the medium in a regular or random manner provided such holes occur frequently in the medium. If these pores are saturated with fluid, then the solid matrix with the fluid is called a fluid-saturated porous medium. This type of analysis in porous media plays an essential role in many fields of science and engineering, for instance, petroleum engineering, groundwater hydrology, agricultural engineering and soil mechanics. But, the flow of the fluid in a saturated porous material is possible only when some of the pores are interconnected.

To study the motion of fluids through porous media, one must have sufficient understanding of the governing equations for the fluid flow through porous medium. Owing to the intricate structure of the porous medium, several models have been proposed to explain mathematical and physical aspects of porous media. Among these, the Darcy model and a series of its modifications have attained much acceptance. Further, the boundary layer assumptions have been successfully applied to these models and much work over the last few decades has been done on them for a wide variety of geometries.

Darcy Model

The governing equation of fluid motion in a vertical porous column was first given by Darcy [23] in 1856. It represents a balance of viscous force, gravitational force and pressure gradient. In mathematical form, it is written as

$$\overrightarrow{q} = -\frac{K_p}{\mu}(\nabla p - \rho\, g) \tag{1.9}$$

where $\overrightarrow{q}$ is the space averaged velocity (or Darcian velocity), K_p is the (intrinsic) permeability of the medium, μ is the coefficient of viscosity. For one-dimensional flow and low porosity system, the above law appears to provide good agreement with experimental results. As this model does not take inertial effects into consideration, it is valid only for seepage flows, i.e., for flows with low Reynolds number $[O(Re) < 1]$.

Darcy-Brinkman Model

It is assumed that the flow through an anisotropic porous medium with high permeability must reduce to the viscous flow in a limit. In viewing this, Brinkman felt the need to account for the viscous force exerted by a flowing fluid on a dense swarm of spherical particles embedded in a porous mass and added the term $\mu' \nabla^2 V$ to balance the pressure gradient. Here μ' is the effective viscosity given by $\mu' = \mu[1 - 2.5(1-\epsilon)]$. The validity of the Brinkman model is restricted to the high porosity medium (as confirmed by the experiments) and its governing equation is given by

$$-\left[\nabla p - \rho g\right] = \frac{\mu}{K_p}\overrightarrow{q} - \mu' \nabla^2 \overrightarrow{q} \tag{1.10}$$

Darcy-Forchheimer Model

In 1901, Forchheimer conducted experiments and proposed that inertial effects can be accounted for by the addition of the square of velocity in the momentum equation. The modification to Darcy′s equation is

$$\left[1 + \frac{\rho\, c\sqrt{K_p}}{\mu}|\overrightarrow{q}|\right]\overrightarrow{q} = -\frac{K_p}{\mu}\left[\nabla p - \rho g\right] \tag{1.11}$$

where c is the dimensionless form drag coefficient and it varies with the nature of the porous medium. The coefficients of Darcy and Forchheimer terms contain both fluid properties and the microstructure of the porous medium. Several other models are found in the literature related to porous media, and the validity and limitations of these models are well discussed in the textbook by Nield and Bejan [84].

1.4 Convective Boundary Condition

It is seen from the literature that several investigators have considered convective heat transfer problems with either wall temperature or heat flux in Newtonian and/or non-Newtonian fluids. But, these conditions cannot explain the supply of heat with a finite heat capacity to the convecting fluid through a bounding surface. To demonstrate this, a novel mechanism for the heating process has drawn the attention of many researchers, known as the Convective Boundary Condition (CBC) (for more details see Aziz [8]). Further, the heat transfer with a convective boundary condition is more general and realistic, especially concerning various engineering and industrial processes including material drying, laser pulse heating and transpiration cooling. Also, it occurs when a solid substrate is in contact with the fluid at a different temperature and involves relative motion between the fluid and the substrate. The magnitude of heat exchange is described in terms of Newton's law of cooling, for which the relevant constitutive property of the system is the convective heat transfer coefficient. The convective boundary condition for heat transfer involves equating Fourier's law of conduction at the solid surface with Newton's law of cooling in the fluid as given below:

$$-k\frac{\partial T}{\partial y} = h_f(T_f - T) \tag{1.12}$$

where h_f is the convective heat transfer coefficient, k is the thermal conductivity of the fluid, and T_f is the temperature of the hot fluid.

1.5 Bivariate Pseudo-Spectral Local Linearization Method

The governing equations of convective heat and mass transfer in Newtonian and/or non-Newtonian fluids are essentially coupled and non-linear partial differential equations. Generally, these non-linear partial differential equations cannot be solved analytically, so recourse must be made to a numerical approach. Various numerical methods, including the finite element methods, finite difference methods, finite volume methods, spectral methods, shooting methods, boundary element methods, homotopy analysis method, cubic spline collocation method, etc., have been used by several researches to solve the system of nonlinear differential equations. Among these, a novel and rapid convergence approach named as the *Bivariate Pseudo-Spectral Local Linearization Method* (BPSLLM) is used to solve the governing partial differential equations in this work. Initially, this method has been introduced by Motsa [63] and it is the combination of local linearization technique and bivariate pseudo-spectral collocation method. This method has several desirable features that make it appropriate for the approximate solutions of partial differential equations. For more details about the pseudo-spectral collocation methods, one can follow the works of Motsa ([63], [64]). Also, an outstanding theoretical results on the various spectral methods, for solving the coupled system of highly non-linear differential equations defined on both regular and irregular domains, have been discussed by Gottlieb and Orszag [32].

In this section, we present the Bivariate Pseudo-Spectral Local Linearization Method (BPSLLM) for approximate solution of the system of non-linear partial differential equations. This method is presented for a general system of n nonlinear partial differential equations. For this, consider a system of n nonlinear partial differential equations of the following form:

$$\Upsilon_k \left[F_1, F_2, F_3, ..., F_n\right] = 0 \ \text{ for } \ k = 1, 2, 3, ..., n \tag{1.13}$$

where

$$\begin{aligned}
F_1 &= \left\{f_1, \frac{\partial f_1}{\partial \eta}, \frac{\partial^2 f_1}{\partial \eta^2}, \cdots, \frac{\partial^p f_1}{\partial \eta^p}, \frac{\partial f_1}{\partial \xi}, \frac{\partial}{\partial \xi}\left(\frac{\partial f_1}{\partial \eta}\right)\right\}, \\
F_2 &= \left\{f_2, \frac{\partial f_2}{\partial \eta}, \frac{\partial^2 f_2}{\partial \eta^2}, \cdots, \frac{\partial^p f_2}{\partial \eta^p}, \frac{\partial f_2}{\partial \xi}, \frac{\partial}{\partial \xi}\left(\frac{\partial f_2}{\partial \eta}\right)\right\}, \\
&\vdots \\
F_n &= \left\{f_n, \frac{\partial f_n}{\partial \eta}, \frac{\partial^2 f_n}{\partial \eta^2}, \cdots, \frac{\partial^p f_n}{\partial \eta^p}, \frac{\partial f_n}{\partial \xi}, \frac{\partial}{\partial \xi}\left(\frac{\partial f_n}{\partial \eta}\right)\right\}
\end{aligned} \tag{1.14}$$

in which p is the order of differentiation with respect to η, $f_k(\eta, \xi)$ are the approximate solutions of Eqs. (1.13) and Υ_k are the non-linear operators including the derivatives of $f_k(\eta, \xi)$ with respect to both η and ξ.

On applying the quasi-linearization technique (see Ref. [10]) independently in each equation, we obtain

$$
\begin{aligned}
F_{1,r+1} \cdot \nabla_{f_1} \Upsilon_1 \left[F_{1,r}, F_{2,r}, \cdots, F_{n,r}\right] = {} & F_{1,r} \cdot \nabla_{f_1} \Upsilon_1 \left[F_{1,r}, F_{2,r}, \cdots, F_{n,r}\right] \\
& - \Upsilon_1 \left[F_{1,r}, F_{2,r}, \cdots, F_{n,r}\right]
\end{aligned} \tag{1.15}
$$

$$
\begin{aligned}
F_{2,r+1} \cdot \nabla_{f_2} \Upsilon_2 \left[F_{1,r+1}, F_{2,r}, \cdots, F_{n,r}\right] = {} & F_{2,r} \cdot \nabla_{f_2} \Upsilon_2 \left[F_{1,r+1}, F_{2,r}, \cdots, F_{n,r}\right] \\
& - \Upsilon_2 \left[F_{1,r+1}, F_{2,r}, \cdots, F_{n,r}\right]
\end{aligned} \tag{1.16}
$$

$$\vdots$$

$$
\begin{gathered}
F_{n,r+1} \cdot \nabla_{f_n} \Upsilon_n \left[F_{1,r+1}, F_{2,r+1}, \cdots, F_{n-1,r+1}, F_{n,r}\right] = \\
F_{n,r} \cdot \nabla_{f_n} \Upsilon_n \left[F_{1,r+1}, F_{2,r+1}, \cdots, F_{n-1,r+1}, F_{n,r}\right] - \Upsilon_n \left[F_{1,r+1}, F_{2,r+1}, \cdots, F_{n-1,r+1}, F_{n,r}\right]
\end{gathered} \tag{1.17}
$$

where

$$
\begin{aligned}
\nabla_{f_1} &= \left\{ \frac{\partial}{\partial f_1}, \frac{\partial}{\partial f_1'}, \frac{\partial}{\partial f_1''}, \cdots, \frac{\partial}{\partial f_1^{(p)}}, \frac{\partial}{\partial \left(\frac{\partial f_1}{\partial \xi}\right)}, \frac{\partial}{\partial \left(\frac{\partial f_1'}{\partial \xi}\right)} \right\}, && (1.18) \\
\nabla_{f_2} &= \left\{ \frac{\partial}{\partial f_2}, \frac{\partial}{\partial f_2'}, \frac{\partial}{\partial f_2''}, \cdots, \frac{\partial}{\partial f_2^{(p)}}, \frac{\partial}{\partial \left(\frac{\partial f_2}{\partial \xi}\right)}, \frac{\partial}{\partial \left(\frac{\partial f_2'}{\partial \xi}\right)} \right\}, && (1.19) \\
&\vdots \\
\nabla_{f_n} &= \left\{ \frac{\partial}{\partial f_n}, \frac{\partial}{\partial f_n'}, \frac{\partial}{\partial f_n''}, \cdots, \frac{\partial}{\partial f_n^{(p)}}, \frac{\partial}{\partial \left(\frac{\partial f_n}{\partial \xi}\right)}, \frac{\partial}{\partial \left(\frac{\partial f_n'}{\partial \xi}\right)} \right\} && (1.20)
\end{aligned}
$$

where the prime denotes the differentiation with respect to η.

Further, the Eqs. (1.15)-(1.17) can be expressed as

$$\begin{aligned}
\sum_{l=0}^{p} \alpha_{l,r}^{(1)}(\eta,\xi) f_{1,r+1}^{(l)} + \beta_r^{(1)}(\eta,\xi) \frac{\partial f_{1,r+1}^{(0)}}{\partial \xi} + \gamma_r^{(1)}(\eta,\xi) \frac{\partial f_{1,r+1}^{(1)}}{\partial \xi} &= K_1(\eta,\xi), \\
\sum_{l=0}^{p} \alpha_{l,r}^{(2)}(\eta,\xi) f_{2,r+1}^{(l)} + \beta_r^{(2)}(\eta,\xi) \frac{\partial f_{2,r+1}^{(0)}}{\partial \xi} + \gamma_r^{(2)}(\eta,\xi) \frac{\partial f_{2,r+1}^{(1)}}{\partial \xi} &= K_2(\eta,\xi), \\
&\vdots \\
\sum_{l=0}^{p} \alpha_{l,r}^{(n)}(\eta,\xi) f_{n,r+1}^{(l)} + \beta_r^{(n)}(\eta,\xi) \frac{\partial f_{n,r+1}^{(0)}}{\partial \xi} + \gamma_r^{(n)}(\eta,\xi) \frac{\partial f_{n,r+1}^{(1)}}{\partial \xi} &= K_n(\eta,\xi) \qquad (1.21)
\end{aligned}$$

where $\alpha_{l,r}^{(k)}(\eta,\xi), \beta_r^{(k)}(\eta,\xi)$ and $\gamma_r^{(k)}(\eta,\xi)$ are the coefficients corresponding to the k^{th} partial differential equation for $k = 1, 2, 3, ..., n$ and $l = 0, 1, 2, ..., p$.

Since the constant p denotes the order of differential equation, we have the following

$$\alpha_{l,r}^{(k)}(\eta,\xi) = \frac{\partial \Upsilon_k}{\partial f_{k,r}^{(l)}}, \quad \beta_r^{(k)}(\eta,\xi) = \frac{\partial \Upsilon_k}{\partial \left(\frac{\partial f_{k,r}^{(0)}}{\partial \xi} \right)}, \quad \gamma_r^{(k)}(\eta,\xi) = \frac{\partial \Upsilon_k}{\partial \left(\frac{\partial f_{k,r}^{(1)}}{\partial \xi} \right)} \qquad (1.22)$$

and

$$K_k(\eta,\xi) = \sum_{l=0}^{p} \alpha_{l,r}^{(k)}(\eta,\xi) f_{k,r}^{(l)} + \beta_r^{(k)}(\eta,\xi) \frac{\partial f_{k,r}^{(0)}}{\partial \xi} + \gamma_r^{(k)}(\eta,\xi) \frac{\partial f_{k,r}^{(1)}}{\partial \xi} - \Upsilon_k \qquad (1.23)$$

The modified system of Eqs.(1.21) forms a system of n decoupled linear partial differential equations. Hence, these equations are to be solved iteratively for $f_1(\eta,\xi), f_2(\eta,\xi), \cdots, f_n(\eta,\xi)$ by using any numerical method. In this work, the bivariate pseudo-spectral collocation method is employed to solve the system of Eqs.(1.21) and it involves the following procedure.

Initially, the solutions can be approximated by a bivariate Lagrangian interpolation polynomials of the following form

$$f_k(\eta,\xi) \approx \sum_{i=0}^{N_x} \sum_{j=0}^{N_t} f_k(\eta_i,\xi_j) L_i(\eta) L_j(\xi), \quad \text{for} \quad k = 1, 2, ..., n \qquad (1.24)$$

where N_x and N_t are the number of collocation points in the η and ξ directions, respectively, and the characteristic Lagrange cardinal polynomial $L_i(\eta)$ is given by

$$L_i(\eta) = \prod_{\substack{i=0 \\ i \neq k}}^{N_x} \frac{\eta - \eta_k}{\eta_i - \eta_k} \text{ such that } L_i(\eta_k) = \delta_{ik} = \begin{cases} 0 & \text{if } i \neq k \\ 1 & \text{if } i = k \end{cases} \tag{1.25}$$

Next, the Chebyshev-Gauss-Lobatto collocation points are introduced to discretize both the domains of ξ and η, as follows

$$\eta_i = \cos\left(\frac{\pi i}{N_x}\right), \quad \xi_j = \cos\left(\frac{\pi j}{N_t}\right) \quad \text{for} \quad i = 0, 1, \ldots, N_x \quad \text{and} \quad j = 0, 1, \ldots, N_t \tag{1.26}$$

The derivatives of the unknown functions $f_k(\eta, \xi)$ with respect to η and ξ at the collocation points η_i and ξ_j are given by (see Canuto [14], Trefethen [119])

$$\left.\frac{\partial f_k}{\partial \eta}\right|_{(\eta_i,\xi_j)} = \sum_{m=0}^{N_x}\sum_{n=0}^{N_t} f_k(\eta_m, \xi_n)\frac{dL_m(\eta_i)}{d\eta}L_n(\xi_j) = \sum_{m=0}^{N_x} D_{i,m} f_k(\eta_m, \xi_j) = \mathbf{D}\mathbf{F}_{k,j}, \tag{1.27}$$

$$\left.\frac{\partial^2 f_k}{\partial \eta^2}\right|_{(\eta_i,\xi_j)} = \mathbf{D}^2\mathbf{F}_{k,j}, \quad \left.\frac{\partial^p f_k}{\partial \eta^p}\right|_{(\eta_i,\xi_j)} = \mathbf{D}^p\mathbf{F}_{k,j}, \tag{1.28}$$

$$\left.\frac{\partial f_k}{\partial \xi}\right|_{(\eta_i,\xi_j)} = \sum_{m=0}^{N_x}\sum_{n=0}^{N_t} f_k(\eta_m, \xi_n)L_m(\eta_i)\frac{dL_n(\xi_j)}{d\xi} = \sum_{n=0}^{N_t} d_{jn} f_k(\eta_i, \xi_n) = \sum_{n=0}^{N_t} \mathbf{dF}_{n,i} \tag{1.29}$$

where $D_{im} = \frac{dL_m(\eta_i)}{d\eta}$ is the $(i, m)^{th}$ entry of the standard first derivative Chebyshev differentiation matrix of size $(N_x + 1) \times (N_x + 1)$, and $d_{jn} = \frac{dL_n(\xi_j)}{d\xi}$ is the $(j, n)^{th}$ entry of the Chebyshev differentiation matrix of size $(N_t + 1) \times (N_t + 1)$ and the vector $\mathbf{F}_{k,j}$ is defined as

$$\mathbf{F}_{k,j} = [f_k(\eta_0, \xi_j), f_k(\eta_1, \xi_j), \ldots, f_k(\eta_{N_x}, \xi_j)]^T \tag{1.30}$$

On solving the system of Eqs. (1.21) at the Chebyshev-Gauss-Lobbatto collocation points

(η_i, ξ_j), we get

$$\begin{aligned}
&B^{(1)}\mathbf{F}_{1,i} + \boldsymbol{\beta}_r^{(1)} \sum_{j=0}^{N_t} d_{ij}\mathbf{F}_{1,j} + \boldsymbol{\gamma}_r^{(1)} \sum_{j=0}^{N_t} d_{ij}\mathbf{D}\mathbf{F}_{1,j} = \mathbf{R}_{1,i}, \\
&B^{(2)}\mathbf{F}_{2,i} + \boldsymbol{\beta}_r^{(2)} \sum_{j=0}^{N_t} d_{ij}\mathbf{F}_{2,j} + \boldsymbol{\gamma}_r^{(2)} \sum_{j=0}^{N_t} d_{ij}\mathbf{D}\mathbf{F}_{2,j} = \mathbf{R}_{2,i}, \\
&\qquad\qquad\qquad\qquad\qquad\qquad\vdots \\
&B^{(n)}\mathbf{F}_{n,i} + \boldsymbol{\beta}_r^{(n)} \sum_{j=0}^{N_t} d_{ij}\mathbf{F}_{n,j} + \boldsymbol{\gamma}_r^{(n)} \sum_{j=0}^{N_t} d_{ij}\mathbf{D}\mathbf{F}_{n,j} = \mathbf{R}_{n,i} \qquad (1.31)
\end{aligned}$$

where

$$B^{(1)} = \sum_{l=0}^{p} \boldsymbol{\alpha}_{l,r}^{(1)}\mathbf{D}^{(l)}, \quad B^{(2)} = \sum_{l=0}^{p} \boldsymbol{\alpha}_{l,r}^{(2)}\mathbf{D}^{(l)}, \cdots, B^{(n)} = \sum_{l=0}^{p} \boldsymbol{\alpha}_{l,r}^{(n)}\mathbf{D}^{(l)} \qquad (1.32)$$

in which $\boldsymbol{\alpha}_{l,r}^{(k)} = diag[\alpha_{l,r}^{(k)}(\eta_i, \xi_j)]$, $\boldsymbol{\beta}_r^{(k)} = diag[\beta_r^{(k)}(\eta_i, \xi_j)]$ and $\boldsymbol{\gamma}_r^{(k)} = diag[\gamma_r^{(k)}(\eta_i, \xi_j)]$ are the diagonal matrices at each k^{th} equations.

Now, the system of Eqs. (1.31) can be expressed as the matrix form with $(N_t+1)(N_x+1) \times (N_t+1)(N_x+1)$ order, as follows

$$\begin{bmatrix} B_{0,0}^{(k)} & B_{0,1}^{(k)} & B_{0,2}^{(k)} & \cdots & B_{0,N_t}^{(k)} \\ B_{1,0}^{(k)} & B_{1,1}^{(k)} & B_{1,2}^{(k)} & \cdots & B_{1,N_t}^{(k)} \\ B_{2,0}^{(k)} & B_{2,1}^{(k)} & B_{2,2}^{(k)} & \cdots & B_{2,N_t}^{(k)} \\ \vdots & \vdots & \vdots & \cdots & \vdots \\ B_{N_t,0}^{(k)} & B_{N_t,1}^{(k)} & B_{N_t,2}^{(k)} & \cdots & B_{N_t,N_t}^{(k)} \end{bmatrix} \begin{bmatrix} \mathbf{F}_{k,0} \\ \mathbf{F}_{k,1} \\ \mathbf{F}_{k,2} \\ \vdots \\ \mathbf{F}_{k,N_t} \end{bmatrix} = \begin{bmatrix} \mathbf{R}_{k,0} \\ \mathbf{R}_{k,1} \\ \mathbf{R}_{k,2} \\ \vdots \\ \mathbf{R}_{k,N_t} \end{bmatrix} \qquad (1.33)$$

where

$$\begin{aligned}
B_{i,i}^{(k)} &= \sum_{l=0}^{p} \boldsymbol{\alpha}_{l,r}^{(k)}\mathbf{D}^{(l)} + \boldsymbol{\beta}_r^{(k)} d_{ii}\mathbf{I} + \boldsymbol{\gamma}_r^{(k)} d_{ii}\mathbf{D}, \quad \text{for} \quad k = 1,2,3,...,n, \ \text{ when } \ i = j \\
B_{i,j}^{(k)} &= \boldsymbol{\beta}_r^{(k)} d_{ij}\mathbf{I} + \boldsymbol{\gamma}_r^{(k)} d_{ij}\mathbf{D}, \quad \text{for} \quad k = 1,2,3,...,n, \ \text{ when } \ i \neq j
\end{aligned}$$

After incorporating the boundary conditions, the above system of equations in matrix form is solved iteratively by taking a suitable initial approximations.

1.6 Literature Review

The study of free and mixed convection due to a heated or cooled vertical surface provides one of the most basic scenarios for heat and mass transfer theory and thus is of considerable theoretical and practical interest. Free convection of heat and mass transfer occurs simultaneously in the fields of design of chemical processing equipment, formation and dispersion of fog, distributions of temperature, moisture over agricultural fields and groves of fruit trees. It also occurs in the context of damage to crops due to freezing and pollution of the environment. The phenomenon of mixed convection occurs in many technical and industrial problems such as electronic devices cooled by fans, nuclear reactors cooled during an emergency shutdown, a heat exchanger placed in a low-velocity environment, solar collectors, and so on.

Convective flow along a vertical surface embedded in a porous medium, is one of the fundamental and classical problems in the heat and mass transfer theory. It has attracted a great deal of interest from many investigators owing to the broad applications such as geothermal systems, energy-storage units, heat insulation, heat exchangers, drying technology, catalytic reactors, nuclear waste repositories, etc. The literature relevant to the convective flows over different surface geometries in Darcy and non-Darcy porous media has been reported by Ingham and Pop [39], Nield and Bejan [84], Vafai [122] (see the citations therein).

During the past decades, the study of nanofluids has gained much interest due to its numerous applications in science and engineering. Nanofluids are prepared by dispersing solid nanoparticles in conventional fluids such as water, oil, or ethylene glycol. Choi *et al.* [22] showed that the addition of small amount (less than 1 by volume) of nanoparticles to conventional heat transfer fluids enhances the thermal conductivity of the fluid. The detailed introduction and applications of nanofluids can be found in Das *et al.* [24]. Buongiorno [13] developed an analytical model for convective transport in nanofluids, which takes Brownian diffusion and thermophoresis effects into account. The literature on nanofluids has been reviewed by Daungthongsuk and Wongwises [25], Trisaksri and Wongwises [120], Wang and Mujumdar [126, 127, 128], Eastman *et al.* [27], and Kakac and Pramuanjaroenkij [45], Gianluca *et al.* [31] among several others. These reviews provide details of the research work carried out by the various authors on the convective transport in nanofluids.

The study of convective heat and mass transfer over the vertical frustum of a cone has attracted the interest of scientists and researchers, as a consequence of their important applications in engineering and industrial processes. Initially, the natural convective flow over the vertical frustum of a cone has been investigated by Na and Chiou [75]. Vasantha *et al.* [124] discussed the natural convective flow over the vertical frustum of a cone embedded in a non-Darcy porous medium. The laminar natural convective flow over the vertical frustum of a cone has been studied by Singh *et al.* [114]. Yih [130] analyzed the heat and mass transfer characteristics over the truncated cone embedded in a porous medium. The natural convective boundary layer flow of a nanofluid over the vertical frustum of a cone embedded in a porous medium has been reported by Cheng [17]. Patrulescu *et al.* [88] proposed a mathematical model for combined free and forced convective flow of a nanofluid over the vertical frustum of a cone.

On the other hand, the study of boundary layer flows with heat and mass transfer over the rotating bodies, is essential for various engineering applications such as the design of turbo-machines and turbines, rotating machinery, estimation of flight path in rotating wheels, transpiration cooling, spin-stabilized missiles, and in the modeling of several geophysical systems. Due to the centrifugal force created by rotational bodies, the fluid close to the surface of the body is enforced in the radial direction, and then this outward fluid is restored with the fluid in the axial direction. Therefore, the fluid velocity in the axial direction over the rotating bodies is larger than that of stationary bodies. This development in the axial velocity helps to increase the heat transfer rate between the contacting fluid and surface of the body. The effect of variable temperature on the convective flow due to a rotating cone has been studied by Hering and Grosh [36]. Wang *et al.* [125] suggested a new streamwise coordinate, which also serves as a mixed convection parameter, for the steady and laminar mixed convective flow of a quiescent fluid over the stationary/rotating cone. Pop and Na [93] examined roles of the half angle and streamwise coordinate on the boundary layer flow over the rotating frustum of a cone. The effects of magnetic field and heat generation/absorption on the laminar, steady and mixed convective flow of a power-law fluid over the rotating permeable cone in a porous medium have been investigated by Chamkha [16]. Narayana *et al.* [77] explored the effects of cross-diffusion on MHD natural convective flow over the spinning cone under two types of temperature boundary conditions (LST and LSHF).

Further, the prediction of heat and mass transfer from the wavy surfaces (irregular or non-uniform or rough surfaces) is of fundamental importance, and is encountered in several heat transfer devices, such as flat-plate solar collectors and flat-plate condensers in refrigerators. Irregularities frequently occur in the process of manufacture. Moreover, surfaces are sometimes intentionally roughened to enhance heat transfer because that the presence of rough surfaces disturbs the flow and alters the heat transfer rate. Among several others, Pop and Na ([90], [91], [92] and [94]) examined the various problems on natural convective flow with heat transfer over the vertical wavy cone/wavy frustum of a cone in a fluid saturated with/without Darcy porous medium. Cheng [19] considered the free convective flow over the vertical wavy cone embedded in a Darcy porous medium, whereas Hossain *et al.* [38] explored the effect of variable viscosity on the natural convective flow of a viscous fluid over the vertical wavy cone. Siddiqa *et al.* [113] obtained the numerical solution for the natural convective flow over the vertical wavy cone in the presence of nonlinear thermal radiation and variable properties. A comprehensive review on the natural and mixed convective flows with heat transfer over wavy surface geometries has been presented by Shenoy *et al.* [111].

During the motion of fluid particles, the viscosity of the fluid converts some kinetic energy into thermal energy. This process, which is caused due to viscosity, is irreversible and is known as dissipation or viscous dissipation. It may arise in several devices which are treated with substantial deceleration or operate at high rotative speed (see Gebhart [30]). The following literature provides some of the most useful and related information on the viscous dissipation in fluid flows. Murthy and Singh [71] studied the free convective flow along an isothermal vertical plate in a non-Darcy porous medium in the presence of viscous dissipation. They noticed that the presence of viscous dissipation parameter reduces the heat transfer rate about 10% in every flow regimes. The effects of viscous dissipation and transverse magnetic field on the boundary layer flow of a nanofluid, with heat transfer and fluid-particle suspension, over an exponentially stretching sheet have been discussed by Krishnamurthy *et al.* [51]. The entropy generation analysis of the free convective flow of a nanofluid over the vertical cone in a non-Darcy porous medium, in the presence of Newtonian heating and viscous dissipation, has been presented by Mahdy *et al.* [58]. Recently, Afify [1] discussed the effects of viscous dissipation and multiple slips on the boundary layer flow of a nanofluid over the stretching surface.

The occurrence of diffusive flux due to temperature gradient is known as the thermal-diffusion or Soret effect. In most of the studies, Soret effect is neglected on the basis that it is of a smaller order of magnitude than the effects described by Fourier's and Fick's laws. This Soret effect plays an important role in many natural activities, viz., in the underlying physics of the solar ponds, the demographics of an ocean and also convection in stars (see Ingham and Pop [39]). Also, it has been utilized for isotope separation and in a mixture between gases with very light weight molecular (H_2, He) and of medium weight molecular (N_2, air) [28]. Due to its significant applications, several authors analyzed the Soret effect on Newtonian and non-Newtonian fluids through different geometries. Dursunkaya and Worek [26] studied the cross-diffusion effects on natural convective flow along a vertical surface. Kafoussias and Williams [43] discussed the mixed convective flow along a vertical plate under the influence of Soret and Dufour effects. Awad *et al.* [7] analyzed the cross-diffusion effects on convective flow from an inverted cone embedded in a porous medium. Cheng [18] examined the effects of Soret and Dufour on the double-diffusive free convective flow over the vertical truncated cone in a porous medium. Kameswaran *et al.* [46] considered the convective heat and mass transfer in a hydromagnetic nanofluid flow over a stretching sheet subject to the Soret and viscous dissipation effects.

Stratification of fluid occurs due to temperature variations, concentration differences, or the presence of different fluids. The analysis of free and mixed convective flows in a doubly stratified medium is fundamentally interesting and relevant problem, due to its broad range of applications in engineering. These applications include heat rejection into the environment such as lakes, rivers, and seas; thermal energy storage systems such as solar ponds; and heat transfer from thermal sources such as the condensers of power plants. However, the effect of double stratification on free and mixed convection in a porous medium has received little attention. Initially, this phenomenon has been reported theoretically by Prandtl [95] for infinite wall problem, whereas for semi-infinite wall has been investigated by Jaluria and Himasekhar [41]. Tewari and Singh [117] examined the natural convection in a thermally stratified fluid saturated porous medium. The problem of natural convective heat and mass transfer along a vertical surface in a doubly stratified porous medium has been addressed by Narayana and Murthy [79]. The effects of thermal and solutal stratification on mixed convection in a non- Darcy porous medium has been studied by Murthy *et al.* [69]. The double-diffusive free convective flow over the vertical wavy frustum of a cone in a non-Newtonian fluid saturated porous medium in the presence of double stratification has been reported by Cheng [20]. He reported that the heat and mass transfer rates between the wavy surface and the fluid decrease with the increase of thermal and solutal stratification parameters. Narayana *et al.* [78] studied the problem of natural convection from a vertical plate in a thermally stratified non-Newtonian fluid saturated porous medium.

In view of the emerging applications of a stratified nanofluid, Rosmila *et al.* [106] analyzed the MHD free convective flow of an incompressible nanofluid past a semi-infinite vertical stretching sheet in the presence of thermal stratification. The effects of thermophoresis and Brownian motion on MHD boundary layer flow of a thermally stratified nanofluid have been studied by Kandaswamy *et al.* [48]. Srinivasacharya and Surender [115] presented the natural convective flow along a vertical plate embedded in a porous medium saturated by a stratified nanofluid. Rashad *et al.* [105] performed a numerical study to investigate the effect of thermal stratification on the convective flow of a nanofluid over the vertical cylinder. The effect of thermal stratification on free convective flow of a nanofluid along a vertical plate embedded in a non-Darcy porous medium has been explored by Ramreddy *et al.* [101].

The uniform wall temperature or flux condition may not valid in some industrial and engineering systems. For instance, material processing, geothermal systems, and in the design of thermal insulation, it has been observed that free convection can induce thermal stresses that lead to critical structural damage in the piping systems of nuclear reactors. To overcome this, a realistic and more generalized representation in the form of convective boundary condition is considered in the heat transfer analysis (for more details, see Aziz [8]). Further, Makinde and Aziz [60] numerically investigated the influence of convective boundary condition on MHD mixed convective heat and mass transfer along a vertical plate embedded in a porous medium. Ishak [40] studied the effects of suction/injection on steady laminar boundary layer flow over a permeable surface in the presence of convective boundary condition. Later, the effects of magnetic field and Biot number on free convective flow of a thermally stratified nanofluid saturated non-Darcy porous medium has been studied by Murthy *et al.* [70]. Recently, Rahman [99] considered the mixed convective boundary layer flow along a vertical plate with the convective boundary condition.

Most of the problems related to the chemically reacting systems occurring in the mechanics of oil and water emulsions, oil reservoir and geothermal engineering demand a finite activation energy along with the species chemical reactions. The term activation energy, initiated by Swante Arrheniusis in 1889, is characterized by the least amount of energy that uses to change the reactants to products. Usually, the interactions between the mass transport and chemical reactions are very complex and frequently noticed in the various rates of production and consumption of reactant species within the fluid medium and mass transfer. Therefore, it is necessary to discuss the theoretical studies rather than experimental studies to investigate the effect of Arrhenius activation energy on the fluid flow and mass transfer models. In the earlier days, Bestman [11] explored the effect of binary chemical reaction along with Arrhenius activation energy on the natural convective flow through the porous media. Subsequently, he presented the heat transfer analysis in the flow of a combustible mixture through a vertical pipe with Arrhenius activation energy and thermal radiation (see Bestman [12]). Recently, few more contributions in this area have been reported by Awad *et al.* [6], Shafique *et al.* [108], and Mustafa *et al.* [73].

The effect of thermal radiation in different fluid flows, is very useful in the nuclear plants, gas turbines, various propulsion devices for aircraft, missiles, satellites, space vehicles, etc. At high temperature, the thermal radiation can significantly affect the heat transfer rate and the temperature distribution within the boundary layer flow of a participating fluid. Also, the thermal radiation may play an essential role in controlling the heat transfer in industries where the quality of final product depends on the heat controlling factors to some extent. Because of these applications, Hossain and Takhar [37] considered the mixed convective boundary layer flow along a heated vertical plate in the presence of thermal radiation. Yih [130] presented a numerical investigation to study the radiation effect on natural convective flow of a viscous fluid over the vertical truncated cone. The effects of thermal radiation and convective boundary condition on free convective flow of a nanofluid over a stretching sheet have been addressed by Rahman and Eltayeb [98]. The effects of thermal radiation, homogeneous chemical reaction and heat source on the stagnation point flow of a nanofluid over the stretching surface have been examined by Makinde *et al.* [61]. Ramzan *et al.* [104] investigated the effects of thermal radiation, MHD and double stratification on a micropolar nanofluid flow in the presence of activation energy with binary chemical reaction.

The effects of thermal and solutal dispersion in a porous medium are essential due to the existence of inertial effects (see Nield and Bejan [84]). The heat and mass transport due to the hydrodynamic mixing is called thermal and solutal dispersions, respectively. These thermal and solutal dispersions cause additional heat and mass transfer rates, which brings further complications in dealing with transport processes in a fluid medium. The interest in the above studies is motivated by numerous engineering applications such as geothermal engineering, thermal insulation systems, petroleum recovery, packed bed reactors, sensible heat storage beds, ceramic processing, groundwater pollution, etc. Further, the natural convection driven by thermal and solutal dispersions play an essential role in the overall heat and mass transfer rates. In view of the above said applications, Telles and Trevisan [116] presented the hydrodynamic dispersion effect on free convective heat and mass transfer near to the vertical surface in a porous medium. The effects of thermal and solutal dispersion in a non-Darcy porous medium have been discussed by Murthy [68]. Murthy and Singh [72] investigated the thermal dispersion effect on the mixed convective flow over the isothermal vertical cone embedded in a non-Darcy porous medium. The effects of double dispersion and variable viscosity on free convective flow of a non-Newtonian fluid over the vertical cone embedded in a non-Darcy porous medium have been explored by Kairi [44]. RamReddy [100] discussed the thermal and solutal dispersion effects on the free convective flow over the vertical cone (also see the references therein).

In a wider range, most of the researchers have considered the linear relationship between temperature-concentration and density variations in the buoyancy force term. But, the presence of various physical conditions like inertia, viscous dissipation, radiation, and different densities in the temperature, the variations of density with temperature-concentration may become nonlinear. This kind of nonlinear relationship is important in various industrial and geothermal engineering applications, for instance, the design of thermal systems, cooling transpiration, cooling of electric components, drying of the surfaces, solar collectors, combustion, space technology, geophysics, etc. Mainly, these nonlinear temperature and density variations show more effect on the velocity of the flow field and heat transfer rate (see Vajravelu and Sastri [123]), when there is a significant change in the wall and ambient temperatures. Partha [87] developed a mathematical model to study the nonlinear variations in the temperature-concentration dependent density in a non-Darcy porous medium. He observed that with the increase of nonlinear temperature and concentration parameters, the heat and mass transfer varies extensively depending on Darcy and non-Darcy porous media. Prasad *et al.* [96] scrutinized the natural convective flow along a vertical flat plate in a non-Darcy porous medium with the nonlinear density-temperature parameter. The nonlinear convective flow over an impulsive stretching sheet has been examined by Motsa *et al.* [65]. The effect of nonlinear density temperature parameter in a nanofluid flow over the stretching sheet has been studied by Shaw *et al.* [109].

From the available literature, it is clear that the study of nanofluid flow over the vertical frustum of a cone under different conditions has not received significant attention so far. Also, it seems from the literature that the similarity solution does not exist in the case of vertical frustum of a cone (see [75], [114], [129], [130]). Hence, one has to use suitable non-similarity transformations to find out the approximate solutions for the governing system of partial differential equations.

Due to the important applications of nanofluid with and/or without saturated non-Darcy porous medium, the usefulness of convective flows over the vertical frustum of a cone has been analyzed in this thesis. In addition, the Buongiorno's nanofluid model which incorporates the effects of Brownian motion and thermophoresis, is considered in the present analysis. The problems considered in this thesis are outlined in the next section.

1.7 Aim and Scope

The objective of the present thesis is to explore the non-similarity solution for convective flows of a nanofluid over the vertical frustum of a cone. The study focusses on the attributes of various effects such as Brownian motion, thermophoresis, Arrhenius activation energy with binary chemical reaction, double stratification, double dispersion, thermal radiation, suction/injection, nonlinear convection, amplitude and angle of the wavy frustum of a cone, Soret and viscous dissipation. In the present study, a nanofluid based on Buongiorno's model is used. The problems undertaken in the thesis deal with the vertical frustum of a cone, rotating frustum of a cone and wavy frustum of a cone for the two cases: (i) free/natural convection and (ii) mixed convection.

1.8 Outline of the Thesis

This thesis consists of EIGHT chapters. Chapter - 1 is introductory in nature and gives motivation to the investigations carried out in the thesis. A survey of pertinent literature is presented to exhibit the importance of problems considered. The basic equations governing the flow, heat and mass transfers of a nanofluid and details of the numerical method (Bivariate Pseudo-Spectral Local Linearization Method) are given.

A numerical investigation on the convective flow of a nanofluid over the vertical frustum of a cone in the presence of Soret and viscous dissipation effects, is presented in Chapter - 2. The non-dimensional velocity, temperature, nanoparticle volume fraction and regular concentration profiles are displayed graphically for different values of Soret number, Eckert number, thermophoresis and Brownian motion parameters. In addition, the non-dimensional surface drag, local heat, nanoparticle and regular mass transfer rates versus streamwise coordinate are presented and discussed for various values of the pertinent parameters.

Chapter - 3 deals with the problem of steady, convective heat and mass transport over the vertical frustum of a cone embedded in a non-Darcy porous medium saturated by a doubly stratified nanofluid. The effects of non-Darcy parameter, thermal and solutal stratification parameters on the non-dimensional velocity, temperature, nanoparticle volume fraction and the regular concentration along with the skin friction, local Nusselt number, local nanoparticle and regular Sherwood numbers are discussed and analyzed through graphs.

The combined effects of Arrhenius activation energy with binary chemical reaction and thermal radiation on the convective flow over the vertical frustum of a cone in a Buongiorno's nanofluid subject to the convective boundary condition, are examined in Chapter-4. The obtained numerical results are exhibited graphically to demonstrate the influence of thermal radiation, Biot number, activation energy, chemical reaction rate and temperature relative parameters on the dimensionless velocity, temperature, nanoparticle volume fraction and regular concentration. Further, the effects of pertinent physical parameters on the non-dimensional surface drag, local heat, nanoparticle and regular mass transfer rates versus streamwise coordinate are also explored and displayed through graphs.

In Chapter - 5, an attempt has been made to investigate the thermal and solutal dispersion effects on the convective flow over the vertical frustum of a cone in a nanofluid saturated non-Darcy porous medium subject to the convective boundary condition. The effects of various parameters, namely Biot number, non-Darcy, thermal dispersion and solutal dispersion parameters on physical quantities of the flow are explored in detail and some interesting results have been obtained.

Chapter - 6 reports a non-similarity solution for the convective flow of a nanofluid due to the vertically rotating permeable frustum of a cone under the influence of convective type thermal boundary condition. The obtained numerical results are exhibited graphically to illustrate the effects of suction/injection parameter, spinning parameter and Biot number on the dimensionless tangential velocity, swirl velocity, temperature, nanoparticle volume fraction and regular concentration profiles. Further, the non-dimensional surface drag, local heat, nanoparticle and regular mass transfer rates against the streamwise coordinate are analyzed and presented through graphs.

A non-similarity solution for the nonlinear convective flow of a nanofluid over the permeable wavy frustum of a cone, in the presence of convective boundary condition, is presented in Chapter - 7. The effects of various parameters, namely wavy amplitude, half angle of the wavy cone, Biot number, suction/injection, nonlinear density temperature (NDT) and nonlinear density concentration (NDC) parameters on physical quantities of the nanofluid flow are explored in detail and some interesting results have been obtained.

In all the above chapters (2 - 7), the nonlinear governing boundary layer equations and their associated boundary conditions are initially cast into dimensionless form by introducing a suitable non-similarity variables. The resulting system of non-similarity equations is then solved numerically by employing Bivariate Pseudo-Spectral Local Linearization Method (BPSLLM). Initially, the governing equations are linearized by using local linearization technique and then solved by applying pseudo-spectral collocation method [14]. The convergence and error analysis tests have conducted to examine the accuracy of the BPSLLM. In a special case of the above chapters, the accuracy test is conducted through comparison with asymptotic series solutions for limiting cases of small and large values of the streamwise coordinate (for more details, see [66]). To validate the BPSLLM, the obtained numerical results are compared with the existing results in some special cases and the outcomes are observed to be in a good agreement.

The main conclusions of the earlier chapters are listed and the directions in which further investigations may be carried out are also indicated in Chapter - 8.

List of references is given at the end of the thesis. The references are arranged in an alphabetical order.

Considerable part of the work in the thesis is published/accepted for publication in reputed journals. The remaining part is communicated for possible publications. The details are presented below.

List of papers published

1. "Bivariate pseudo-spectral local linearisation approach for the Soret and viscous dissipation effects on natural convective flow of Buongiorno nanofluid model over vertical frustum of a cone", ***Journal of Nanofluids***, Vol. 6(3), pp. 530-540, (2017).

2. "Bivariate pseudo-spectral local linearisation method for mixed convective flow over the vertical frustum of a cone in a nanofluid with Soret and viscous dissipation effects", ***Journal of Mechanics***, Vol. 33(5), pp. 687-702, (2017).

3. "Non-similarity solutions for natural convective flow of a nanofluid over vertical frustum of a cone embedded in a doubly stratified non-Darcy porous medium", ***International Journal of Applied and Computational Mathematics***, Vol. 3(1), pp. 99-113, (2017).

4. "Double stratification effects on mixed convection boundary layer flow of a nanofluid over vertical frustum of a cone: A Darcy-Forchheimers model", ***Journal of Nanofluids***, Vol. 6(5), pp. 971-981, (2017).

5. "Effects of Arrhenius activation energy and binary chemical reaction on convective flow of a nanoflluid over frustum of a cone with convective boundary condition", ***International Journal of Chemical Reactor Engineering***, Vol. 16(3), (2018), DOI: 10.1515/ijcre-2016-0188.

6. "Double dispersion effects on non-Darcy free convective boundary layer flow of a nanofluid over vertical frustum of a cone with convective boundary condition", ***Nonlinear Engineering***, Vol. 6(4), pp. 277-292, (2017).

7. "Bivariate pseudo-spectral local linearisation method for non-Darcy convection flow of a nanofluid over vertical frustum of a cone with Biot number and double dispersion", ***Heat Transfer Research***, DOI: 10.1615/HeatTransRes.2018018754.

8. "Non-similarity analysis for nonlinear convective flow of a nanofluid over the permeable wavy frustum of a cone with convective boundary condition", ***Journal of Nanofluids***, Vol. 7, pp. 1258-1271, (2018).

List of papers accepted

9. “Numerical study for mixed convective flow of a radiative nanofluid over the vertical frustum of a cone with Arrhenius activation energy and binary chemical reaction”, Accepted for publication in ***Advanced Science, Engineering and Medicine***.

List of papers communicated

10. “Non-similarity solution for natural convective flow of a nanofluid over the vertically rotating frustum of a permeable cone with convective boundary condition”, Communicated to ***Sadhana-Academy Proceedings in Engineering Sciences***.
11. “Mixed convective flow of a nanofluid over the vertically rotating frustum of a permeable cone with convective boundary condition: A non-similarity solution”, Communicated to ***Zeitschrift fuer Angewandte Mathematik und Physik (ZAMP)***.
12. “Nonlinear Boussinesq approximation for mixed convective flow of a nanofluid over the permeable wavy frustum of a cone with convective boundary condition”, Communicated to ***International Journal of Numerical Methods for Heat and Fluid Flow***.

Chapter 2

Non-Similarity Solution for a Nanofluid Flow over the Vertical Frustum of a Cone with Soret and Viscous Dissipation Effects [1]

2.1 Introduction

A broad area of research on convective flows over the vertical frustum of a cone in Newtonian and/or non-Newtonian fluids, has received continuous attention due to its significant engineering applications such as heat exchangers, cooling of electronic devices, etc. (For more details, see Nakamura *et al.* [76]). Ahmed and Mahdy [3] studied the laminar, natural convective boundary layer flow over the isothermal frustum of a cone under the influence of transverse magnetic field. Recently, the natural convective flow over the vertical frustum of a cone in the presence of thermal radiation and heat generation/absorption effects, has been discussed by Elbashbeshy *et al.* [29].

---

[1] Case(a): Published in "**Journal of Nanofluids**" 6(3) (2017) 530–540, Case(b): Published in "**Journal of Mechanics**" 33(5) (2017) 687–702

In a fluid flow system, the Soret (thermal-diffusion) effect is a thermodynamic phenomenon in which the molecules in fluids are carried in a multi-component mixture impelled by temperature gradients. It becomes more significant when the large density differences exist in a flow regime. For example, the Soret effect can be notable when a species is introduced at the surface in a fluid domain with a density lower than the surrounding fluid (see [110], [102]). Many investigators have been tried to explore the importance of viscous dissipation in Newtonian and/or non-Newtonian fluids through various geometries in the recent past. Because the viscous dissipation acts as a heat source and initiates substantial temperature in the surrounding medium. From the literature, it seems that a limited work has been reported on the convective flows of a nanofluid over the vertical frustum of a cone in the presence of Soret and viscous dissipation effects. The effect of Soret on the laminar boundary layer flow over the vertical cone embedded in a porous medium saturated by a nanofluid has been analyzed by Hady *et al.* [33]. Recently, RamReddy and Pradeepa [103] explored the effects of Soret and viscous dissipation on the mixed convective flow a non-Newtonian fluid over the vertical frustum of a cone (for more details, see the references therein).

The problem of Soret and viscous dissipation effects on the convective flow of a nanofluid over the isothermal frustum of a cone is considered in this chapter. According to the author's knowledge, the present study has not been addressed in the literature. From the literature survey, it seems that the similarity solution does not exist for the convective flow of over the frustum of a cone (see [75], [114], [129], [130]). Hence, a suitable set of non-similarity transformations is used to transform the governing dimensional equations into non-dimensional form. The resulting system of non-similarity equations is then solved numerically by employing Bivariate Pseudo-Spectral Local Linearization Method (BPSLLM). The convergence and error analysis tests have conducted to validate the BPSLLM. Further, the accuracy of the present numerical solution is undertaken in a special case through comparison with the asymptotic series solution for limiting cases of small and large values of ξ (Ref. Motsa *et al.* [66]). The effects of pertinent parameters on the non-dimensional velocity, temperature, nanoparticle volume fraction and regular concentration profiles as well as, on the surface drag, and local heat and mass transfer rates are analyzed and shown graphically.

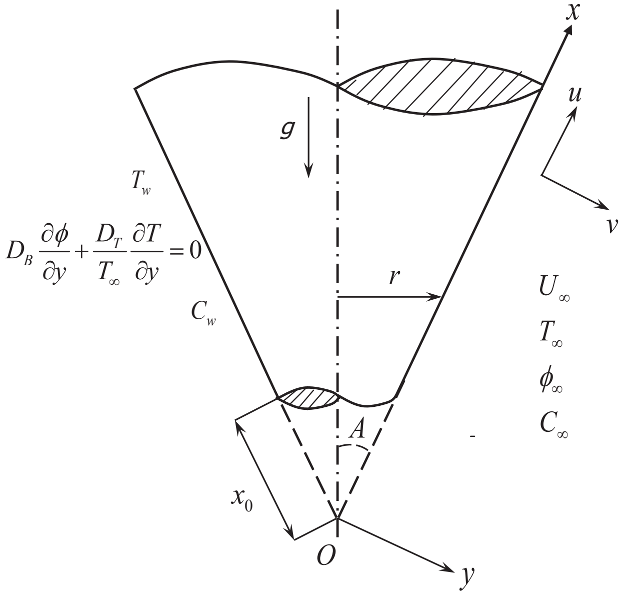

Figure 2.1: Physical model and coordinate system.

2.2 Mathematical Formulation

Consider a steady, laminar and two dimensional flow of an incompressible nanofluid over the vertical frustum of a cone with half angle A. The coordinate geometry of the problem is chosen such that x-axis is along the surface of full cone and y-axis is normal to the surface of vertical frustum of a cone with the origin O at the vertex of full cone. The physical model of the problem is shown in Fig. (2.1). The surface is maintaining at uniform temperature T_w, solutal concentration C_w and zero nanoparticle flux $D_B \frac{\partial \phi}{\partial y} + \frac{D_T}{T_\infty} \frac{\partial T}{\partial y} = 0$ (see Kuznetsov and Nield [54]). The velocity, temperature, nanoparticle volume fraction and regular concentration of the ambient nanofluid are taken as U_∞, T_∞, C_∞, and ϕ_∞, respectively. The boundary layers are assumed to develop at the leading edge of the vertical frustum of a cone ($x = x_0$), which implies that the temperature and regular concentration of the surrounding fluid and circular base are same.

By employing standard boundary layer assumptions and linear Boussinesq approximation, the governing equations of the present investigation are given by (see [75])

$$\frac{\partial (u\,r)}{\partial x} + \frac{\partial (v\,r)}{\partial y} = 0 \tag{2.1}$$

$$\rho_{f\infty}\left(u\frac{\partial u}{\partial x} + v\frac{\partial u}{\partial y}\right) = \mu\frac{\partial^2 u}{\partial y^2} + \rho_{f\infty} g\,(1-\phi_\infty)\left[\beta_T(T-T_\infty) + \beta_C(C-C_\infty)\right]\cos A \\ -(\rho_p - \rho_{f\infty})g(\phi-\phi_\infty)\cos A \tag{2.2}$$

$$u\frac{\partial T}{\partial x} + v\frac{\partial T}{\partial y} = \alpha_m\frac{\partial^2 T}{\partial y^2} + \mathcal{J}\left[D_B\frac{\partial \phi}{\partial y}\frac{\partial T}{\partial y} + \frac{D_T}{T_\infty}\left(\frac{\partial T}{\partial y}\right)^2\right] + \frac{\mu}{\rho_{f\infty} C_p}\left(\frac{\partial u}{\partial y}\right)^2 \tag{2.3}$$

$$u\frac{\partial \phi}{\partial x} + v\frac{\partial \phi}{\partial y} = D_B\frac{\partial^2 \phi}{\partial y^2} + \frac{D_T}{T_\infty}\frac{\partial^2 T}{\partial y^2} \tag{2.4}$$

$$u\frac{\partial C}{\partial x} + v\frac{\partial C}{\partial y} = D_S\frac{\partial^2 C}{\partial y^2} + D_{CT}\frac{\partial^2 T}{\partial y^2} \tag{2.5}$$

where u and v are the components of velocity along x and y–axes, respectively, T is the temperature, ϕ is the nanoparticle volume fraction, C is the regular concentration, g is the acceleration due to gravity, $\alpha_m = k/(\rho c)_f$ is the thermal diffusivity of the fluid, $\nu = \mu/\rho_{f_\infty}$ is the coefficient of kinematic viscosity and $\mathcal{J} = (\rho c)_p/(\rho c)_f$. Moreover, ρ_{f_∞} is the density of the base fluid, and k, μ, ρ, β_T and β_C are the thermal conductivity, viscosity, density, volumetric thermal and solutal expansion coefficients of the nanofluid. Further, ρ_p is the density of the nanoparticles, $(\rho c)_f$ and $(\rho c)_p$ are the heat capacity of the fluid and nanoparticle material, respectively. In Eqs. (2.3) - (2.5), D_B is the Brownian diffusion coefficient, D_T is the thermophoretic diffusion coefficient, D_S is the solutal diffusivity and D_{CT} is the Soret-type diffusivity. The same notations are used throughout the thesis unless otherwise specified.

The associated boundary conditions are

$$u = 0,\;\; v = 0,\;\; T = T_w,\;\; D_B\frac{\partial \phi}{\partial y} + \frac{D_T}{T_\infty}\frac{\partial T}{\partial y} = 0,\;\; C = C_w \quad \text{at} \quad y = 0 \tag{2.6a}$$

$$u = U_\infty,\;\; T = T_\infty,\;\; \phi = \phi_\infty,\;\; C = C_\infty \quad \text{as} \quad y \to \infty \tag{2.6b}$$

where the subscripts w and ∞ indicate the conditions at the wall and the outer edge of a boundary layer respectively.

We also assumed that the thickness of boundary layers are sufficiently small as comparing with the local radius of the vertical frustum of a cone. Therefore, the local radius to a point in the boundary layer can be approximated by the radius of vertical frustum of a cone r, i.e., $r = x \sin A$ (Ref. Singh *et al.* [114]). The Eqs. (2.1) - (2.5) along with the corresponding boundary conditions (2.6) are valid in $x_0 < x < \infty$, where x_0 is the distance of leading edge of the vertical frustum of a cone which is measured from the origin O.

Now, we introduce a stream function ψ such that it satisfies the continuity equation (2.1) automatically, and it is defined as

$$u = \frac{1}{r}\frac{\partial \psi}{\partial y},\ v = -\frac{1}{r}\frac{\partial \psi}{\partial x} \tag{2.7}$$

In this chapter, two types (cases) of problems are considered: (a) free/natural convection and (b) mixed convection.

2.2.1 Case(a): Natural Convection

The flow is assumed to be a natural convection which is caused by buoyancy forces only without any external agent, and hence the velocity of the external flow becomes zero, $i.e., U_\infty = 0$. Initially, we introduce the following non-similarity variables

$$\xi = \frac{\overline{x}}{x_0} = \frac{x - x_0}{x_0},\ \eta = \frac{y}{\overline{x}}\, Gr_{\overline{x}}^{1/4},\ \psi = r\nu Gr_{\overline{x}}^{1/4}\, f\left(\xi, \eta\right),$$

$$\theta\left(\xi, \eta\right) = \frac{T - T_\infty}{T_w - T_\infty},\ \gamma\left(\xi, \eta\right) = \frac{\phi - \phi_\infty}{\phi_\infty},\ S\left(\xi, \eta\right) = \frac{C - C_\infty}{C_w - C_\infty} \tag{2.8}$$

where $\overline{x} = x - x_0$ and $Gr_{\overline{x}} = \dfrac{g\beta_T(T_w - T_\infty)(1-\phi_\infty)\overline{x}^3 \cos A}{\nu^2}$ is the local Grashof number.

Substituting Eqs. (2.7)-(2.8) into Eqs.(2.2)-(2.5), the governing equations reduces to the following form:

$$f''' + \left(R + \frac{3}{4}\right) f\, f'' - \frac{1}{2}\,(f')^2 + \theta + Nc\, S - Nr\,\gamma = \xi \left(f' \frac{\partial f'}{\partial \xi} - \frac{\partial f}{\partial \xi} f'' \right) \tag{2.9}$$

$$\frac{1}{Pr}\theta'' + \left(R + \frac{3}{4}\right) f\, \theta' + Nb\, \gamma'\, \theta' + Nt\, (\theta')^2 + Ec\, \xi\, (f'')^2 = \xi \left(f' \frac{\partial \theta}{\partial \xi} - \frac{\partial f}{\partial \xi} \theta' \right) \tag{2.10}$$

$$\frac{1}{Le}\gamma'' + \left(R + \frac{3}{4}\right) f\, \gamma' + \frac{1}{Le}\frac{Nt}{Nb}\,\theta'' = \xi \left(f' \frac{\partial \gamma}{\partial \xi} - \frac{\partial f}{\partial \xi} \gamma' \right) \tag{2.11}$$

$$\frac{1}{Sc}S'' + \left(R + \frac{3}{4}\right) f\, S' + S_T \theta'' = \xi \left(f' \frac{\partial S}{\partial \xi} - \frac{\partial f}{\partial \xi} S' \right) \tag{2.12}$$

where the prime represents the partial differentiation with respect to η, $Pr = \dfrac{\nu}{\alpha_m}$ is the Prandtl number, $Nr = \dfrac{(\rho_p - \rho_{f\infty})\phi_\infty}{\rho_{f\infty}\beta_T(T_w - T_\infty)(1 - \phi_\infty)}$ is the nanofluid buoyancy ratio, $Nc = \dfrac{\beta_C(C_w - C_\infty)}{\beta_T(T_w - T_\infty)}$ is the regular buoyancy ratio, $Sc = \dfrac{\nu}{D_S}$ is the Schmidt number, $Nb = \dfrac{(\rho c)_p D_B \phi_\infty}{(\rho c)_f \nu}$ is the Brownian motion parameter, $Le = \dfrac{\nu}{D_B}$ is the Lewis number, $Nt = \dfrac{(\rho c)_p D_T (T_w - T_\infty)}{(\rho c)_f \nu T_\infty}$ is the thermophoresis parameter, $S_T = \dfrac{D_{CT}(T_w - T_\infty)}{\nu(C_w - C_\infty)}$ is the Soret number and $Ec = \dfrac{u_e^2}{C_p(T_w - T_\infty)}$ is the Eckert number.

The corresponding boundary conditions become

$$f(\xi,\eta) + \frac{\xi}{\left(R + \frac{3}{4}\right)}\frac{\partial f}{\partial \xi} = 0,\ f'(\xi,\eta) = 0,\ \theta(\xi,\eta) = 1,\ Nb\,\gamma'(\xi,\eta) + Nt\,\theta'(\xi,\eta) = 0,$$

$$S(\xi,\eta) = 1, \quad \text{at} \quad \eta = 0 \tag{2.13a}$$

$$f'(\xi,\eta) = 0,\ \theta(\xi,\eta) = 0,\ \gamma(\xi,\eta) = 0,\ S(\xi,\eta) = 0 \quad \text{as} \quad \eta \to \infty \tag{2.13b}$$

where $R = \dfrac{\xi}{(1+\xi)}$. When $\xi = 0$, R becomes zero, and hence the present problem reduces to the problem of natural convective flow of a nanofluid along a vertical plate. Since $\xi = \dfrac{(x - x_0)}{x_0}$, ξ becomes large means x is far down-stream or the cross-section radius of the leading edge of the frustum of a cone is very small. In this situation, the similarity solutions are expected for the natural convective flow over a full cone (see Hering [35]).

The wall shear stress, local heat, nanoparticle mass and regular mass fluxes over the vertical frustum of a cone are

$$\tau_w = \mu \left[\frac{\partial u}{\partial y}\right]_{y=0},\ q_w = -k\left[\frac{\partial T}{\partial y}\right]_{y=0},\ q_n = -D_B\left[\frac{\partial \phi}{\partial y}\right]_{y=0} \text{ and } q_m = -D_S\left[\frac{\partial C}{\partial y}\right]_{y=0} \tag{2.14}$$

The non-dimensional skin friction $C_f = \dfrac{2\tau_w}{\rho_{f\infty} U_*^2}$, the local Nusselt number $Nu_{\overline{x}} = \dfrac{q_w \overline{x}}{k(T_w - T_\infty)}$, the local nanoparticle Sherwood number $NSh_{\overline{x}} = \dfrac{q_n \overline{x}}{D_B \phi_\infty}$ and the local regular Sherwood number $Sh_{\overline{x}} = \dfrac{q_m \overline{x}}{D_S(C_w - C_\infty)}$, are given by

$$\left.\begin{array}{l} C_f Gr_{\overline{x}}^{1/4} = 2\, f''(\xi,0),\ \dfrac{Nu_{\overline{x}}}{Gr_{\overline{x}}^{1/4}} = -\theta'(\xi,0), \\ \dfrac{NSh_{\overline{x}}}{Gr_{\overline{x}}^{1/4}} = -\gamma'(\xi,0),\ \dfrac{Sh_{\overline{x}}}{Gr_{\overline{x}}^{1/4}} = -S'(\xi,0) \end{array}\right\} \tag{2.15}$$

where U_* is the characteristic velocity.

Numerical Solution

The governing Eqs. (2.9)-(2.12) subject to the boundary conditions (2.13) are solved numerically using the Bivariate Pseudo-Spectral Local Linearization Method (BPSLLM) (for more details, see Motsa *et al.* [66]). The following procedure describes the main steps of the Bivariate Pseudo-Spectral Local Linearization Method.

Assume that the solutions f_r, θ_r, γ_r and S_r of Eqs.(2.9)-(2.12) at the $(r+1)^{th}$ iteration are f_{r+1}, θ_{r+1}, γ_{r+1} and S_{r+1}, respectively. If the solutions at the previous iteration are sufficiently close to the solutions at the present iteration, then the nonlinear components of Eqs.(2.9)-(2.12) can be locally linearised using one–term Taylor series so that the Eqs.(2.9)-(2.12) give the following iterative sequence of linear differential equations

$$f'''_{r+1} + a_{1,r}\, f''_{r+1} + a_{2,r}\, f'_{r+1} + a_{3,r}\, f_{r+1} + a_{4,r}\,\frac{\partial f'_{r+1}}{\partial \xi} + a_{5,r}\,\frac{\partial f_{r+1}}{\partial \xi} = K_{1,r} \tag{2.16}$$

$$\frac{1}{Pr}\,\theta''_{r+1} + b_{1,r}\,\theta'_{r+1} + b_{2,r}\,\frac{\partial \theta_{r+1}}{\partial \xi} = K_{2,r} \tag{2.17}$$

$$\frac{1}{Le}\,\gamma''_{r+1} + c_{1,r}\,\gamma'_{r+1} + c_{2,r}\,\frac{\partial \gamma_{r+1}}{\partial \xi} = K_{3,r} \tag{2.18}$$

$$\frac{1}{Sc}\,S''_{r+1} + e_{1,r}\,S'_{r+1} + e_{2,r}\,\frac{\partial S_{r+1}}{\partial \xi} = K_{4,r} \tag{2.19}$$

where the coefficients $a_{s_1,r}(s_1 = 1, 2, .., 5)$, $b_{s_2,r}(s_2 = 1, 2)$, $c_{s_3,r}(s_3 = 1, 2)$, $e_{s_4,r}(s_4 = 1, 2)$ and $K_{s_5,r}(s_5 = 1, 2, .., 4)$ are known functions, which are evaluated from the previous iterations, and are given by

$$a_{1,r} = \left(R + \frac{3}{4}\right)\,f_r + \xi\frac{\partial f_r}{\partial \xi},\;\; a_{2,r} = -f'_r - \xi\frac{\partial f'_r}{\partial \xi},\;\; a_{3,r} = \left(R + \frac{3}{4}\right)\,f''_r,\;\; a_{4,r} = -\xi f'_r,$$

$$a_{5,r} = \xi f''_r,\;\; K_{1,r} = \left(R + \frac{3}{4}\right)\,f_r\,f''_r - \frac{1}{2}\,(f'_r)^2 + \xi\left(f''_r\frac{\partial f_r}{\partial \xi} - f'_r\frac{\partial f'_r}{\partial \xi}\right) - \theta_r - Nc\,S_r + Nr\,\gamma_r,$$

$$b_{1,r} = \left(R + \frac{3}{4}\right)\,f_{r+1} + Nb\,\gamma'_r + 2\,Nt\,\theta'_r + \xi\frac{\partial f_{r+1}}{\partial \xi},\;\; b_{2,r} = -\xi f'_{r+1},\;\; K_{2,r} = Nt\,\left(\theta'_r\right)^2 - Ec\,\left(f''_r\right)^2,$$

$$c_{1,r} = \left(R + \frac{3}{4}\right)\,f_{r+1} + \xi\frac{\partial f_{r+1}}{\partial \xi},\;\; c_{2,r} = -\xi f'_{r+1},\;\; K_{3,r} = -\frac{1}{Le}\,\frac{Nt}{Nb}\,\theta''_{r+1},$$

$$e_{1,r} = \left(R + \frac{3}{4}\right)\,f_{r+1} + \xi\frac{\partial f_{r+1}}{\partial \xi},\;\; e_{2,r} = -\xi f'_{r+1},\;\; K_{4,r} = -S_T\,\theta''_{r+1}$$

The system of Eqs. (2.16)-(2.19) constitute a linear system of coupled partial differential equations with variable coefficients and it can be solved iteratively using any numerical method. In this work, the bivariate pseudo-spectral collocation method is employed to solve the system of Eqs. (2.16)-(2.19) with the boundary conditions (2.13). Starting from the following set of initial approximations

$$f_0(\eta) = \frac{1}{2} + \frac{1}{2}e^{-2\eta} - e^{-\eta},\; \theta_0(\eta) = e^{-\eta},\; \gamma_0(\eta) = -\frac{Nt}{Nb}\,e^{-\eta},\; S_0(\eta) = e^{-\eta} \tag{2.20}$$

the system of linearized Eqs. (2.16)-(2.19) is solved iteratively for $f_{r+1}(\eta)$, $\theta_{r+1}(\eta)$, $\gamma_{r+1}(\eta)$ and $S_{r+1}(\eta)$.

For this, the physical region $[0, \infty) \times [0, \infty)$ is transformed into the region $[-1, 1] \times [-1, 1]$

using the domain truncation technique, in which the problem is solved on the region $[0, \eta_\infty] \times [0, \xi_\infty]$ instead of $[0, \infty) \times [0, \infty)$. This leads to the following mappings

$$\frac{\eta}{\eta_\infty} = \frac{\zeta + 1}{2} \quad \text{and} \quad \frac{\xi}{\xi_\infty} = \frac{\tau + 1}{2} \quad \text{for} \quad -1 \leq \zeta, \tau \leq 1 \tag{2.21}$$

where η_∞ and ξ_∞ are the scaling parameters, which are used to invoke the boundary conditions at infinity.

To discretize the unknown functions in the truncated region, the following Gauss–Lobatto collocation points are introduced

$$\zeta_i = \cos\left(\frac{\pi i}{N_x}\right), \quad \tau_j = \cos\left(\frac{\pi j}{N_\tau}\right) \quad \text{for} \quad i = 0, 1, \ldots, N_x \quad \text{and} \quad j = 0, 1, \ldots, N_\tau \tag{2.22}$$

where N_x and N_τ are the number of collocation points in η and ξ – directions, respectively.

The unknown functions are approximated by the bivariate Lagrange's polynomials of the form

$$f(\eta, \xi) \approx \sum_{m=0}^{N_x} \sum_{j=0}^{N_\tau} f(\zeta_m, \tau_j) L_m(\zeta) L_j(\tau) \tag{2.23}$$

which interpolates $f(\eta, \xi)$ at the collocation points defined by Eq. (2.22). The similar expressions are used to obtain the approximate functions for $\theta(\eta, \xi)$, $\gamma(\eta, \xi)$ and $S(\eta, \xi)$. Here, the functions $L_m(\zeta)$ and $L_j(\tau)$ are known as the characteristic Lagrange cardinal polynomials.

The derivatives of the unknown function $f(\eta, \xi)$ with respect to η and ξ, at the collocation points ζ_k and τ_i, are defined as (see Canuto *et al.* [14] and Trefethen [119])

$$\left.\frac{\partial f}{\partial \eta}\right|_{(\zeta_k, \tau_i)} = \frac{2}{\eta_\infty} \sum_{m=0}^{N_x} \sum_{j=0}^{N_\tau} f(\zeta_m, \tau_j) \frac{dL_m(\zeta_k)}{d\zeta} L_j(\tau_i) = \mathbf{D}\mathbf{F}_i, \tag{2.24}$$

$$\left.\frac{\partial^2 f}{\partial \eta^2}\right|_{(\zeta_k, \tau_i)} = \mathbf{D}^2\mathbf{F}_i, \quad \left.\frac{\partial^3 f}{\partial \eta^3}\right|_{(\zeta_k, \tau_i)} = \mathbf{D}^3\mathbf{F}_i, \tag{2.25}$$

$$\left.\frac{\partial f}{\partial \xi}\right|_{(\zeta_k, \tau_i)} = \frac{2}{\xi_\infty} \sum_{m=0}^{N_x} \sum_{j=0}^{N_\tau} f(\zeta_m, \tau_j) \frac{dL_j(\tau_i)}{d\tau} L_m(\zeta_k) = \frac{2}{\xi_\infty} \sum_{j=0}^{N_\tau} d_{ij}\mathbf{F}_j = \sum_{j=0}^{N_\tau} \mathbf{d}\mathbf{F}_j. \tag{2.26}$$

In the above, d_{ij}'s are entries of the standard Chebyshev differentiation matrix $\mathbf{d} = \frac{2}{\xi_\infty}[d_{ij}]$ of size $(N_\tau + 1) \times (N_\tau + 1)$ and $\mathbf{D} = (2/\eta_\infty)[D_{rs}]$ being an $(N_x + 1) \times (N_x + 1)$ Chebyshev spectral differentiation matrix and the vector $\mathbf{F}_i$ is defined as

$$\mathbf{F}_i = [f_i(\zeta_0), f_i(\zeta_1), \ldots, f_i(\zeta_{N_x})]^T \tag{2.27}$$

where $0 \le i, j \le N_t$ and $0 \le r, s \le N_x$.

Similar kind of expressions are used for derivatives of the unknown functions θ, γ and S with respect to η and ξ. On applying the pseudo-spectral collocation method to Eqs. (2.16)-(2.19) in both η and ξ–directions gives

$$A^{(1)}\mathbf{F}_i + \mathbf{a}_{4,i}\sum_{j=0}^{N_t}\mathbf{d}_{ij}\mathbf{D}\mathbf{F}_j + \mathbf{a}_{5,i}\sum_{j=0}^{N_t}\mathbf{d}_{ij}\mathbf{F}_j = \mathbf{K}_{1,i} \tag{2.28}$$

$$A^{(2)}\mathbf{\Theta}_i + \mathbf{b}_{2,i}\sum_{j=0}^{N_t}\mathbf{d}_{ij}\mathbf{\Theta}_j = \mathbf{K}_{2,i} \tag{2.29}$$

$$A^{(3)}\mathbf{G}_i + \mathbf{c}_{2,i}\sum_{j=0}^{N_t}\mathbf{d}_{ij}\mathbf{G}_j = \mathbf{K}_{3,i} \tag{2.30}$$

$$A^{(4)}\mathbf{S}_i + \mathbf{e}_{2,i}\sum_{j=0}^{N_t}\mathbf{d}_{ij}\mathbf{S}_j = \mathbf{K}_{4,i} \tag{2.31}$$

where

$$A^{(1)} = \mathbf{D}^3 + \mathbf{a}_{1,i}\mathbf{D}^2 + \mathbf{a}_{2,i}\mathbf{D} + \mathbf{a}_{3,i}, \;\; A^{(2)} = \frac{1}{Pr}\mathbf{D}^2 + \mathbf{b}_{1,i}\mathbf{D},$$

$$A^{(3)} = \frac{1}{Le}\mathbf{D}^2 + \mathbf{c}_{1,i}\mathbf{D}, \;\; A^{(4)} = \frac{1}{Sc}\mathbf{D}^2 + \mathbf{e}_{1,i}\mathbf{D}.$$

The system of Eqs. (2.28) can be written in matrix form as

$$\begin{bmatrix} A^{(1)}_{0,0} & A^{(1)}_{0,1} & A^{(1)}_{0,2} & \cdots & A^{(1)}_{0,N_t} \\ A^{(1)}_{1,0} & A^{(1)}_{1,1} & A^{(1)}_{1,2} & \cdots & A^{(1)}_{1,N_t} \\ A^{(1)}_{2,0} & A^{(1)}_{2,1} & A^{(1)}_{2,2} & \cdots & A^{(1)}_{2,N_t} \\ \vdots & \vdots & \vdots & \cdots & \vdots \\ A^{(1)}_{N_t,0} & A^{(1)}_{N_t,1} & A^{(1)}_{N_t,2} & \cdots & A^{(1)}_{N_t,N_t} \end{bmatrix} \begin{bmatrix} \mathbf{F}_0 \\ \mathbf{F}_1 \\ \mathbf{F}_2 \\ \vdots \\ \mathbf{F}_{N_t} \end{bmatrix} = \begin{bmatrix} \mathbf{K}_{1,0} \\ \mathbf{K}_{1,1} \\ \mathbf{K}_{1,2} \\ \vdots \\ \mathbf{K}_{1,N_t} \end{bmatrix} \tag{2.32}$$

for $i = 0, 1, \ldots, N_t$ and

$$A^{(1)}_{i,j} = A^{(1)} + \mathbf{a}_{4,i}\mathbf{d}_{ii}\mathbf{D} + \mathbf{a}_{5,i}\mathbf{d}_{ii}\mathbf{I}, \quad i = j, \tag{2.33}$$

$$A^{(1)}_{i,j} = \mathbf{a}_{4,i}\mathbf{d}_{ij}\mathbf{D} + \mathbf{a}_{5,i}\mathbf{d}_{ij}\mathbf{I}, \quad i \neq j. \tag{2.34}$$

In the similar way, the matrix form of Eqs. (2.29)-(2.31) can be obtained. To find the approximate solution, the system of equations in matrix form is solved iteratively by starting with a suitable initial approximations as given in Eq. (2.20).

In this chapter, a finite computational domain of extent $\eta_\infty = 30$ and $\xi_\infty = 15$ are taken in the η and ξ-directions, respectively. Through numerical experimentation, these values have been found to give accurate results for all the selected physical parameters. Moreover, the results have not been changed with the increase of η_∞ and ξ_∞ to significant extent. The number of collocation points N_x and N_t used in the pseudo-spectral collocation method for discretization are 60 and 15, respectively. The iteration calculations are carried until some appropriate tolerance level is obtained. In this analysis, the tolerance level has fixed to be 10^{-4}.

Validation of the BPSLLM

To validate the numerical solution obtained by using the method as described in the above section, the series solutions about small and large values of ξ have been computed for residual errors. It can be noticed that the residual errors decrease with an increase in the number of iterations for both small and large values of ξ. This trend indicates the convergence of the series solutions and the convergence is much faster for both small and large values of ξ (For more details, one can refer the work of Motsa *et al.* [66]).

Further, the residual errors for the solutions of f, θ, γ and S have been evaluated to show the accuracy and convergence of the BPSLLM. These residuals are defined as the norm of the difference between two successive iterations, and it is said to have converged when the norms are less than a given tolerance level. The residual error norms are given by

$$\left.\begin{aligned} E_f &= \max_{0\le i\le Nx} \|f_{r+1,i} - f_{r,i}\|_\infty,\ E_\theta = \max_{0\le i\le Nx} \|\theta_{r+1,i} - \theta_{r,i}\|_\infty, \\ E_\gamma &= \max_{0\le i\le Nx} \|\gamma_{r+1,i} - \gamma_{r,i}\|_\infty,\ E_S = \max_{0\le i\le Nx} \|S_{r+1,i} - S_{r,i}\|_\infty \end{aligned}\right\} \tag{2.35}$$

Figures 2.2(a)-2.2(d) depict the variations in the norm of residual errors of the four governing equations (2.9)-(2.12) across ξ, at different iteration levels of the BPSLLM. It can be seen from Figs. 2.2(a)-2.2(d) that the residual errors decrease with an increase in the number of iterations. This trend is an indication for the convergence of present numerical solutions. It can be also observed that the residual errors are uniform and very small across ξ, as shown in Figs. 2.2(a)-2.2(d). These results reveal that the accuracy of BPSLLM does not depend on the length of streamwise coordinate ξ. Therefore, the residual error analysis gives a clear sign to use BPSLLM for solving the partial differential equations.

Results and Discussion

In order to assess the generated code, for the special case of $Nt = 0.0$, $Ec = 0.0$, $S_T = 0.0$, $Nc = 0.0$, $Nr = 0.0$, $Sc = 1.0$, $Le = 1.0$ and $Nb \to 0.0$, the results of the present problem have been compared with those of Na and Chiou [75], Kays and Crawford [49], Lin and Chen [55] and Yih [130]. It is found that they are in good agreement as shown in Tab. (2.1). To analyze the effects of Soret number S_T, Brownian motion parameter Nb, thermophoresis parameter Nt and Eckert number Ec, the computations are carried out for $Pr = 1.0$,

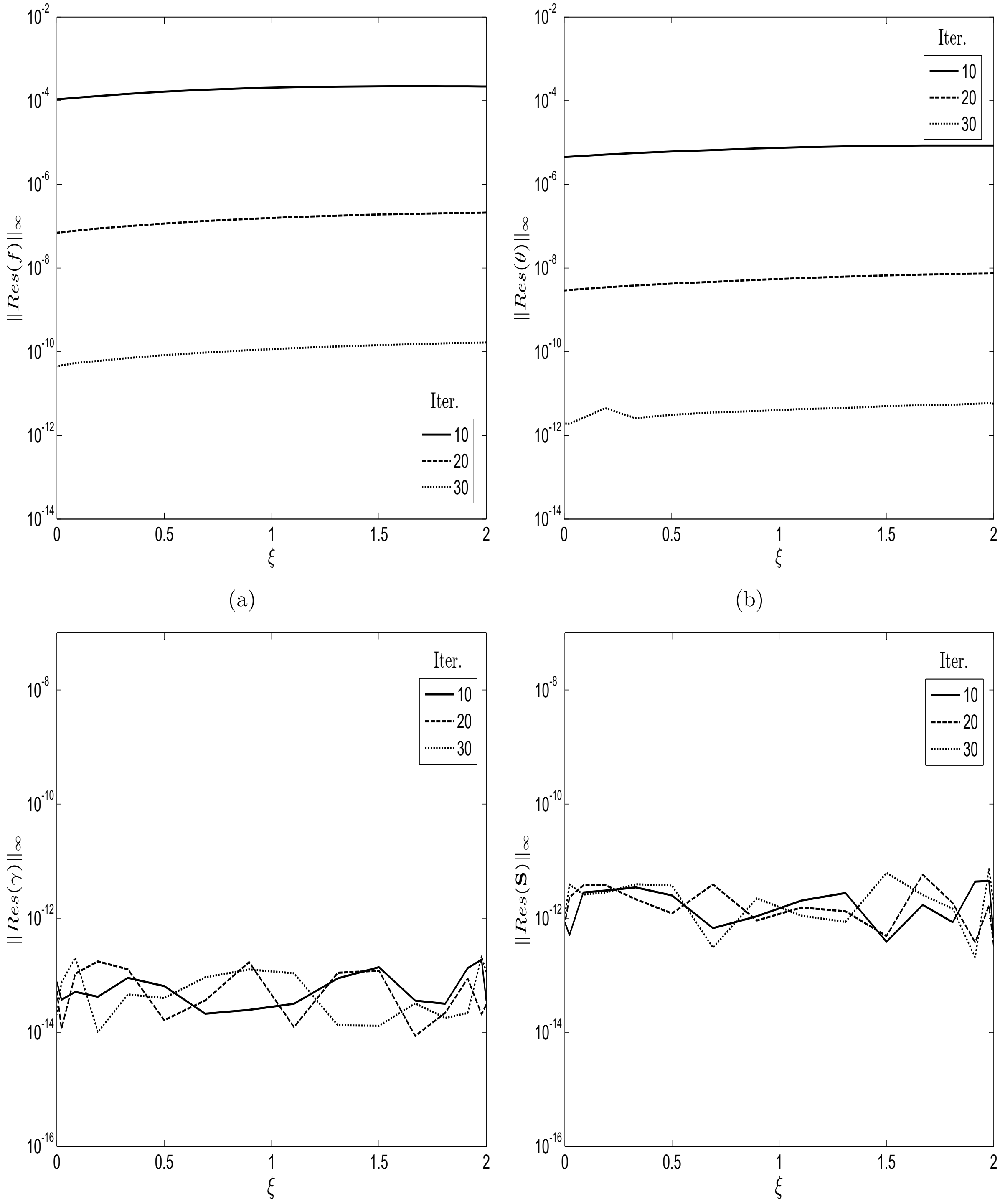

(a) (b)

(c) (d)

Figure 2.2: *Residual errors over number of iterations when* $Pr = 1.0$, $Sc = 0.6$, $Nr = 0.5$, $Nc = 1.0$, $S_T = 1.0$, $Le = 10.0$, $Nb = 0.2$, $Nt = 0.3$ *and* $Ec = 0.2$.

Table 2.1: *Comparison of* $f''(0,\,0)$ *and* $-\theta'(0,\,0)$ *for various values of* Pr.

	$f''(0,\,0)$		$-\theta'(0,\,0)$				
Pr	[130]	Present	[75]	[49]	[55]	[130]	Present
0.1	1.2144	1.21446092	——	0.1640	0.1627	0.1629	0.16275771
1.0	0.9084	0.90819121	0.4010	0.4010	0.4009	0.4012	0.40103314
10.0	0.5927	0.59283234	0.8269	0.8270	0.8258	0.8266	0.82684304
100.0	0.3559	0.35587198	1.5493	1.5500	1.5490	1.5493	1.54948222
1000.0	0.2049	0.19648944	——	2.8000	2.8035	2.8035	2.79895132

$Sc = 0.6$, $Nr = 0.5$, $Nc = 1.0$, and $Le = 10.0$. These values are fixed in this analysis unless otherwise mentioned.

The distributions of non-dimensional velocity f', temperature θ, nanoparticle volume fraction γ and regular concentration S, under the influence of Soret number (S_T) and Eckert number (Ec), are displayed in Figs. 2.3(a)-2.3(d). From Figs. 2.3(a)-2.3(d), it is evident that an increase in the Soret number leads to increase the velocity and regular concentration, but decrease the temperature and nanoparticle volume fraction. The velocity, temperature and nanoparticle volume fraction profiles increase with the increase of viscous dissipation parameter. This is due to the fact that the viscous dissipation acts as a heat source and affects the fluid flow. Hence, it increases the thermal buoyancy effects which causes to increase the velocity and temperature. As the viscous dissipation parameter increases, the regular concentration shows a reverse behavior within the boundary layer.

Figures 2.4(a)-2.4(d) explore the effects of thermophoresis parameter (Nt) and Brownian motion parameter (Nb) on the dimensionless velocity f', temperature θ, nanoparticle volume fraction γ and regular concentration S, across the corresponding boundary layers. As expected the strengthening of Brownian motion parameter (i.e., the diffusion of nanoparticles into the fluid) leads to strengthen the velocity and temperature, as shown in Figs. 2.4(a) and 2.4(b). But, the nanoparticle volume fraction increases near to the vertical frustum of a cone and decreases far away from the surface, with the increase of Brownian motion parameter, as plotted in Fig. 2.4(c). Figure 2.4(d) shows that as Brownian motion parameter increases, the regular concentration decreases for fixed value of thermophoresis parameter. On the other hand, an increase in the thermophoresis parameter causes to increase the velocity and decrease the regular concentration, as given in Figs. 2.4(a) and 2.4(d). This is due to the enhancement of thermophoresis force. Furthermore, an increase in the thermophoresis parameter increases the temperature and nanoparticle volume fraction near to the surface.

The variations of surface drag, local heat, local nanoparticle mass and regular mass transfer rates over the streamwise coordinate ξ for different values of Soret number (S_T) and Eckert number (Ec), are plotted in Figs. 2.5(a)-2.5(d). From Fig. 2.5(a), it is seen that the skin friction coefficient increases with the increase of Soret and Eckert numbers. As the Soret number enhances, the heat transfer rate enhances for $Ec = 0.01$ and $Ec = 0.1$. But, the heat transfer rate reduces by enhancing the values of Eckert number, as shown in Fig. 2.5(b). It is perceived that, with the increase of Soret number, the local nanoparticle and regular mass transfer rates decrease. But, the local nanoparticle and regular mass transfer rates increase with the increase of Eckert number, as depicted in Figs. 2.5(c) and 2.5(d). Moreover, the local heat and regular mass transfer rates enhance, whereas the skin friction coefficient and local nanoparticle mass transfer rate reduce along with the streamwise coordinate ξ.

Figures 2.6(a)-2.6(d) determine the influence of Brownian motion parameter (Nb) and thermophoresis parameter (Nt) on the surface drag, local heat transfer rate, local nanoparticle and regular mass transfer rates, over ξ. From these figures, it is noticed that the surface drag and local nanoparticle mass transfer rate decrease, with increasing values of Brownian motion parameter. But, the local nanoparticle mass transfer rate increases with the increase of Brownian motion parameter. As the thermophoresis parameter enhances, the surface drag and local regular mass transfer enhance, whereas the local nanoparticle mass transfer rate reduces, as plotted in Figs. 2.6(a) and 2.6(d). However, with the increase of thermophoresis parameter, the local nanoparticle mass transfer rate decreases. The thermophoresis force is proportional to the temperature gradient from hot fluid to cold fluid, whereas the Brownian motion is proportional to the volumetric fraction of nanoparticles in the direction from high concentration to low concentration. Hence, it is noted that the presence of Brownian motion enhance the local heat transfer rate, whereas the presence of thermophoresis reduce the local heat transfer rate, as shown in Fig. 2.6(b).

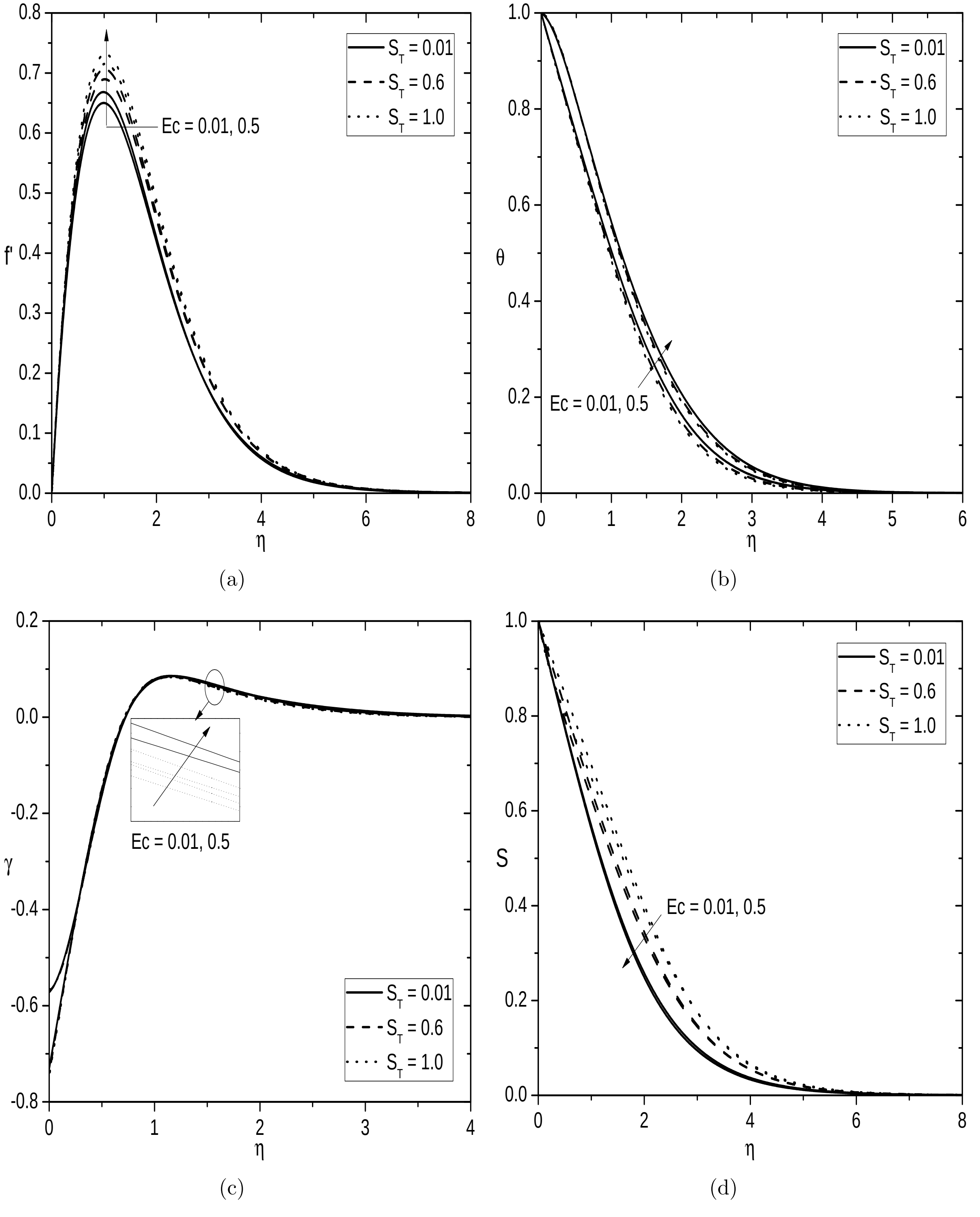

(a)

(b)

(c)

(d)

Figure 2.3: *Effects of Ec and S_T on (a) Velocity, (b) Temperature, (c) Nanoparticle volume fraction, and (d) Regular concentration for $Nt = 0.5$ and $Nb = 0.2$.*

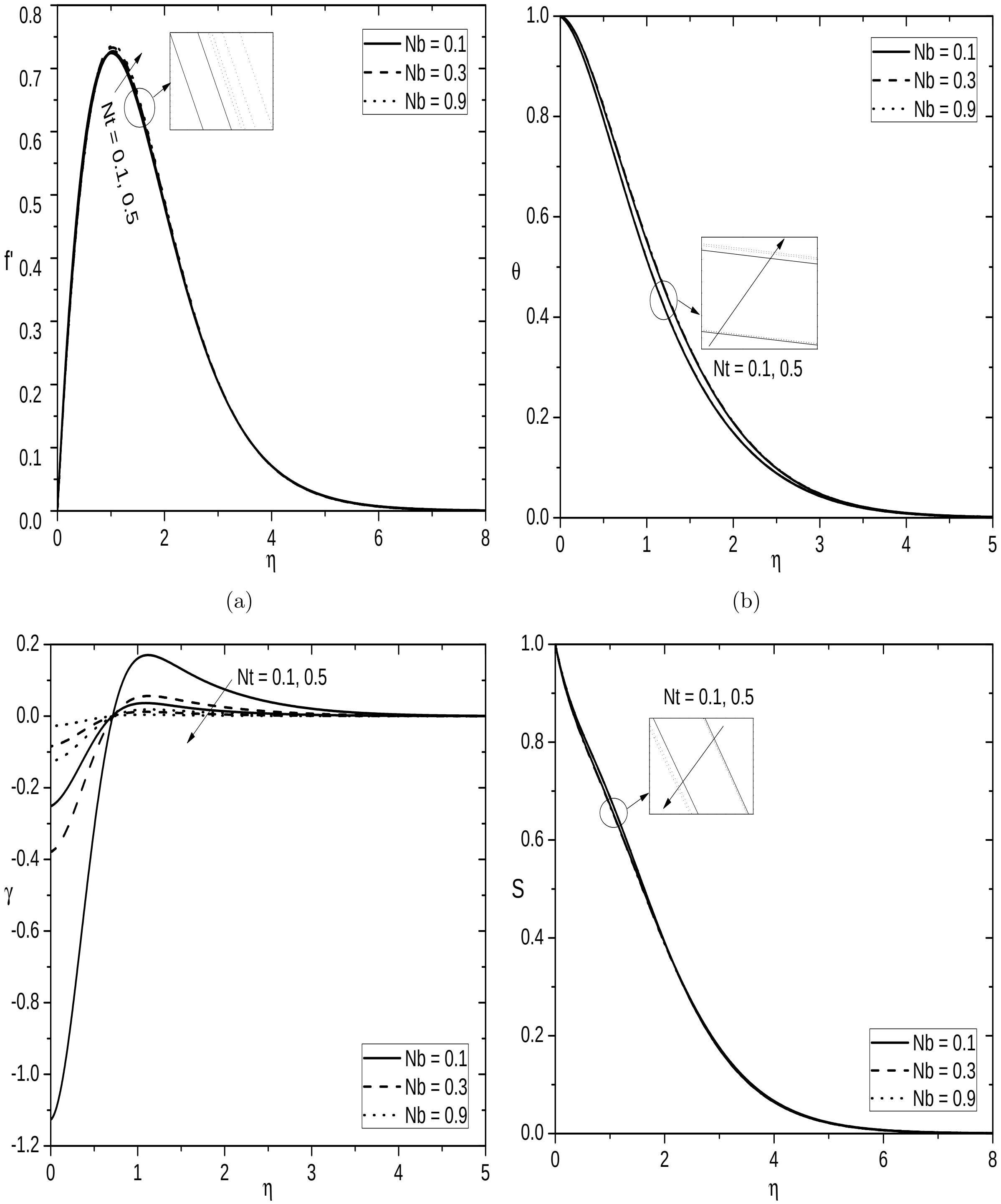

(a) (b)

(c) (d)

Figure 2.4: *Effects of Nt and Nb on (a) Velocity, (b) Temperature, (c) Nanoparticle volume fraction, and (d) Regular concentration for $Ec = 0.5$ and $S_T = 1.0$.*

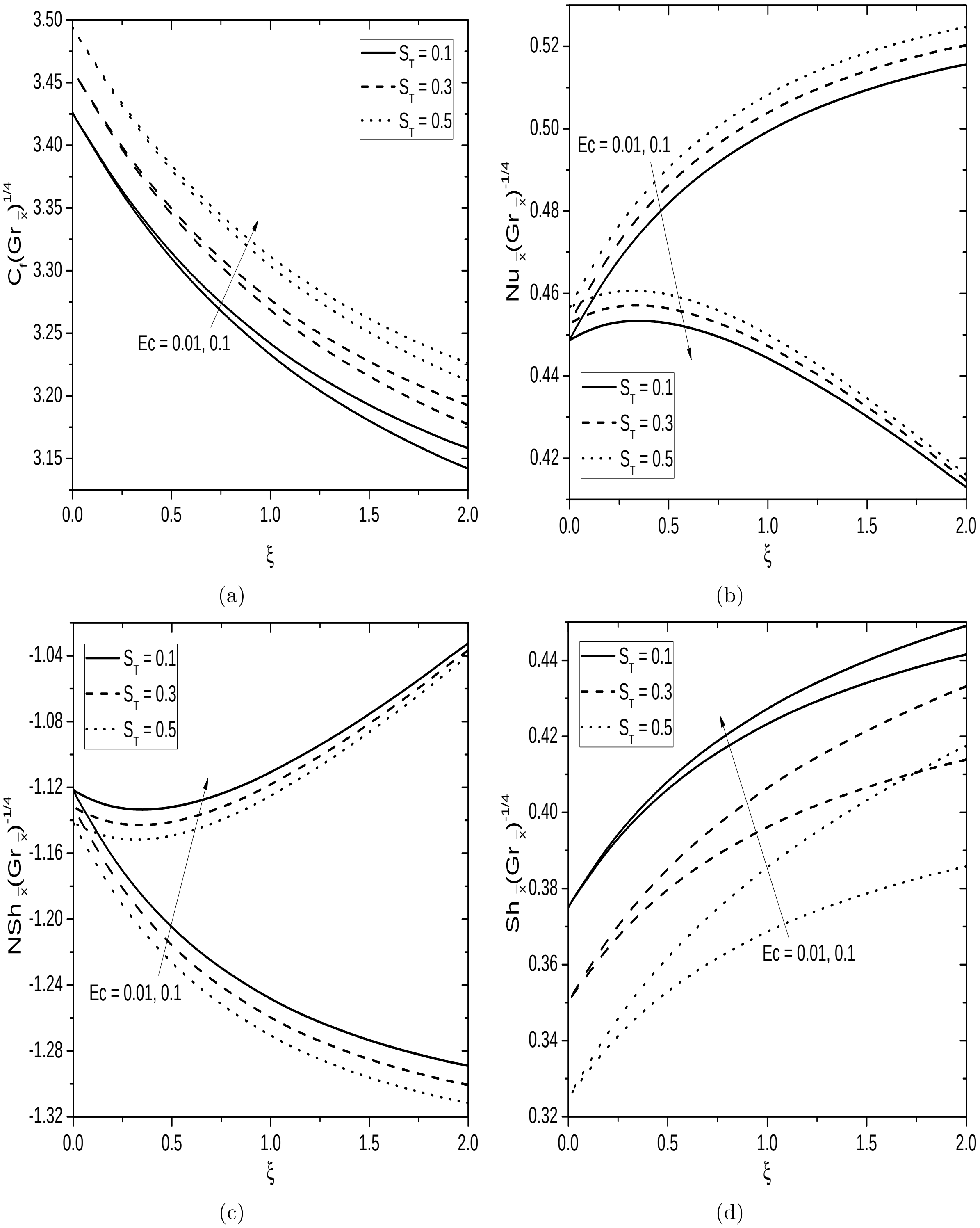

(a)

(b)

(c)

(d)

Figure 2.5: *Effects of* Ec *and* S_T *on (a) Skin friction, (b) Heat transfer rate, (c) Nanoparticle mass transfer rate, and (d) Regular mass transfer rate for* $Nt = 0.5$ *and* $Nb = 0.2$.

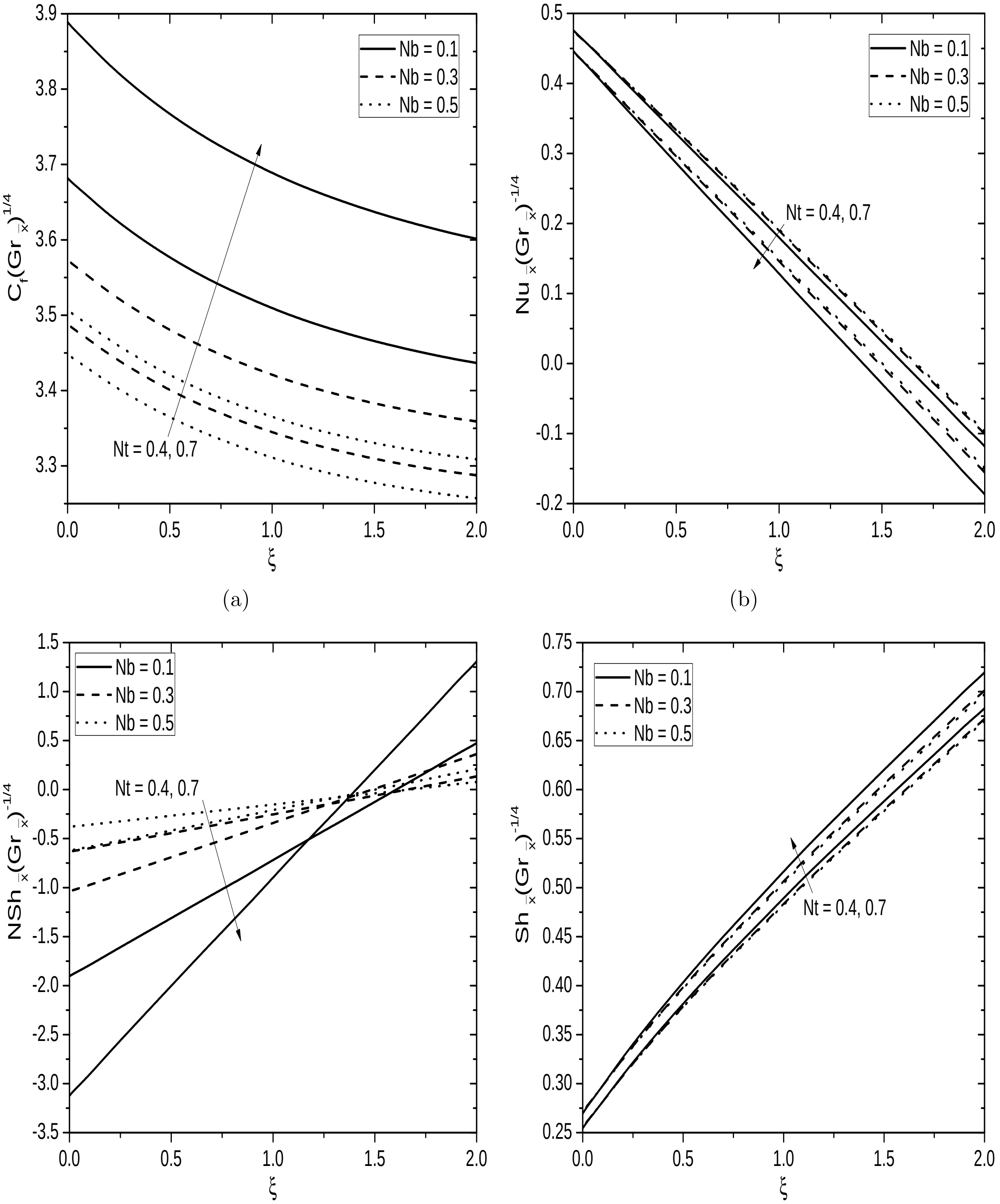

(a) (b)

(c) (d)

Figure 2.6: *Effects of Nt and Nb on (a) Skin friction, (b) Heat transfer rate, (c) Nanoparticle mass transfer rate, and (d) Regular mass transfer rate for $Ec = 0.5$ and $S_T = 1.0$.*

2.2.2 Case(b): Mixed Convection

The flow is assumed to be a mixed convection, which arises from both buoyancy forces and external flow with velocity U_∞. We introduce the following non-similarity variables

$$\xi = \frac{\overline{x}}{x_0} = \frac{x - x_0}{x_0},\ \eta = \frac{y}{\overline{x}} Re_{\overline{x}}^{1/2},\ \psi = r\nu Re_{\overline{x}}^{1/2} f(\xi, \eta),$$

$$\theta(\xi, \eta) = \frac{T - T_\infty}{T_w - T_\infty},\ \gamma(\xi, \eta) = \frac{\phi - \phi_\infty}{\phi_\infty}, S(\xi, \eta) = \frac{C - C_\infty}{C_w - C_\infty} \tag{2.36}$$

where $\overline{x} = x - x_0$ and $Re_{\overline{x}} = \dfrac{U_\infty \, \overline{x}}{\nu}$ is the local Reynolds number.

Substituting Eq.(2.7) and Eq.(2.36) into Eqs.(2.2)- (2.5), we obtain the following system of differential equations:

$$f''' + \left(R + \frac{1}{2}\right) f\, f'' + \lambda\xi(\theta + Nc\, S - Nr\, \gamma) = \xi \left(f' \frac{\partial f'}{\partial \xi} - \frac{\partial f}{\partial \xi} f''\right) \tag{2.37}$$

$$\frac{1}{Pr}\theta'' + \left(R + \frac{1}{2}\right) f\, \theta' + Nb\, \gamma'\, \theta' + Nt\ (\theta')^2 + Ec\, (f'')^2 = \xi \left(f' \frac{\partial \theta}{\partial \xi} - \frac{\partial f}{\partial \xi} \theta'\right) \tag{2.38}$$

$$\frac{1}{Le}\gamma'' + \left(R + \frac{1}{2}\right) f\, \gamma' + \frac{1}{Le}\frac{Nt}{Nb}\, \theta'' = \xi \left(f' \frac{\partial \gamma}{\partial \xi} - \frac{\partial f}{\partial \xi} \gamma'\right) \tag{2.39}$$

$$\frac{1}{Sc}S'' + \left(R + \frac{1}{2}\right) f\, S' + S_T\theta'' = \xi \left(f' \frac{\partial S}{\partial \xi} - \frac{\partial f}{\partial \xi} S'\right) \tag{2.40}$$

where $Ec = \dfrac{U_\infty^2}{C_p(T_w - T_\infty)}$ is the Eckert number, $Re_{x_0} = \dfrac{U_\infty \, x_0}{\nu}$ is the Reynolds number based on x_0 and $\lambda = \dfrac{Gr_{x_0}}{Re_{x_0}^2}$ is the mixed convection parameter.

The corresponding non-dimensional boundary conditions become

$$f(\xi, \eta) + \frac{\xi}{\left(R + \frac{1}{2}\right)} \frac{\partial f}{\partial \xi} = 0,\ f'(\xi, \eta) = 0,\ \theta(\xi, \eta) = 1,$$

$$Nb\, \gamma'(\xi, \eta) + Nt\, \theta'(\xi, \eta) = 0,\ \ S(\xi, \eta) = 1 \quad \text{at} \quad \eta = 0 \tag{2.41a}$$

$$f'(\xi, \eta) = 1,\ \theta(\xi, \eta) = 0,\ \gamma(\xi, \eta) = 0,\ S(\xi, \eta) = 0 \quad \text{as} \quad \eta \to \infty \tag{2.41b}$$

The non-dimensional skin friction $C_f = \dfrac{2\tau_w}{\rho U_\infty^2}$, local Nusselt number $Nu_{\overline{x}} = \dfrac{q_w \overline{x}}{k(T_w - T_\infty)}$, local nanoparticle Sherwood number $NSh_{\overline{x}} = \dfrac{q_n \overline{x}}{D_B \phi_\infty}$ and loacl regular sherwood number $Sh_{\overline{x}} = \dfrac{q_m \overline{x}}{D_S(C_w - C_\infty)}$, are given by

$$\left.\begin{array}{l} C_f Re_{\overline{x}}^{1/2} = 2\, f''(\xi, 0),\ \dfrac{Nu_{\overline{x}}}{Re_{\overline{x}}^{1/2}} = -\theta'(\xi, 0), \\ \dfrac{NSh_{\overline{x}}}{Re_{\overline{x}}^{1/2}} = -\gamma'(\xi, 0),\ \dfrac{Sh_{\overline{x}}}{Re_{\overline{x}}^{1/2}} = -S'(\xi, 0) \end{array}\right\} \tag{2.42}$$

Results and Discussion

The reduced non-linear partial differential equations (2.37)-(2.40) together with the boundary conditions (2.41) are solved numerically using the Bivariate Pseudo-Spectral Local Linearization Method, as explained in the case (a). In order to validate the generated code, the present numerical results have been compared with those of Lloyd and Sparrow [56] for the special case of $Nt = 0.0$, $S_T = 0.0$, $Ec = 0.0$, $Nc = 0.0$, $Nr = 0.0$, $Sc = 1.0$, $Le = 1.0$, $Nb \to 0.0$ and $\lambda = 0.0$. Also, the results of present problem have been compared with those of Kafoussias [42] for the special of $Sc = 0.24$, $Pr = 0.73$, $Le = 1.0$, $Nr = 0.0$, $S_T = 0.0$, $Ec = 0.0$, $Nt = 0.0$ and $Nb \to 0.0$. It is found that the present results are in good agreement as shown in Tabs. (2.2) and (2.3). To investigate the effects of Brownian motion parameter (Nb), thermophoresis parameter (Nt), Soret number (S_T) and Eckret number (Ec) on the various profiles and physical quantities in both aiding and opposing flow situations, the computations have been carried out for $Nr = 1.0$, $Nc = 1.0$, $Pr = 1.0$, $Sc = 0.6$ and $Le = 10.0$. These values are fixed in the present study unless particularly specified.

The distributions of non-dimensional velocity f', temperature θ, nanoparticle volume fraction γ and regular concentration S, under the influence of Eckert number (Ec) and mixed convection parameter (λ), are shown in Figs. 2.7(a)-2.7(d). It is observed that an increase in the Eckert number leads to increase the velocity in the aiding flow, and decrease in the opposing flow, as displayed in Fig. 2.7(a). From Fig. 2.7(b), it is noticed that the fluid temperature increases for both opposing and aiding flows with an increase in Ec.

Table 2.2: *Comparison of* $-\theta'(0,\ 0)$ *for various values of* Pr.

	$-\theta'(0,\ 0)$	
Pr	Lloyd and Sparrow [56]	Present
0.72	0.2956	0.29563518
10.0	0.7281	0.72814119
100.0	1.572	1.57165763

Table 2.3: *Comparison of* $f''(0,0)$ *and* $-\theta'(0,0)$ *for various values of* λ *and* Nc.

		$f''(0,0)$		$-\theta'(0,0)$	
λ	Nc	Kafoussias [42]	Present	Kafoussias [42]	Present
0.10	0.5	0.5538	0.55394797	0.3296	0.32962694
0.10	1.0	0.6317	0.63189857	0.3404	0.34045600
0.10	2.0	0.7776	0.77789469	0.3589	0.35898224
1.00	0.5	1.4452	1.44516615	0.4129	0.41289888
1.00	1.0	1.5007	1.50072839	0.4179	0.41794525
1.00	2.0	1.6096	1.60970732	0.4274	0.42748233

Figure 2.7(c) reports that the nanoparticle volume fraction increases near to the frustum of a cone, and decreases far away from the surface, with the increase of Eckert number in both opposing and aiding flows. However, the regular concentration reduces in both opposing and aiding flows with the enhancement of Eckert number, as plotted in Fig. 2.7(d). Moreover, the velocity and nanoparticle volume fraction are more, but the temperature and regular concentration are less in the aiding flow when compared to that of the opposing flow.

Figures 2.8(a)-2.8(d) exhibit the non-dimensional velocity f', temperature θ, nanoparticle volume fraction γ and regular concentration S, for different values of the Soret number (S_T) in both aiding and opposing flow situations. Figure 2.8(a) reveals that the velocity decreases in the opposing flow, and increases in the aiding flow with the increase of Soret number. It is seen from Fig. 2.8(b) that as the Soret number enhances, the temperature diminishes in the aiding flow, but it enhances in the opposing flow. Figure 2.8(c) shows that the nanoparticle volume fraction increases for aiding flow, whereas it decreases for opposing flow with the increase of Soret number. Since, the existence of diffusive flux due to temperature gradient is known as the Soret effect and it shows that diffusive species along with the higher values of Soret number accelerates the concentration. Hence, the regular concentration enhances with the enhancement of Soret number in both aiding and opposing flows, as depicted in Fig. 2.8(d).

Considering the aiding and opposing flows, the influence of thermophoresis parameter (Nt) on the dimensionless velocity f', temperature θ, nanoparticle volume fraction γ and regular concentration S, are displayed in Figs. 2.9(a)-2.9(d). The diffusion of nanoparticles under the influence of a temperature gradient is known as the thermophoresis. When the thermophoresis parameter increases, the solid nanoparticles in a nanofluid experience a force which is opposite to the direction of temperature gradient. Hence, increasing values of the thermophoresis parameter leads to increase the velocity in the case of aiding flow, but it reduces in the case of opposing flow, as shown in Fig. 2.9(a). With the increase of thermophoresis parameter, the temperature of nanofluid increases in both aiding and opposing flows, as given in Fig. 2.9(b). Figures 2.9(c) and 2.9(d) reports that the nanoparticle volume fraction and regular concentration profiles decrease with increasing values of thermophoresis parameter.

Figures 2.10(a)-2.10(b) explore the effect of Brownian motion parameter (Nb) on the non-dimensional velocity f' and nanoparticle volume fraction γ, for both aiding and opposing flows. It is noticed that an increase in the intensity of Brownian motion parameter leads to increase the velocity within the momentum boundary layer, in both aiding and opposing flows. Moreover, an increase in the Brownian motion parameter tends to increase the nanoparticle volume fraction near to the frustum of a cone and the trend is reversed far away from the cone for both aiding and opposing flow situations.

Figures 2.11(a)-2.11(d) illustrate the effects of Eckert number (Ec) and Soret number (S_T) on the non-dimensional skin friction, local Nusselt number, local nanoparticle and regular Sherwood numbers, for aiding flow situation ($\lambda = 0.5$). As a result of Fig. 2.11(a), the skin friction enhances with an enhancement in the Eckert number. Since the positive values of Eckert number ($Ec > 0$) indicates the fluid heating (i.e., heat supplied across the surface into the fluid region) and hence the temperature increases, and the regular concentration decreases with the increase of Eckert number. Consequently, the local Nusselt number decreases, whereas the local regular Sherwood number increases with increasing values of Ec, as shown in Figs. 2.11(b) and 2.11(d). But, with rising values of Eckert number, the local nanoparticle Sherwood number reduces, as shown in Fig. 2.11(c). On the other hand, it is seen that the dimensionless surface drag and local Nusselt number enhance, whereas the local nanoparticle and regular Sherwood numbers diminish with the enhancement of Soret number. This is because of the fact that the regular concentration increases with an additional mass diffusion term in the regular concentration equation.

For opposing flow situation ($\lambda = -0.05$), the streamwise variations of the above discussed physical quantities under the influence of Soret and viscous dissipation, are plotted in 2.12(a)-2.12(d). Figure 2.12(a) reveals that the skin friction reduces with enhancing values of both Eckert and Soret numbers. From Fig. 2.12(b), it is seen that the temperature decreases with the increase of Eckert number as well as Soret number. With the increase of both Eckert and Soret numbers, the local nanoparticle Sherwood number increases as shown in Fig. 2.12(c). Figure 2.12(d) portrays that the local regular Sherwood number enhances with the enhancement of Eckert number, but reduces with the increase of Soret number.

The effects of thermophoresis parameter (Nt) and Brownian motion parameter (Nb) on the dimensionless surface drag, local heat transfer rate, local nanoparticle mass and regular mass transfer rates over the streamwise coordinate ξ, for aiding flow situation ($\lambda = 0.5$), are depicted in Figs. 2.13(a)-2.13(d). It is seen from these figures that an increase in thermophoresis parameter strengthens the force acting on the nanoparticles away from the hot surface of vertical frustum of a cone and thus, the diffusion of nanoparticles rises with the nanofluid. Therefore, with the increasing values of thermophoresis parameter, the skin friction and local regular mass transfer rate increase, but the local heat and nanoparticle mass transfer rates decrease. Figures 2.13(a) and 2.13(d) reveal that the surface drag and local regular Sherwood number diminish with the enhancement of Brownian motion parameter. It is also observed from these figures that the local heat transfer rate and local nanoparticle mass transfer rate increase with the increase of Brownian motion parameter.

Figures 2.14(a)-2.14(d) exhibit the effects of thermophoresis parameter (Nt) and Brownian motion parameter (Nb) on the above mentioned physical quantities, for opposing flow situation ($\lambda = -0.05$). The Brownian motion parameter is attributed as the random motion of nanoparticles within the base fluid. Further, the diffusion of Brownian motion is always inversely proportional to the diameter of nanoparticles. From Figs.2.14(a)-2.14(d), it is seen that the surface drag, local heat transfer rate, local nanoparticle mass and regular mass transfer rates increase with the increase of Brownian motion parameter. Since, the solid nanoparticles in a nanofluid experience a force which is opposite to the direction of temperature gradient and hence $Nt < 0$ represents a hot surface, while $Nt > 0$ indicates a cold surface. For a hot surface, thermophoresis tends to blow the nanoparticle volume fraction away from the surface and it repels the sub-micron sized particles from it, thereby forming a relative particle-free layer near the surface. As a result, an increase of thermophoresis parameter leads to decrease the surface drag, local heat, local nanoparticle and regular mass transfer rates, as displayed in Figs.2.14(a)-2.14(d).

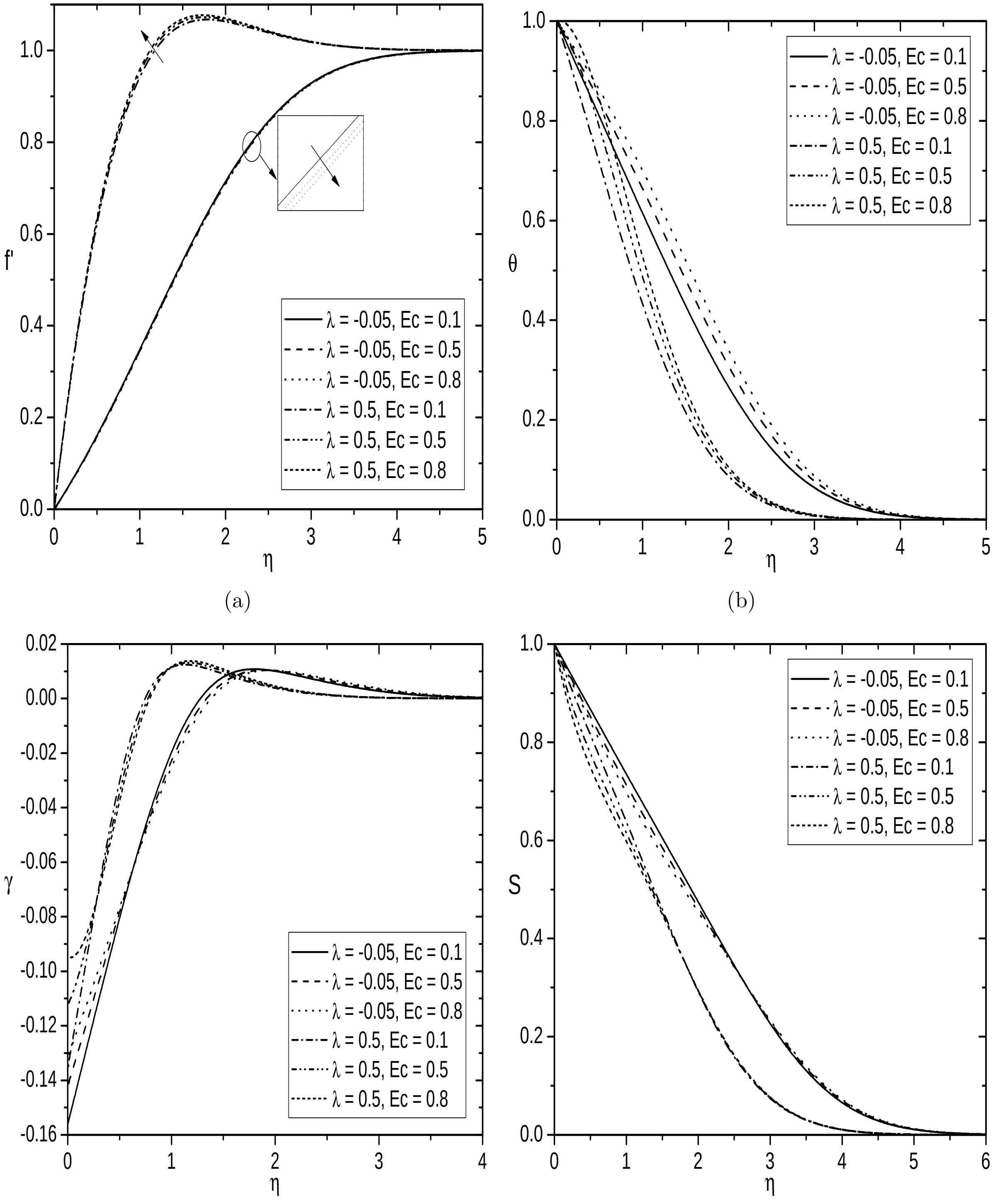

(a)

(b)

(c)

(d)

Figure 2.7: *Effects of λ and Ec on (a) Velocity, (b) Temperature, (c) Nanoparticle volume fraction and (d) Regular concentration for $S_T = 1.0$, $Nt = 0.5$ and $Nb = 0.2$.*

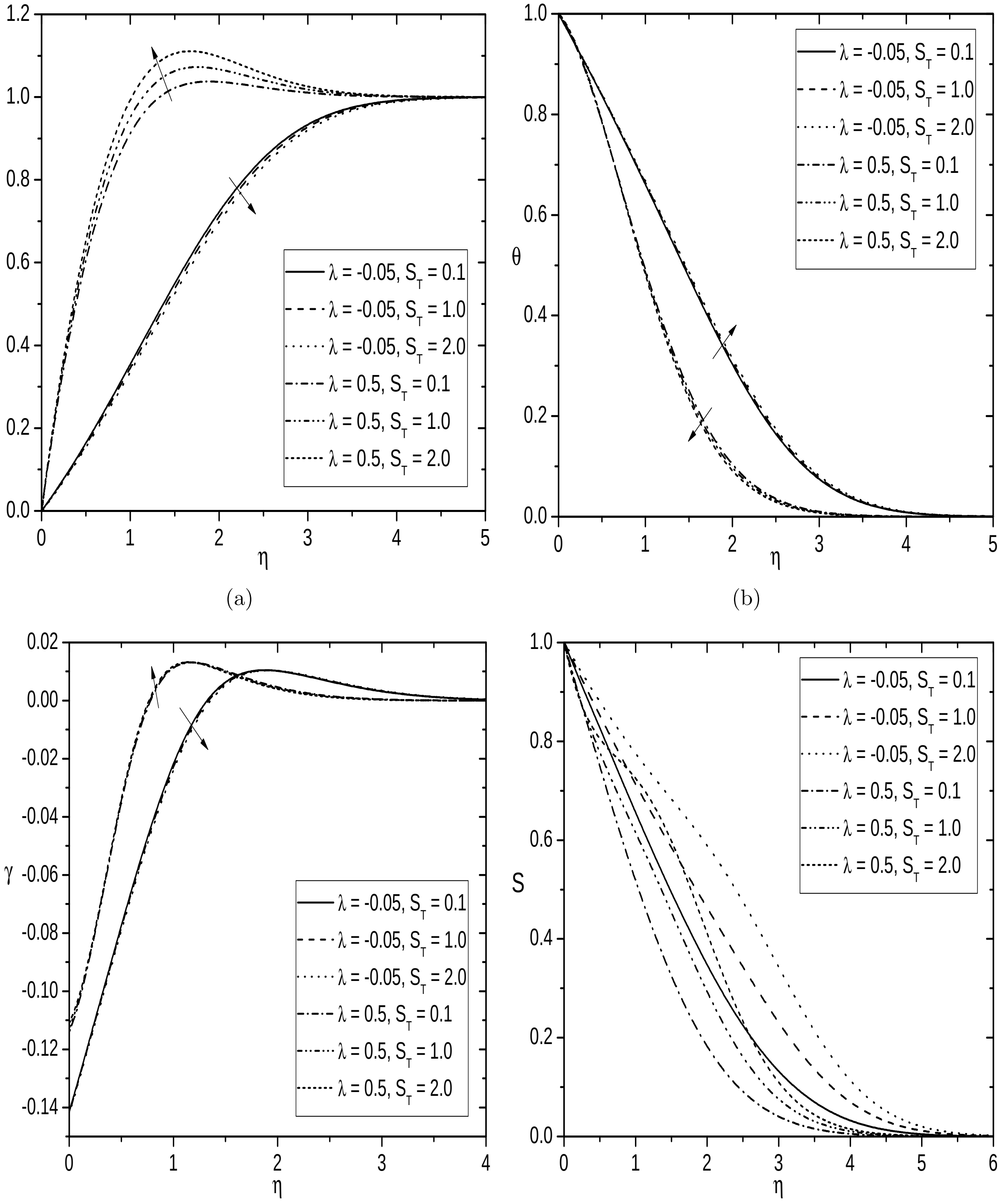

(a) (b)

(c) (d)

Figure 2.8: *Effects of* λ *and* S_T *on (a) Velocity, (b) Temperature, (c) Nanoparticle volume fraction and (d) Regular concentration for* $Ec = 0.5$*,* $Nt = 0.5$ *and* $Nb = 0.2$*.*

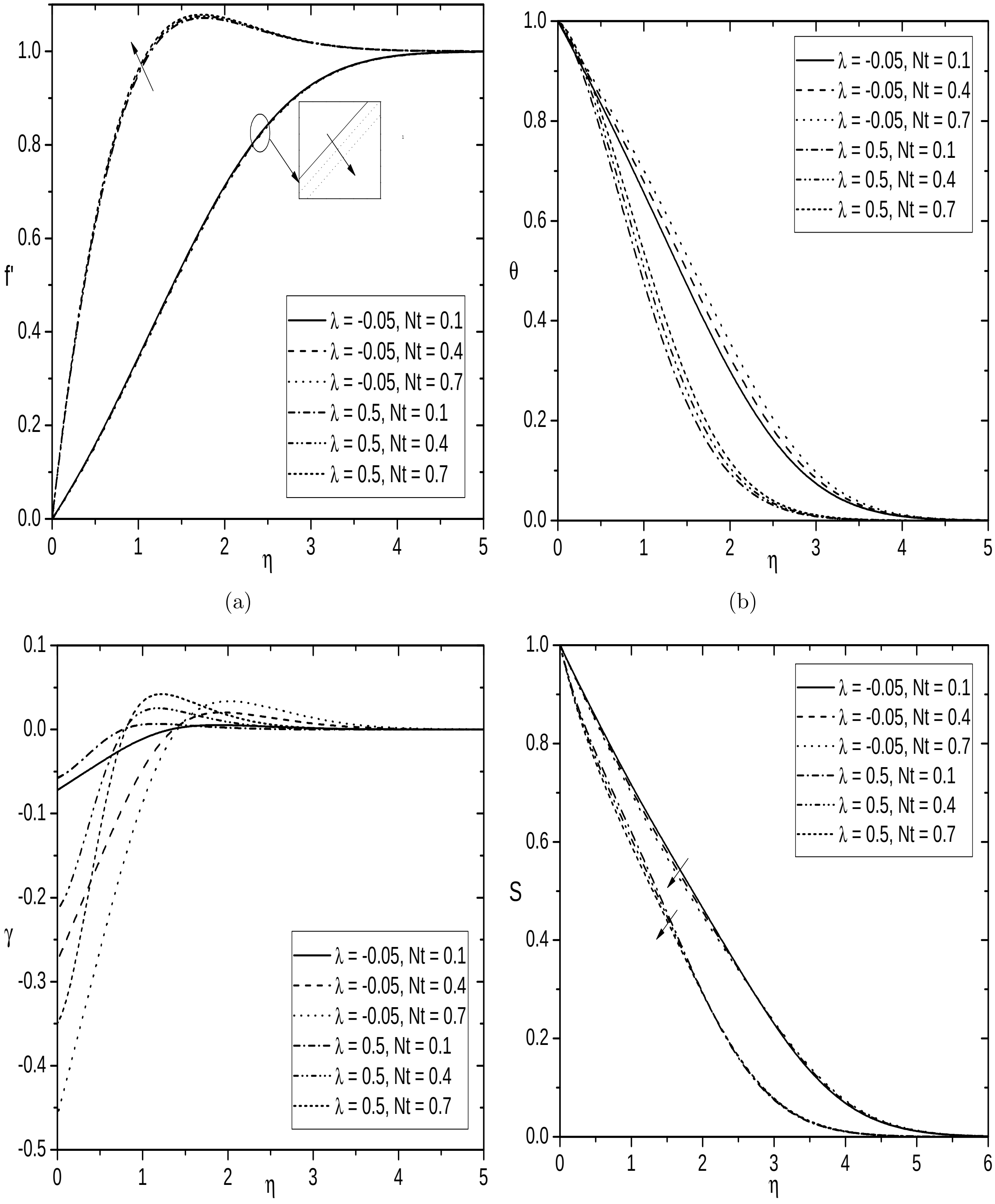

(a) (b)

(c) (d)

Figure 2.9: *Effects of* λ *and* Nt *on (a) Velocity, (b) Temperature, (c) Nanoparticle volume fraction and (d) Regular concentration for* $Ec = 0.5$*,* $S_T = 1.0$ *and* $Nb = 0.2$*.*

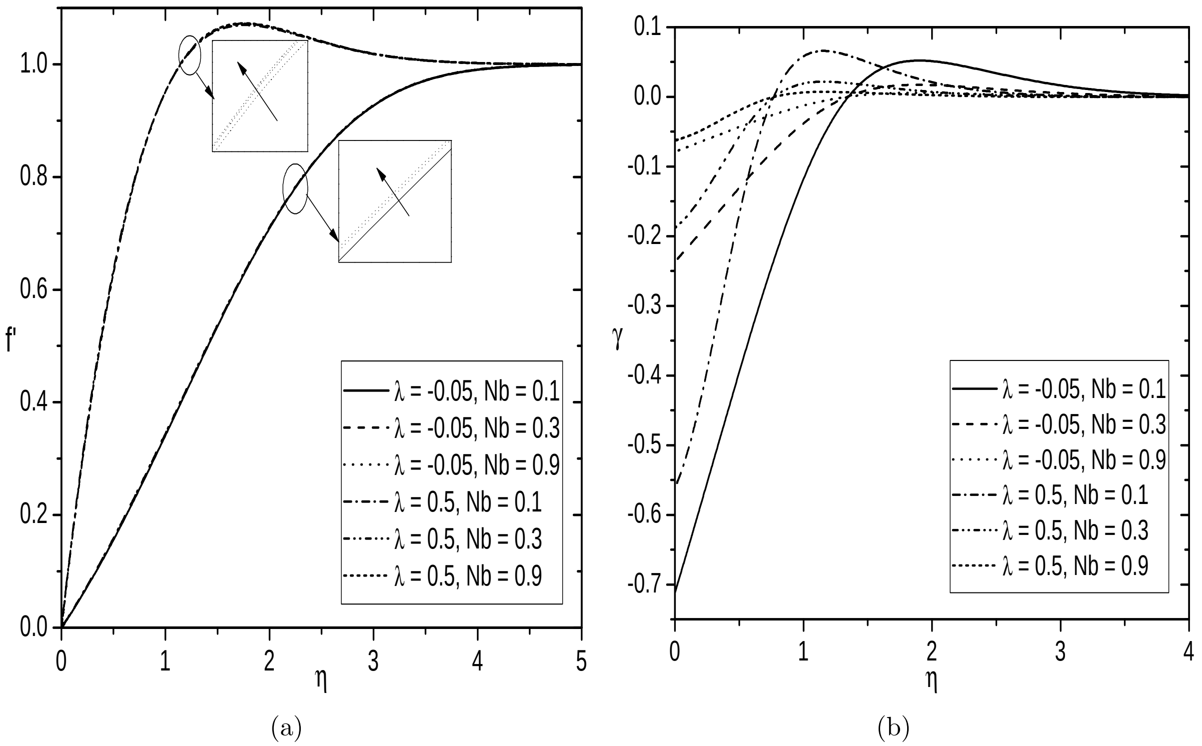

(a) (b)

Figure 2.10: *Effects of* λ *and* Nb *on (a) Velocity and (b) Nanoparticle volume fraction for* $Ec = 0.5$, $S_T = 1.0$ *and* $Nt = 0.5$.

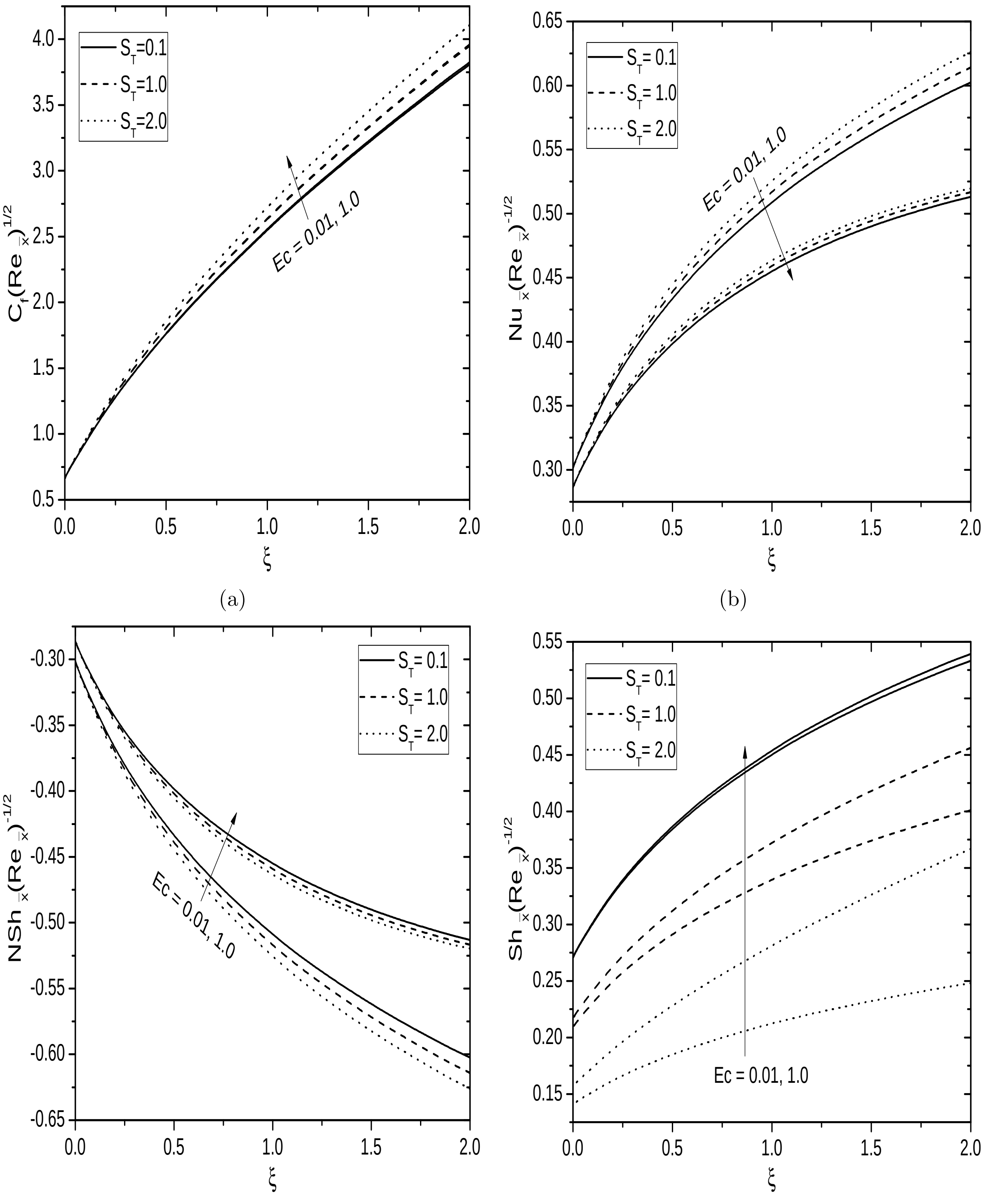

(a)

(b)

(c)

(d)

Figure 2.11: *Effects of* Ec *and* S_T *on (a) Skin friction, (b) Heat transfer rate, (c) Nanoparticle mass transfer rate, and (d) Regular mass transfer rate (Aiding flow case) for* $Nt = 0.5$ *and* $Nb = 0.2$.

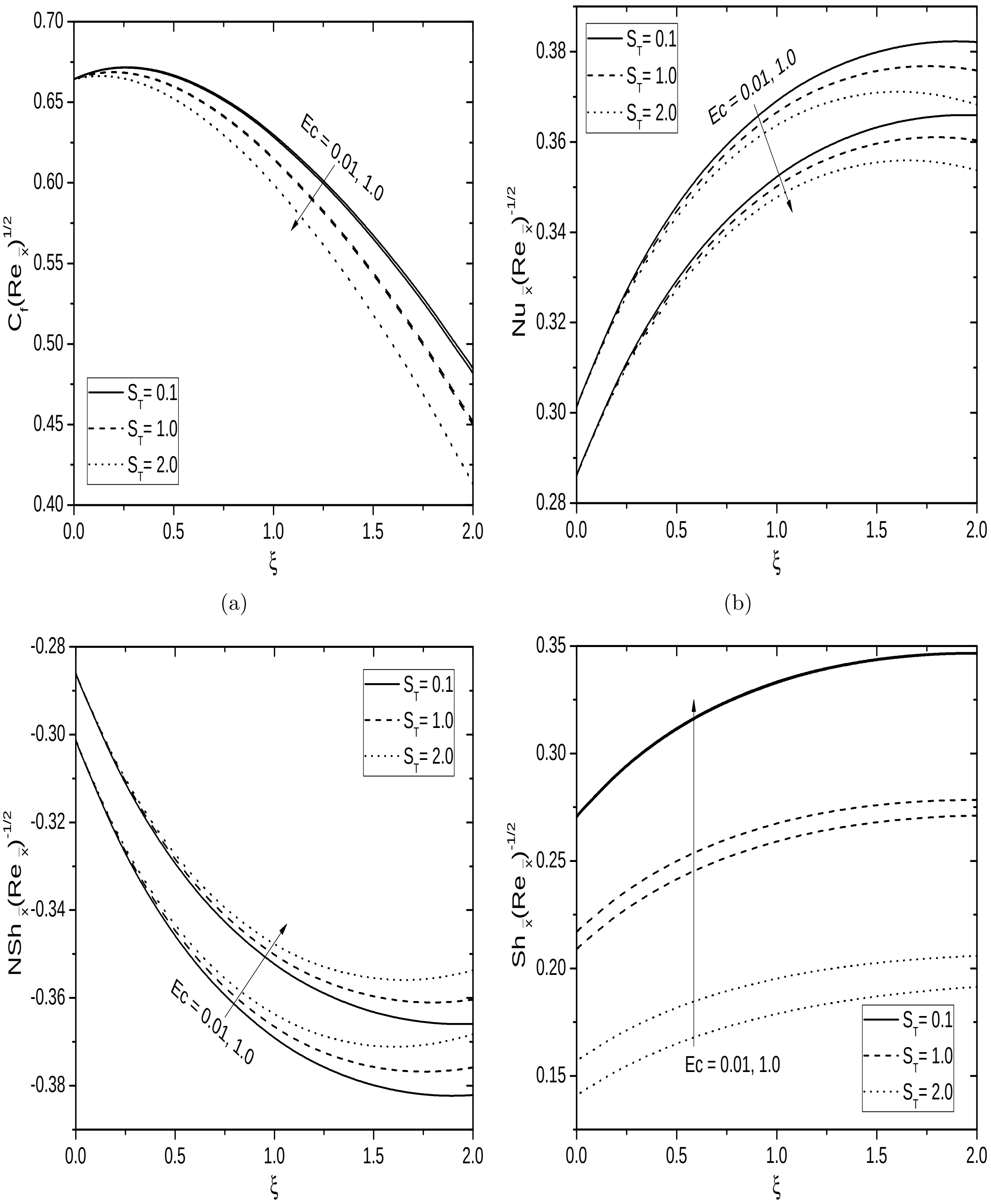

(a)

(b)

(c)

(d)

Figure 2.12: *Effects of Ec and S_T on (a) Skin friction, (b) Heat transfer rate, (c) Nanoparticle mass transfer rate, and (d) Regular mass transfer rate (Opposing flow case) for $Nt = 0.5$ and $Nb = 0.2$.*

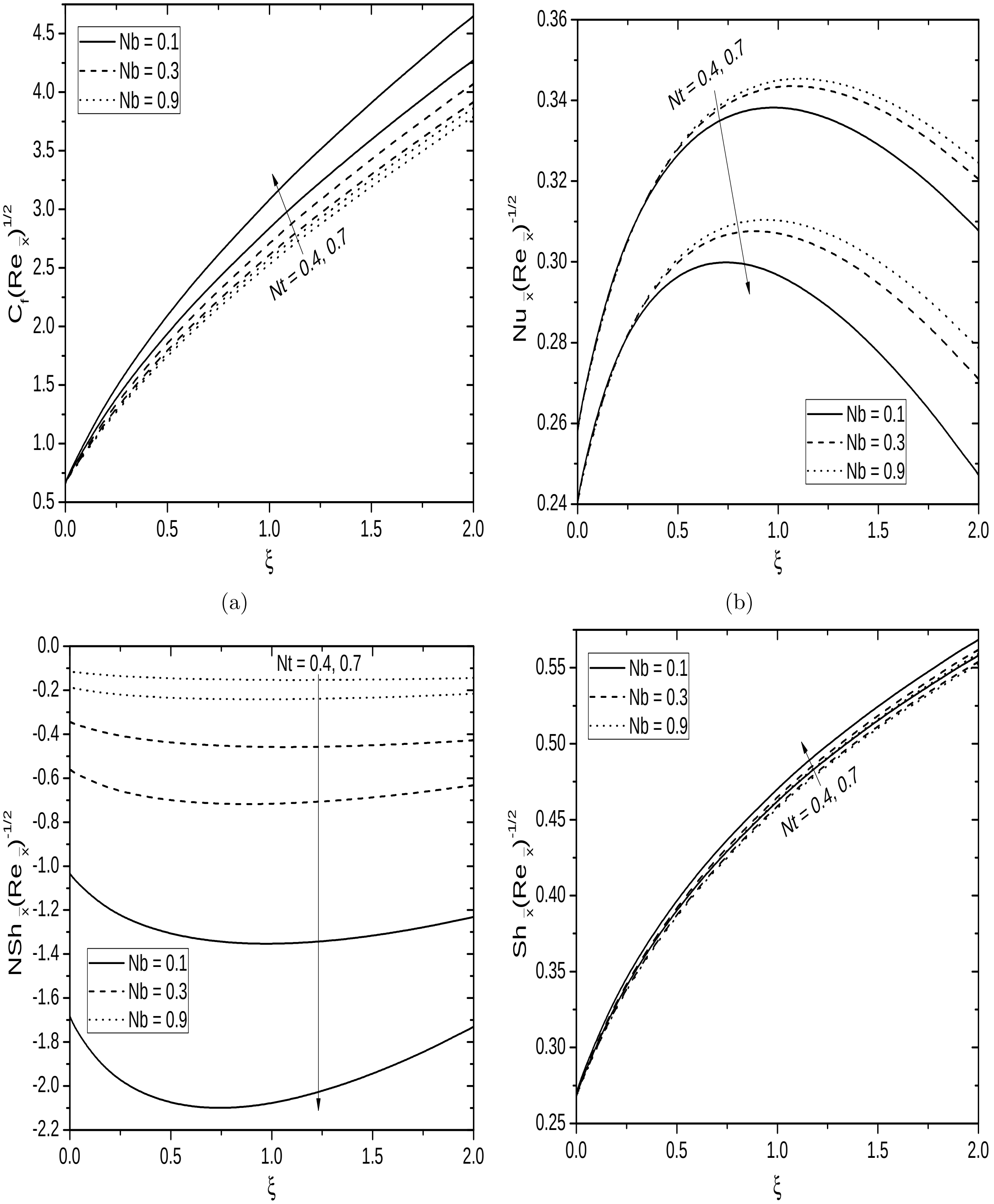

(a) (b)

(c) (d)

Figure 2.13: *Effects of* Nt *and* Nb *on (a) Skin friction, (b) Heat transfer rate, (c) Nanoparticle mass transfer rate, and (d) Regular mass transfer rate (Aiding flow case) for* $Ec = 0.5$ *and* $S_T = 1.0$.

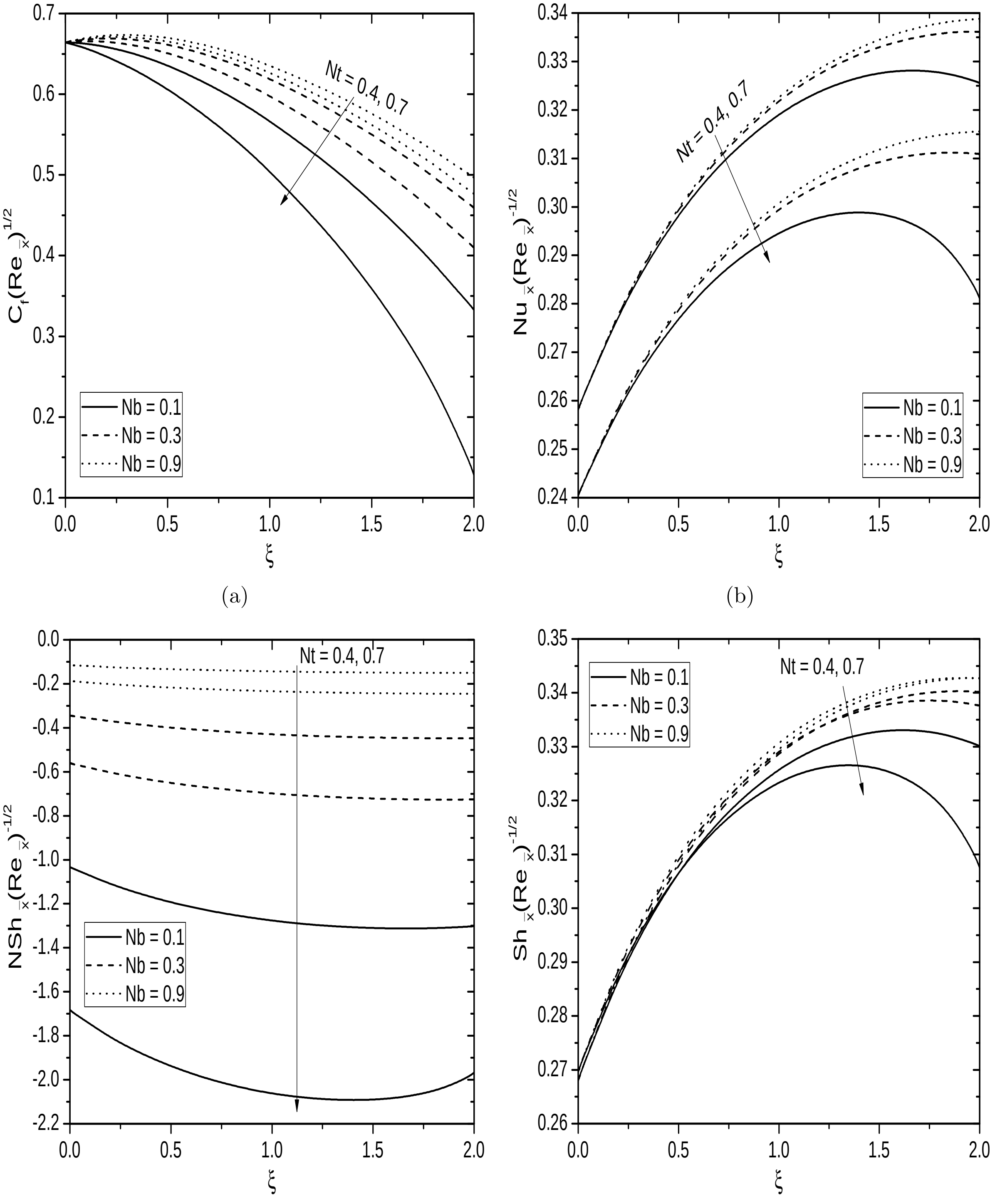

(a) (b)

(c) (d)

Figure 2.14: *Effects of Nt and Nb on (a) Skin friction, (b) Heat transfer rate, (c) Nanoparticle mass transfer rate, and (d) Regular mass transfer rate (Opposing flow case) for* $Ec = 0.5$ *and* $S_T = 1.0$.

2.3 Conclusions

In this chapter, the non-similarity solution for a nanofluid flow over the vertical frustum of a cone with Soret and viscous dissipation effects, is obtained in two cases: (a) natural convection and (b) mixed convection. From this analysis, the following conclusions can be drawn for both the cases (a) and (b).

An increase in the Eckert number tends to increase the temperature, nanoparticle volume fraction, local nanoparticle and regular Sherwood numbers, but decrease the regular concentration and local Nusselt number. Further, the velocity increases in case (a) and aiding flow of case (b), whereas it decreases in opposing flow of case (b). With the increase of Soret number, the velocity, regular concentration, surface drag and local Nusselt number enhance, but the temperature, local nanoparticle and regular Sherwood numbers reduce in case (a) and aiding flow of case (b). The velocity, temperature, surface drag, local Nusselt and nanoparticle Sherwood numbers show a reverse trend in the opposing flow of case (b). The velocity, temperature, local Nusselt number and local nanoparticle Sherwood number increase, but the regular concentration, surface drag and local regular Sherwood number decrease, with the increase of thermophoresis parameter in case (a) and aiding flow of case (b). However, with the increase of thermophoresis parameter, the velocity, surface drag, and local regular Sherwood number depict reverse behavior in opposing flow of case (b). An increase in the Brownian motion parameter, increases the velocity, temperature, nanoparticle volume fraction, local Nusselt number and local nanoparticle Sherwood number, but reduces the surface drag and local regular Sherwood number in case (a) and aiding flow of case (b). Further, the velocity and nanoparticle volume fraction are more, whereas the temperature and regular concentration are less in the aiding flow of case (b) when compared to those of opposing flow of case (b).

Chapter 3

Effects of Double Stratification on Convective Flow over the Frustum of a Cone in a Nanofluid Saturated Non-Darcy Porous Medium [1]

3.1 Introduction

The study of convective heat and mass transfer in a porous medium arises in various applications including, pollutant dispersion in aquifers, storage of nuclear waste material, a heat exchanger placed in a low-velocity environment, solar energy collecting devices, etc. A detailed review of convective heat and mass transfer in a Darcy and non-Darcy porous medium can be found in the text books by Ingham and Pop [39], Nield and Bejan [84] and Vafai [122] (also see the citations therein).

In practical situations, where the heat and mass transfer mechanism takes place simultaneously, mainly in porous media applications, it is worth analyzing the effects of thermal

---

[1] Case(a): Published in "**International Journal of Applied and Computational Mathematics**" 3 (2017) 99–113, Case(b): Published in "**Journal of Nanofluids**" 6 (2017) 971–981

and solutal stratifications on the convective heat and mass transfer. For example, the thermal stratification and concentration differences of hydrogen and oxygen in lakes and ponds is one instance that needs examination, as this may directly affect the growth rate of all cultured species. Several authors have explored the importance of convective transport in a doubly stratified porous medium due to its immense applications in various fields of science and engineering. The effect of double stratification on the natural convective flow of a nanofluid along a vertical flat plate embedded in a porous medium has been investigated by Srinivasacharya and Surender [115]. Using Tiwari-Das nanofluid model, Peddisetty [89] discussed the natural convective flow of a thermally stratified nanofluid along a vertical plate. Recently, Hayat *et al.* [34] analyzed the effect of double stratification on a MHD flow of nanofluid by a stretching cylinder. (For more details, see the references therein).

Survey of the literature reveal that the problem of free and mixed convective flows of a nanofluid over the vertical frustum of a cone embedded in a doubly stratified porous medium has not been investigated so far. Hence, the present chapter aims to explore the effects of thermal and solutal stratifications on the convective flow of a nanofluid over the frustum of a cone in a non-Darcy porous medium. The effects of pertinent parameters on the physical quantities are studied, and the results are displayed graphically.

3.2 Mathematical Formulation

Consider a steady, laminar and two-dimensional convective flow of an incompressible nanofluid over the vertical frustum of a cone embedded in a non-Darcy porous medium. The x-axis is taken along the surface of a full cone and y-axis is normal to the surface, while the origin O of the reference system is taken at the vertex of a full cone, as displayed in Fig. (3.1). The ambient medium is assumed to be linearly stratified with respect to temperature and regular concentration in the form $T_\infty(x-x_0) = T_{\infty,0}+B\,(x-x_0)$ and $C_\infty(x-x_0) = C_{\infty,0}+D\,(x-x_0)$, where B and D are constants, which are varied to adjust the intensity of stratification in the medium. The values of T_w and C_w are assumed to be greater than the ambient temperature $T_{\infty,0}$ and regular concentration $C_{\infty,0}$ at any arbitrary reference point in the medium (inside

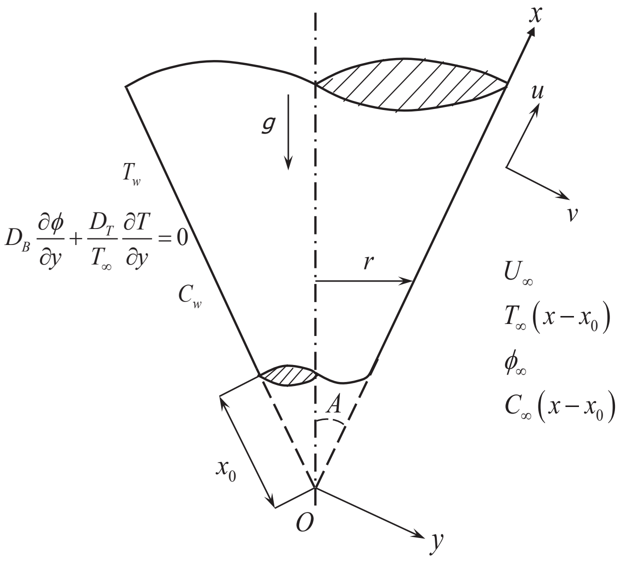

Figure 3.1: *Physical model and coordinate system*

the boundary layer). The nanoparticle volume fraction at the surface and ambient medium are considered as in the Chapter-2. In addition, the following assumptions are taken into account: (i) the porous medium is isotropic and homogeneous, (ii) the properties of the fluid and porous medium are constant except for the density variation required by the Boussinesq approximation, (iii) the fluid and the porous medium are in local thermodynamic equilibrium, and (iv) the fluid flow is moderate and the permeability of the medium is low, so that the Forchheimer flow model is applicable (See Nield and Bejan [84]).

Under the above assumptions and Oberbeck-Boussinesq approximations, the governing boundary layer equations for the conservation of mass, momentum, energy, nanoparticle volume fraction and regular concentration are given by

$$\frac{\partial (u\,r)}{\partial x} + \frac{\partial (v\,r)}{\partial y} = 0 \tag{3.1}$$

$$\frac{\rho_{f\infty}}{\varepsilon^2}\left(u\frac{\partial u}{\partial x} + v\frac{\partial u}{\partial y}\right) = \frac{\mu}{\varepsilon}\frac{\partial^2 u}{\partial y^2} + \rho_{f\infty}\, g\, (1-\phi_\infty)\left[\beta_T\,(T - T_{\infty,0}) + \beta_C\,(C - C_{\infty,0})\right]\cos A$$
$$-(\rho_p - \rho_{f\infty})\, g(\phi - \phi_\infty)\cos A - \frac{\mu}{K_p}(u - U_\infty) - \frac{\rho_{f\infty}\, b}{K_p}(u^2 - U_\infty^2) \tag{3.2}$$

$$u\,\frac{\partial T}{\partial x}+v\,\frac{\partial T}{\partial y}=\alpha_m\,\frac{\partial^2 T}{\partial y^2}+\mathcal{J}\left[D_B\frac{\partial\phi}{\partial y}\frac{\partial T}{\partial y}+\frac{D_T}{T_{\infty,0}}\left(\frac{\partial T}{\partial y}\right)^2\right] \tag{3.3}$$

$$u\,\frac{\partial\phi}{\partial x}+v\,\frac{\partial\phi}{\partial y}=D_B\,\frac{\partial^2\phi}{\partial y^2}+\frac{D_T}{T_{\infty,0}}\frac{\partial^2 T}{\partial y^2} \tag{3.4}$$

$$u\,\frac{\partial C}{\partial x}+v\,\frac{\partial C}{\partial y}=D_S\,\frac{\partial^2 C}{\partial y^2} \tag{3.5}$$

where u and v are the Darcy velocity components in x and y-directions, respectively. Further, ε is the porosity, b is the empirical constant related to Forchheimer porous inertia term and K_p is the (intrinsic) permeability of the medium.

The corresponding boundary conditions are

$$u=0,\;\; v=0,\;\; T=T_w,\;\; D_B\frac{\partial\phi}{\partial y}+\frac{D_T}{T_{\infty,0}}\frac{\partial T}{\partial y}=0,\;\; C=C_w \quad \text{at} \quad y=0 \tag{3.6a}$$

$$u=U_\infty,\;\; T=T_\infty(x-x_0),\;\; \phi=\phi_\infty,\;\; C=C_\infty(x-x_0) \quad \text{as} \quad y\to\infty \tag{3.6b}$$

In this chapter also, two types (cases) of problems are considered: (a) free/natural convection and (b) mixed convection.

3.2.1 Case(a): Natural Convection

In this case, the fluid flow is due to buoyancy forces only and hence, the velocity of the outer flow becomes zero ($i.e., U_\infty = 0$). Introduce the following non-similarity variables

$$\xi=\frac{x-x_0}{x_0}=\frac{\overline{x}}{x_0},\; \eta=\frac{y}{\overline{x}}\,Gr_{\overline{x}}^{1/4},\; \psi=r\,\nu Gr_{\overline{x}}^{1/4}f\left(\xi,\,\eta\right),$$

$$\theta\left(\xi,\,\eta\right)=\frac{T-T_\infty(x-x_0)}{T_w-T_{\infty,0}},\; \gamma\left(\xi,\,\eta\right)=\frac{\phi-\phi_\infty}{\phi_\infty},\; S\left(\xi,\,\eta\right)=\frac{C-C_\infty(x-x_0)}{C_w-C_{\infty,0}} \tag{3.7}$$

where $Gr_{\overline{x}}=\dfrac{g\beta_T(T_w-T_{\infty,0})(1-\phi_\infty)\overline{x}^3\cos A}{\nu^2}$ is the local Grashof number.

Using (2.7) and (3.7) in Eqs.(3.2)-(3.5), we get the following non-dimensional form of the governing equations

$$\begin{aligned}\frac{1}{\varepsilon}f''' + \frac{1}{\varepsilon^2}\left(R+\frac{3}{4}\right) f\,f'' - \frac{1}{2\,\varepsilon^2}(f')^2 + \theta + Nc\,S - Nr\,\gamma - \frac{\xi^{1/2}}{Da\,Gr^{1/2}}f' \\ -\frac{Fs}{Da}\,\xi(f')^2 = \frac{\xi}{\varepsilon^2}\left(f'\frac{\partial f'}{\partial \xi} - \frac{\partial f}{\partial \xi}f''\right)\end{aligned} \tag{3.8}$$

$$\frac{1}{Pr}\theta'' + \left(R+\frac{3}{4}\right) f\,\theta' + Nb\,\gamma'\,\theta' + Nt\,(\theta')^2 - \varepsilon_1\,\xi\,f' = \xi\,\left(f'\frac{\partial \theta}{\partial \xi} - \frac{\partial f}{\partial \xi}\theta'\right) \tag{3.9}$$

$$\frac{1}{Le}\gamma'' + \left(R+\frac{3}{4}\right) f\,\gamma' + \frac{1}{Le}\frac{Nt}{Nb}\,\theta'' = \xi\,\left(f'\frac{\partial \gamma}{\partial \xi} - \frac{\partial f}{\partial \xi}\gamma'\right) \tag{3.10}$$

$$\frac{1}{Sc}S'' + \left(R+\frac{3}{4}\right) f\,S' - \varepsilon_2\,\xi\,f' = \xi\,\left(f'\frac{\partial S}{\partial \xi} - \frac{\partial f}{\partial \xi}S'\right) \tag{3.11}$$

where $Da = \dfrac{K_p}{x_0^2}$ is the Darcy parameter, $\varepsilon_1 = \dfrac{B\,x_0}{T_w - T_{\infty,0}}$ is the thermal stratification parameter, $Fs = \dfrac{b}{x_0}$ is the Forchheimer number, and $\varepsilon_2 = \dfrac{D\,x_0}{C_w - C_{\infty,0}}$ is the solutal stratification parameter.

The boundary conditions (3.6) in terms of f, θ, γ and S become

$$\begin{aligned}f'(\xi,\eta) = 0,\ f(\xi,\eta) + \frac{\xi}{\left(R+\frac{3}{4}\right)}\frac{\partial f}{\partial \xi} = 0,\ \theta(\xi,\eta) = 1 - \varepsilon_1\,\xi, Nb\,\gamma'(\xi,\eta) + Nt\,\theta'(\xi,\eta) = 0, \\ S(\xi,\eta) = 1 - \varepsilon_2\,\xi \quad \text{at} \quad \eta = 0\end{aligned} \tag{3.12a}$$

$$f'(\xi,\eta) = 0,\ \theta(\xi,\eta) = 0,\ \gamma(\xi,\eta) = 0,\ S(\xi,\eta) = 0 \quad \text{as} \quad \eta \to \infty \tag{3.12b}$$

The non-dimensional skin friction C_f, local Nusselt number $Nu_{\overline{x}}$, local nanoparticle Sherwood number $NSh_{\overline{x}}$ and local regular Sherwood number $Sh_{\overline{x}}$, are given by

$$\left.\begin{aligned}\frac{1}{2}C_f Gr_{\overline{x}}^{1/4} = f''(\xi,0),\ \frac{Nu_{\overline{x}}}{Gr_{\overline{x}}^{1/4}} = -\theta'(\xi,0), \\ \frac{NSh_{\overline{x}}}{Gr_{\overline{x}}^{1/4}} = -\gamma'(\xi,0),\ \frac{Sh_{\overline{x}}}{Gr_{\overline{x}}^{1/4}} = -S'(\xi,0)\end{aligned}\right\} \tag{3.13}$$

Results and Discussion

The coupled non-linear partial differential equations (3.8)-(3.11) along with the boundary conditions (3.12) are solved numerically using the Bivariate Pseudo-Spectral Local Linearization Method, as explained in the previous chapter. In order to validate the code generated, the results of the present problem have been compared with those of Yih [130], Na and Chiou [75], Kays and Crawford [49] and Lin and Chen [55] for the special case of $Gr = 1.0$, $\varepsilon = 1.0$, $Fs = 0.0$, $Da = 1.0$, $\varepsilon_1 = 0.0$ and $\varepsilon_2 = 0.0$. It is found that they are in good agreement as shown in Tab. (2.1). To explore the physical significance of non-Darcy parameter (Fs), thermal stratification parameter (ε_1) and solutal stratification parameter (ε_2), the computations have been carried out for $Pr = 1.0$, $Sc = 0.6$, $Nt = 0.5$, $Nb = 0.2$, $Nc = 1.0$, $Nr = 0.5$, $Gr = 5.0$, $\varepsilon = 0.5$ and $Da = 0.1$. These values are fixed throughout in this case (a) unless specified separately.

For various values of Forchhiemer number (Fs) and thermal stratification parameter (ε_1), the non-dimensional velocity f', temperature θ, nanoparticle volume fraction γ, and regular concentration S, are shown in Figs. 3.2(a)-3.2(d). An increase in thermal stratification parameter reduces the effective convective potential between the heated surface and the ambient nanofluid in the medium. This factor leads to decrease the buoyancy force and hence, decreases the velocity for both Darcy and non-Darcy flows. It is also seen that the velocity reduces with the enhancement of Forchheimer number, as depicted in Fig. 3.2(a). Since, the porous medium offers more resistance to the fluid flow and therefore the fluid velocity is less in the case of non-Darcy porous medium when compared to that of Darcy porous medium. However, the temperature and nanoparticle volume fraction profiles decrease, whereas the regular concentration increases with the increase of thermal stratification parameter for both Darcy and non-Darcy flows. Further, it is noticed from Figs. 3.2(b)-3.2(d) that the temperature, nanoparticle volume fraction and regular concentration are more in the case of non-Darcy porous medium when compared to that of Darcy porous medium.

Figures 3.3(a)-3.3(d) exhibit the non-dimensional velocity f', temperature θ, nanoparticle volume fraction γ, and regular concentration S for various values of the solutal stratification parameter (ε_2). From Fig. 3.3(a), it is found that the velocity of the fluid flow decreases with the increase of solutal stratification parameter. But, the temperature increases with increasing values of the solutal stratification parameter, as plotted in Fig. 3.3(b). With the increase of solutal stratification parameter, the nanoparticle volume fraction decreases near to the surface of the vertical frustum of a cone and increases far away from the surface, as shown in Fig. 3.3(c). From Fig. 3.3(d), it is observed that the regular concentration reduces with the enhancement of solutal stratification parameter.

Considering the Darcy and non-Darcy porous medium cases, the streamwise distribution of the surface drag, local Nusselt number, local nanoparticle and regular Sherwood numbers for various values of the thermal stratification parameter (ε_1), are depicted in Figs. 3.4(a)-3.4(d). The Forchheimer number represents the inertial drag in a non-Darcy porous medium and also, it is applicable only for high permeability cases. As $Fs \to 0$, the nanofluid saturated non-Darcy porous medium tends to the nanofluid saturated Darcy porous medium. It is seen from Fig. 3.4(a) that the drag coefficient decreases with the increase of thermal stratification parameter for both $Fs = 0.0$ and $Fs = 1.0$. Also, the local Nusselt and regular Sherwood numbers reduces with the enhancement of both Forchheimer number and thermal stratification parameter, as plotted in Figs. 3.4(b) and 3.4(d). As the thermal stratification parameter enhances, the local nanoparticle Sherwood number is also enhances in both Darcy and non-Darcy porous media, as shown in Fig. 3.4(c). Moreover, the surface drag, local Nusselt and regular Sherwood numbers are less and, the local nanoparticle Sherwood number is more in the non-Darcy porous medium as compared with those of the Darcy porous medium.

Figures 3.5(a)-3.5(d) display the streamwise distribution of the surface drag, local Nusselt number, local nanoparticle and regular Sherwood numbers in the presence of solutal stratification (ε_2). From Fig. 3.5(a), it is observed that the drag coefficient reduces with the enhancement of solutal stratification parameter. It is also noticed that the local Nusselt number decreases, whereas the local nanoparticle Sherwood number increases with the increase of solutal stratification parameter, as displayed in Figs. 3.5(b) and 3.5(c). However, the local regular Sherwood number decreases with the increase of solutal stratification parameter, as shown in Fig. 3.5(d).

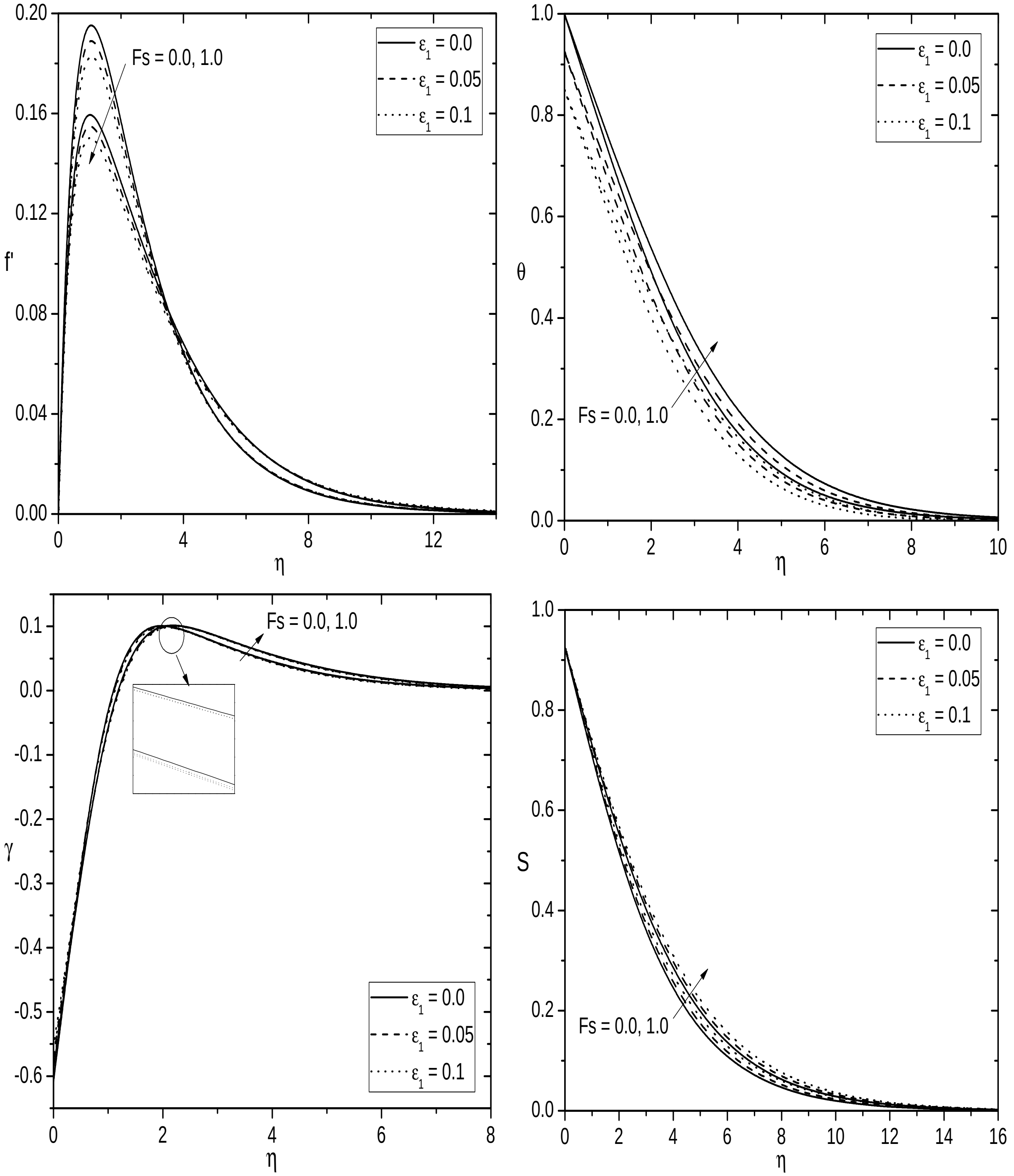

Figure 3.2: *Effects of Fs and ε_1 on (a) Velocity, (b) Temperature, (c) Nanoparticle volume fraction, and (d) Regular concentration for $\varepsilon_2 = 0.05$.*

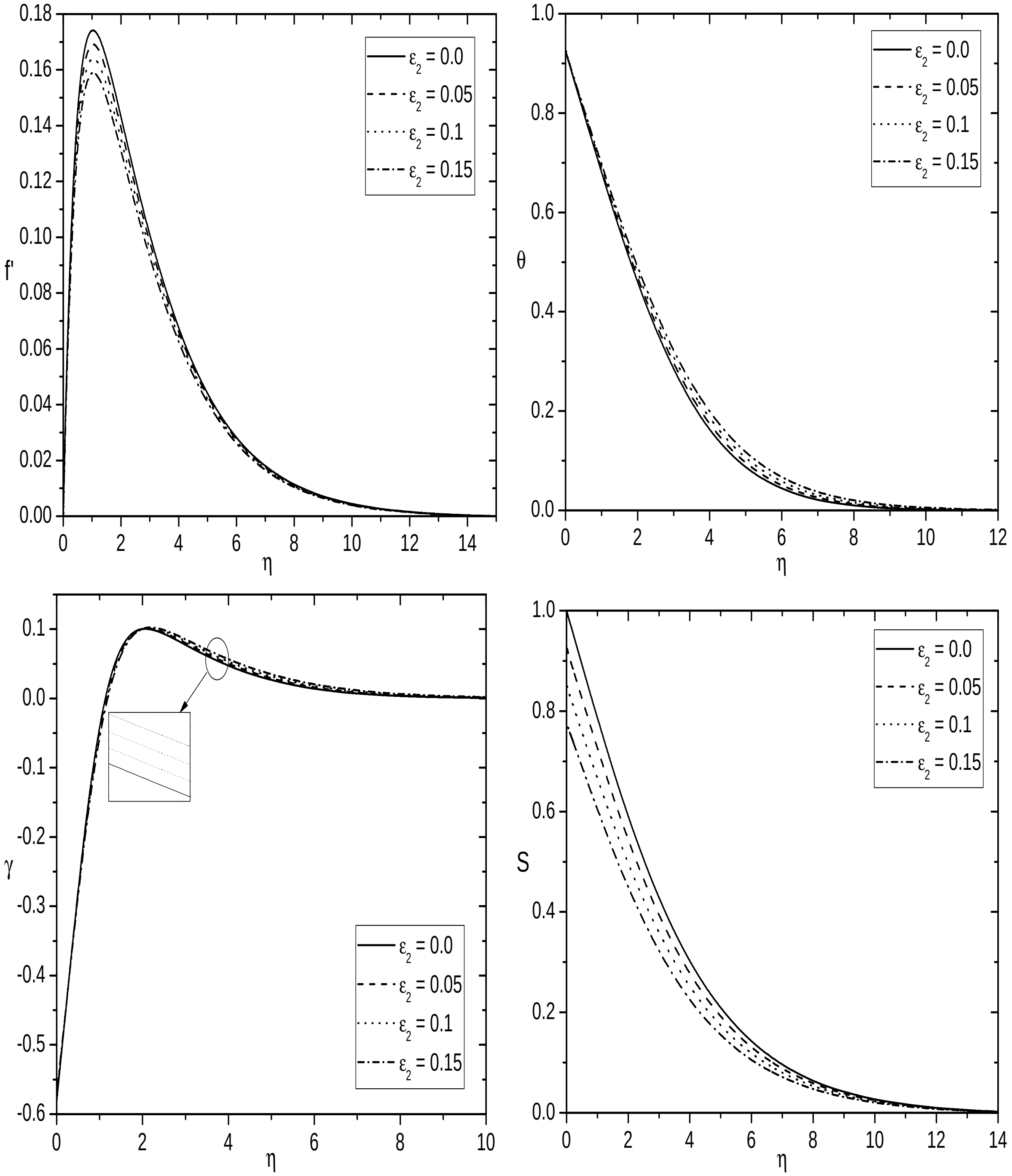

Figure 3.3: *Effect of* ε_2 *on (a) Velocity, (b) Temperature, (c) Nanoparticle volume fraction, and (d) Regular concentration for* $Fs = 0.5$ *and* $\varepsilon_1 = 0.05$.

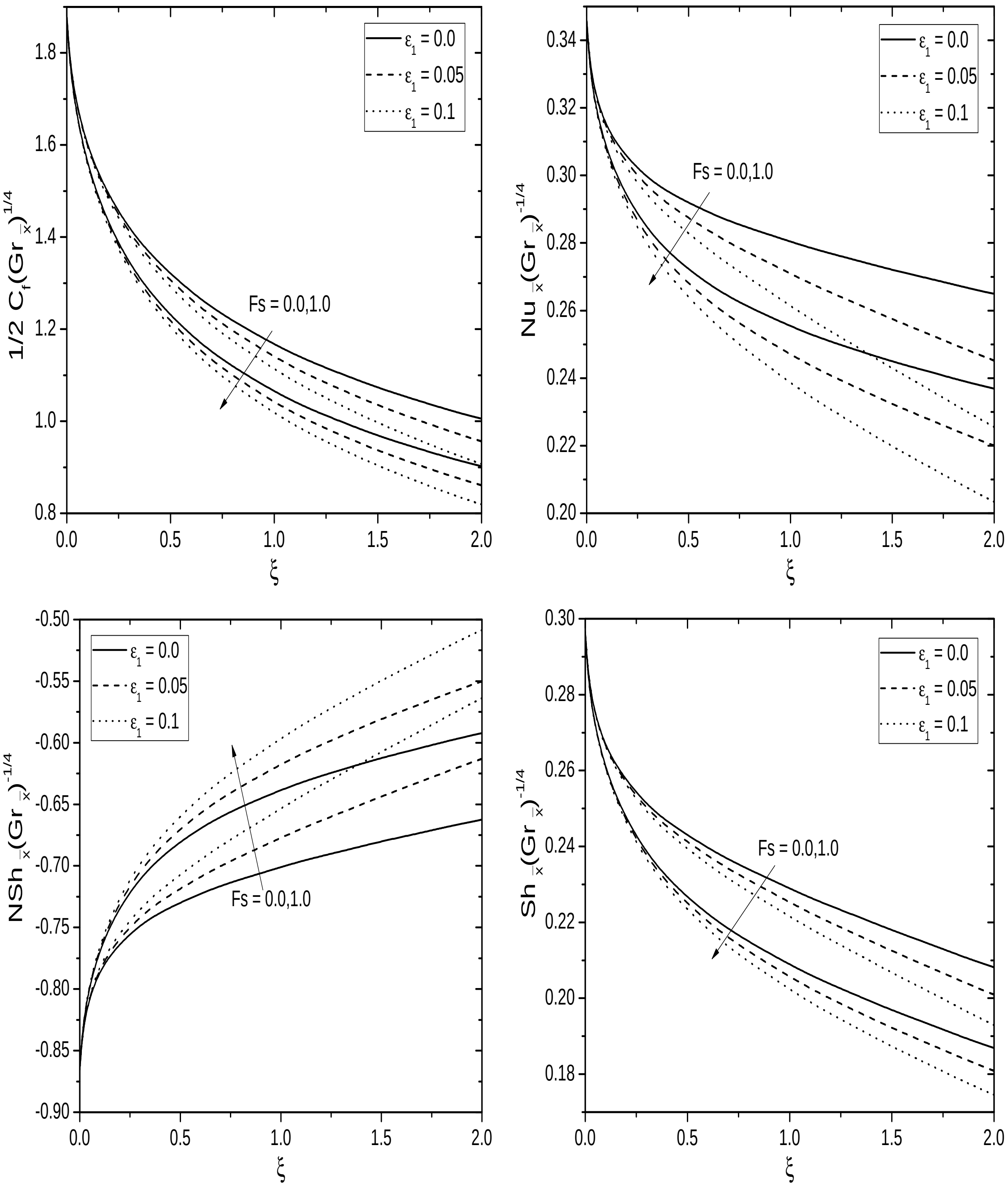

Figure 3.4: *Effects of Fs and ε_1 on (a) Skin friction, (b) Heat transfer rate, (c) Nanoparticle mass transfer rate, and (d) Regular mass transfer rate for $\varepsilon_2 = 0.05$.*

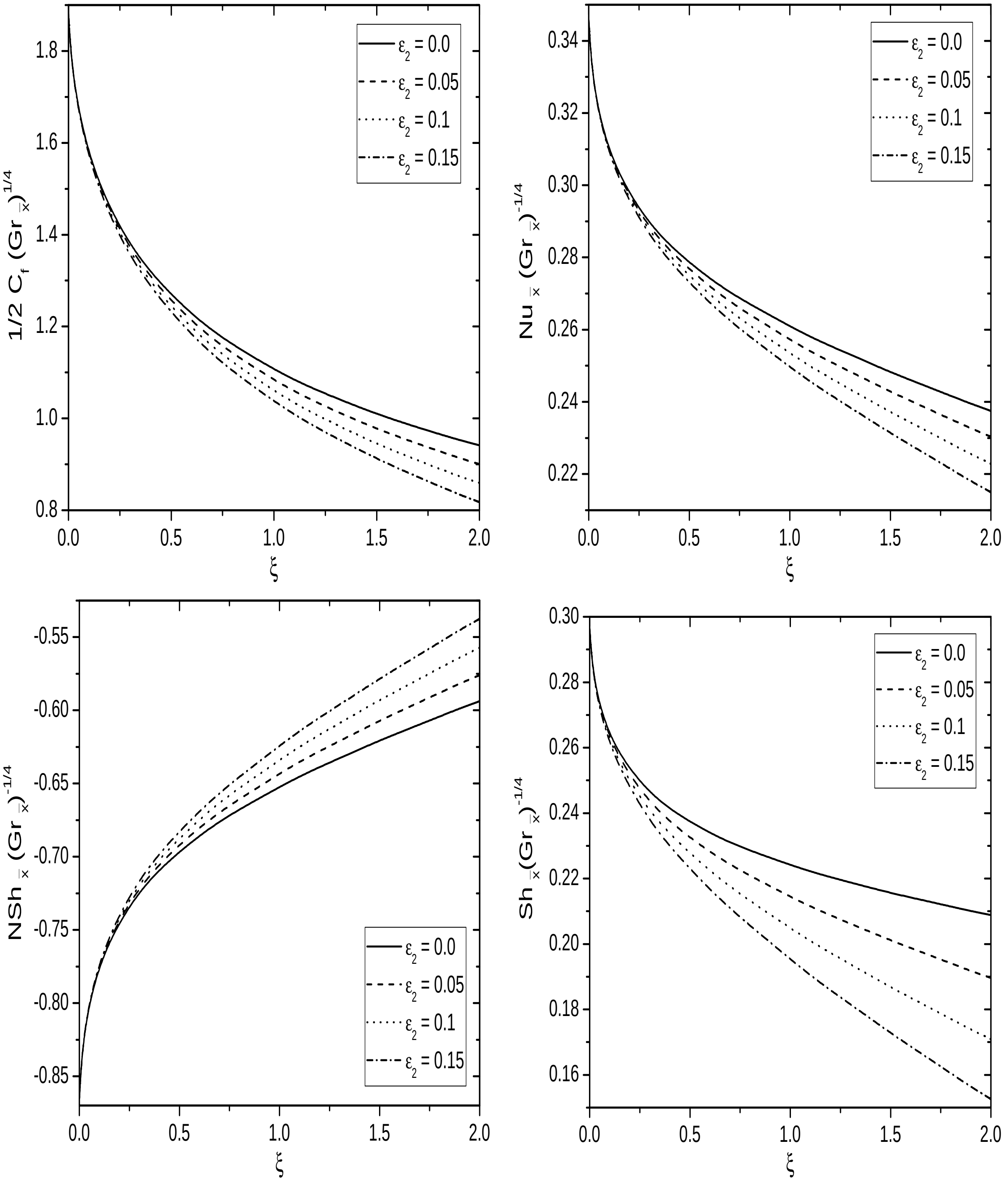

Figure 3.5: *Effect of ε_2 on (a) Skin friction, (b) Heat transfer rate, (c) Nanoparticle mass transfer rate, and (d) Regular mass transfer rate for $Fs = 0.5$ and $\varepsilon_1 = 0.05$.*

3.2.2 Case(b): Mixed Convection

Consider the flow to be a mixed convection, which arises from an external flow with the velocity U_∞ and buoyancy forces. we introduce the following dimensionless variables

$$\xi = \frac{\overline{x}}{x_0} = \frac{x - x_0}{x_0},\ \eta = \frac{y}{\overline{x}}\, Re_{\overline{x}}^{1/2},\ \psi = r\,\nu Re_{\overline{x}}^{1/2} f\,(\xi,\eta),\ \theta\,(\xi,\eta) = \frac{T - T_\infty(x - x_0)}{T_w - T_{\infty,0}},$$

$$\gamma\,(\xi,\eta) = \frac{\phi - \phi_\infty}{\phi_\infty},\ S\,(\xi,\eta) = \frac{C - C_\infty(x - x_0)}{C_w - C_{\infty,0}} \tag{3.14}$$

Using (2.7) and (3.14) in Eqs.(3.2)-(3.5), we get the following momentum, energy, nanoparticle volume fraction and regular concentration equations

$$\frac{1}{\varepsilon} f''' + \frac{1}{\varepsilon^2}\left(R + \frac{1}{2}\right) f f'' + \lambda\,\xi\,(\theta + Nc\,S - Nr\,\gamma) + \frac{1}{Da\,Re}\,\xi(1 - f')$$
$$+ \frac{Fs}{Da}\,\xi(1 - f'^2) = \frac{\xi}{\varepsilon^2}\left(f'\frac{\partial f'}{\partial \xi} - \frac{\partial f}{\partial \xi} f''\right) \tag{3.15}$$

$$\frac{1}{Pr}\theta'' + \left(R + \frac{1}{2}\right) f\theta' + Nb\,\gamma'\,\theta' + Nt\ (\theta')^2 - \varepsilon_1\,\xi\,f' = \xi\left(f'\frac{\partial \theta}{\partial \xi} - \frac{\partial f}{\partial \xi}\theta'\right) \tag{3.16}$$

$$\frac{1}{Le}\gamma'' + \left(R + \frac{1}{2}\right) f\gamma' + \frac{1}{Le}\,\frac{Nt}{Nb}\theta'' = \xi\left(f'\frac{\partial \gamma}{\partial \xi} - \frac{\partial f}{\partial \xi}\gamma'\right) \tag{3.17}$$

$$\frac{1}{Sc}S'' + \left(R + \frac{1}{2}\right) f S' - \varepsilon_2\,\xi\,f' = \xi\left(f'\frac{\partial S}{\partial \xi} - \frac{\partial f}{\partial \xi}S'\right) \tag{3.18}$$

where $Re_{x_0} = \dfrac{U_\infty\, x_0}{\nu}$ is the Reynolds number based on x_0, and $\lambda = \dfrac{Gr_{x_0}}{Re_{x_0}^2}$ is the mixed convection parameter.

The boundary conditions (3.6) in terms of f, θ, γ and S become

$$f'(\xi,\eta) = 0,\ f(\xi,\eta) + \frac{\xi}{\left(R + \frac{1}{2}\right)}\frac{\partial f}{\partial \xi} = 0,\ \theta(\xi,\eta) = 1 - \varepsilon_1\,\xi, Nb\,\gamma'(\xi,\eta) + Nt\,\theta'(\xi,\eta) = 0,$$
$$S(\xi,\eta) = 1 - \varepsilon_2\,\xi \quad \text{at} \quad \eta = 0 \tag{3.19a}$$

$$f'(\xi,\eta) = 1,\ \theta(\xi,\eta) = 0,\ \gamma(\xi,\eta) = 0,\ S(\xi,\eta) = 0 \quad \text{as} \quad \eta \to \infty \tag{3.19b}$$

The non-dimensional skin friction C_f, local Nusselt number $Nu_{\overline{x}}$, local nanoparticle Sherwood number $NSh_{\overline{x}}$ and local Sherwood number $Sh_{\overline{x}}$, are given by

$$\left.\begin{array}{l} \frac{1}{2}C_f\, Re_{\overline{x}}^{1/2} = f''(\xi,0),\ \frac{Nu_{\overline{x}}}{Re_{\overline{x}}^{1/2}} = -\theta'(\xi,0), \\ \frac{NSh_{\overline{x}}}{Re_{\overline{x}}^{1/2}} = -\gamma'(\xi,0),\ \frac{Sh_{\overline{x}}}{Re_{\overline{x}}^{1/2}} = -S'(\xi,0) \end{array}\right\} \tag{3.20}$$

Results and Discussion

The reduced system of non-linear partial differential equations (3.15)-(3.18) together with the boundary conditions (3.19) is solved numerically using the Bivariate Pseudo-Spectral Local Linearization Method, as discussed in the Chapter-2. In order to validate the generated code, for the special case of $Nc = 0.0$, $Nr = 0.0$, $Re = 200.0$, $\varepsilon = 1.0$, $\lambda = 1.0$, $Sc = 1.0$, $Le = 1.0$, $Da = 1.0$, $Nt = 0.0$, $Nb \to 0.0$, $Fs = 0.0$, $\varepsilon_1 = 0.0$ and $\varepsilon_2 = 0.0$, the results of the present problem have been compared with those of Lloyd and Sparrow [56] and it is found that they are in good agreement as shown in Tab. 2.2. To explore the effects of Forchheimer number (Fs), thermal stratification parameter (ε_1) and solutal stratification parameter (ε_2) on the physical quantities of the flow, heat and mass transfer characteristics, the computations have been carried out for both aiding and opposing flow situations by taking $Pr = 1.0$, $Sc = 0.6$, $Le = 10.0$, $Nc = 1.0$, $Nr = 0.5$, $Re = 200.0$, $\varepsilon = 0.8$, $Da = 0.5$, $Nt = 0.5$ and $Nb = 0.2$.

Figures 3.6(a)-3.6(b) explore the influence of thermal stratification parameter (ε_1) on the dimensionless velocity f' and temperature θ for aiding flow, whereas these results in the case of opposing flow are displayed in Figs. 3.7(a)-3.7(b). Figures 3.6(a) and 3.7(a) reveal that the velocity decreases with the increase of thermal stratification parameter for aiding flow, but it increases for opposing flow. As the thermal stratification parameter enhances, the temperature reduces in both the aiding and opposing flows as given in Figs. 3.6(b) and 3.7(b).

The effect of solutal stratification parameter (ε_2) on the non-dimensional velocity f' and regular concentration S in the case of aiding flow, are exhibited in Figs. 3.8(a)-3.8(b), whereas these results in the case of opposing flow are shown in Figs. 3.9(a)-3.9(b). An increase in the solutal stratification parameter leads to decrease the velocity in aiding flow, but it increases in opposing flow [see Figs. 3.8(a) and 3.9(a)]. However, the regular concentration reduces with the increase of solutal stratification parameter in both the aiding and opposing flows, as interpreted in Figs. 3.8(b) and 3.9(b).

Figures 3.10(a)-3.10(d) show the influence of Forchhiemer number (Fs) on the non-dimensional velocity f', temperature θ, nanoparticle volume fraction γ, and regular concentration S for aiding flow, whereas these results in opposing flow are explored in Figures 3.11(a)-3.11(d). As the non-Darcy parameter increases, the porous medium offers more resistance to the fluid flow and hence, the velocity is more in the non-Darcy porous medium (Fs = 0.5) when compared to that of the Darcy porous medium (Fs = 0.0), for both aiding and opposing flows. The temperature decreases with the increase of Forchhiemer number in both aiding and opposing flows, as exhibited in Figs. 3.10(b) and 3.11(b). As the Forchhiemer number rises, the nanoparticle volume fraction increases for aiding and opposing flows, as given in Figs. 3.10(c) and 3.11(c). For aiding and opposing flows, the regular concentration decreases with the increase of Forchhiemer number, as portrayed in Figs. 3.10(d) and 3.11(d).

Figures 3.12(a)-3.12(d) illustrate the variations of non-dimensional surface drag, local Nusselt number, local nanoparticle and regular Sherwood numbers over the streamwise coordinate ξ, in the presence of thermal stratification parameter for both aiding and opposing flow situations. Here $\varepsilon_1 = 0.0$ represents the ambient medium with no thermal stratification (i.e., the isothermal surface case). It can be seen from Fig. 3.12(a) that the surface drag coefficient decreases with the increase of thermal stratification parameter in the aiding flow whereas, it increases in the opposing flow. It is known that the presence of stable thermal stratification decreases the temperature differences between a surface of the frustum of a cone and surrounding nanofluid. Hence, a rapid increase in the local Nusselt number is found with increasing values of thermal stratification parameter for opposing flow, and a reduction is noticed for aiding flow as shown in Fig. 3.12(b). As the thermal stratification parameter rises, the local nanoparticle Sherwood number rises and the local regular Sherwood number falls in the aiding flow, whereas an opposite trend is observed in the opposing flow, as depicted in Fig. 3.12(c)- 3.12(d). Moreover, the surface drag, local Nusselt and regular Sherwood numbers are more in the case of aiding flow as a comparison with those of opposing flow.

The streamwise distributions of dimensionless surface drag, local Nusselt number, local nanoparticle and regular Sherwood numbers for various values of the solutal stratification parameter for both aiding and opposing flow cases, are displayed in Figs. 3.13(a)-3.13(d). Here $\varepsilon_2 = 0.0$ represents the ambient medium with no solutal stratification (i.e., the uniform wall concentration case). It is observed from Fig. 3.13(a) that the surface drag enhances with enhancing values of the solutal stratification parameter for opposing flow, whereas it diminishes in the aiding flow. Figure 3.13(b) illustrates that as the solutal stratification parameter increases, the local Nusselt number increases in case of the opposing flow, whereas it decreases in aiding flow case. The local nanoparticle Sherwood number increases, but the local regular Sherwood number decreases, with an increase in the solutal stratification parameter for aiding flow. But, an opposite trend is noticed for opposing flow, as shown in Figs. 3.13(c) and 3.13(d). The results under the influence of both thermal and solutal stratifications are due to the less temperature and concentration at the surface of the frustum of a cone compared those at the ambient medium. Consequently, an expansion in the double stratification parameters ε_1 and ε_2 causes a reduction in the local Nusselt and regular Sherwood numbers for aiding flow.

For aiding and opposing flows, the streamwise distributions of the non-dimensional surface drag, local Nusselt number, local nanoparticle and regular Sherwood numbers under the influence of non-Darcy parameter are exhibited in Figs. 3.14(a)-3.14(d). The surface drag coefficient in the case of non-Darcy porous medium ($Fs \neq 0$) is higher than the case of Darcy porous medium ($Fs = 0$) for both opposing and aiding flows. Also, it increases with the increase of non-Darcy parameter, as plotted in Fig. 3.14(a). As the non-Darcy parameter enhances, the local Nusselt number enhances in both the aiding and opposing flows, but the local Nusselt number in aiding flow is higher than that of the opposing flow, as shown in Fig. 3.14(b). It is noted from Fig. 3.14(c) that the local nanoparticle Sherwood number diminishes with the enhancement of non-Darcy parameter. Further, Fig. 3.14(d) reveals that the local regular Sherwood number increases with the increase of non-Darcy parameter. Moreover, the local nanoparticle Sherwood number is more in the opposing flow, whereas the local regular Sherwood number is more in the aiding flow.

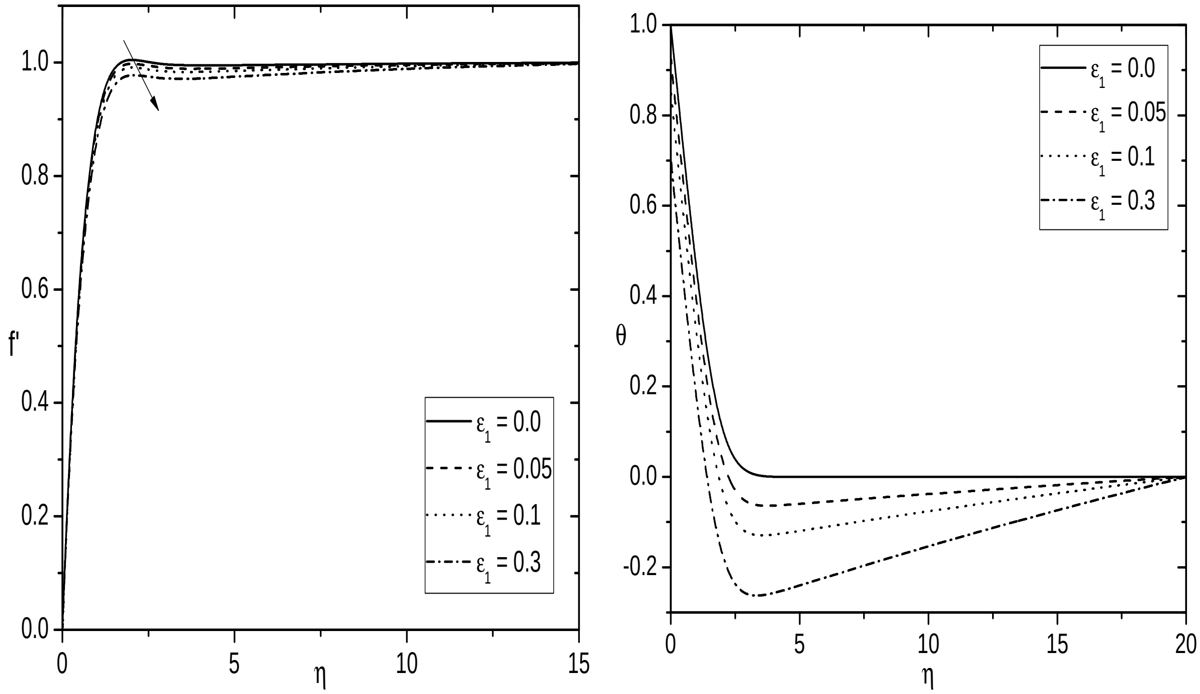

(a) (b)

Figure 3.6: *Effect of* ε_1 *on (a) Velocity and (b) Temperature (Aiding flow case) for* $Fs = 0.5$ *and* $\varepsilon_2 = 0.1$.

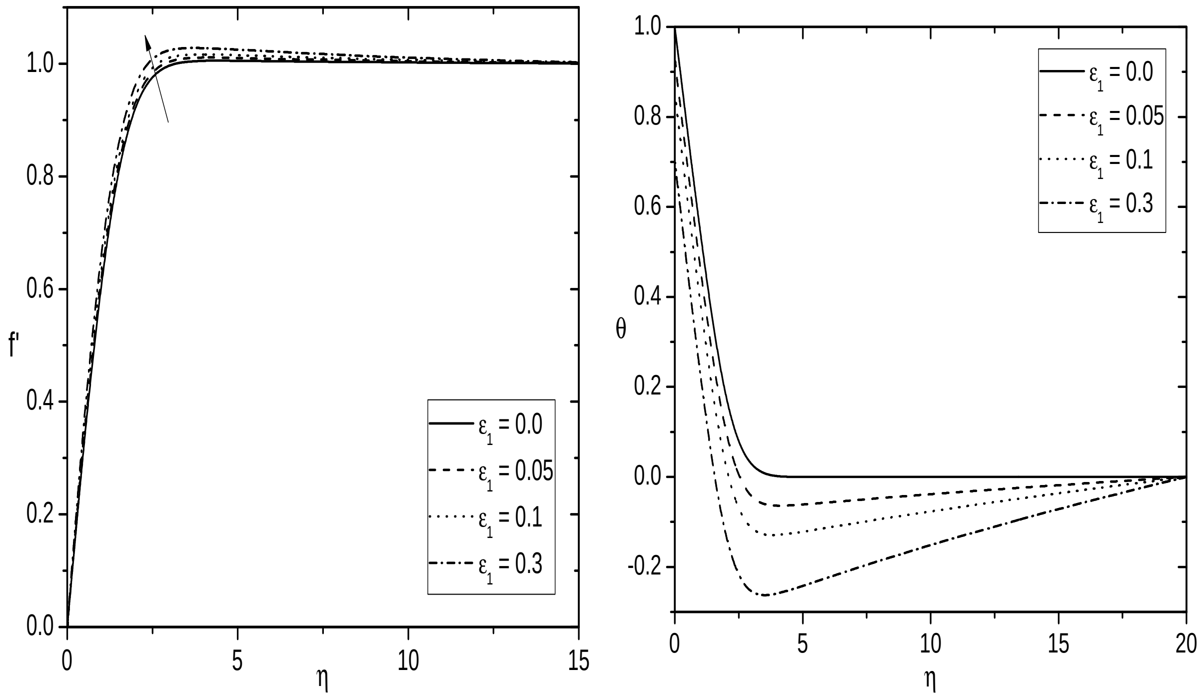

(a) (b)

Figure 3.7: *Effect of* ε_1 *on (a) Velocity and (b) Temperature (Opposing flow case) for* $Fs = 0.5$ *and* $\varepsilon_2 = 0.1$.

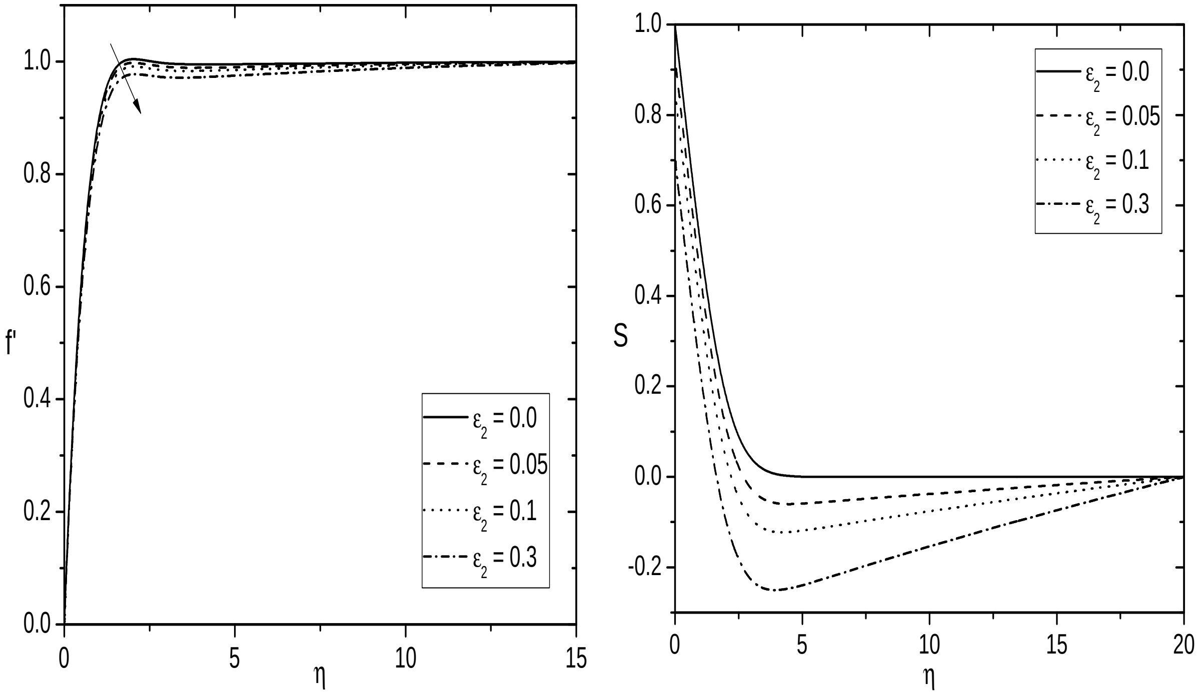

(a) (b)

Figure 3.8: *Effect of* ε_2 *on (a) Velocity and (b) Regular Concentration (Aiding flow case) for* $Fs = 0.5$ *and* $\varepsilon_1 = 0.1$.

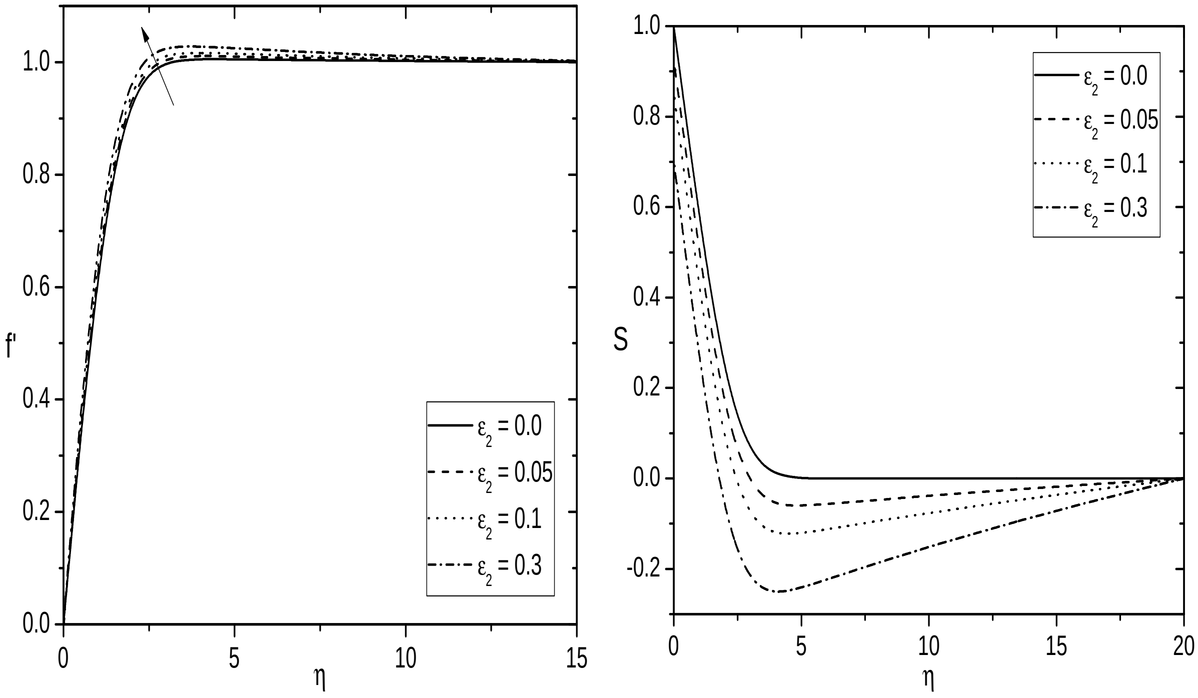

(a) (b)

Figure 3.9: *Effect of* ε_2 *on (a) Velocity and (b) Regular Concentration (Opposing flow case) for* $Fs = 0.5$ *and* $\varepsilon_1 = 0.1$.

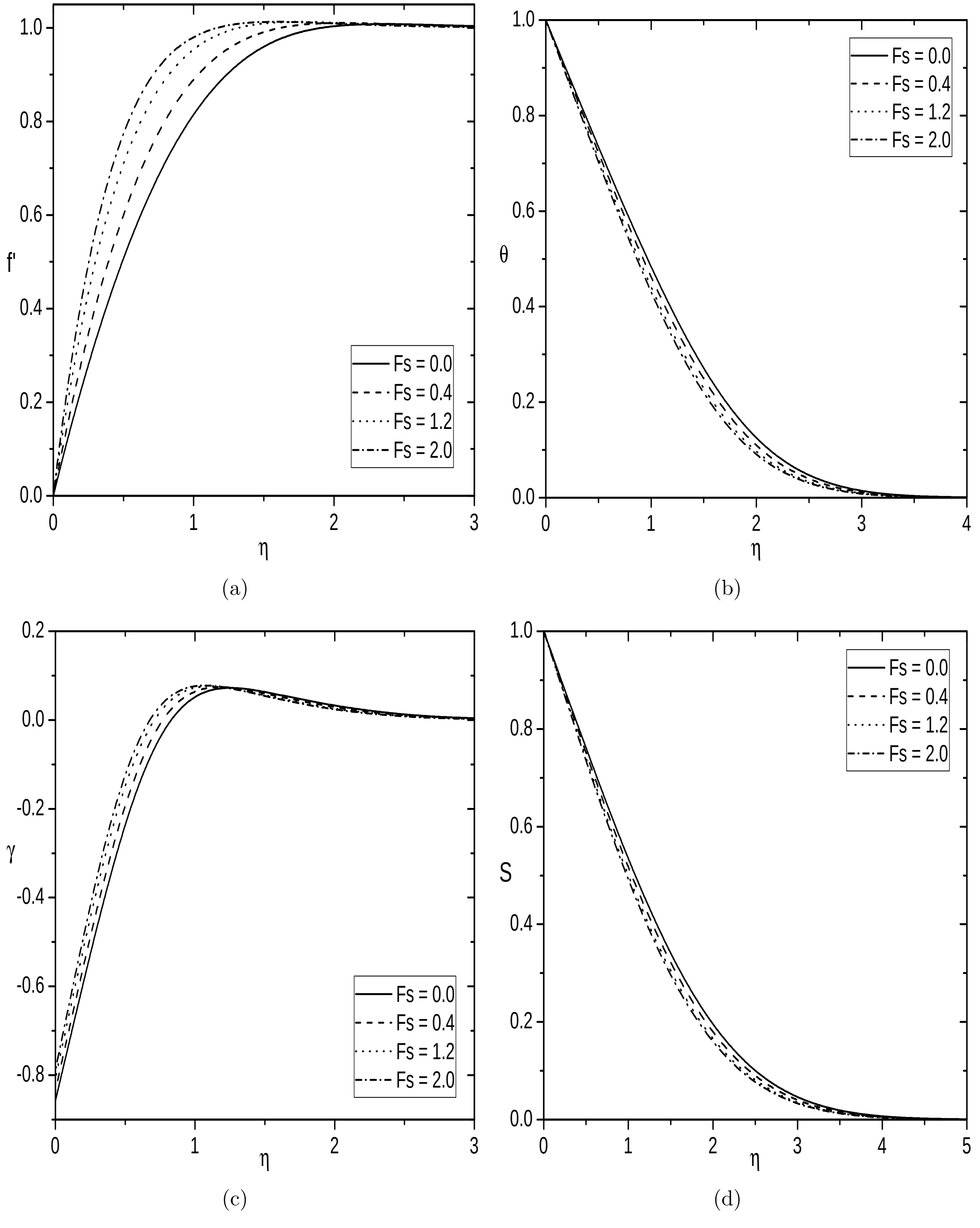

(a) (b)

(c) (d)

Figure 3.10: *Variation of Fs on (a)Velocity, (b) Temperature, (c) Nanoparticle volume fraction and (d) Regular concentration (Aiding flow case) for* $\varepsilon_1 = 0.1$ *and* $\varepsilon_2 = 0.1$.

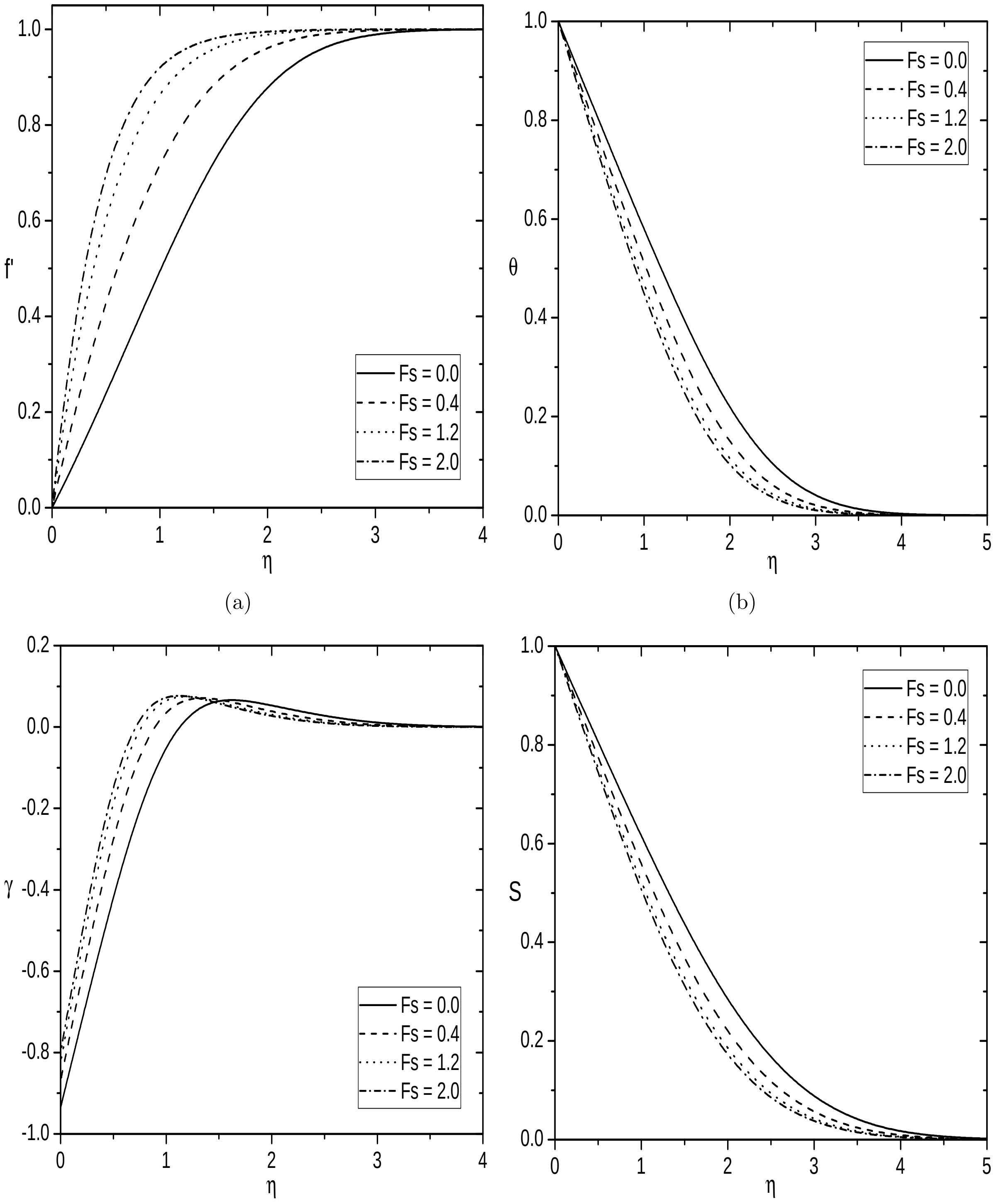

(a) (b)

(c) (d)

Figure 3.11: *Variation of Fs on (a)Velocity, (b) Temperature, (c) Nanoparticle volume fraction and (d) Regular concentration (Opposing flow case) for $\varepsilon_1 = 0.1$ and $\varepsilon_2 = 0.1$.*

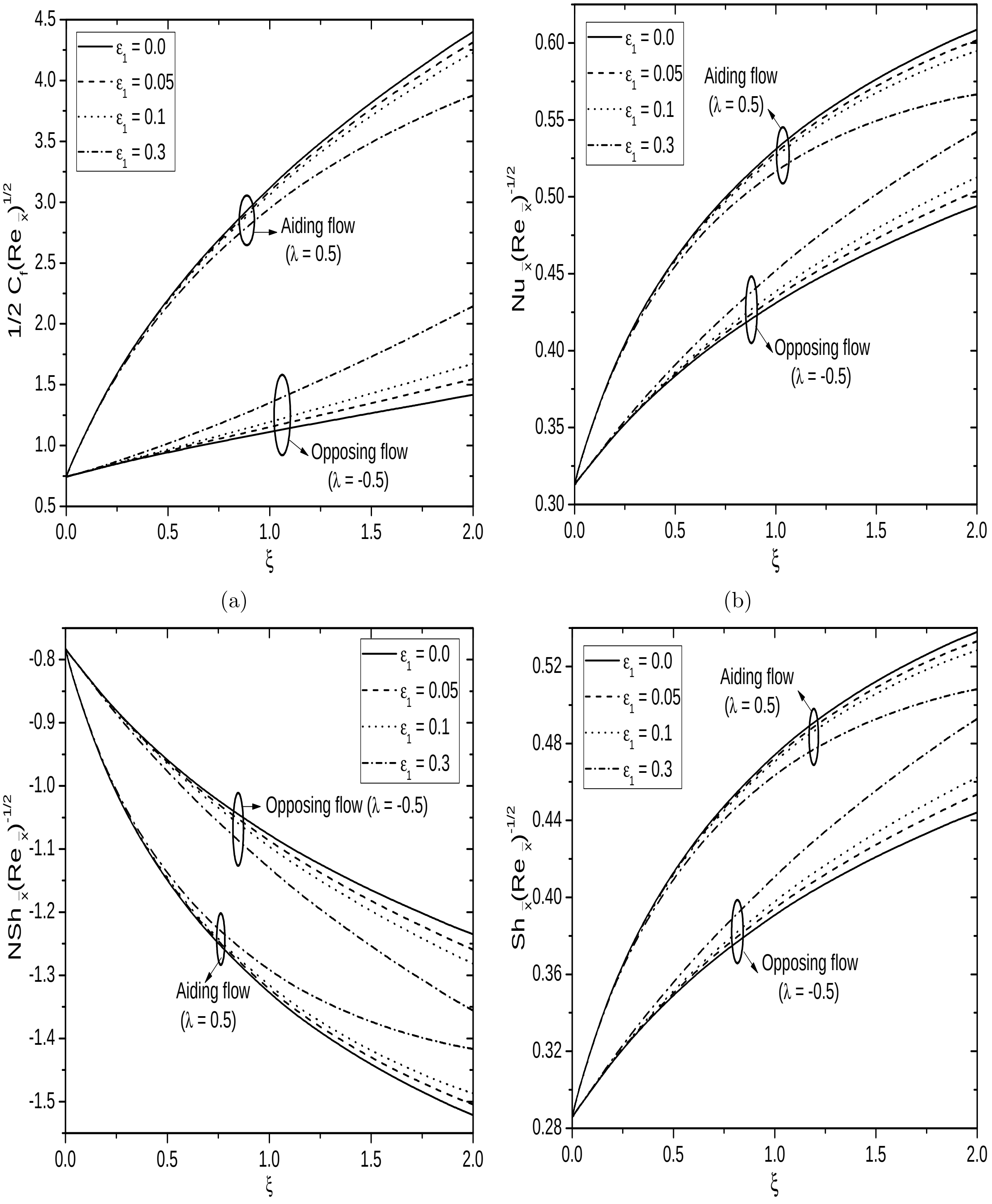

(a) (b)

(c) (d)

Figure 3.12: *Effects of* ε_1 *and* λ *on (a) Skin friction, (b) Heat transfer rate, (c) Nanoparticle mass transfer rate, and (d) Regular mass transfer rate for* $Fs = 0.5$ *and* $\varepsilon_2 = 0.1$.

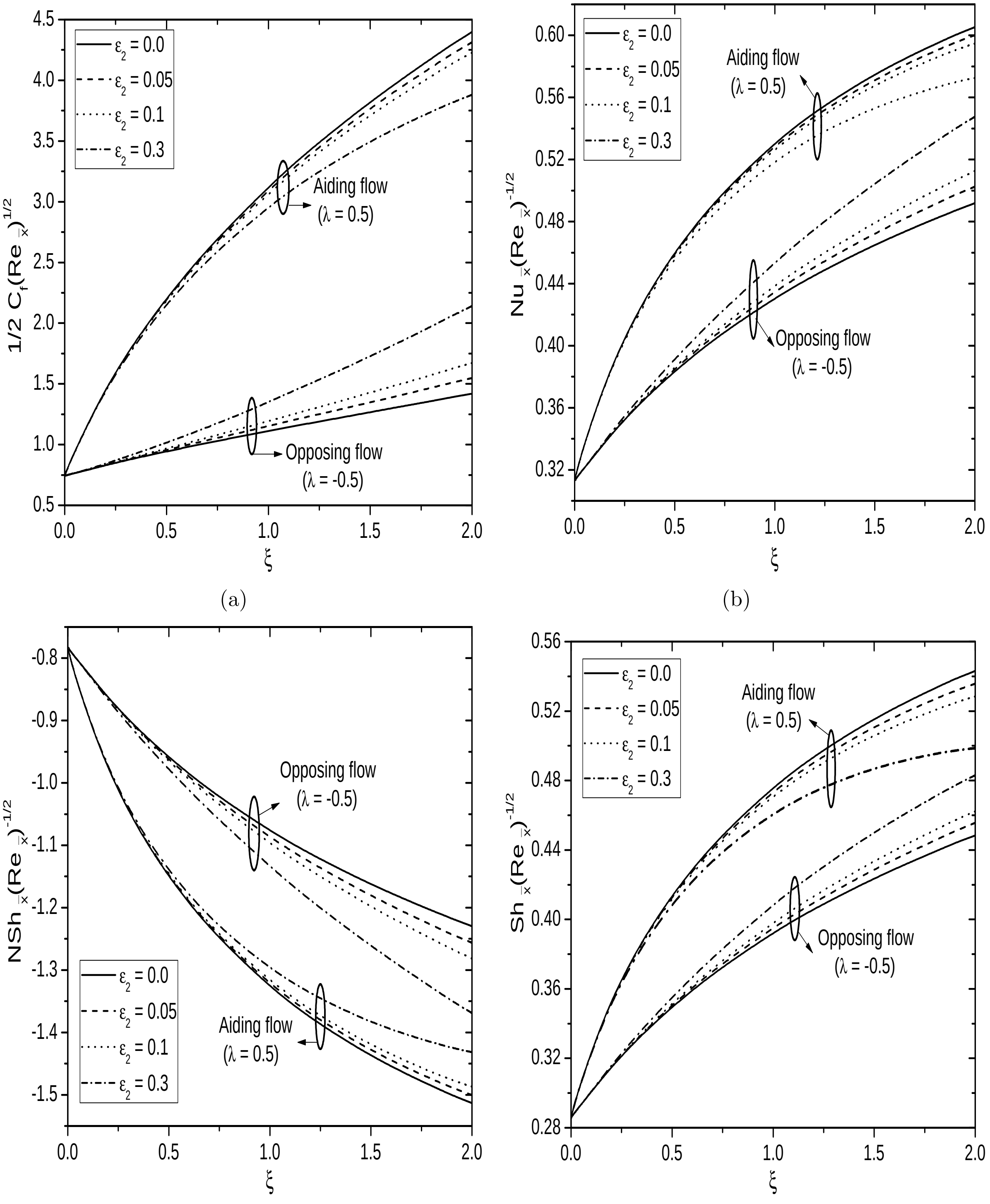

(a)

(b)

(c)

(d)

Figure 3.13: *Effects of* ε_2 *and* λ *on (a) Skin friction, (b) Heat transfer rate, (c) Nanoparticle mass transfer rate, and (d) Regular mass transfer rate for* $Fs = 0.5$ *and* $\varepsilon_1 = 0.1$.

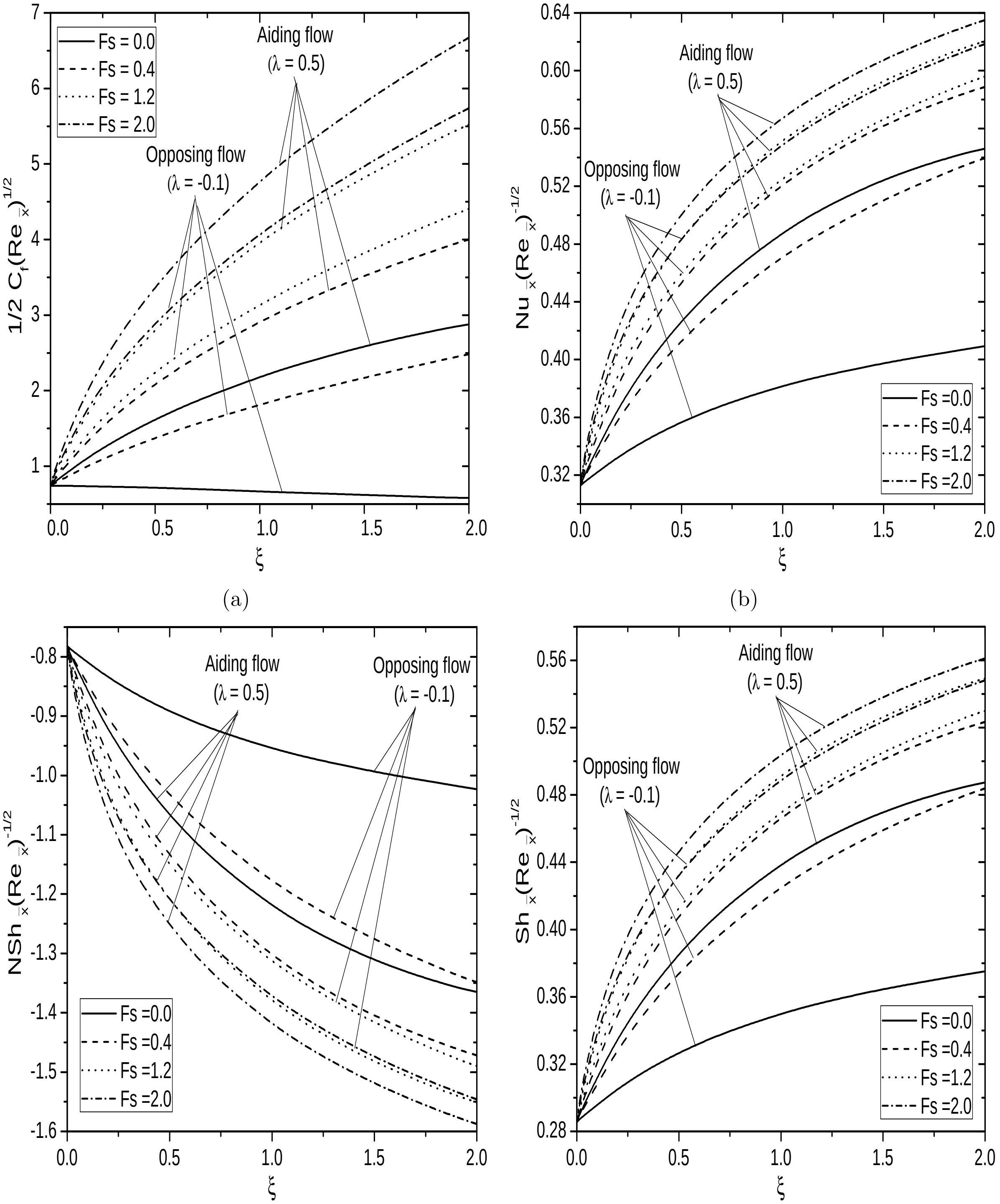

Figure 3.14: *Effect of Fs and λ on (a) Skin friction, (b) Heat transfer rate, (c) Nanoparticle mass transfer rate, and (d) Regular mass transfer rate for* $\varepsilon_1 = 0.1$ *and* $\varepsilon_2 = 0.1$.

3.3 Conclusions

The natural and mixed convective transport over the vertical frustum of a cone embedded in a porous medium saturated by a nanofluid is, analyzed in this chapter. From this computational analysis, the following conclusions are drawn for both case (a) and case (b):

An increase in the thermal stratification parameter reduces the velocity, temperature, local Nusselt and regular Sherwood numbers, but increases the regular concentration and local nanoparticle Sherwood number in case (a) and aiding flow of case (b). However, the velocity, local Nusselt number, and local Sherwood numbers show an opposite trend in the opposing flow case (b). The higher values of the solutal stratification parameter results in a lower velocity, regular concentration, local Nusselt number and local regular Sherwood number, and higher local nanoparticle Sherwood number in case (a) and aiding flow of case (b). An increase in Fs leads to decreases the velocity, surface drag, local Nusselt number and local regular Sherwood number, but increases the temperature, regular concentration and local nanoparticle Sherwood number in case (a). These profiles and physical quantities show a reverse trend in case (b). Moreover, the surface drag, local Nusselt number, and local regular Sherwood number are high in the aiding flow when compared to those of the opposing flow.

Chapter 4

Effect of Arrhenius Activation Energy with Binary Chemical Reaction on Convective Flow of a Nanofluid with Convective Boundary Condition [1]

4.1 Introduction

The analysis of mass transfer with Arrhenius activation energy and binary chemical reaction has been gained a lot of attention due to its immense applications in chemical engineering, cooling of nuclear reacting, oil reservoir, geothermal engineering, etc. But, very few studies have been reported in the literature to examine the boundary layer flows in the presence of Arrhenius activation energy with binary chemical reaction (see Awad *et al.* [6], Shafique *et al.* [108], Mustafa *et al.* [73]).

The effect of thermal radiation on the fluid flow and heat transfer has significant applications in the design of many advanced energy conversion systems operating at high

---

[1] Case(a): Published in "**International Journal of Chemical Reactor Engineering**" 16(3) (2017) DOI: 10.1515/ijcre-2016-0188, Case(b): Accepted in "**Advanced Science, Engineering and Medicine**"

temperature. The thermal radiation occurs because of the emission by the hot walls and working fluid. Hence, several investigations have been carried out on the natural and mixed convective flows of different fluids under the influence of thermal radiation. Merely, it is essential to study the effect of thermal radiation due to its relevance to various applications involving high temperatures such as nuclear power plant, gas turbines missiles, satellites, space vehicles, and aircrafts, etc.

Convective boundary condition plays a vital role in the analysis of heat transfer, due to diverse engineering and industrial applications such as the transpiration cooling process, textile drying, laser pulse heating, etc. In this mechanism, heat is supplied to the convecting fluid through a bounding surface with a finite heat capacity. Noghrehabadi *et al.* [86] investigated the role of slip velocity and convective surface boundary condition on the convective flow of a nanofluid along a stretching surface. Recently, the combined effects of convective and diffusive boundary conditions on the natural convective flow of a dilatant nanofluid over the vertical full cone/vertical flat plate in a Darcy porous medium has been analyzed by Uddin *et al.* [121] (For more details, see the references therein).

In this chapter, the effects of thermal radiation and Arrhenius activation energy with binary chemical reaction on the convective flow of a nanofluid over the vertical frustum of a cone under the convective boundary condition, are studied. The Rosseland approximation is considered to investigate the effect of thermal radiation. The governing coupled and nonlinear partial differential equations are solved by using a Bivariate Pseudo-Spectral Local Linearization Method. The influence of various physical parameters on the nanofluid flow with heat and mass transfer characteristics, are examined and displayed graphically.

4.2 Mathematical Formulation

Consider a laminar, steady and two dimensional flow of an incompressible nanofluid over the vertical frustum of a cone. The origin O of the coordinate system is placed at the vertex of a full cone, where x-axis is taken along the surface of the cone measured from the origin

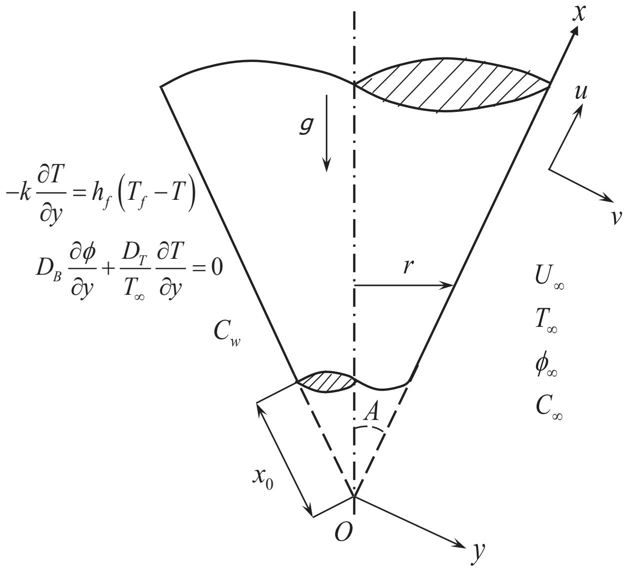

Figure 4.1: *Physical model and coordinate system*

and y-axis is normal to the surface [see Fig. (4.1)]. The temperature difference between the surface and the medium is assumed to be large, so that the convection region is thick. The fluid is considered to be a gray, absorbing and emitting radiation, but non-scattering medium and the Rosseland approximation is used to describe the radiative heat flux in the energy equation. Assume that the velocity of the outer flow is U_∞. The temperature, nanoparticle volume fraction, and regular concentration of the ambient medium are assumed to be T_∞, ϕ_∞ and C_∞, respectively. The surface of the vertical frustum of a cone is either cooled or heated by convection from a fluid of temperature T_f with $T_f < T_\infty$ (cooled surface) and $T_f > T_\infty$ (heated surface), respectively. The surface of the vertical frustum of a cone is held at uniform regular concentration C_w.

By employing Oberbeck-Boussinesq approximation and making use of the standard boundary layer assumptions, the governing equations for the nanofluid flow over the vertical frustum of a cone are given by

$$\frac{\partial(u\,r)}{\partial x} + \frac{\partial(v\,r)}{\partial y} = 0 \tag{4.1}$$

$$\rho_{f\infty}\left(u\,\frac{\partial u}{\partial x}+v\,\frac{\partial u}{\partial y}\right)=\mu\,\frac{\partial^2 u}{\partial y^2}+\rho_{f\infty}\,g\,\left(1-\phi_\infty\right)\left[\beta_T\left(T-T_\infty\right)+\beta_C\left(C-C_\infty\right)\right]\cos A$$
$$-g(\rho_p-\rho_{f_\infty})(\phi-\phi_\infty)\cos A \quad (4.2)$$

$$u\,\frac{\partial T}{\partial x}+v\,\frac{\partial T}{\partial y}=\alpha_m\frac{\partial^2 T}{\partial y^2}+\mathcal{J}\left[D_B\frac{\partial \phi}{\partial y}\frac{\partial T}{\partial y}+\frac{D_T}{T_\infty}\left(\frac{\partial T}{\partial y}\right)^2\right]+\frac{4\alpha_m\sigma^*}{3kk^*}\,\frac{\partial^2}{\partial y^2}(4T_\infty^3 T-3T_\infty^4) \quad (4.3)$$

$$u\,\frac{\partial \phi}{\partial x}+v\,\frac{\partial \phi}{\partial y}=D_B\,\frac{\partial^2 \phi}{\partial y^2}+\frac{D_T}{T_\infty}\frac{\partial^2 T}{\partial y^2} \quad (4.4)$$

$$u\,\frac{\partial C}{\partial x}+v\,\frac{\partial C}{\partial y}=D_S\,\frac{\partial^2 C}{\partial y^2}-K_r^2\left(\frac{T}{T_\infty}\right)^n\,e^{\frac{-E_a}{\mathrm{k}T}}\,\left(C-C_\infty\right) \quad (4.5)$$

where k^* is the Rosseland mean absorption coefficient, σ^* is the Stefan Boltzmann constant, K_r^2 is the rate of chemical reaction, $\left(\frac{T}{T_\infty}\right)^n\,e^{\frac{-E_a}{\mathrm{k}T}}$ is the modified Arrhenius function in which k is the Boltzmann constant and n is the rate of exponent fitted constant $(-1<n<1)$.

The associated boundary conditions are

$$u=0,\;v=0,\;-k\,\frac{\partial T}{\partial y}=h_f\,\left(T_f-T\right),\;\;D_B\,\frac{\partial \phi}{\partial y}+\frac{D_T}{T_\infty}\frac{\partial T}{\partial y}=0,\;C=C_w\quad\text{at}\quad y=0 \quad (4.6a)$$
$$u=U_\infty,\;T=T_\infty,\;\phi=\phi_\infty,\;C=C_\infty\quad\text{as}\quad y\to\infty \quad (4.6b)$$

where h_f is the coefficient of convective heat transfer.

In this chapter also, two types (cases) of problems are considered: (a) free/natural convection and (b) mixed convection.

4.2.1 Case(a): Natural Convection

The flow is assumed to be a natural convection which is caused by buoyancy forces only without any external agent, and hence the velocity of the external flow becomes zero $i.e., U_\infty=0$. Now, we introduce the following non-similarity variables

$$\xi=\frac{x-x_0}{x_0}=\frac{\overline{x}}{x_0},\;\eta=\frac{y}{\overline{x}}\,Gr_{\overline{x}}^{1/4},\;\psi=r\,\nu Gr_{\overline{x}}^{1/4}f\left(\xi,\,\eta\right),$$

$$\theta\,(\xi,\,\eta) = \frac{T - T_\infty}{T_f - T_\infty},\; \gamma\,(\xi,\,\eta) = \frac{\phi - \phi_\infty}{\phi_\infty},\; S\,(\xi,\,\eta) = \frac{C - C_\infty}{C_w - C_\infty} \tag{4.7}$$

Using (2.7) and (4.7) in Eqs.(4.2)-(4.5), we get the following dimensionless equations

$$f''' + \left(R + \frac{3}{4}\right) f\, f'' - \frac{1}{2}(f')^2 + \theta + Nc\, S - Nr\, \gamma = \xi\, \left(f'\, \frac{\partial f'}{\partial \xi} - \frac{\partial f}{\partial \xi} f''\right) \tag{4.8}$$

$$\frac{1}{Pr}\, \left(1 + \frac{4}{3}\, Rd\right)\, \theta'' + \left(R + \frac{3}{4}\right)\, f\, \theta' + Nb\, \gamma'\, \theta' + Nt\, (\theta')^2 = \xi\, \left(f' \frac{\partial \theta}{\partial \xi} - \frac{\partial f}{\partial \xi} \theta'\right) \tag{4.9}$$

$$\frac{1}{Le}\, \gamma'' + \left(R + \frac{3}{4}\right) f\, \gamma' + \frac{1}{Le}\frac{Nt}{Nb}\, \theta' = \xi\, \left(f' \frac{\partial \gamma}{\partial \xi} - \frac{\partial f}{\partial \xi} \gamma'\right) \tag{4.10}$$

$$\frac{1}{Sc}\, S'' + \left(R + \frac{3}{4}\right) f\, S' - \left(\frac{\xi}{Gr}\right)^{1/2} \Lambda^2\, (1 + n\delta\theta)\, e^{-\frac{E}{1+\delta\theta}}\, S = \xi\, \left(f' \frac{\partial S}{\partial \xi} - \frac{\partial f}{\partial \xi} S'\right) \tag{4.11}$$

where $Rd = \dfrac{4\,\sigma^*\, T_\infty^3}{k\, k^*}$ is the thermal radiation parameter, $\Lambda = \dfrac{K_r\, x_0}{\nu^{1/2}}$ is the rate of chemical reaction, $\delta = \dfrac{T_f - T_\infty}{T_\infty}$ is the temperature relative parameter and $E = \dfrac{E_a}{\mathrm{k}\, T_\infty}$ is the Arrhenius activation energy parameter.

The boundary conditions (4.6) in terms of f, θ, γ and S become

$$f'(\xi, \eta) = 0,\; f(\xi, \eta) + \frac{\xi}{\left(R + \frac{3}{4}\right)}\, \frac{\partial f}{\partial \xi} = 0,\; \theta'(\xi, \eta) = -Bi\, \xi^{1/4}\, [1 - \theta(\xi, \eta)],$$

$$Nb\, \gamma'(\xi, \eta) + Nt\, \theta'(\xi, \eta) = 0,\; S(\xi, \eta) = 1 \quad \text{at} \quad \eta = 0 \tag{4.12a}$$

$$f'(\xi, \eta) = 0,\; \theta(\xi, \eta) = 0,\; \gamma(\xi, \eta) = 0,\; S(\xi, \eta) = 0 \quad \text{as} \quad \eta \to \infty \tag{4.12b}$$

The shear stress, local heat flux, local nanoparticle and regular mass fluxes are defined as

$$\tau_w = \mu\, \left[\frac{\partial u}{\partial y}\right]_{y=0},\; q_w = -k\, \left[\left(\frac{\partial T}{\partial y}\right) + \frac{4\, \alpha_m\, \sigma^*}{3\, k\, k^*} \frac{\partial}{\partial y}(4\, T_\infty^3\, T - 3\, T_\infty^4)\right]_{y=0},$$

$$q_n = -D_B\, \left[\frac{\partial \phi}{\partial y}\right]_{y=0} \text{ and } q_m = -D_S\, \left[\frac{\partial C}{\partial y}\right]_{y=0} \tag{4.13}$$

The quantities of physical interest are the non-dimensional skin friction $C_f = \dfrac{2\, \tau_w}{\rho_{f\infty} U_*^2}$, the

Nusselt number $Nu_{\overline{x}} = \dfrac{q_w\,\overline{x}}{k(T_f - T_\infty)}$, the nanoparticle Sherwood number $NSh_{\overline{x}} = \dfrac{q_n\,\overline{x}}{D_B\,\phi_\infty}$ and the regular Sherwood number $Sh_{\overline{x}} = \dfrac{q_m\,\overline{x}}{D_S\,(C_w - C_\infty)}$, are given by

$$\left.\begin{aligned} C_f\,Gr_{\overline{x}}^{1/4} = 2\,f''(\xi,\,0),\ \frac{Nu_{\overline{x}}}{Gr_{\overline{x}}^{1/4}} &= -\left[1 + \frac{4}{3}\,Rd\right]\,\theta'(\xi,\,0),\\ \frac{NSh_{\overline{x}}}{Gr_{\overline{x}}^{1/4}} = -\gamma'(\xi,\,0),\ \frac{Sh_{\overline{x}}}{Gr_{\overline{x}}^{1/4}} &= -S'(\xi,\,0), \end{aligned}\right\} \tag{4.14}$$

where $Gr_{\overline{x}} = \dfrac{\overline{x}^3\,g\,\beta_T\,(T_f - T_\infty)\,(1 - \phi_\infty)\cos A}{\nu^2}$ is the local Grashof number.

Results and Discussion

The reduced governing Eqs. (4.8)-(4.11) along with the boundary conditions (4.12) are solved numerically using the Bivariate Pseudo-Spectral Local Linearization Method, as explained in the case (a) of Chapter-2. In order to assess the accuracy of the generated code, for $Rd = 0.0$, $Ec = 0.0$, $\Lambda = 0.0$ and $Bi \to \infty$, the results of the present problem have been compared with those of Na and Chiou [75], Kays and Crawford [49], Lin and Chen [55] and Yih [130] and found to be a good agreement, as shown in Tab. (2.1). The investigation is carried out to analyze the effects of Arrhenius activation energy (E), thermal radiation parameter (Rd), Biot number (Bi), chemical reaction rate constant (Λ), temperature relative parameter (δ) and exponent fitted rate constant (n), for fixed values of $Nc = 1.0, Nr = 0.5, Sc = 0.6, Pr = 1.0, Le = 10.0, Gr = 5.0, Nt = 0.5$ and $Nb = 0.2$.

The set of Figs. 4.2(a)-4.2(d) is prepared to explore the effects of Arrhenius activation energy (E) and Biot number (Bi) on the dimensionless velocity f', temperature θ, nanoparticle volume fraction γ, and regular concentration S. The Arrhenius activation energy is the minimum energy that required to start a chemical reaction. It can also be defined as the height of potential barrier (energy barrier) dividing two minima of potential energy of the products and reactants in a reaction. For a reasonable rate of chemical reaction, there must be some molecules with energy greater than or equal to the activation energy. It is evident from Fig. 4.2(a) and Fig. 4.2(b) that the increasing value of activation energy leads to increase the momentum boundary layer thickness and decrease the thermal boundary layer thickness. The nanoparticle volume fraction enhances with the enhancement of activation energy, as shown in Fig. 4.2(c). But, the improving value of activation energy (E) leads to decrease $\lambda^2 \ e^{-\frac{E}{1+\delta\theta}}$ as well as, enhances the regular concentration profile within the boundary layer. Further, the ratio of the internal thermal resistance of a solid to the boundary layer thermal resistance is defined as the Biot number (Bi). For $Bi = 0$, the vertical frustum of a cone surface is insulated, and therefore the surface is maintained at high thermal resistance, and no heat transfer to the cold fluid take places on the upper part of the surface. For $Bi \to \infty$, the convective boundary condition reduces into an isothermal boundary condition (i.e., wall condition). It is seen from Figs. 4.2(a)-4.2(c) that the non-dimensional velocity, temperature, and the regular concentration profiles enhance but, the non-dimensional nanoparticle volume fraction reduces near to the surface of the frustum of a cone with an increase of the Biot number.

Figures 4.3(a)-4.3(d) show the non-dimensional velocity f', temperature θ, nanoparticle volume fraction γ, and regular concentration S under the influence of thermal radiation parameter (Rd) and rate of chemical reaction (Λ). With the increase of radiation parameter, the velocity and temperature distributions increase within the corresponding boundary layers, and the maximum velocity is noticed near to the surface of frustum of a cone. The boundary layer thickness of nanoparticle volume fraction enhances near to the surface and diminishes far away from the surface with an enhancing values of the radiation parameter. However, the regular concentration boundary layer thickness decreases with an increase of radiation parameter. Further, increasing the rate of chemical reaction reduces the momentum and nanoparticle boundary layer thickness, as shown in Figs. 4.3(a) and 4.3(c). It is also seen from Figs. 4.3(b) and 4.3(d) that the regular concentration distribution decreases, whereas the temperature distribution increase with an increase in chemical reaction rate.

The influence of temperature relative parameter (δ) and exponent fitted rate constant (n) on the distribution of velocity f' and regular concentration S, are given in Figs. 4.4(a)-4.4(b). The distribution of velocity and regular concentration profiles decrease with the increase of exponent fitted rate constant and temperature relative parameter. The effects of Arrhenius activation energy (E) and Biot number (Bi) on the non-dimensional surface drag, local Nusselt, local nanoparticle Sherwood number and local regular Sherwood number are, presented in Figs. 4.5(a)-4.5(d). Figure 4.5(a) reveals that the drag coefficient increases with an increase of activation energy parameter, and a huge increment is noticed for $Bi = 1.0$. The regular Sherwood number diminishes with an increase of activation energy parameter, whereas it enhances with an increase of Biot number, as plotted in Fig. 4.5(d). As activation energy parameter increases, the local Nusselt number increases, but the local nanoparticle Sherwood number decreases. This variation is negligible for the case of $Bi = 0.1$ (i.e., non-isothermal surface), as shown in Figs. 4.5(b) and 4.5(c). It is interesting to note that, the drag coefficient, local Nusselt number, and local regular Sherwood number along the vertical plate ($i.e., \xi = 0$) are lower when compared to those of the full cone ($i.e., \xi \to \infty$). Whereas, the local nanoparticle Sherwood number along the vertical plate is higher than the case of full cone.

The influence of thermal radiation (Rd) and chemical reaction rate constant (Λ) on the dimensionless surface drag, local Nusselt number, local nanoparticle and regular Sherwood numbers over the vertical frustum of a cone, are displayed in Figs. 4.6(a)-4.6(d). With the rise of thermal radiation parameter, a considerable increment is noticed in the all above mentioned physical quantities along ξ, as shown in Figs. 4.6(a)-4.6(d). The reason for above change is that the large values of thermal radiation parameter will produce a large amount of heat to the fluid medium. Then, the fluid medium enhances the fluid motion along the frustum of a cone surface. So that the thermal radiation can be used as a heat source and consequently, the velocity, temperature, nanoparticle volume fraction and regular concentration profiles increase. Further, the presence of chemical reaction rate reduces the drag coefficient and local Nusselt number while the reverse trend is noticed for both local nanoparticle and regular Sherwood numbers. Furthermore, the surface drag, local Nusselt number and local regular Sherwood number across the full cone problem ($i.e., \xi \to \infty$) are higher than those of the vertical plate problem ($i.e., \xi = 0$), whereas the nanoparticle Sherwood number shows an opposite behavior.

The effects of temperature relative parameter (δ) and exponent fitted rate constant (n) on the surface drag and local regular Sherwood number, are given in Figs. 4.7(a)-4.7(b). The drag coefficient diminishes with enhanced values of exponent fitted rate constant and temperature relative parameter, whereas the local Sherwood number shows a reverse trend.

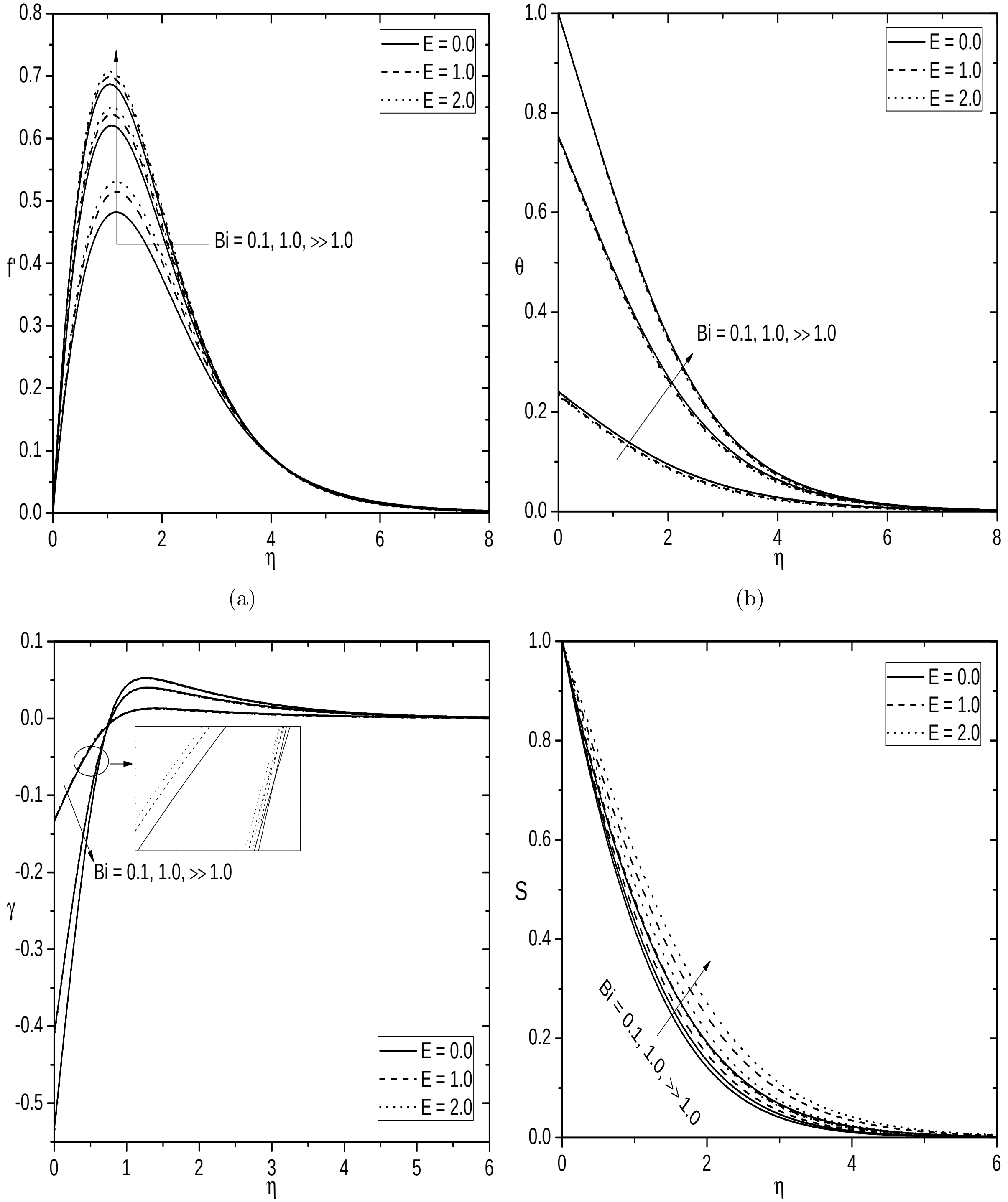

(a) (b)

(c) (d)

Figure 4.2: *Effects of Bi and E on (a) Velocity, (b) Temperature, (c) Nanoparticle volume fraction, and (d) Regular concentration for $Rd = 1.0$, $\Lambda = 1.0$, $\delta = 1.0$ and $n = 0.5$.*

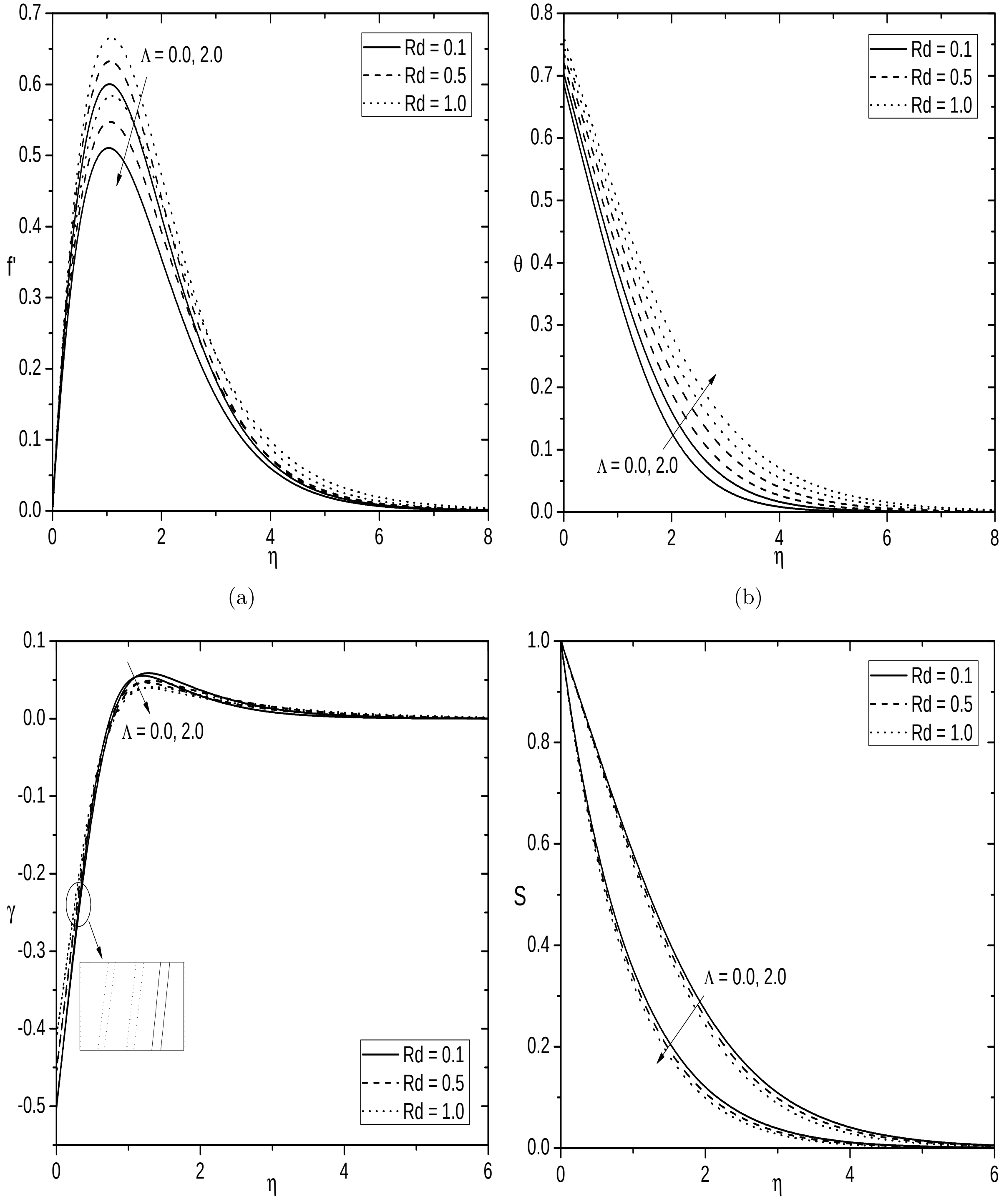

(a)

(b)

(c)

(d)

Figure 4.3: *Effects of* Λ *and* Rd *on (a) Velocity, (b) Temperature, (c) Nanoparticle volume fraction, and (d) Regular concentration for* $E = 1.0$, $Bi = 1.0$, $\delta = 1.0$ *and* $n = 0.5$.

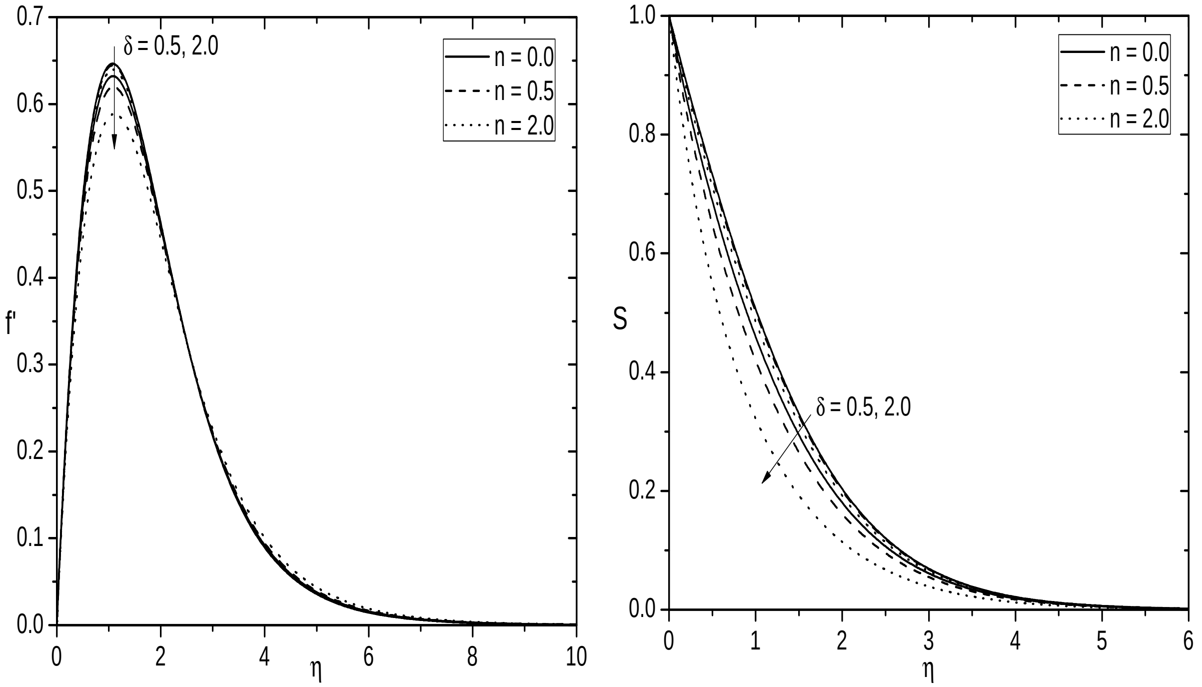

(a) (b)

Figure 4.4: *Effects of* δ *and* n *on (a) Velocity and (b) Regular concentration for* $E = 1.0$, $Bi = 1.0$, $\Lambda = 1.0$ *and* $Rd = 1.0$.

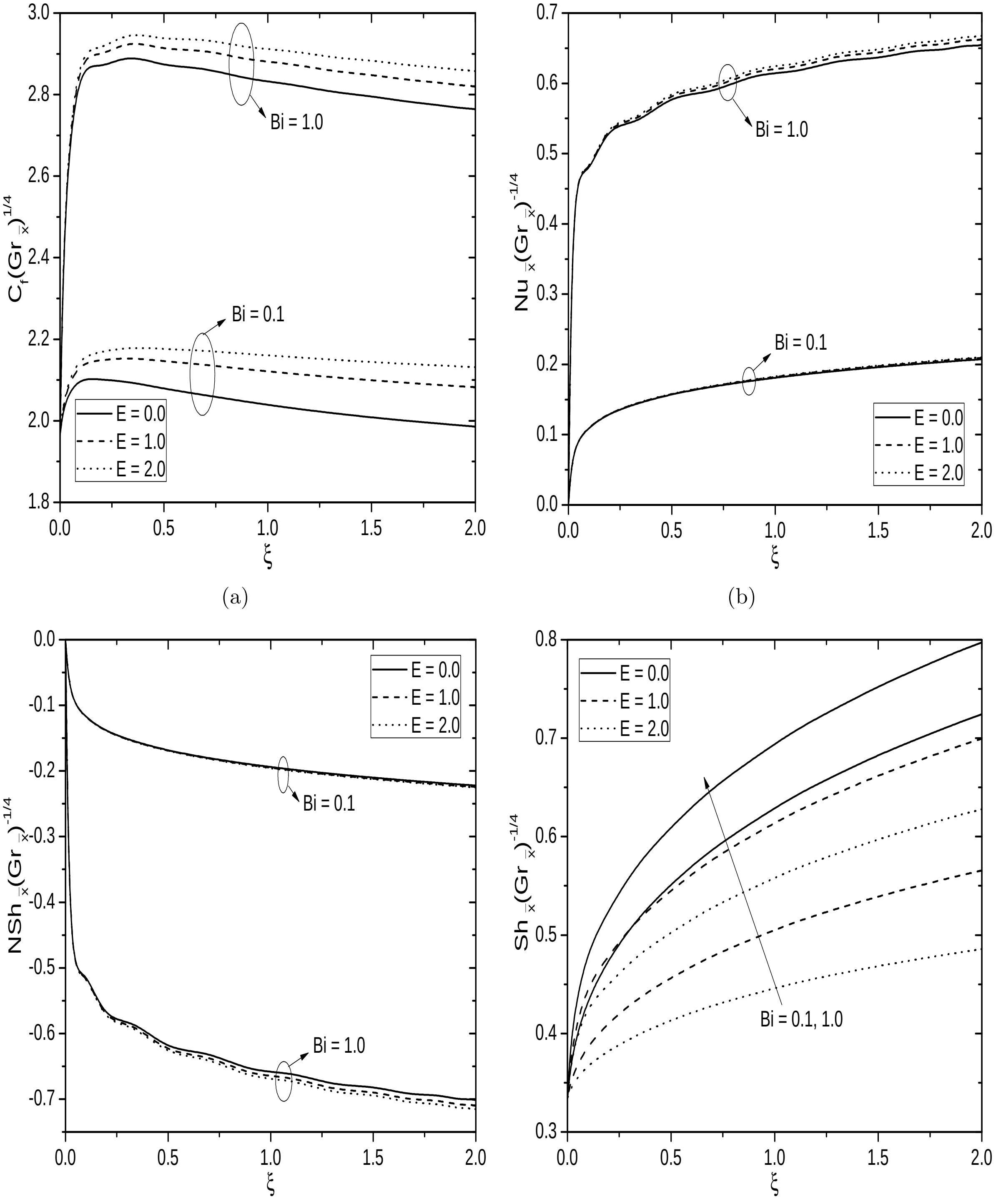

(a) (b)

(c) (d)

Figure 4.5: *Effects of Bi and E on (a) Skin friction, (b) Heat transfer rate, (c) Nanoparticle mass transfer rate, and (d) Regular mass transfer rate for $Rd = 1.0$, $\Lambda = 1.0$, $\delta = 1.0$ and $n = 0.5$.*

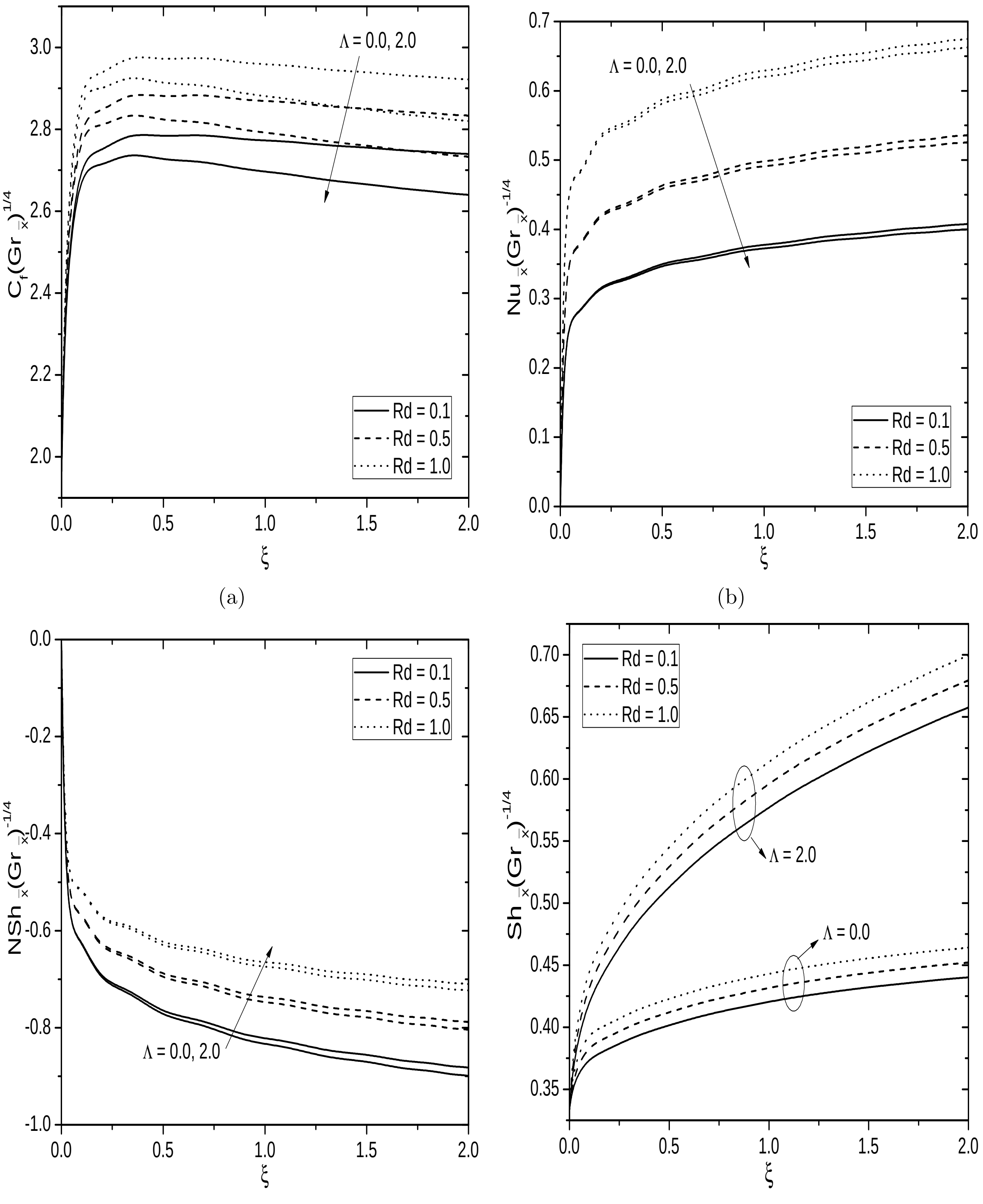

(a) (b)

(c) (d)

Figure 4.6: *Effects of* Λ *and* Rd *on (a) Skin friction, (b) Heat transfer rate, (c) Nanoparticle mass transfer rate, and (d) Regular mass transfer rate for* $E = 1.0$, $Bi = 1.0$, $\delta = 1.0$ *and* $n = 0.5$.

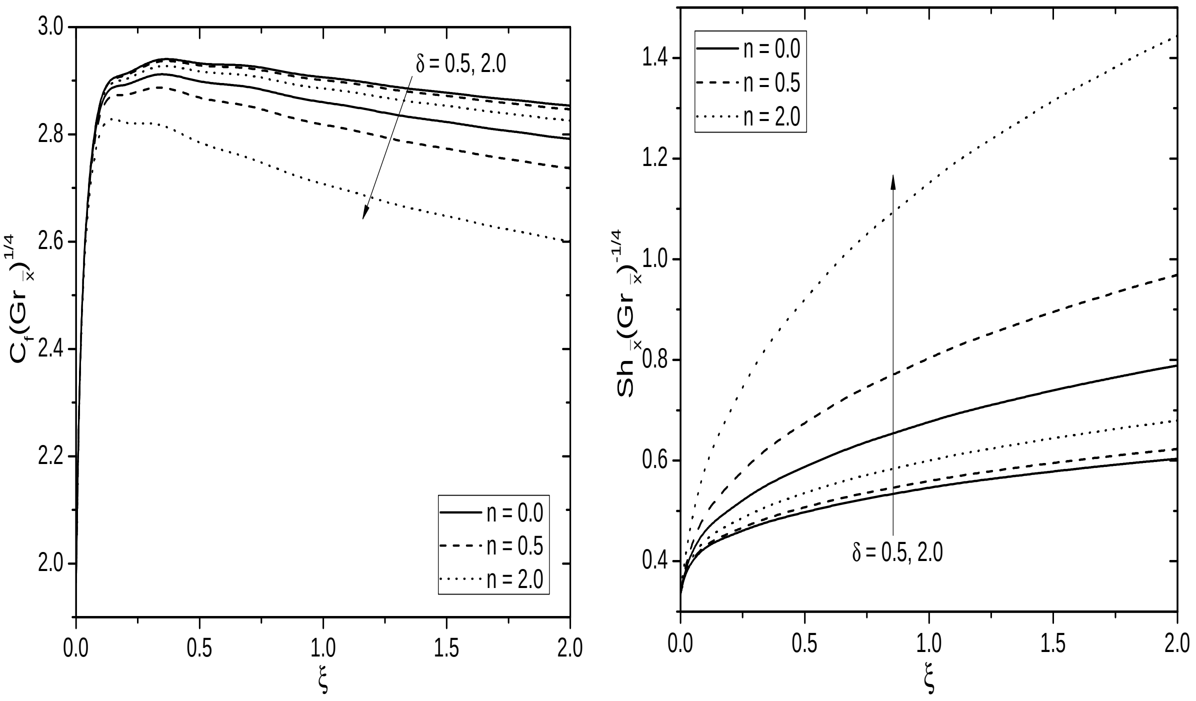

(a) (b)

Figure 4.7: *EffectS of δ and n on (a) Skin friction and (b) Regular mass transfer rate for* $E = 1.0$, $Bi = 1.0$, $\Lambda = 1.0$ *and* $Rd = 1.0$.

4.2.2 Case(b): Mixed Convection

Consider the flow to be a mixed convection, which arises from an external flow with velocity U_∞ and buoyancy forces. We introduce the following non-similarity variables

$$\xi = \frac{\overline{x}}{x_0} = \frac{x - x_0}{x_0},\ \eta = \frac{y}{\overline{x}}\, Re_{\overline{x}}^{1/2},\ \psi = r\,\nu Re_{\overline{x}}^{1/2}\, f\,(\xi,\eta)\,,\ \theta\,(\xi,\eta) = \frac{T - T_\infty}{T_f - T_\infty},$$

$$\gamma\,(\xi,\eta) = \frac{\phi - \phi_\infty}{\phi_\infty},\ S\,(\xi,\eta) = \frac{C - C_\infty}{C_w - C_\infty} \tag{4.15}$$

Using (2.7) and (4.15) in Eqs.(4.2)-(4.5), we get

$$f''' + \left(R + \frac{1}{2}\right) f\, f'' + \lambda\,\xi\,(\theta + Nc\,S - Nr\,\gamma) = \xi\,\left(f'\frac{\partial f'}{\partial \xi} - \frac{\partial f}{\partial \xi} f''\right) \tag{4.16}$$

$$\frac{1}{Pr}\,\left(1 + \frac{4}{3}\,Rd\right)\,\theta'' + \left(R + \frac{1}{2}\right) f\,\theta' + Nb\,\gamma'\,\theta' + Nt\,\left(\theta'\right)^2 = \xi\,\left(f'\frac{\partial \theta}{\partial \xi} - \frac{\partial f}{\partial \xi}\theta'\right) \tag{4.17}$$

$$\frac{1}{Le}\,\gamma'' + \left(R + \frac{1}{2}\right) f\,\gamma' + \frac{1}{Le}\,\frac{Nt}{Nb}\,\theta'' = \xi\,\left(f'\frac{\partial \gamma}{\partial \xi} - \frac{\partial f}{\partial \xi}\gamma'\right) \tag{4.18}$$

$$\frac{1}{Sc}\,S'' + \left(R + \frac{1}{2}\right) f\,S' - \left(\frac{\xi}{Re_{x_0}}\right)\,\Lambda^2(1 + n\,\delta\,\theta)\,e^{-\frac{E}{1+\delta\,\theta}}\,S = \xi\,\left(f'\frac{\partial S}{\partial \xi} - \frac{\partial f}{\partial \xi}S'\right) \tag{4.19}$$

The associated boundary conditions (4.6) become

$$f'(\xi,\eta) = 0,\ f(\xi,\eta) + \frac{\xi}{\left(R + \frac{1}{2}\right)}\,\frac{\partial f}{\partial \xi} = 0,\ \theta'(\xi,\eta) = -Bi\,\xi^{1/2}\,[1 - \theta(\xi,\eta)],$$

$$Nb\,\gamma'(\xi,\eta) + Nt\,\theta'(\xi,\eta) = 0,\ S(\xi,\eta) = 1 \quad \text{at} \quad \eta = 0 \tag{4.20a}$$

$$f'(\xi,\eta) = 1,\ \theta(\xi,\eta) = 0,\ \gamma(\xi,\eta) = 0,\ S(\xi,\eta) = 0 \quad \text{as} \quad \eta \to \infty \tag{4.20b}$$

The physical quantities of interest in real life applications are the local skin friction C_f, local Nusselt number $Nu_{\overline{x}}$, local nanoparticle Sherwood number $NSh_{\overline{x}}$ and local Sherwood number $Sh_{\overline{x}}$, are given by

$$\left.\begin{aligned} C_f\, Re_{\overline{x}}^{1/2} = 2\, f''(\xi,0), \ \ \frac{Nu_{\overline{x}}}{Re_{\overline{x}}^{1/2}} = -\left[1+\frac{4}{3}\,Rd\right]\,\theta'(\xi,0), \\ \frac{NSh_{\overline{x}}}{Re_{\overline{x}}^{1/2}} = -\gamma'(\xi,0), \ \ \frac{Sh_{\overline{x}}}{Re_{\overline{x}}^{1/2}} = -S'(\xi,0) \end{aligned}\right\} \tag{4.21}$$

Results and Discussion

As in the previous case, here also the non-linear partial differential equations (4.16) - (4.19) along with the boundary conditions (4.20) are solved numerically using the Bivariate Pseudo-Spectral Local Linearization Method. In the special case of $Rd = 0.0$, $\Lambda = 0.0$, $Re = 2.0$, $\lambda = 1.0$, $E = 1.0$, $\delta = 1.0$, $n = 0.5$ and $Bi \to \infty$, the results of the present problem have been compared with those of Lloyd and Sparrow [56] and found that they are in good agreement [see Tab. 2.2]. To examine the effects of thermal radiation (Rd), Arrhenius activation energy (E), Biot number (Bi) and chemical reaction rate constant (Λ), computations have been carried out for $Nc = 1.0, Nr = 0.5, Sc = 0.6, Pr = 1.0, Le = 10.0, Re = 2.0, Nt = 0.5, Nb = 0.2, \delta = 1.0$ and $n = 0.5$.

The effects of Biot number (Bi) and thermal radiation (Rd) on the non-dimensional velocity f', temperature θ, nanoparticle volume fraction γ, and regular concentration S, are depicted in Figs. 4.8(a)-4.8(d) for aiding flow ($\lambda = 0.5$) and opposing flow ($\lambda = -0.05$) at $\xi = 1.5$. The Biot number is characterized as the ratio between the internal thermal resistance of a solid and the thermal resistance of a boundary layer. When $Bi = 0$, the surface of a frustum is completely insulated, and there is no heat transfer from the cold fluid to the surface. From Fig. 4.8(a), it is noticed that the thickness of momentum boundary layer increases, as Rd increases for both aiding and opposing flow cases. But, the enhancement of Biot number accelerates the flow velocity for aiding flow and decelerates for opposing flow. It is seen that the thermal boundary layer thickness increases with increasing values of thermal radiation and Biot number for both opposing and aiding flows, as plotted in Fig. 4.8(b). Figure 4.8(c) demonstrates that the nanoparticle volume fraction increases with the increase of Rd, whereas decreases with an increase of Bi, for both aiding and opposing flows.

For opposing and aiding flow cases, rising values of thermal radiation parameter and Biot number leads to reduce the regular concentration, as given in Fig. 4.8(d).

Figures 4.9(a)-4.9(b) represent the dimensionless velocity f' and regular concentration S under the combined effects of chemical reaction constant (Λ) and Arrhenius activation energy (E) for both aiding flow ($\lambda = 0.5$) and opposing flow ($\lambda = -0.05$) at $\xi = 1.5$. As the Arrhenius activation energy parameter increases, the thickness of momentum boundary layer increases for aiding flow and decreases for opposing flow. An increasing value of activation energy parameter causes to decrease $\Lambda^2 e^{\frac{-E}{1+\delta\theta}}$ and therefore the regular concentration profile increases for both the aiding and opposing flows. However, an opposite behavior is observed for chemical reaction rate parameter, as plotted in Fig. 4.9(b).

For aiding flow case ($\lambda = 0.5$), the effects of thermal radiation and Biot number on the streamwise distribution of surface drag, local Nusselt number, local nanoparticle and regular Sherwood numbers, are depicted in Figs. 4.10(a)-4.10(d). With the increase of thermal radiation parameter, the surface drag, local Nusselt number, local nanoparticle and regular Sherwood numbers increase. For large values of Rd, thermal radiation produces a high temperature. Therefore it can be used as a source of heat, and subsequently it enhances the quantity of heat added to the fluid medium and the fluid motion along the surface of the frustum of a cone. As Biot number enhances, the non-dimensional surface drag, local Nusselt and regular Sherwood numbers enhance, whereas the local nanoparticle Sherwood number diminishes, as shown in Figs. 4.10(a)-4.10(d). By this study, it is noted that the surface drag, local Nusselt and regular Sherwood numbers over the full cone ($i.e., \xi \to \infty$) are higher than those of a vertical plate ($i.e., \xi = 0$).

For opposing flow case, ($\lambda = -0.05$), the streamwise distribution of surface drag, local Nusselt number, local nanoparticle and regular Sherwood numbers under the combined effects of Biot number and thermal radiation, are exhibited in Figs. 4.11(a)-4.11(d). It indicates that the local Nusselt number, local nanoparticle and regular Sherwood numbers increase, but the surface drag decreases with the increase of thermal radiation parameter. As Biot number rises, the surface drag and local nanoparticle Sherwood number diminish, whereas the local Nusselt and regular Sherwood numbers enhance. Moreover, the local Nusselt and Sherwood numbers over the full cone ($i.e., \xi \to \infty$) are higher than those of a vertical plate ($i.e., \xi = 0$), as shown in Figs. 4.11(a)-4.11(d). From the above discussion, it is remarked that the presence of convective boundary condition and thermal radiation highly influences the local Nusselt and Sherwood numbers for opposing and aiding flows.

Figures 4.12(a)-4.12(b) and 4.13(a)-4.13(b) explore the impact of Arrhenius activation energy and rate of chemical reaction parameters on the dimensionless surface drag and local regular Sherwood number for aiding and opposing flow cases, respectively. The surface drag coefficient increases for aiding flow and decreases for opposing flow with an increase of Arrhenius activation energy parameter. As the chemical reaction rate parameter rises, the surface drag enhances for opposing flow and reduces for aiding flow. But, the local regular Sherwood number decreases with E and increases with Λ for both aiding and opposing flows, respectively.

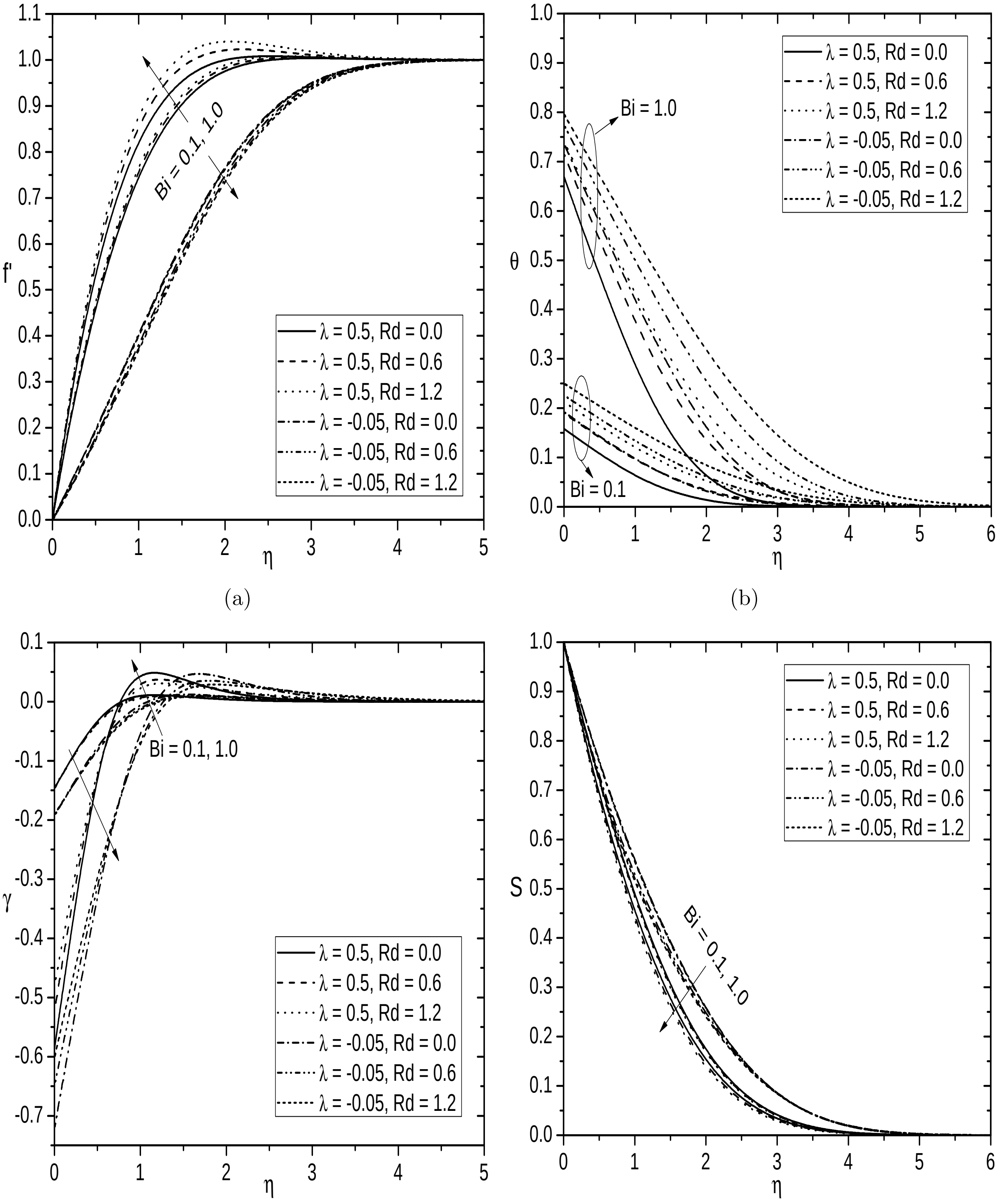

(a) (b)

(c) (d)

Figure 4.8: *Effects of Bi and Rd on (a) Velocity, (b) Temperature, (c) Nanoparticle volume fraction, and (d) Regular concentration for* $\Lambda = 1.0$, $\delta = 1.0$, $n = 0.5$ *and* $E = 1.0$.

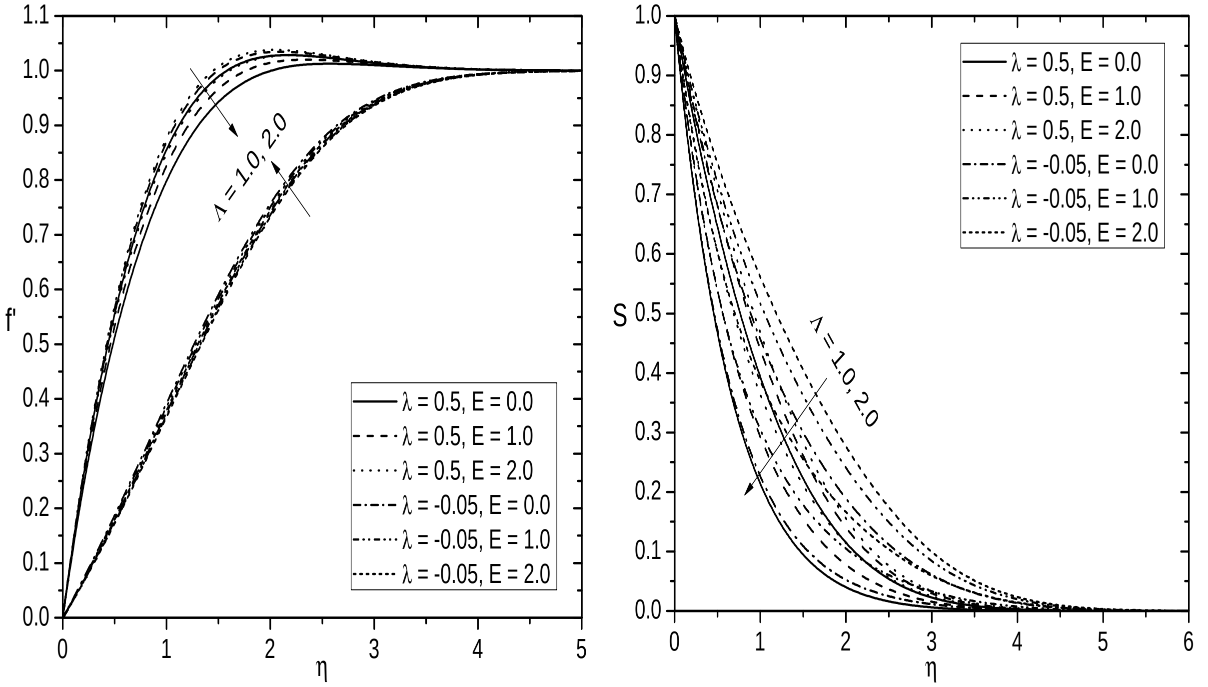

(a) (b)

Figure 4.9: *Effect of* Λ *and* E *on (a) Velocity and (b) Regular concentration for* $Rd = 1.0$, $\delta = 1.0$, $n = 0.5$ *and* $Bi = 1.0$.

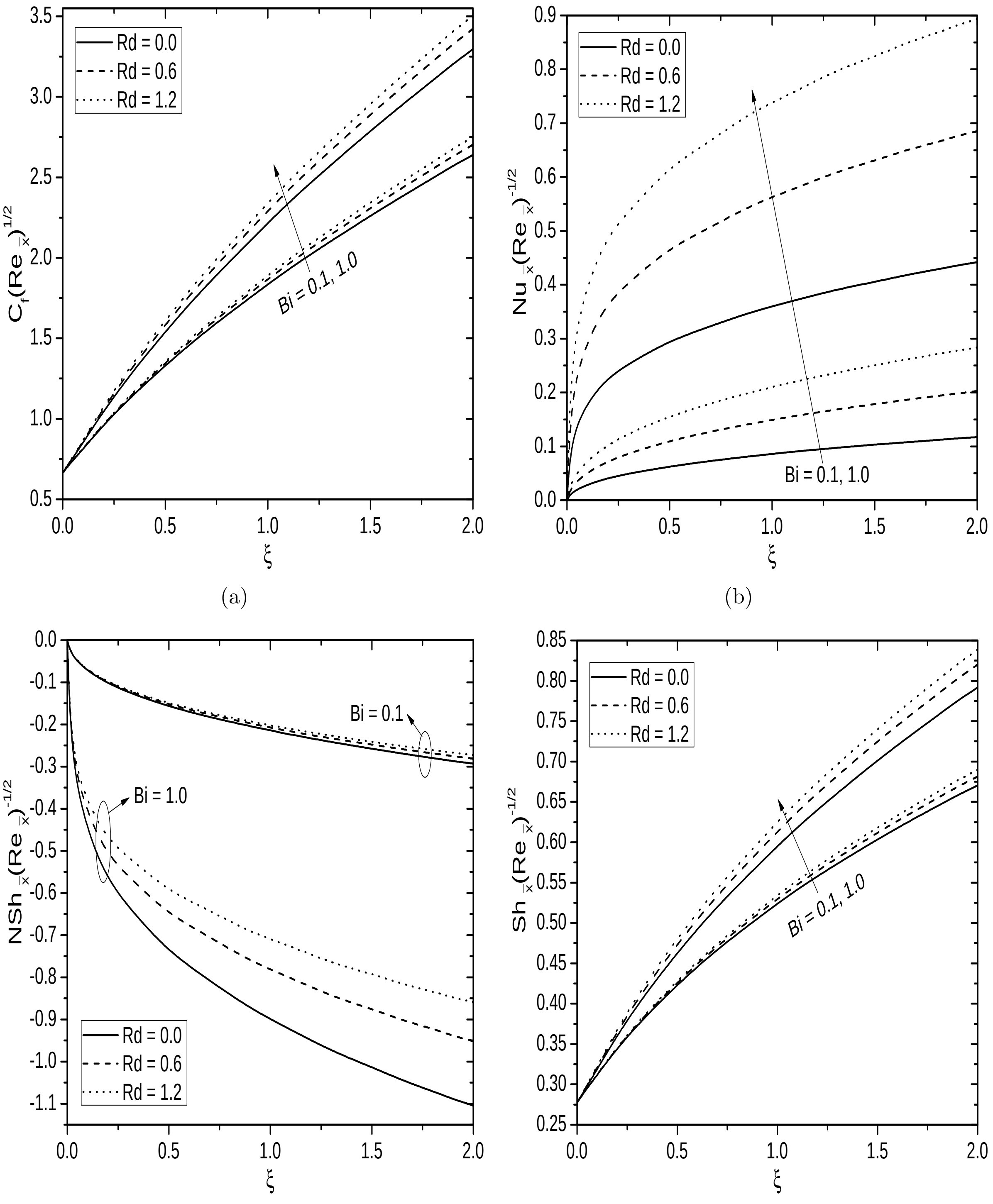
(a)
(b)
(c)
(d)

Figure 4.10: *Effects of Bi and Rd on (a) Skin friction, (b) Heat transfer rate, (c) Nanoparticle mass transfer rate, and (d) Regular mass transfer rate (Aiding flow case) for* $\Lambda = 1.0$, $\delta = 1.0$, $n = 0.5$ *and* $E = 1.0$.

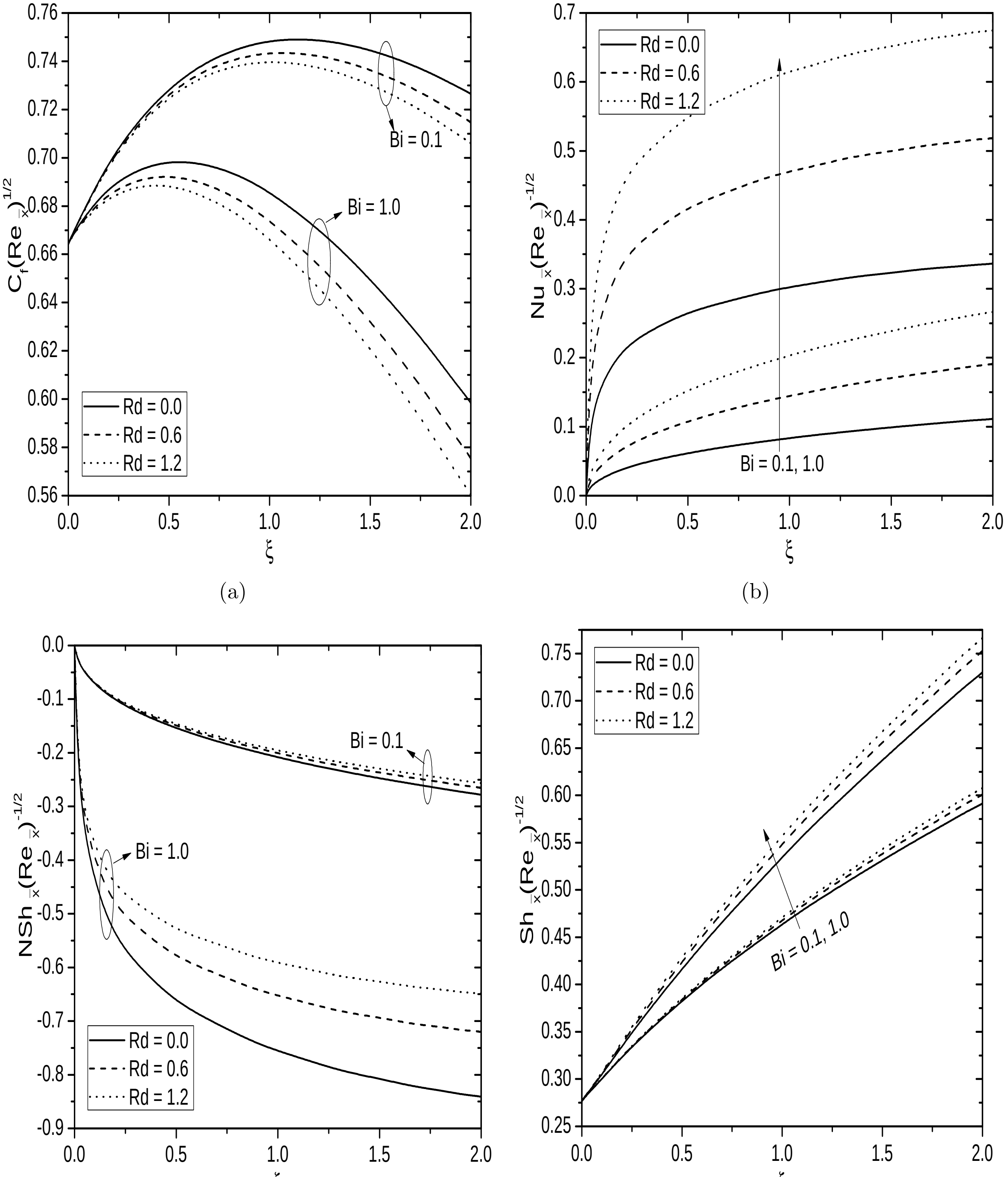

(a) (b)

(c) (d)

Figure 4.11: *Effects of Bi and Rd on (a) Skin friction, (b) Heat transfer rate, (c) Nanoparticle mass transfer rate, and (d) Regular mass transfer rate (Opposing flow case) for* $\Lambda = 1.0$, $\delta = 1.0$, $n = 0.5$ *and* $E = 1.0$.

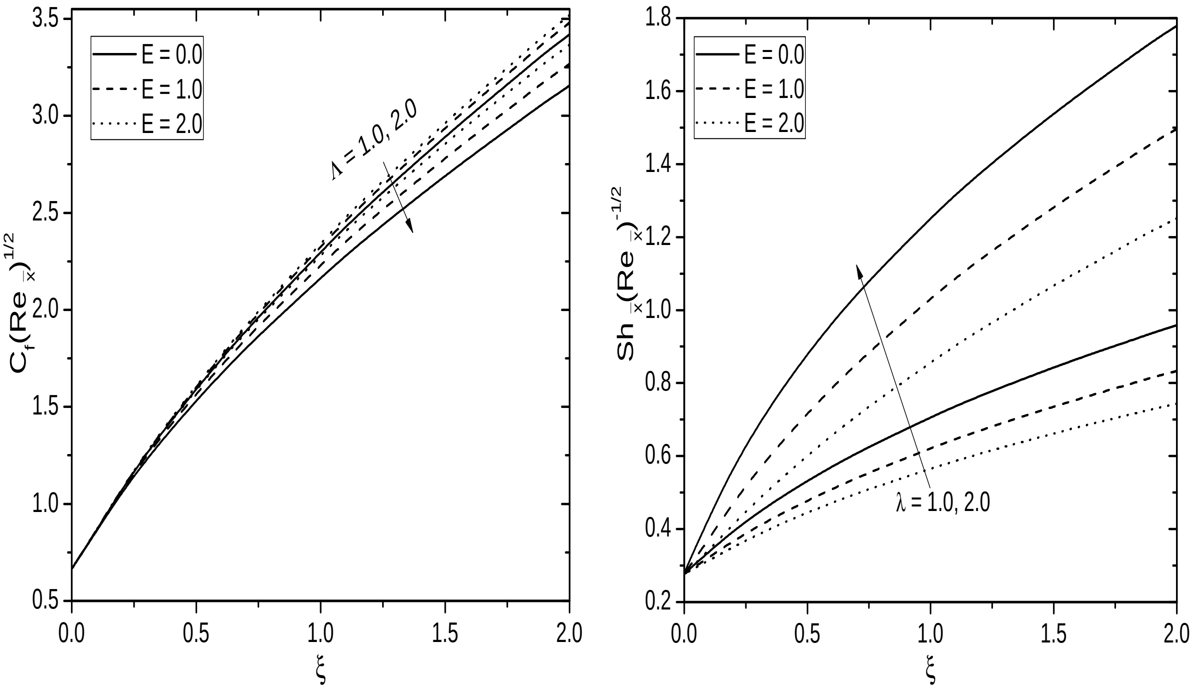

(a) (b)

Figure 4.12: *Effects of* Λ *and* E *on (a) Skin friction and (b) Regular mass transfer rate (Aiding flow case) for* $Rd = 1.0$*,* $\delta = 1.0$*,* $n = 0.5$ *and* $Bi = 1.0$*.*

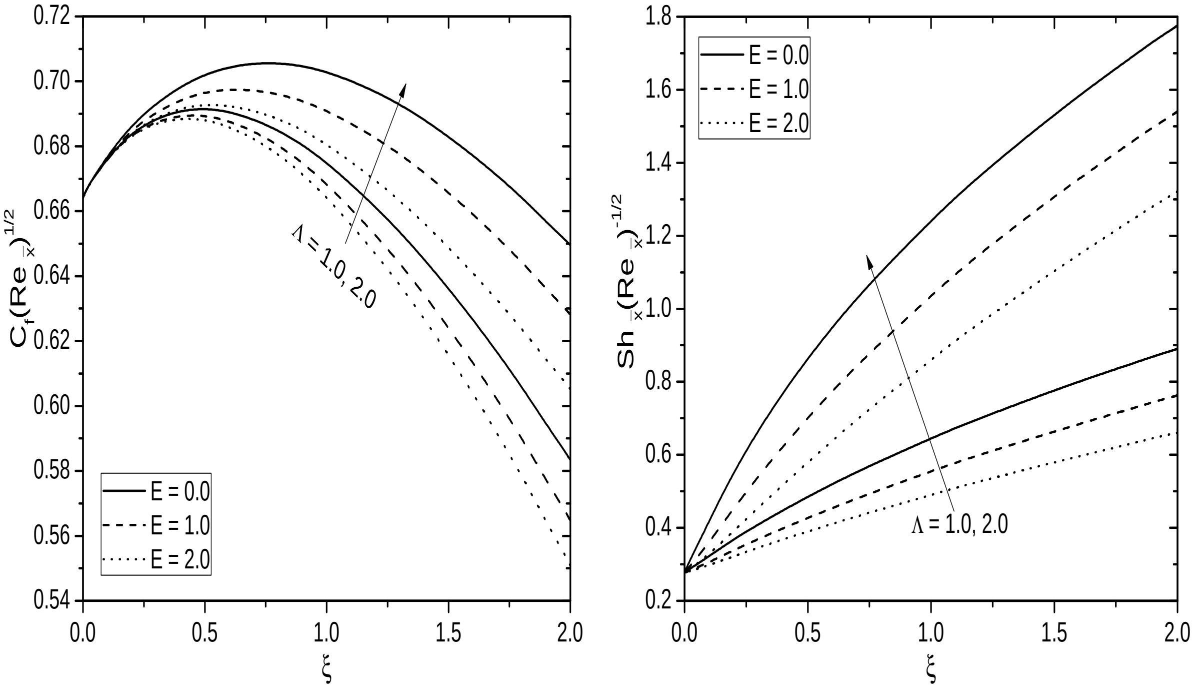

(a) (b)

Figure 4.13: *Effects of* Λ *and* E *on (a) Skin friction and (b) Regular mass transfer rate (Opposing flow case) for* $Rd = 1.0$*,* $\delta = 1.0$*,* $n = 0.5$ *and* $Bi = 1.0$*.*

4.3 Conclusions

In this chapter, the influence of thermal radiation and Arrhenius activation energy with binary chemical reaction on the convective flow of a nanofluid over the vertical frustum of a cone in the presence of convective boundary condition, is studied. The resulting equations are solved numerically by employing the Bivariate Pseudo-Spectral Local Linearization Method. The main findings are summarized as follows:

As activation energy parameter E increases, the velocity and regular concentration increase but the temperature and regular Sherwood number decrease in both case (a) and case (b). However, the drag coefficient increases in case (a) and aiding flow of case (b), whereas it decreases in opposing flow of case (b). The higher values of thermal radiation parameter Rd results in a higher velocity, temperature, local Nusselt and Sherwood numbers, but a lower regular concentration for both case (a) and case (b). Further, the temperature, local Nusselt and regular Sherwood number enhance, whereas the distribution of nanoparticle volume fraction, local nanoparticle Sherwood number diminish with an enhancement of Rd. The temperature, local heat and regular mass transfer rates enhance, whereas the nanoparticle volume fraction and local nanoparticle mass transfer rate reduce with the enhancement of Biot number in both the cases (a) and (b). But, the velocity and surface drag increase, and regular concentration decreases in free convective flow and aiding flow of case (b), whereas they show reverse trend in opposing flow of case (b). However, the velocity and drag coefficient improve in case (a) and aiding flow of case (b), but reduce in opposing flow of case (b). It is observed that with an increase of chemical reaction rate Λ, the regular concentration decreases and regular Sherwood number increases. But, the velocity and drag coefficient decrease in case (a) and aiding flow of case (b).

Chapter 5

Effects of Double Dispersion on Non-Darcy Flow of a Nanofluid over the Frustum of a Cone with Convective Boundary Condition [1]

5.1 Introduction

Convective heat and mass transfer in a porous medium is the subject of great interest in the recent years owing to its wide range of engineering and industrial applications. In many practical situations, the porous medium is bounded by an impermeable surface which has high flow rates and hence, the Darcy law is inapplicable. To model this kind of physical situation, it is therefore, necessary to include the non-Darcian terms in the analysis of convective transport in a porous medium. Various models have been proposed in the literature to study the convective transport phenomena in a non-Darcy porous medium. Among these, the Darcy-Forchheimer model is one, which is an extension of classical Darcy formulation,

---

[1] Case(a): Published in "**Nonlinear Engineering**" 6(4) (2017) 277–292, Case(b): Published in "**Heat Transfer Research**" DOI: 10.1615/HeatTransRes.2018018754

obtained by adding a squared term of velocity in the momentum equation to account for the inertial effects. Considerable work has been discussed on the nanofluid flow, heat, and mass transfer characteristics in a Darcy and non- Darcy porous medium (see Nield and Kuznetsov [81], [83], Cheng [17], Noghrehabadi *et al.* [85]).

The energy and concentration transport due to the hydrodynamic mixing is called thermal and solutal dispersions, respectively. The effects of thermal and solutal dispersions (double dispersion) in a non-Darcy porous medium are necessary due to the presence of inertial effects (see Nield and Bejan [84]). Because of various engineering applications, Narayana and Sibanda [80] analyzed the double dispersion effects on MHD mixed convective flow along a vertical flat plate embedded in a non-Darcy porous medium. The combined convective heat and mass transfer along a vertical surface in a non-Darcy porous medium in the presence of double dispersion effects has been discussed by Afify and Elgazery [2] (For more details, see the references therein).

Survey on earlier studies reveal that the natural and mixed convective flows of a nanofluid over the vertical frustum of a cone in a non-Dary porous medium with double dispersion effects, are not studied so far. Hence, the present chapter aims to analyze the influence of double dispersion effects on the convective flow over the vertical frustum of a cone in a non-Darcy porous medium saturated with a nanofluid. The effects of pertinent parameters on the physical quantities are studied, and the results are displayed graphically.

5.2 Mathematical Formulation

Consider a steady, laminar and two dimensional convective flow of a nanofluid over the vertical frustum of a cone embedded in a non-Darcy porous medium. Choose the coordinate system such that x-axis is along the surface and y-axis is normal to the surface of vertical frustum of a cone, as shown in Fig. (5.1). Let x_0 is the distance of the leading edge of vertical frustum of a cone measured from the origin O. Assume that the velocity of the outer flow is U_∞, whereas the temperature, nanoparticle volume fraction and regular concentration at

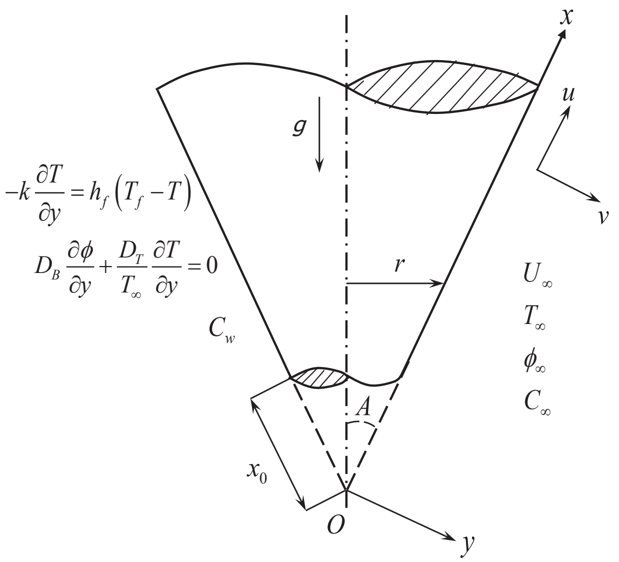

Figure 5.1: *Physical model and coordinate system*

ambient medium are T_∞, ϕ_∞ and C_∞, respectively. The regular concentration at surface of the vertical frustum of a cone is C_w. In addition, the following assumptions are taken into account in the present analysis: (i) the porous medium is isotropic and homogeneous, (ii) the properties of the fluid and porous medium are constant except for the Oberbeck-Boussinesq approximation, and (iii) the fluid and porous medium are in local thermodynamic equilibrium, and (iv) the fluid flow is moderate and the permeability of the medium is low, so that the Forchheimer flow model is applicable (See Nield and Bejan [84]).

Implementing the above said assumptions and Oberbeck-Boussinesq approximations, the governing equations can be written as:

$$\frac{\partial(u\,r)}{\partial x}+\frac{\partial(v\,r)}{\partial y}=0 \tag{5.1}$$

$$\begin{aligned}\frac{\rho_{f\infty}}{\varepsilon^2}\left(u\,\frac{\partial u}{\partial x}+v\,\frac{\partial u}{\partial y}\right) &= \frac{\mu}{\varepsilon}\frac{\partial^2 u}{\partial y^2}+\rho_{f\infty}\,g\,\left(1-\phi_\infty\right)\,\left[\beta_T(T-T_\infty)+\beta_C(C-C_\infty)\right]\cos A\\ &\quad -(\rho_p-\rho_{f\infty})\,g\,(\phi-\phi_\infty)\cos A-\frac{\mu}{K_p}(u-U_\infty)-\frac{\rho_{f\infty}b}{K_p}\,(u^2-U_\infty^2)\end{aligned} \tag{5.2}$$

$$u\,\frac{\partial T}{\partial x}+v\,\frac{\partial T}{\partial y}=\frac{\partial}{\partial y}\left(\alpha_y\,\frac{\partial T}{\partial y}\right)+\mathcal{J}\left[D_B\,\frac{\partial \phi}{\partial y}\,\frac{\partial T}{\partial y}+\frac{D_T}{T_\infty}\left(\frac{\partial T}{\partial y}\right)^2\right] \tag{5.3}$$

$$u\,\frac{\partial \phi}{\partial x}+v\,\frac{\partial \phi}{\partial y}=D_B\,\frac{\partial^2 \phi}{\partial y^2}+\frac{D_T}{T_\infty}\,\frac{\partial^2 T}{\partial y^2} \tag{5.4}$$

$$u\,\frac{\partial C}{\partial x}+v\,\frac{\partial C}{\partial y}=\frac{\partial}{\partial y}\left(D_y\,\frac{\partial C}{\partial y}\right) \tag{5.5}$$

where u and v are the Darcy velocity components in x and y-directions, respectively. Further, K_p is the permeability, b is the empirical constant associated with the Forchheimer porous inertia term, ε is the porosity, $\alpha_y = \alpha_m + \sigma\, d\, u$ and $D_y = D_m + \zeta\, d\, u$ are the effective thermal and solutal diffusivities in which d is the pore diameter, σ and ζ are the coefficients of the thermal and solutal dispersions, respectively.

The associated boundary conditions are

$$u=0,\ v=0,\ -k\,\frac{\partial T}{\partial y}=h_f\,(T_f-T)\,,\ D_B\,\frac{\partial \phi}{\partial y}+\frac{D_T}{T_\infty}\,\frac{\partial T}{\partial y}=0,\ C=C_w \quad \text{at} \quad y=0 \tag{5.6a}$$

$$u=U_\infty,\ T=T_\infty,\ \phi=\phi_\infty,\ C=C_\infty \quad \text{as} \quad y\to\infty \tag{5.6b}$$

In this chapter also, two types (cases) of problems are considered: (a) free/natural convection and (b) mixed convection.

5.2.1 Case(a): Natural Convection

The flow is assumed to be a natural convection, which is caused by buoyancy forces only without any external agent, and hence the velocity of the external flow becomes zero $i.e., U_\infty = 0$. We introduce the following non-similarity variables

$$\xi=\frac{\overline{x}}{x_0}=\frac{x-x_0}{x_0},\ \eta=\frac{y}{\overline{x}}\,Gr_{\overline{x}}^{1/4},\ \psi=r\nu Gr_{\overline{x}}^{1/4}\,f\,(\xi,\eta)\,,$$

$$\theta\,(\xi,\eta)=\frac{T-T_\infty}{T_f-T_\infty},\ \gamma\,(\xi,\eta)=\frac{\phi-\phi_\infty}{\phi_\infty},\ S\,(\xi,\eta)=\frac{C-C_\infty}{C_w-C_\infty} \tag{5.7}$$

Substituting (2.7) and (5.7) into Eqs. (5.2)-(5.5), the momentum, energy, nanoparticle volume fraction and regular concentration equations can be written as

$$\frac{1}{\varepsilon} f''' + \frac{1}{\varepsilon^2}\left(R+\frac{3}{4}\right) f\, f'' - \frac{1}{2\,\varepsilon^2}(f')^2 + \theta + Nc\, S - Nr\, \gamma - \frac{\xi^{1/2}}{Da\, Gr^{1/2}}\, f' \\ -\frac{Fs}{Da}\, \xi\, (f')^2 = \frac{\xi}{\varepsilon^2}\left(f' \frac{\partial f'}{\partial \xi} - \frac{\partial f}{\partial \xi} f''\right) \tag{5.8}$$

$$\frac{1}{Pr}\, \theta'' + \left(R+\frac{3}{4}\right) f\, \theta' + Nb\, \gamma'\, \theta' + Nt\, (\theta')^2 + Ds\, \xi^{1/2}\, (f'\theta')' = \xi\, \left(f' \frac{\partial \theta}{\partial \xi} - \frac{\partial f}{\partial \xi} \theta'\right) \tag{5.9}$$

$$\frac{1}{Le}\, \gamma'' + \left(R+\frac{3}{4}\right) f\, \gamma' + \frac{1}{Le}\frac{Nt}{Nb}\, \theta'' = \xi\, \left(f' \frac{\partial \gamma}{\partial \xi} - \frac{\partial f}{\partial \xi} \gamma'\right) \tag{5.10}$$

$$\frac{1}{Sc}\, S'' + \left(R+\frac{3}{4}\right) f\, S' + Dc\, \xi^{1/2}\, (f'S')' = \xi\, \left(f' \frac{\partial S}{\partial \xi} - \frac{\partial f}{\partial \xi} S'\right) \tag{5.11}$$

where $Ds = \dfrac{\sigma\, d\, Gr^{1/2}}{x_0}$ is the thermal dispersion parameter, $Dc = \dfrac{\zeta\, d\, Gr^{1/2}}{x_0}$ is the solutal dispersion parameter, $Da = \dfrac{K_p}{x_0^2}$ is the Darcy parameter, and $Fs = \dfrac{b}{x_0}$ is the Forchheimer number.

The associated boundary conditions (5.6) in terms of f, θ, γ and S are

$$f'(\xi,\eta) = 0,\ f(\xi,\eta) + \frac{\xi}{\left(R+\frac{3}{4}\right)}\frac{\partial f}{\partial \xi} = 0,\ \theta'(\xi,\eta) = -Bi\, \xi^{1/4}\, [1-\theta(\xi,\eta)], \\ Nb\, \gamma'(\xi,\eta) + Nt\, \theta'(\xi,\eta) = 0,\ S(\xi,\eta) = 1 \quad \text{at} \quad \eta = 0 \tag{5.12a}$$

$$f'(\xi,\eta) = 0,\ \theta(\xi,\eta) = 0,\ \gamma(\xi,\eta) = 0,\ S(\xi,\eta) = 0 \quad \text{as} \quad \eta \to \infty \tag{5.12b}$$

The shear stress, local heat, nanoparticle mass and regular mass fluxes are given by

$$\tau_w = \mu\, \left[\frac{\partial u}{\partial y}\right]_{y=0},\ q_w = -k_e\, \left[\frac{\partial T}{\partial y}\right]_{y=0},\ q_n = -D_B\, \left[\frac{\partial \phi}{\partial y}\right]_{y=0} \text{ and } q_m = -D_e\, \left[\frac{\partial C}{\partial y}\right]_{y=0} \tag{5.13}$$

where $k_e = (k+k_d)$ and $D_e = (D_m+D_d)$ are the effective thermal and solutal conductivities of the porous medium, in which k_d and D_d are the dispersion thermal and solutal conductivities.

The non-dimensional skin friction $C_f = \dfrac{2\,\tau_w}{\rho_{f\infty}\, U_*^2}$, local Nusselt number $Nu_{\overline{x}} = \dfrac{q_w\, \overline{x}}{k\,(T_f - T_\infty)}$, the nanoparticle Sherwood number $NSh_{\overline{x}} = \dfrac{q_n\, \overline{x}}{D_B\, \phi_\infty}$ and the regular Sherwood number

$Sh_{\overline{x}} = \dfrac{q_m\,\overline{x}}{D_m\,(C_w - C_\infty)}$, are given by

$$\left.\begin{aligned} C_f\,Gr_{\overline{x}}^{1/4} = 2\,f''(\xi,0),\ \frac{Nu_{\overline{x}}}{Gr_{\overline{x}}^{1/4}} &= -\left[1+\xi^{1/2}\,Ds\,Pr\,f'(\xi,0)\right]\,\theta'(\xi,0),\\ \frac{NSh_{\overline{x}}}{Gr_{\overline{x}}^{1/4}} = -\gamma'(\xi,0),\ \frac{Sh_{\overline{x}}}{Gr_{\overline{x}}^{1/4}} &= -\left[1+\xi^{1/2}\,Dc\,Sc\,f'(\xi,0)\right]\,S'(\xi,0) \end{aligned}\right\} \tag{5.14}$$

Results and Discussion

The resultant partial differential equations (5.8) - (5.11) along with the boundary conditions (5.12) have been solved numerically using the Bivariate Pseudo-Spectral Local Linearization Method. In order to assess the accuracy of the generated code, for a special case of $Ds = 0.0$, $Dc = 0.0$, $Gr = 1.0$, $\varepsilon = 1.0$, $Da = 1.0$ and $Bi \to \infty$, the present results have been compared with those of Na and Chiou [75], Kays and Crawford [49], Lin and Chen [55] and Yih [130] and found that they are in good agreement [see Tab. 2.1]. To study the effects of non-Darcy parameter (Fs), Biot number (Bi), thermal dispersion (Ds) and solutal dispersion (Dc), the computations have been carried out for $Pr = 1.0$, $Sc = 0.6$, $Le = 10.0$, $Nc = 1.0$, $Nr = 0.5$, $Gr = 5.0$, $\varepsilon = 0.8$, $Da = 0.5$, $Nt = 0.5$ and $Nb = 0.2$.

Figures 5.2(a)-5.2(d) are prepared to show the non-dimensional velocity f', temperature θ, nanoparticle volume fraction γ, and regular concentration S, for various values of the non-Darcy parameter (Fs) and Biot number (Bi). It is observed that an increase in the Biot number leads to increase the velocity and decrease the regular concentration in both Darcy and non-Darcy porous media cases. The temperature is maximum at the surface of the frustum and decreases exponentially to zero far away from the surface, and further, it is seen that the temperature increases with an increase in the Biot number, as depicted in Fig. 5.2(b). The nanoparticle volume fraction decreases near to the surface of the vertical frustum of a cone and then increases far away from the surface in both the cases of Darcy and non-Darcy porous media. Moreover, it is seen that the velocity decreases with an increase in the non-Darcy parameter, as plotted in Fig. 5.2(a). The reason for above said trend is that the non-Darcy parameter represents the Forchheimer effect, which is the second order non-linear porous medium inertial resistance. It means increasing the inertial effects, the Forchheimer drag will be dominant, and then causes a strong deceleration in the fluid flow. From Figs. 5.2(b)-5.2(d), it is clear that the temperature and regular concentration enhance, but the nanoparticle volume fraction reduces with an enhancement in the non-Darcy parameter. From these results, it is concluded that the fluid temperature and regular concentration are more, whereas the velocity and nanoparticle volume fraction are less, in the case of non-Darcy porous medium ($Fs \neq 0$) when compared to the case of Darcy porous medium ($Fs = 0$).

The effects of thermal dispersion (Ds) and solutal dispersion (Dc) on the non-dimensional velocity f', temperature θ, nanoparticle volume fraction γ, and regular concentration S, are displayed in Figs. 5.3(a)-5.3(d). Figure 5.3(a) depicts that the velocity increases with the increase of both thermal and solutal dispersion parameters. The presence of thermal dispersion in the energy equation leads to dominate the conduction over the convection. That is, supplementing dispersion effects to the energy equation gives more thermal conduction. Hence, as the thermal dispersion parameter enhances, the temperature reduces near to the surface and then enhances far away from the surface, whereas the nanoparticle volume fraction profiles show the reverse trend. It is perceived from Figs. 5.3(b) and 5.3(c) that the temperature and nanoparticle volume fraction reduce with an increase in the solutal dispersion parameter. However, the regular concentration increases with the increase of solutal dispersion parameter and it decreases with the increase of thermal dispersion parameter, as shown in Fig. 5.3(d).

Figures 5.4(a)-5.4(d) depict the streamwise variations of non-dimensional skin friction, local Nusselt number, local nanoparticle and regular Sherwood numbers under the influence of Biot number for $Fs = 0.0$ and $Fs = 1.0$. An increase in the Biot number tends to increase the magnitude of skin friction coefficient, whereas it decreases with the increase of non-Darcy parameter, as given in Fig. 5.4(a). As $Bi \to \infty$, the thermal boundary condition at the surface reaches the isothermal surface condition (i,e., uniform wall condition). In this case, the internal thermal resistance of the vertical frustum of a cone is more compared to the thermal resistance of boundary layer. Hence, the local Nusselt and regular Sherwood numbers enhance as the Biot number enhances, but an opposite behavior is observed in the case of the non-Darcy parameter, as plotted in Figs. 5.4(b) and 5.4(d). It is noted from Fig. 5.4(c) that the local nanoparticle Sherwood number increases with the increase of Biot number and it shows a reverse trend with the increase of non-Darcy parameter. Moreover, the local Nusselt and regular Sherwood numbers are more in the Darcy porous medium when compared with those of the non-Darcy porous medium.

The significance of both thermal dispersion (Ds) and solutal dispersion (Dc) effects on the dimensionless skin friction, local Nusselt number, local nanoparticle and regular Sherwood numbers, are exhibited in Figs. 5.5(a)-5.5(d). By strengthening the values of thermal dispersion parameter, the skin friction coefficient and local nanoparticle Sherwood number reduce, but the local Nusselt and regular Sherwood numbers enhance. Further, it is perceived that the skin friction, local Nusselt number and local regular Sherwood number increase, whereas the local nanoparticle Sherwood number decreases with an increase in the solutal dispersion parameter, as shown in Figs. 5.5(a)-5.5(d). Moreover, the influence of both thermal and solutal dispersion is more prominent on the local Nusselt and regular Sherwood numbers.

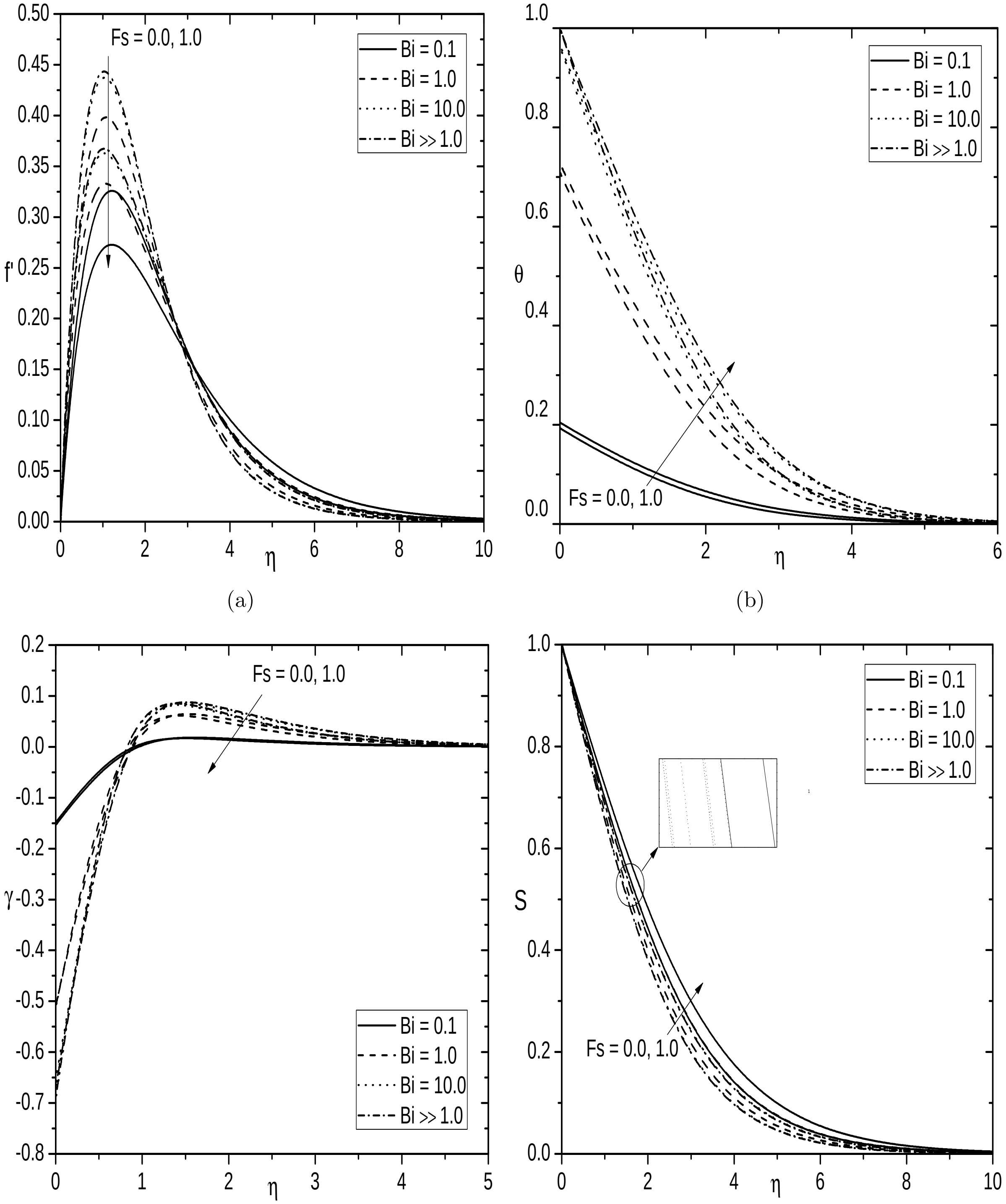

(a) (b)

(c) (d)

Figure 5.2: *Effects of Fs and Bi on (a) Velocity, (b) Temperature, (c) Nanoparticle volume fraction, and (d) Regular concentration for $Ds = 0.2$ and $Dc = 0.3$.*

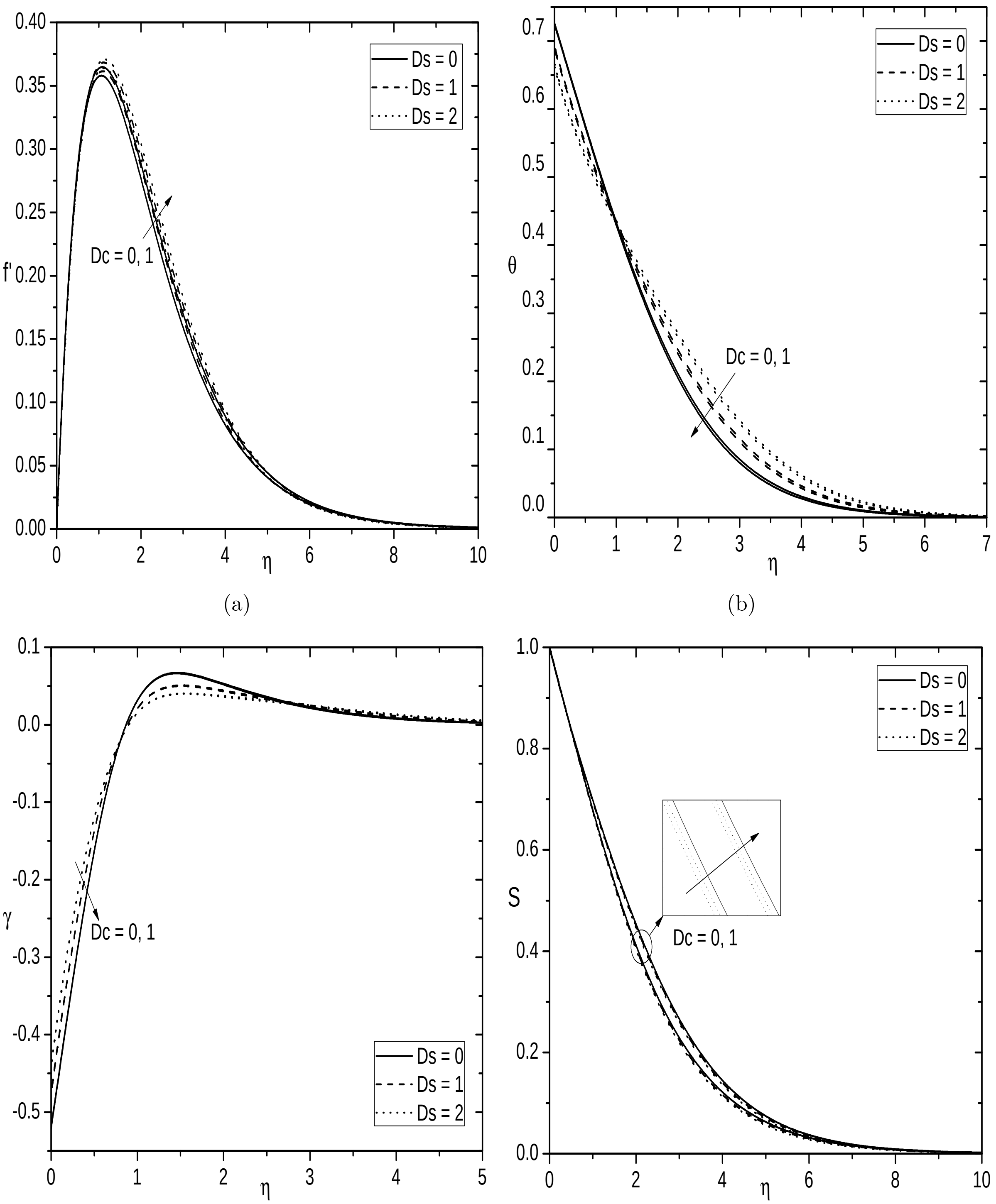

Figure 5.3: *Effects of Dc and Ds on (a) Velocity, (b) Temperature, (c) Nanoparticle volume fraction, and (d) Regular concentration for* $Fs = 0.5$ *and* $Bi = 1.0$.

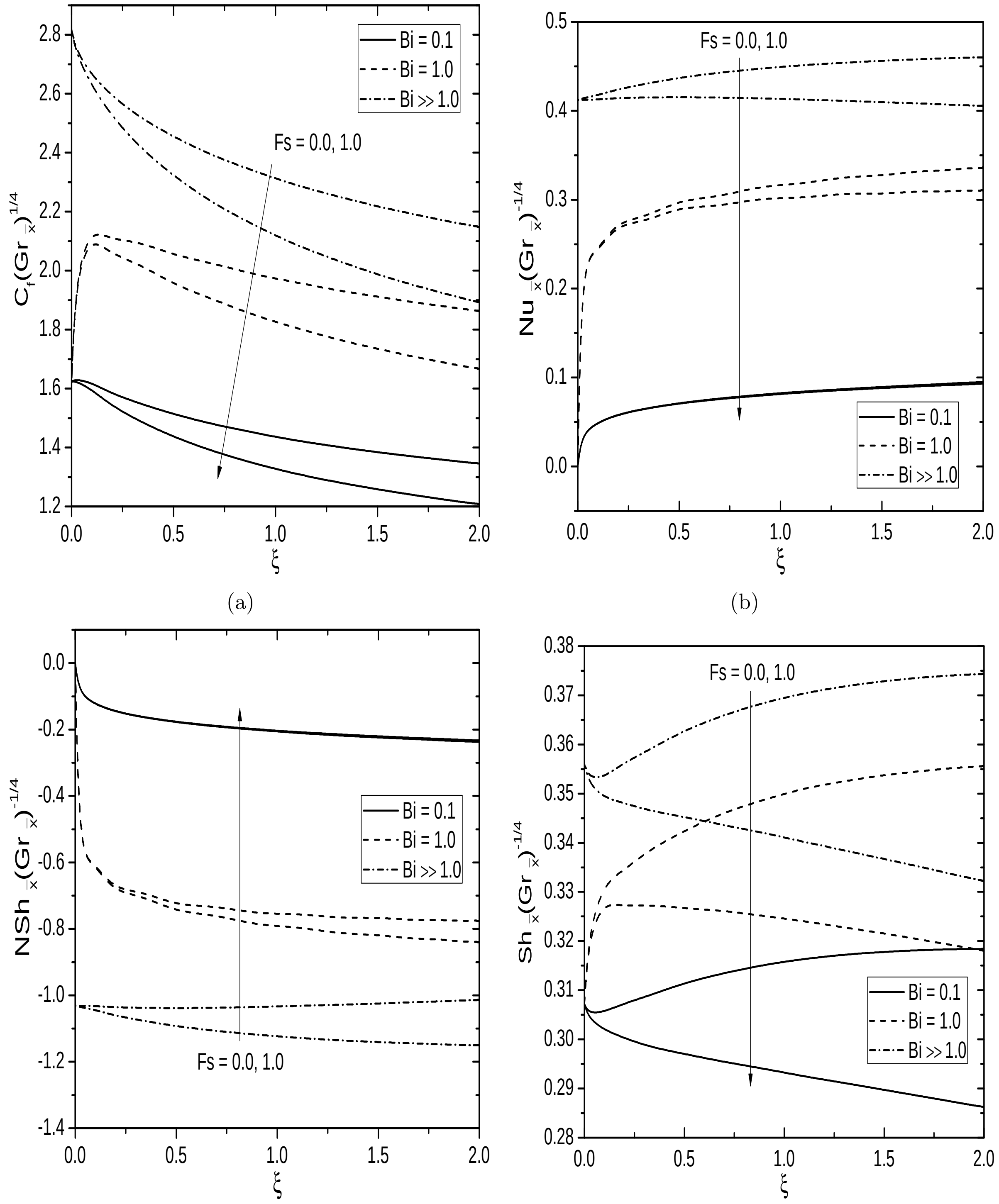

(a)

(b)

(c)

(d)

Figure 5.4: *Effects of Fs and Bi on (a) Skin friction, (b) Heat transfer rate, (c) Nanoparticle mass transfer rate, and (d) Regular mass transfer rate for $Ds = 0.2$ and $Dc = 0.3$.*

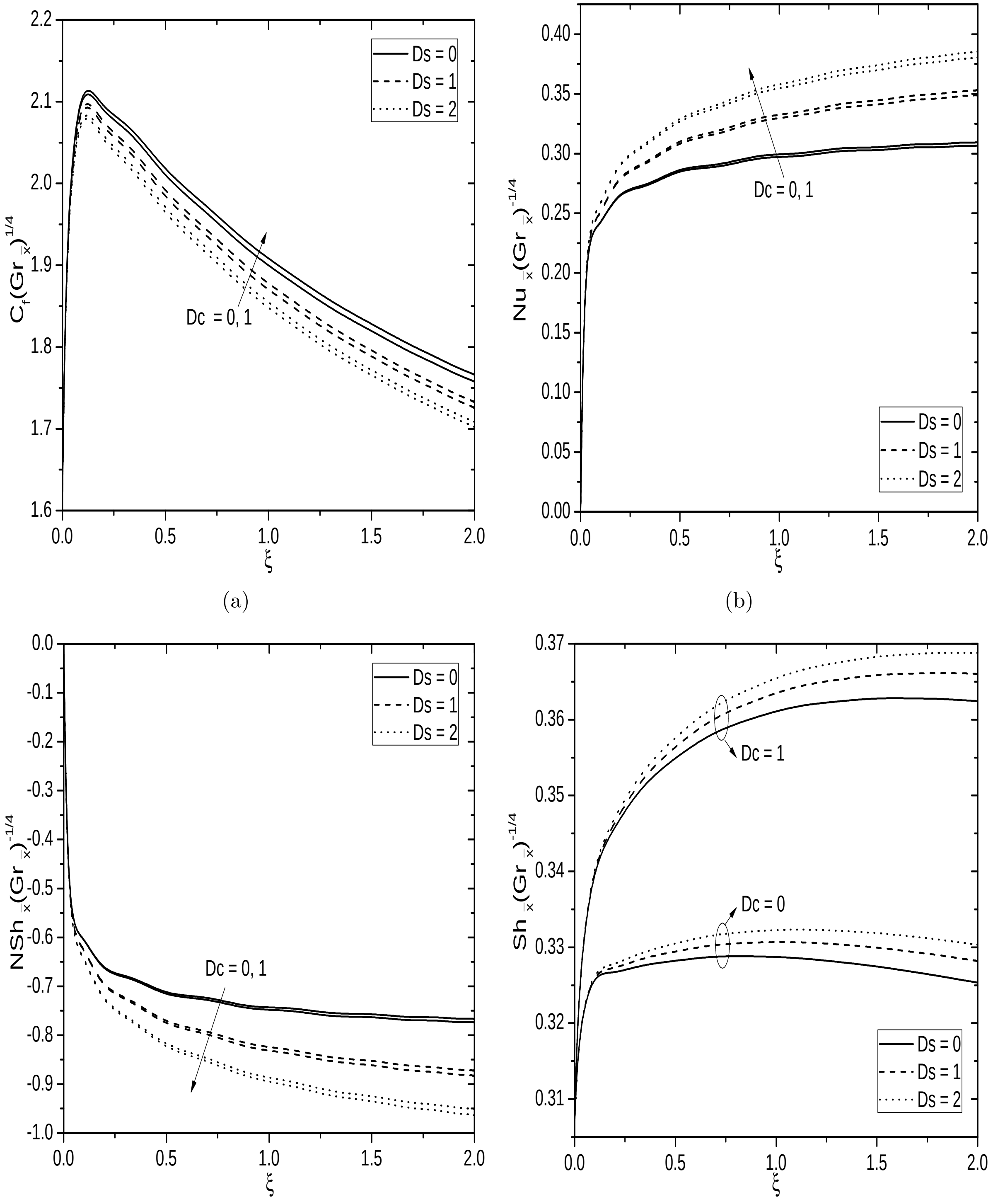

(a) (b)

(c) (d)

Figure 5.5: *Effects of* Dc *and* Ds *on (a) Skin friction, (b) Heat transfer rate, (c) Nanoparticle mass transfer rate, and (d) Regular mass transfer rate for* $Fs = 0.5$ *and* $Bi = 1.0$.

5.2.2 Case(b): Mixed Convection

Consider the flow to be a mixed convection, which arises from an external flow with velocity U_∞ and buoyancy forces. We introduce the non-similarity variables as follows

$$\xi = \frac{\overline{x}}{x_0},\ \eta = \frac{y}{\overline{x}}\, Re_{\overline{x}}^{1/2},\ \psi = r\,\nu\, Re_{\overline{x}}^{1/2}\, f\left(\xi,\eta\right),$$

$$\theta\left(\xi,\eta\right) = \frac{T - T_\infty}{T_f - T_\infty},\ \gamma\left(\xi,\eta\right) = \frac{\phi - \phi_\infty}{\phi_\infty},\ S\left(\xi,\eta\right) = \frac{C - C_\infty}{C_w - C_\infty} \tag{5.15}$$

Using (2.7) and (5.15) in Eqs.(5.2)-(5.5), we get the following non-similarity equations

$$\frac{1}{\varepsilon}\, f''' + \frac{1}{\varepsilon^2}\left(R + \frac{1}{2}\right) f\, f'' + \lambda\,\xi\ \left(\theta + Nc\, S - Nr\,\gamma\right) + \frac{1}{Da\, Re}\,\xi\ \left(1 - f'\right)$$
$$+ \frac{Fs}{Da}\,\xi\ \left(1 - f'^2\right) = \frac{\xi}{\varepsilon^2}\left(f'\frac{\partial f'}{\partial \xi} - \frac{\partial f}{\partial \xi} f''\right) \tag{5.16}$$

$$\frac{1}{Pr}\,\theta'' + \left(R + \frac{1}{2}\right) f\,\theta' + Nb\,\gamma'\,\theta' + Nt\ \left(\theta'\right)^2 + Ds\ \left(f'\theta'\right)' = \xi\ \left(f'\frac{\partial \theta}{\partial \xi} - \frac{\partial f}{\partial \xi}\theta'\right) \tag{5.17}$$

$$\frac{1}{Le}\,\gamma'' + \left(R + \frac{1}{2}\right) f\,\gamma' + \frac{1}{Le}\,\frac{Nt}{Nb}\,\theta'' = \xi\ \left(f'\frac{\partial \gamma}{\partial \xi} - \frac{\partial f}{\partial \xi}\gamma'\right) \tag{5.18}$$

$$\frac{1}{Sc}\,S'' + \left(R + \frac{1}{2}\right) f\,S' + Dc\ \left(f'S'\right)' = \xi\ \left(f'\frac{\partial S}{\partial \xi} - \frac{\partial f}{\partial \xi}S'\right) \tag{5.19}$$

along with the reduced boundary conditions

$$f'(\xi,\eta) = 0,\ f(\xi,\eta) + \frac{\xi}{\left(R + \frac{1}{2}\right)}\frac{\partial f}{\partial \xi} = 0,\ \theta'(\xi,\eta) = -Bi\,\xi^{1/2}\left[1 - \theta(\xi,\eta)\right],$$
$$Nb\,\gamma'(\xi,\eta) + Nt\,\theta'(\xi,\eta) = 0,\ S(\xi,\eta) = 1 \quad \text{at} \quad \eta = 0 \tag{5.20a}$$

$$f'(\xi,\eta) = 1,\ \theta(\xi,\eta) = 0,\ \gamma(\xi,\eta) = 0,\ S(\xi,\eta) = 0 \quad \text{as} \quad \eta \to \infty \tag{5.20b}$$

The quantities of physical interest are the non-dimensional skin friction $C_f = \dfrac{2\,\tau_w}{\rho_{f\infty}\, U_\infty^2}$, local Nusselt number $Nu_{\overline{x}} = \dfrac{q_w\,\overline{x}}{k(T_f - T_\infty)}$, local nanoparticle Sherwood number $NSh_{\overline{x}} =$

$\dfrac{q_n\,\overline{x}}{D_B\,\phi_\infty}$ and local regular Sherwood number $Sh_{\overline{x}} = \dfrac{q_m\,\overline{x}}{D_m(C_w - C_\infty)}$, are given by

$$\left.\begin{aligned} C_f\,Re_{\overline{x}}^{1/2} &= 2\,f''(\xi,0),\ \frac{Nu_{\overline{x}}}{Re_{\overline{x}}^{1/2}} = -[1 + Ds\,Pr\,f'(\xi,0)]\,\theta'(\xi,0),\\ \frac{NSh_{\overline{x}}}{Re_{\overline{x}}^{1/2}} &= -\gamma'(\xi,0),\ \frac{Sh_{\overline{x}}}{Re_{\overline{x}}^{1/2}} = -[1 + Dc\,Sc\,f'(\xi,0)]\,S'(\xi,0) \end{aligned}\right\} \tag{5.21}$$

Results and Discussion

The reduced non-linear system of partial differential Eqs. (5.16) - (5.19) together with the boundary conditions (5.20) are solved numerically using the Bivariate Pseudo-Spectral Local Linearization Method. In order to validate the code generated, for the special case of $Dc = 0.0$, $Ds = 0.0$, $Re = 200.0$, $\varepsilon = Da = 1.0$, $Fs = 0.0$ and $Bi \to \infty$, the results of present problem have been compared with those of Lloyd and Sparrow [56], and found that they are in good agreement, as shown in Tab. (2.2). To investigate the effects of non-Darcy parameter (Fs), Biot number (Bi), thermal and solutal dispersion parameters (Ds) and (Dc), the computations have been carried out for $Pr = 1.0$, $Sc = 0.6$, $Le = 10.0$, $Nc = 1.0$, $Nr = 0.5$, $Re = 200.0$, $\varepsilon = 0.8$, $Da = 0.5$, $Nt = 0.5$ and $Nb = 0.2$.

The influence of non-Darcy parameter (Fs) on the dimensionless velocity f', temperature θ, nanoparticle volume fraction γ, and regular concentration S for aiding and opposing flows, is depicted in Figs. 5.6(a)-5.6(d). From Fig. 5.6(a), it is observed that the velocity enhances with the enhancement of non-Darcy parameter in both aiding and opposing flows. With an increase of Fs, the temperature decreases for both aiding and opposing flows, as plotted in Fig. 5.6(b). But, the nanoparticle volume fraction enhances near to the surface of the frustum of a cone, whereas it shows a reverse trend far away from the surface, as displayed in Fig. 5.6(c). It is seen from Fig. 5.6(d) that the regular concentration decreases with the increase of non-Darcy parameter in both the cases of aiding and opposing flows. Moreover, the temperature and regular concentration are more in the opposing flow situation in comparison with those of aiding flow situation.

The set of Figs. 5.7(a)-5.7(d) explores the effect of Biot number (Bi) on the non-dimensional velocity f', temperature θ, nanoparticle volume fraction γ, and regular concentration S, for aiding and opposing flows. It is seen from Fig. 5.7(a) that an increase in the Biot number leads to increase the velocity when the flow is aiding, but it reveals the opposite trend when the flow is opposing. An enhancement in the Biot number enhances the convective heating and hence, $Bi \to \infty$ provides the isothermal surface, which is noticed from Fig. 5.7(b). From this figure, it is clear that the temperature increases with the increase of Biot number in both opposing and aiding flows. As the Biot number enhances, the nanoparticle volume fraction reduces near to the surface and then it enhances far away from the surface for aiding and opposing flows, as depicted in Fig. 5.7(c). However, the regular concentration rises with rising values of Bi in both aiding and opposing flows, as shown Fig. 5.7(d).

For both aiding and opposing flows, the effect of thermal dispersion parameter (Ds) on the dimensionless velocity f', temperature θ, nanoparticle volume fraction γ, and regular concentration S, is shown in Figs. 5.8(a)-5.8(d). It is clear from Fig. 5.8(a) that the velocity increases in the aiding flow case, whereas it decreases in the opposing flow case with the increase of thermal dispersion parameter. The temperature reduces near to the surface and gradually enhances far away from the surface with the enhancement of thermal dispersion parameter in both aiding and opposing flows, as plotted in Fig. 5.8(b). For both aiding and opposing flows, as the thermal dispersion parameter increases, the nanoparticle volume fraction increases near to the surface and then decreases far away from the surface, as given in Fig. 5.8(c). Further, the regular concentration diminishes with the enhancement of thermal dispersion parameter for both aiding and opposing flows, as shown in Fig. 5.8(d).

Figures 5.9(a)-5.9(b) exhibit the effect of solutal dispersion parameter (Dc) on the non-dimensional velocity f' and regular concentration S for both aiding and opposing flows. Figure 5.9(a) illustrates that the velocity enhances in the aiding flow, whereas it decreases in the opposing flow with the increase of solutal dispersion parameter. It can be seen that the regular concentration increases with an increase in the solutal dispersion parameter for both aiding and opposing flows, as portrayed in Fig. 5.9(b).

The effect of non-Darcy parameter (Fs) on the streamwise distribution of non-dimensional skin friction, local Nusselt number, local nanoparticle and regular Sherwood numbers for both aiding and opposing flows, is depicted in Figs. 5.10(a)-5.10(d). Figure 5.10(a) shows that an increase in the non-Darcy parameter leads to increase the skin friction in aiding and opposing flow situations. This is because of more velocity created by a large pressure drop due to the drag forces. It is observed from Figs. 5.10(b) and 5.10(d) that the local Nusselt and regular Sherwood numbers increase with the increase of non-Darcy parameter for opposing and aiding flows. However, an increase in the non-Darcy parameter corresponds to reduce the local nanoparticle Sherwood number, as plotted in Fig. 5.10(c).

Figures 5.11(a)-5.11(d) show the variations of dimensionless skin friction, local Nusselt number, local nanoparticle and regular Sherwood numbers versus streamwise coordinate ξ, in the presence of Biot number (Bi) for both aiding and opposing flows. With the increase of Biot number, the skin friction and local regular Sherwood number increase in the aiding flow, but these show opposite trend in the opposing flow, as given in Figs. 5.11(a) and 5.11(d). It is noted from Fig. 5.11(b) that the local Nusselt number reduces with an increase in the Biot number for both aiding and opposing flows. For both aiding and opposing flows, an increase in the Biot number causes to decrease the local nanoparticle Sherwood number, as plotted in Fig. 5.11(c). Moreover, the skin friction, local Nusselt number, and local regular Sherwood number are more in the aiding flow in comparison with those of the opposing flow.

For both aiding and opposing flow situations, the impact of thermal dispersion parameter (Ds) on the non-dimensional skin friction, local Nusselt number, local nanoparticle and regular Sherwood numbers over the streamwise coordinate ξ, is shown in Figs. 5.12(a)-5.12(d). It is seen from Fig. 5.12(a) that the skin friction increases in the opposing flow and it decreases in the aiding flow with an increase of thermal dispersion parameter. When the thermal dispersion parameter enhances, the temperature gradient increases considerably in a small region near to the surface. Therefore, the local Nusselt number substantially enhances with increasing values of the thermal dispersion parameter, as plotted in Fig. 5.12(b). But, the local nanoparticle Sherwood number decreases with the increase of thermal dispersion parameter for both aiding and opposing flows, as portrayed in Fig. 5.12(c). However, the thermal dispersion effect is negligible for the local regular Sherwood number in both opposing and aiding flow situations.

Figures 5.13(a)-5.13(d) exhibit the effect of solutal dispersion parameter (Dc) on the dimensionless skin friction, local Nusselt number, local nanoparticle and regular Sherwood numbers across ξ for aiding and opposing flows. It is observed from Figs. 5.13(a) and 5.13(b) that the skin friction and local Nusselt number decrease for opposing flow, whereas these show revere trend for aiding flow, with the increase of solutal dispersion parameter. As the solutal dispersion parameter enhances, the local nanoparticle Sherwood number reduces for aiding flow, but there is no considerable effect in the opposing flow, as shown in Fig. 5.13(c). Further, it can be noticed that the local regular Sherwood number increases with the increase of solutal dispersion parameter for both aiding and opposing flows, as depicted in Fig. 5.13(d). Moreover, the effects of thermal and solutal dispersions are more prominent in the local Nusselt number and local regular Sherwood number, respectively.

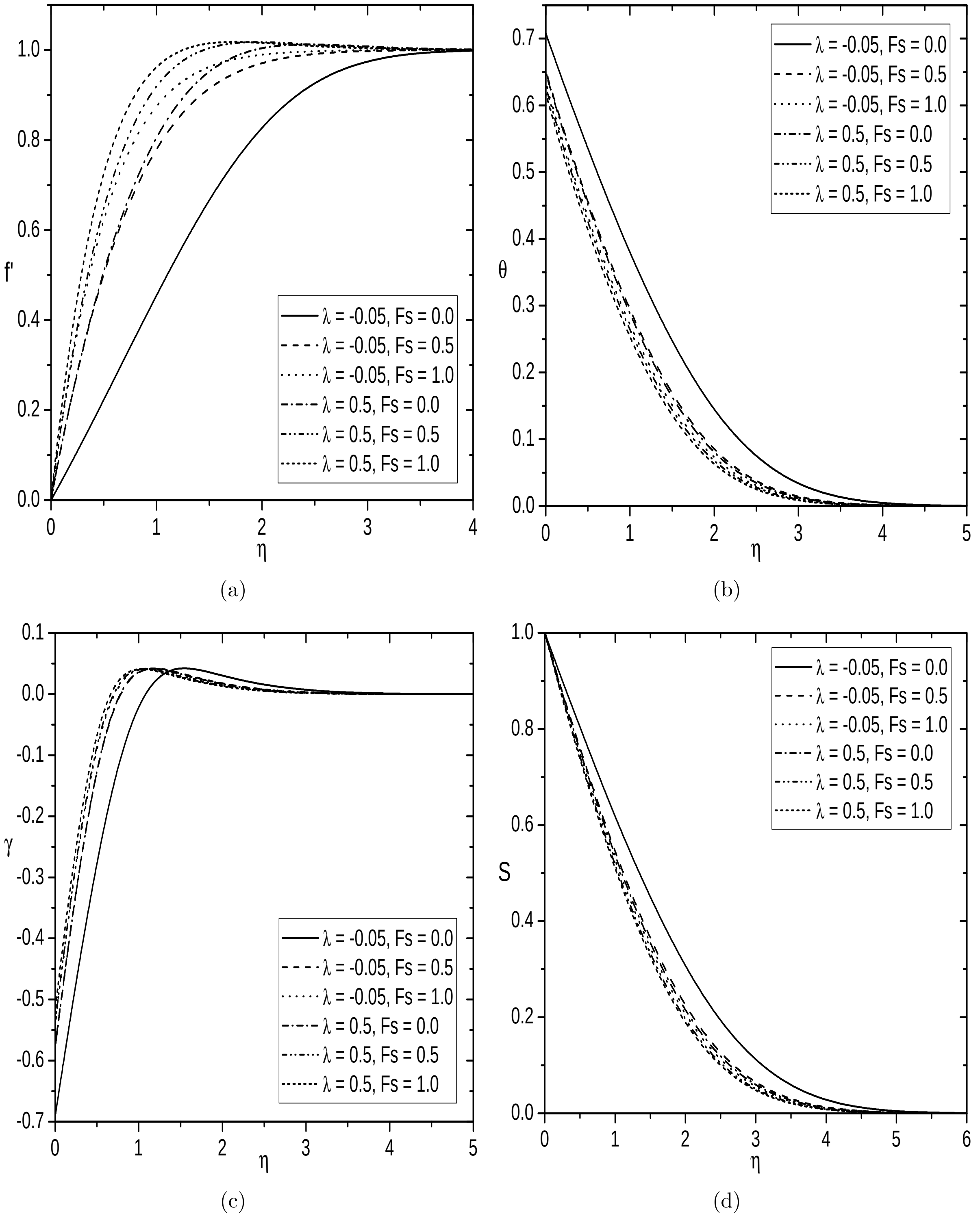

Figure 5.6: *Effects of λ and Fs on (a) Velocity, (b) Temperature, (c) Nanoparticle volume fraction and (d) Regular concentration for $Bi = 1.0$, $Ds = 0.2$ and $Dc = 0.3$.*

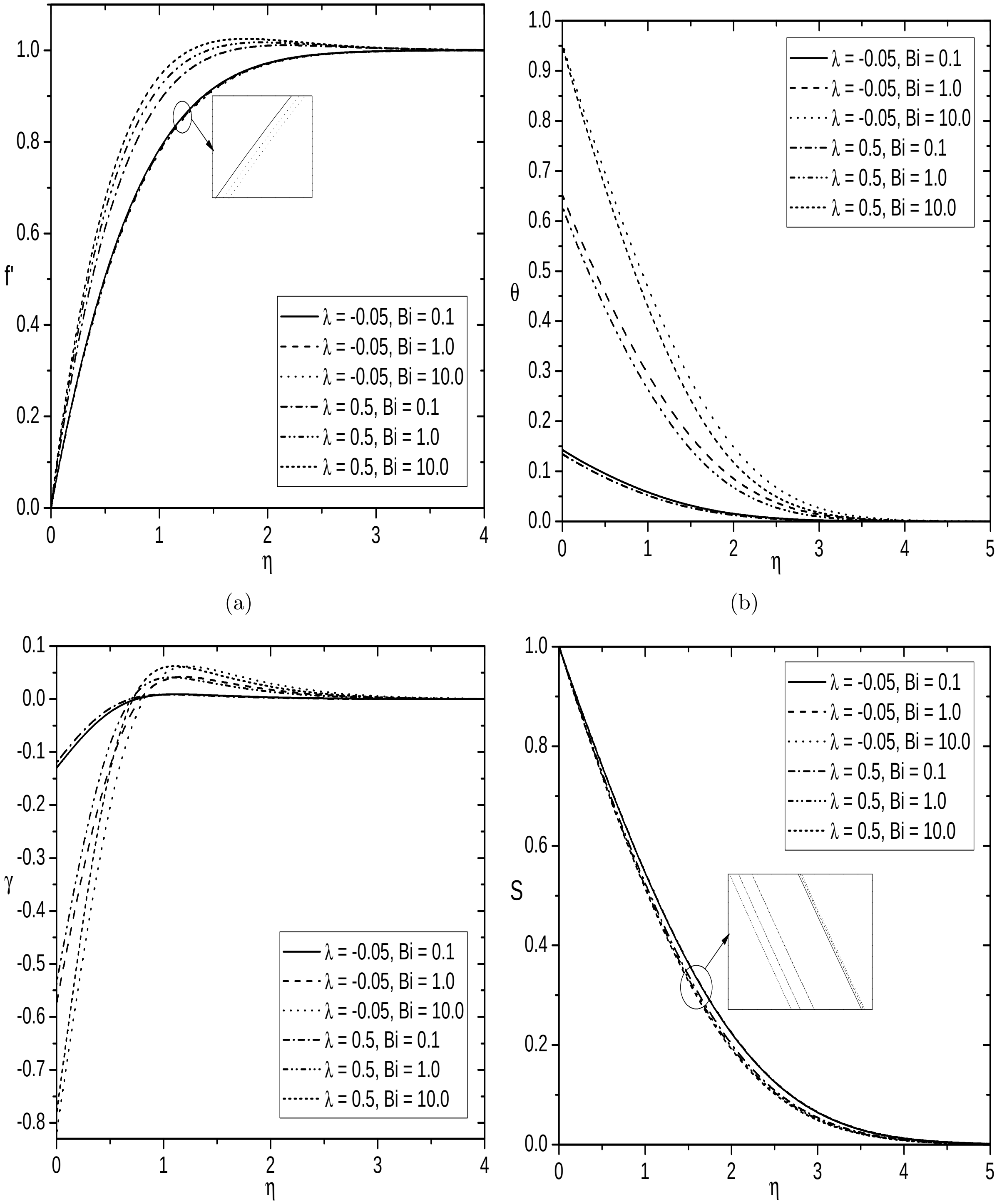

(a)

(b)

(c)

(d)

Figure 5.7: *Effects of λ and Bi on (a) Velocity, (b) Temperature, (c) Nanoparticle volume fraction and (d) Regular concentration for $Fs = 0.5$, $Ds = 0.2$ and $Dc = 0.3$.*

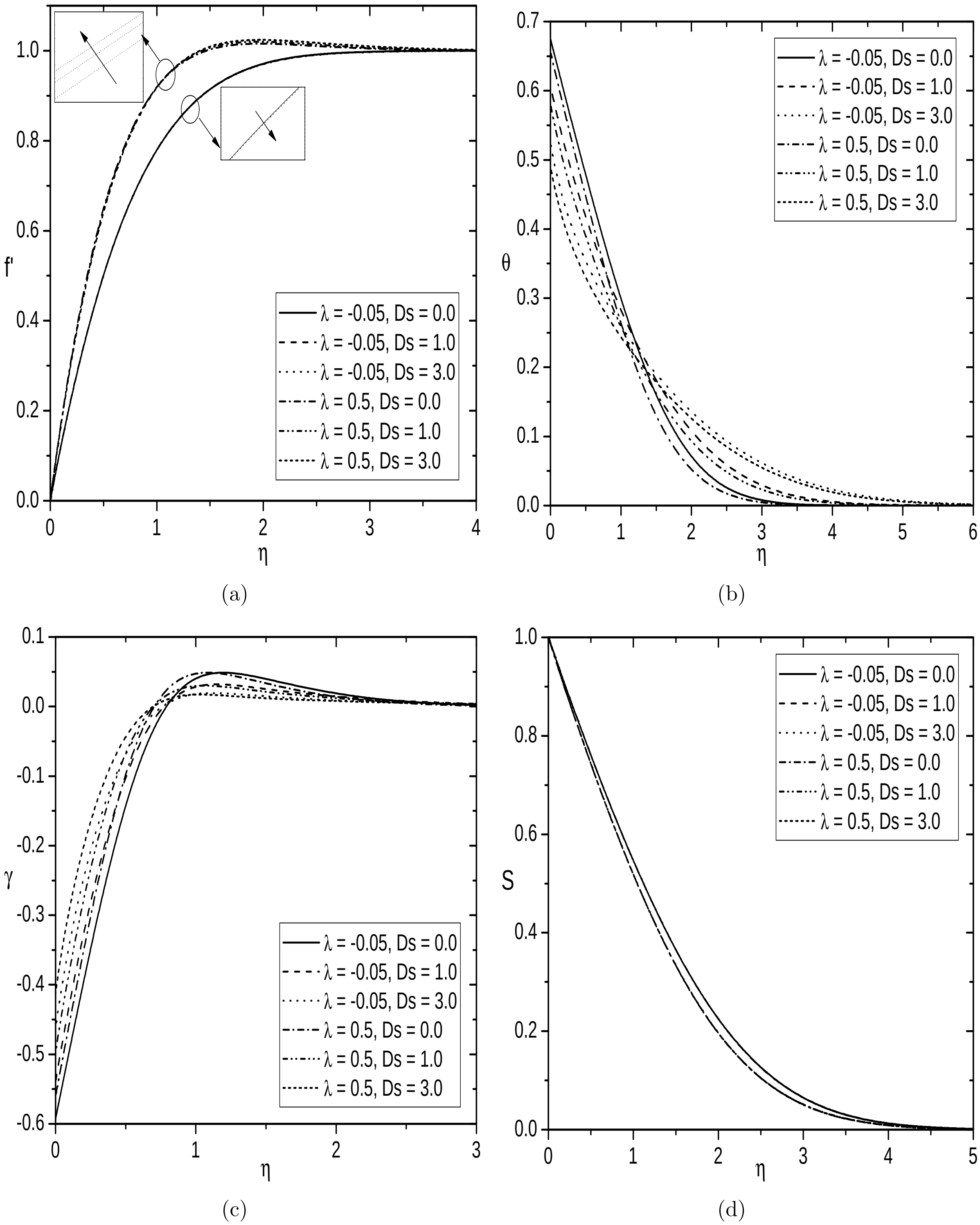

(a) (b)

(c) (d)

Figure 5.8: *Effects of* λ *and* Ds *on (a) Velocity, (b) Temperature, (c) Nanoparticle volume fraction and (d) Regular concentration for* $Fs = 0.5$*,* $Bi = 1.0$ *and* $Dc = 0.3$*.*

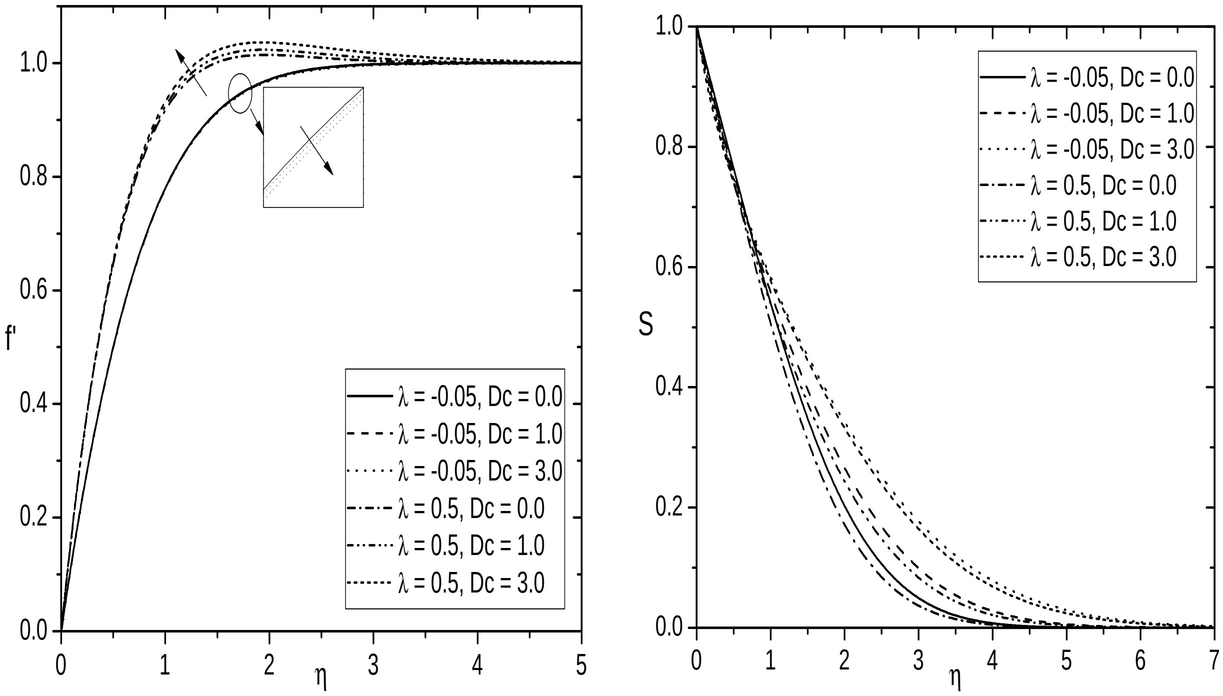

(a) (b)

Figure 5.9: *Effects of* λ *and* Dc *on (a) Velocity and (B) Regular concentration for* $Fs = 0.5$, $Bi = 1.0$ *and* $Ds = 0.2$.

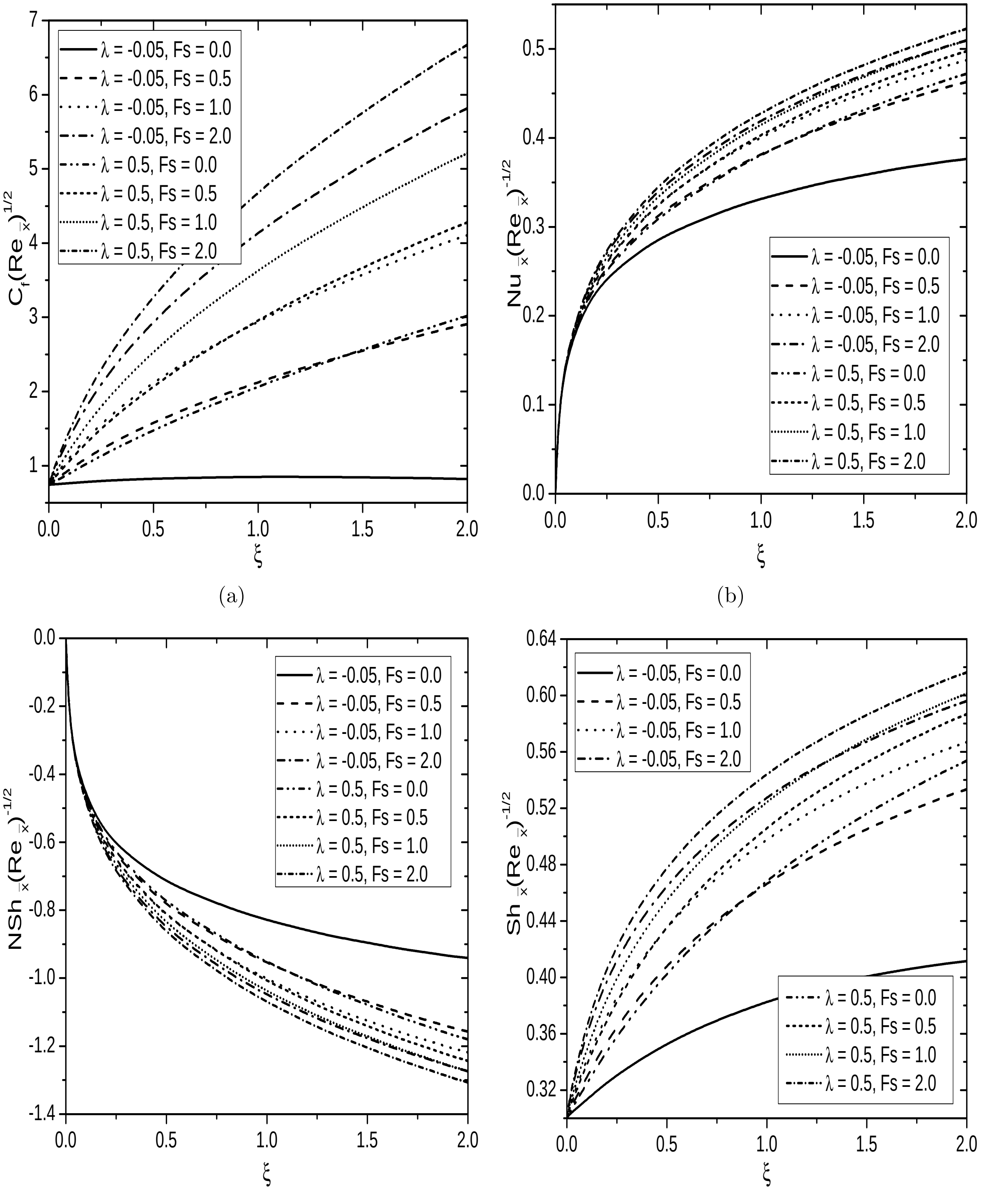

(a)

(b)

(c)

(d)

Figure 5.10: *Effects of* λ *and* Fs *on (a) Skin friction, (b) Heat transfer rate, (c) Nanoparticle mass transfer rate, and (d) Regular mass transfer rate for* $Bi = 1.0$, $Ds = 0.2$ *and* $Dc = 0.3$.

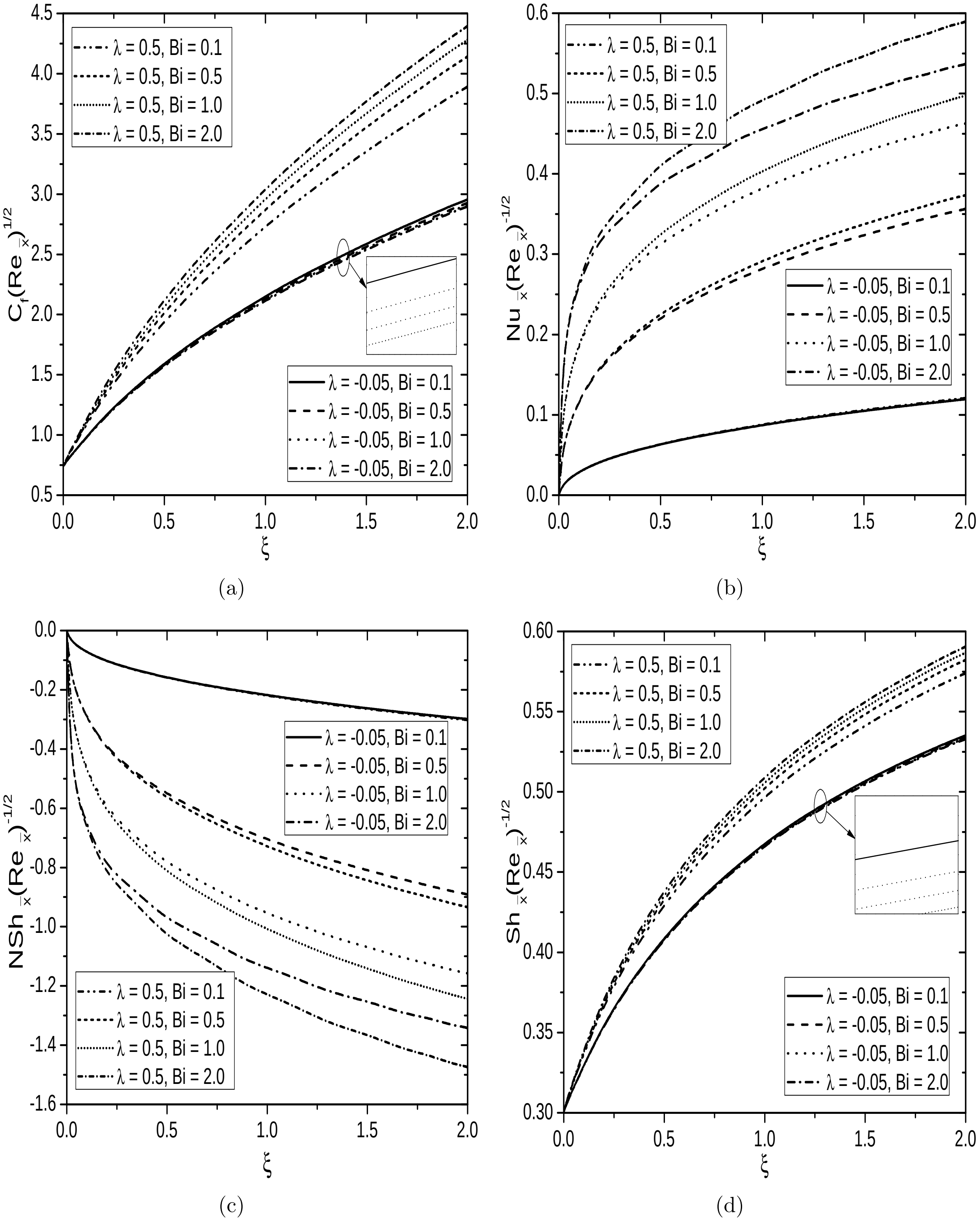

Figure 5.11: *Effects of* λ *and* Bi *on (a) Skin friction, (b) Heat transfer rate, (c) Nanoparticle mass transfer rate, and (d) Regular mass transfer rate for* $Fs = 0.5$*,* $Ds = 0.2$ *and* $Dc = 0.3$*.*

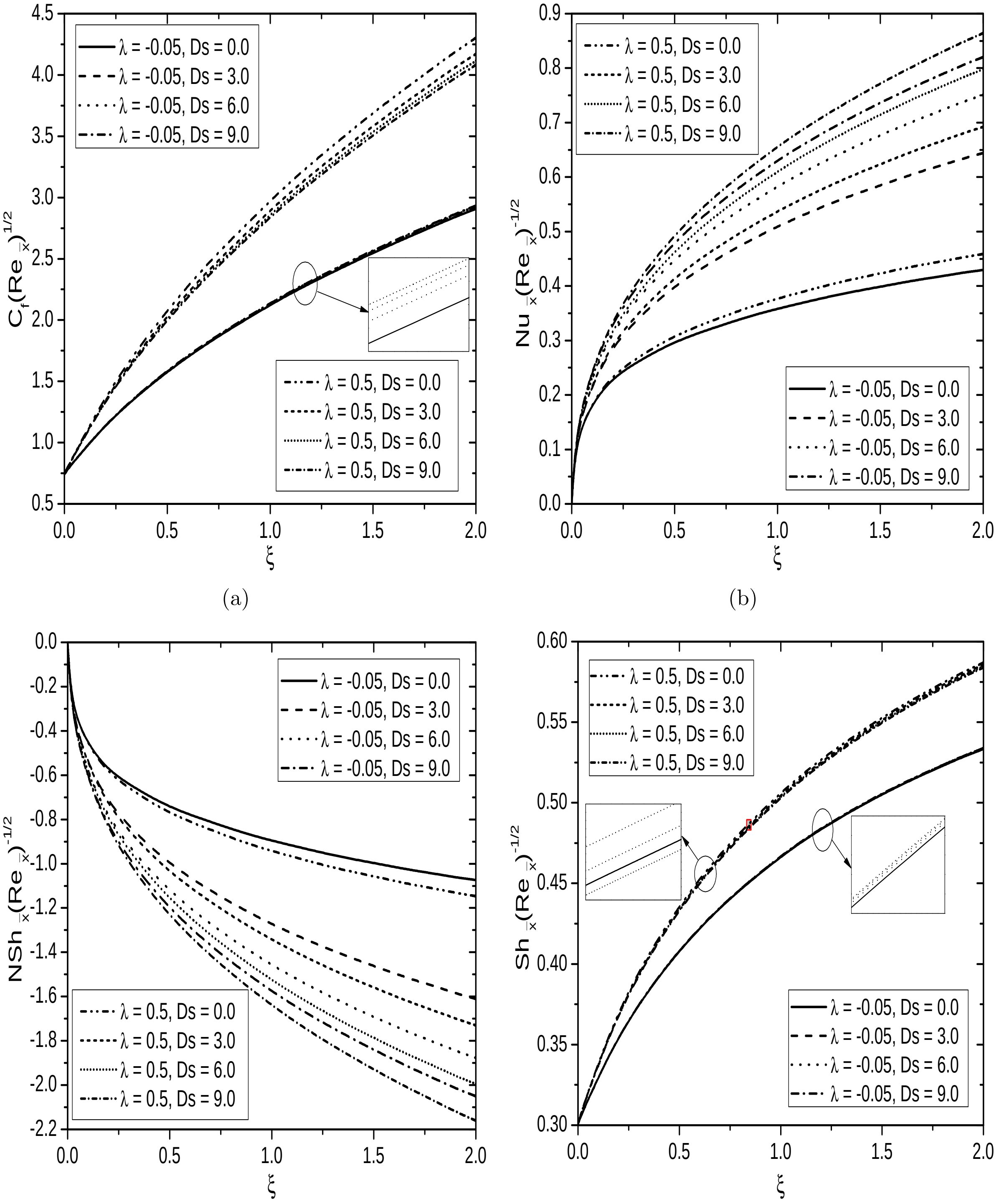

(a) (b)

(c) (d)

Figure 5.12: *Effects of* λ *and* Ds *on (a) Skin friction, (b) Heat transfer rate, (c) Nanoparticle mass transfer rate, and (d) Regular mass transfer rate for* $Fs = 0.5$, $Bi = 1.0$ *and* $Dc = 0.3$.

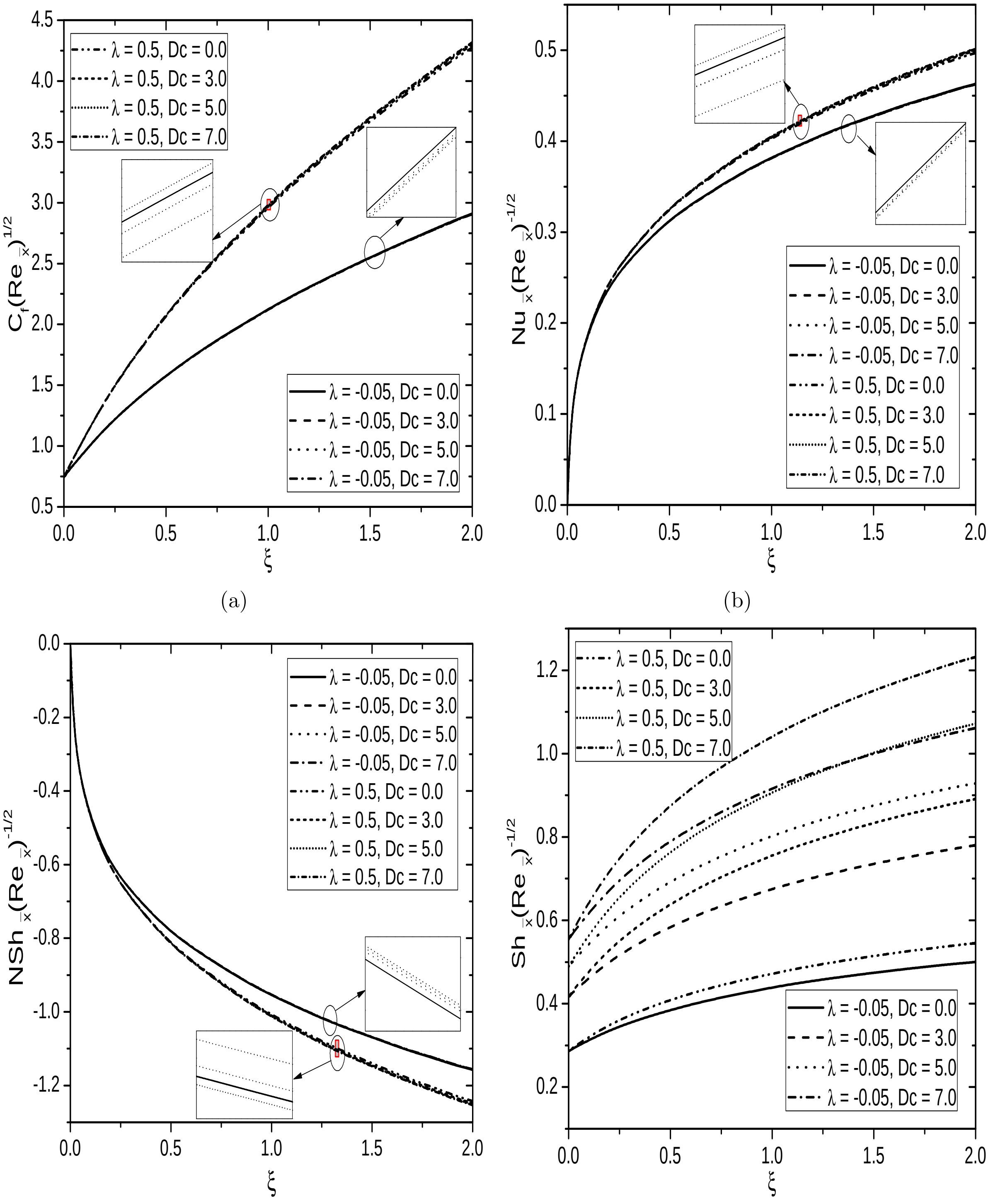

(a) (b)

(c) (d)

Figure 5.13: *Effects of* λ *and* Dc *on (a) Skin friction, (b) Heat transfer rate, (c) Nanoparticle mass transfer rate, and (d) Regular mass transfer rate for* $Fs = 0.5$, $Bi = 1.0$ *and* $Ds = 0.2$.

5.3 Conclusions

The present chapter investigates the double dispersion effects on the convective flow of a nanofluid over the frustum of a cone embedded in a non-Darcy porous medium in the presence of convective boundary condition. From this study, the conclusions can be drawn in both cases (a) and (b) as follows:

The behavior of non-Darcy parameter (i.e., Forchheimer number) on the various profiles, and local Nusselt and Sherwood numbers in both case (a) and case (b) are similar to the results of chapter-3. Also, the effect of Biot number on the different profiles and physical quantities show the similar behavior as reported in the previous chapter. Further, it is found that the velocity, nanoparticle volume fraction and local Nusselt number increase, whereas the regular concentration, surface drag and local nanoparticle Sherwood number decrease with the increase of thermal dispersion parameter, in case (a) and aiding flow of case (b). As the solutal dispersion parameter enhances, the regular concentration and local regular Sherwood number enhance. But, the velocity, surface drag and local Nusselt number increase, whereas the local nanoparticle Sherwood number decreases with Dc in case (a) and aiding flow of case (b).

Chapter 6

Convective Flow of a Nanofluid over the Rotating Frustum of a Permeable Cone with Convective Boundary Condition [1]

6.1 Introduction

In Chapters 2-5, the convective transport over the stationary vertical frustum of a cone in a nanofluid has been analyzed. But, the detailed analysis of heat and mass transfer over the rotating bodies is essential for various engineering applications such as the design of turbomachines and turbines, rotating machinery, estimation of flight path in rotating wheels, transpiration cooling, spin-stabilized missiles, modeling of several geophysical systems, etc. Anilkumar and Roy [5] presented a self-similar solution for the unsteady mixed convective flow of a rotating fluid due to the rotating cone in the presence of thermal and mass diffusion effects. Recently, the effects of cross-diffusion, viscous dissipation, and thermal radiation on

---

[1] Case(a): Communicated to "**Sadhana–Academy Proceedings in Eng. Sci.**", Case(b): Communicated to "**Indian Journal of Physics**"

the natural convective flow of a Casson fluid over the spinning cone in a non-Darcy porous medium have been reported by Makanda and Sibanda [59]. Beg *et al.* [9] discussed the problem of MHD natural convective flow over the vertically rotating cone in an orthotropic Darcian porous medium. (For more details, see the references therein).

From the literature survey, it is observed that the study of free and mixed convective flows of a nanofluid over the rotating frustum of a permeable cone has not been investigated so far. Therefore, the problem of convective flow of a nanofluid due to the rotating frustum of a permeable cone under the influence of convective boundary condition, is considered in this chapter. Further, the reduced system of non-dimensional partial differential equations is solved numerically by employing Bivariate Pseudo-Spectral Local Linearization Method. The effects of various physical parameters on the non-dimensional tangential and swirl velocities, temperature, nanoparticle volume fraction, and regular concentration along with the surface drag, local Nusselt and Sherwood numbers are, examined numerically and displayed graphically.

6.2 Mathematical Formulation

A steady, laminar and two-dimensional flow of an incompressible nanofluid caused by the rotating frustum of a permeable cone is considered. The velocity of the outer flow is assumed to be U_∞. The co-ordinate system and configuration of the rotating frustum of a cone are shown in Fig. (6.1). Choose (x, y, z) as the rectangular coordinate system in which x-axis is taken along the surface, y-axis is normal to the surface, and z-axis is taken along a circular section. The angle of rotating frustum of a cone is assumed to be large so that the effect of transverse curvature is negligible (Ref. Hering and Grosh [36]). The temperature, nanoparticle volume fraction and regular concentration of the ambient medium are assumed to be T_∞, ϕ_∞ and C_∞, respectively. The surface of a permeable frustum of a cone is either cooled or heated by convection from a nanofluid of temperature T_f with $T_f < T_\infty$ (cooled surface) and $T_f > T_\infty$ (heated surface), respectively. The rotating surface is held at uniform regular concentration C_w. The thickness of boundary layer is assumed to be

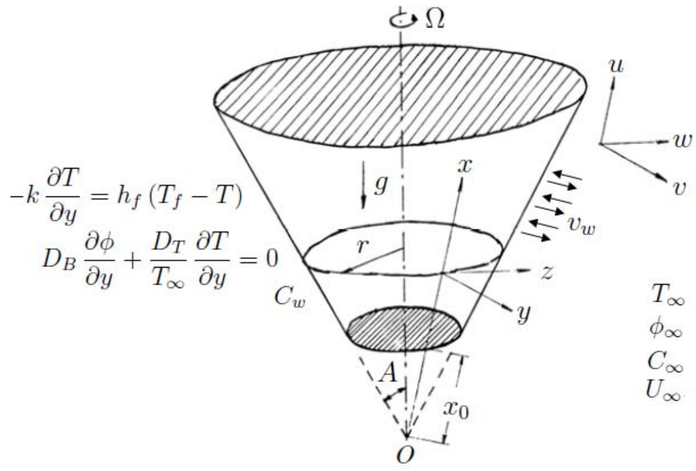

Figure 6.1: *Physical geometry of the problem*

small in comparison with the radius of a cone and hence the local radius to a point can be approximated by $r = x\,\sin A$ (Ref. Singh *et al.* [114]).

Following the above assumptions and Oberbeck-Boussinesq approximations, the governing boundary layer equations can be written as

$$\frac{\partial (r\,u)}{\partial x} + \frac{\partial (r\,v)}{\partial y} = 0 \tag{6.1}$$

$$\rho_{f\infty}\left(u\,\frac{\partial u}{\partial x} + v\,\frac{\partial u}{\partial y} - \frac{w^2}{x}\right) = \mu\,\frac{\partial^2 u}{\partial y^2} + \rho_{f\infty}\,g\,\left(1-\phi_\infty\right)\,\left[\beta_T (T - T_\infty) + \beta_C (C - C_\infty)\right]\cos A$$
$$-(\rho_p - \rho_{f\infty})\,g(\phi - \phi_\infty)\cos A \tag{6.2}$$

$$u\,\frac{\partial w}{\partial x} + v\,\frac{\partial w}{\partial y} + \frac{u\,w}{x} = \nu\,\frac{\partial^2 w}{\partial y^2} \tag{6.3}$$

$$u\,\frac{\partial T}{\partial x} + v\,\frac{\partial T}{\partial y} = \alpha_m\,\frac{\partial^2 T}{\partial y^2} + \mathcal{J}\,\left[D_B\,\frac{\partial \phi}{\partial y}\frac{\partial T}{\partial y} + \frac{D_T}{T_\infty}\,\left(\frac{\partial T}{\partial y}\right)^2\right] \tag{6.4}$$

$$u\,\frac{\partial \phi}{\partial x} + v\,\frac{\partial \phi}{\partial y} = D_B\,\frac{\partial^2 \phi}{\partial y^2} + \frac{D_T}{T_\infty}\,\frac{\partial^2 T}{\partial y^2} \tag{6.5}$$

$$u\,\frac{\partial C}{\partial x} + v\,\frac{\partial C}{\partial y} = D_S\,\frac{\partial^2 C}{\partial y^2} \tag{6.6}$$

where u, v and w are the components of velocity along the tangential (x), normal (y) and azimuthal (z)-directions, respectively.

The associated boundary conditions are

$$u = 0,\ v = v_w,\ w = r\,\Omega,\ -k\,\frac{\partial T}{\partial y} = h_f\,(T_f - T),\ D_B\,\frac{\partial \phi}{\partial y} + \frac{D_T}{T_\infty}\,\frac{\partial T}{\partial y} = 0,\ C = C_w \ \text{ at } \ y = 0 \tag{6.7a}$$

$$u = U_\infty,\ w = 0,\ T = T_\infty,\ \phi = \phi_\infty,\ C = C_\infty \ \text{ as } \ y \to \infty \tag{6.7b}$$

In this chapter also, two types (cases) of problems are considered: (a) free/natural convection and (b) mixed convection.

6.2.1 Case(a): Natural Convection

The flow is assumed to be a natural convection, which is caused by buoyancy forces only without any external agent, hence the velocity of the external flow become zero ($i.e., U_\infty = 0$). Next, introduce the following non-similarity transformations

$$\xi = \frac{x - x_0}{x_0} = \frac{\overline{x}}{x_0},\ \eta = \frac{y}{\overline{x}}\,Gr_{\overline{x}}^{1/4},\ W\,(\xi,\,\eta) = \frac{w}{r\,\omega},\ \psi = r\,\nu\,Gr_{\overline{x}}^{1/4}\,f\,(\xi,\eta)\,,$$

$$\theta\,(\xi,\eta) = \frac{T - T_\infty}{T_f - T_\infty},\ \gamma\,(\xi,\eta) = \frac{\phi - \phi_\infty}{\phi_\infty},\ S\,(\xi,\eta) = \frac{C - C_\infty}{C_w - C_\infty} \tag{6.8}$$

where $\overline{x} = x - x_0$ and $Gr_{\overline{x}} = \dfrac{g\,\beta_T(T_f - T_\infty)(1 - \phi_\infty)\overline{x}^3\cos A}{\nu^2}$ is the local Grashof number.

Substituting (2.7) and (6.8) into Eqs.(6.2)-(6.6), the governing equations reduces to the following form

$$f''' + \left(R + \frac{3}{4}\right) f\,f'' - \frac{1}{2}\,(f')^2 + \chi\,R\,W^2 + \theta + Nc\,S - Nr\,\gamma = \xi\,\left(f'\frac{\partial f'}{\partial \xi} - \frac{\partial f}{\partial \xi}f''\right) \tag{6.9}$$

$$W'' + \left(R + \frac{3}{4}\right) f\,W' - 2\,R\,f'\,W = \xi\,\left(f'\frac{\partial W}{\partial \xi} - \frac{\partial f}{\partial \xi}W'\right) \tag{6.10}$$

$$\frac{1}{Pr}\,\theta'' + \left(R + \frac{3}{4}\right) f\,\theta' + Nb\,\gamma'\,\theta' + Nt\,(\theta')^2 = \xi\,\left(f'\frac{\partial \theta}{\partial \xi} - \frac{\partial f}{\partial \xi}\theta'\right) \tag{6.11}$$

$$\frac{1}{Le}\,\gamma'' + \left(R + \frac{3}{4}\right) f\,\gamma' + \frac{1}{Le}\,\frac{Nt}{Nb}\,\theta'' = \xi\,\left(f'\frac{\partial \gamma}{\partial \xi} - \frac{\partial f}{\partial \xi}\gamma'\right) \tag{6.12}$$

$$\frac{1}{Sc}\,S'' + \left(R + \frac{3}{4}\right) f\,S' = \xi\,\left(f'\frac{\partial S}{\partial \xi} - \frac{\partial f}{\partial \xi}S'\right) \tag{6.13}$$

The reduced boundary conditions in terms of f, W, θ, γ and S are

$$f'(\xi,\eta) = 0,\; \xi\,\frac{\partial f}{\partial \xi} + \left(R + \frac{3}{4}\right) f(\xi,\eta) = \xi^{1/4}\,f_w,\; W(\xi,\eta) = 1,\; \theta'(\xi,\eta) = -Bi\,\xi^{1/4}\,\left[1 - \theta(\xi,\eta)\right],$$
$$Nb\,\gamma'(\xi,\eta) + Nt\,\theta'(\xi,\eta) = 0,\; S(\xi,\eta) = 1 \quad \text{at} \quad \eta = 0 \tag{6.14a}$$

$$f'(\xi,\eta) = 0,\; W(\xi,\eta) = 0,\; \theta(\xi,\eta) = 0,\; \gamma(\xi,\eta) = 0,\; S(\xi,\eta) = 0 \quad \text{as} \quad \eta \to \infty \tag{6.14b}$$

where the prime represents the partial differentiation with respect to η and $R = \dfrac{\xi}{1+\xi}$. Next, $\chi = \dfrac{\Omega^2\,x_0^4\,\sin^2 A}{\nu\,Gr_{\overline{x}}}$ is the spinning parameter, $Bi = \dfrac{h_f\,x_0}{k\,Gr_{\overline{x}}^{1/4}}$ is the Biot number, $f_w = -\dfrac{v_w\,x_0}{\nu\,Gr_{\overline{x}}^{1/4}}$ is the suction/injection parameter with $f_w < 0$ for injection, $f_w > 0$ for suction and $f_w = 0$ for impermeable surface.

The wall shear stress, local heat, nanoparticle mass and regular mass fluxes over the rotating frustum of a cone are

$$\tau_w = \mu\,\left[\frac{\partial u}{\partial y}\right]_{y=0},\; q_w = -k\,\left[\frac{\partial T}{\partial y}\right]_{y=0},\; q_n = -D_B\,\left[\frac{\partial \phi}{\partial y}\right]_{y=0} \text{ and } q_m = -D_S\,\left[\frac{\partial C}{\partial y}\right]_{y=0} \tag{6.15}$$

The non-dimensional skin friction $C_f = \dfrac{2\,\tau_w}{\rho_{f\infty}\,U_*^2}$, local Nusselt number $Nu_{\overline{x}} = \dfrac{q_w\,\overline{x}}{k\,(T_f - T_\infty)}$, local nanoparticle Sherwood number $NSh_{\overline{x}} = \dfrac{q_n\,\overline{x}}{D_B\,\phi_\infty}$ and local regular Sherwood number $Sh_{\overline{x}} = \dfrac{q_m\,\overline{x}}{D_S\,(C_w - C_\infty)}$, are given by

$$\left.\begin{array}{l} \dfrac{1}{2}\,C_f\,Gr_{\overline{x}}^{1/4} = f''(\xi,0),\; \dfrac{Nu_{\overline{x}}}{Gr_{\overline{x}}^{1/4}} = -\theta'(\xi,0), \\ \dfrac{NSh_{\overline{x}}}{Gr_{\overline{x}}^{1/4}} = -\gamma'(\xi,0),\; \dfrac{Sh_{\overline{x}}}{Gr_{\overline{x}}^{1/4}} = -S'(\xi,0) \end{array}\right\} \tag{6.16}$$

Results and Discussion

The system of Eqs. (6.9)-(6.13) along with the boundary conditions (6.14) have been solved numerically using the Bivariate Pseudo-Spectral Local Linearization Method. In order to assess the accuracy of the generated code, for $Nr = Nc = Nt = 0, Sc = Le = 1, Nb \to 0, f_w = 0, Bi \to \infty$, $\chi = 0$ and $\xi = 0$, the results of the present problem have been compared with those of Na and Chiou [75], Na [74], Yih [130] and Cebeci and Bradshaw [15], as shown in Tab. (6.1). Also, for $Nr = Nc = Nt = 0, Sc = Le = 1, Nb \to 0, f_w = 0, Bi \to \infty$, $\chi = 0$ and $\xi \to \infty$, the present results have been compared with the results given by Na and Chiou [75], Yih [130], Roy [107] and Alamgir [4], as given in Tab. (6.2). From Tabs. (6.1) and (6.2), it is found that the present numerical results are in a good agreement. To study the effects of Biot number (Bi), spinning parameter (χ), and suction/injection parameter (f_w), the computations have been carried out for $Nc = 1.0, Nt = 0.2, Nb = 0.2, Nr = 0.5, Pr = 1.0, Sc = 0.6$ and $Le = 10.0$. Also, the present analysis is carried out with all possible cases of suction/injection parameter (f_w).

The set of Figs. 6.2(a)-6.2(d) are prepared to analyze the effect of spinning parameter (χ) on the non-dimensional tangential velocity f', swirl velocity W, temperature θ and nanoparticle volume fraction γ. With the increase of χ (i.e., the higher rotation of the frustum of a cone), the tangential velocity enhances near to the surface and then gradually decreases up to its free stream velocity, as given in Fig. 6.2(a). The above effect is due to the more induced axial flow caused by the more rotation of the frustum of a cone. However, the swirl velocity is not much affected by the spinning parameter, as plotted in Fig. 6.2(b). It is also seen from Figs. 6.2(c) that the temperature enhances with the enhancement of spinning parameter. The above observations are found to be same in both the suction and injection cases. But, the nanoparticle volume fraction profile enlarges for the injection and impermeability cases, whereas it shows an opposite behavior for the suction case. Further, the tangential velocity, swirl velocity and temperature are high in the case of injection, when compared to those of the impermeability and suction cases. But, the nanoparticle volume fraction shows a reverse behavior, as displayed in Fig. 6.2(d).

Table 6.1: *Comparison of* $f''(0,0)$ *and* $-\theta'(0,0)$ *for various values of* Pr*.*

	$f''(0, 0)$			$-\theta'(0, 0)$				
Pr	[130]	[15]	Present	[74]	[75]	[130]	[15]	Present
0.1	1.2144	1.2104	1.21165028	——	——	0.1629	0.1637	0.16340582
1	0.9084	0.9081	0.90819101	0.4010	0.4011	0.4012	0.4009	0.40103279
10	0.5927	0.5930	0.59282356	0.8269	0.8269	0.8266	0.8266	0.82682956
100	0.3558	0.3564	0.35588168	1.5493	1.5493	1.5493	1.5495	1.54930393
1000	0.2049	——	0.20574836	——	——	2.8035	——	2.80311089

Figures 6.3(a)-6.3(d) explore the tangential velocity f', swirl velocity W, temperature θ and nanoparticle volume fraction γ, under the influence of Biot number (Bi). Biot number is characterized by the ratio of the thermal resistance of the boundary layer and the solid surface. With an increase in the Biot number, the tangential velocity increases, whereas the swirl velocity decreases in the injection, impermeable and suction cases. But, the maximum tangential and swirl velocities are found in the case of injection, as shown in Figs. 6.3(a) and 6.3(b). Also, the convective heating increases with the Biot number and the case of $Bi \to \infty$ gives the isothermal surface which is clearly shown in Fig. 6.3(c). The higher values of the Biot number (strong convection) leads to a higher temperature, and consequently enhances the temperature, for all cases of f_w. For a fixed f_w, the nanoparticle volume fraction diminishes with an increase in the Biot number. But, the minimum values of nanoparticle volume fraction, and the maximum values of temperature are found in the injection case.

The variations of regular concentration for different values of χ and Bi, are exhibited in Figs. 6.4(a) and 6.4(b), respectively. With the increase of both χ and Bi, the regular concentration diminishes for all cases of f_w. However, the regular concentration of the nanofluid is more with the injection, but less with suction in comparison to that of impermeable surface.

The streamwise distribution of non-dimensional skin friction $[f''(\xi, 0)]$, local Nusselt number $[-\theta'(\xi, 0)]$, local nanoparticle Sherwood number $[-\gamma'(\xi, 0)]$ and local regular Sherwood number $[-S'(\xi, 0)]$ in the presence of spinning parameter (χ), are shown in Figs. 6.5(a)-6.5(d). It is evident from Fig. 6.5(a) that the drag coefficient substantially increases with an increase in the spinning parameter for different cases of f_w. But, more surface drag is

Table 6.2: *Comparison of $f''(\infty, 0)$ and $-\theta'(\infty, 0)$ for various values of Pr.*

	$f''(\infty, 0)$			$-\theta'(\infty, 0)$				
Pr	[107]	[130]	Present	[107]	[4]	[75]	[130]	Present
0.1	——	1.0960	1.09464314	——	0.2141	——	0.2116	0.21130560
1	0.8600	0.7699	0.76944922	0.5275	0.5280	0.5104	0.5109	0.51039548
10	0.4899	0.4877	0.48769819	1.0354	1.0159	1.0340	1.0339	1.03398025
100	0.2897	0.2896	0.28960777	1.9229	1.8237	1.9220	1.9226	1.92271470
1000	0.1661	0.1661	0.16168925	3.4700	3.2463	——	3.4696	3.46515335

found in the injection case. For a fixed f_w, the local Nusselt and regular Sherwood numbers increase with an increase of the spinning parameter, as depicted in Figs. 6.5(b) and 6.5(d). Also, a substantial increase in the local Nusselt and regular Sherwood numbers are noticed in the case of suction. The above effect is due to a decrease in the thickness of the thermal and regular concentration boundary layers. As spinning parameter enhances, the local nanoparticle Sherwood number diminishes at a fixed value of f_w. It is also found that the local nanoparticle Sherwood number is high in the case of injection.

The effect of Biot number (Bi) on the dimensionless surface drag [$f''(\xi, 0)$], local Nusselt number [$-\theta'(\xi, 0)$], local nanoparticle Sherwood number [$-\gamma'(\xi, 0)$] and local regular Sherwood number [$-S'(\xi, 0)$], are exhibited in Figs. 6.6(a)-6.6(d). For all cases of f_w, the surface drag increases with an increase in the Biot number, as plotted in Fig. 6.6(a) whereas the local nanoparticle Sherwood number decreases, as shown in Fig. 6.6(c). However, the maximum values of the surface drag and local nanoparticle Sherwood number are noticed in the case of injection. When the Biot number increases, the local Nusselt and regular Sherwood numbers increase in all cases of f_w. But, more local Nusselt and regular Sherwood numbers are found in the case of suction, as depicted in Figs. 6.6(b) and 6.6(d).

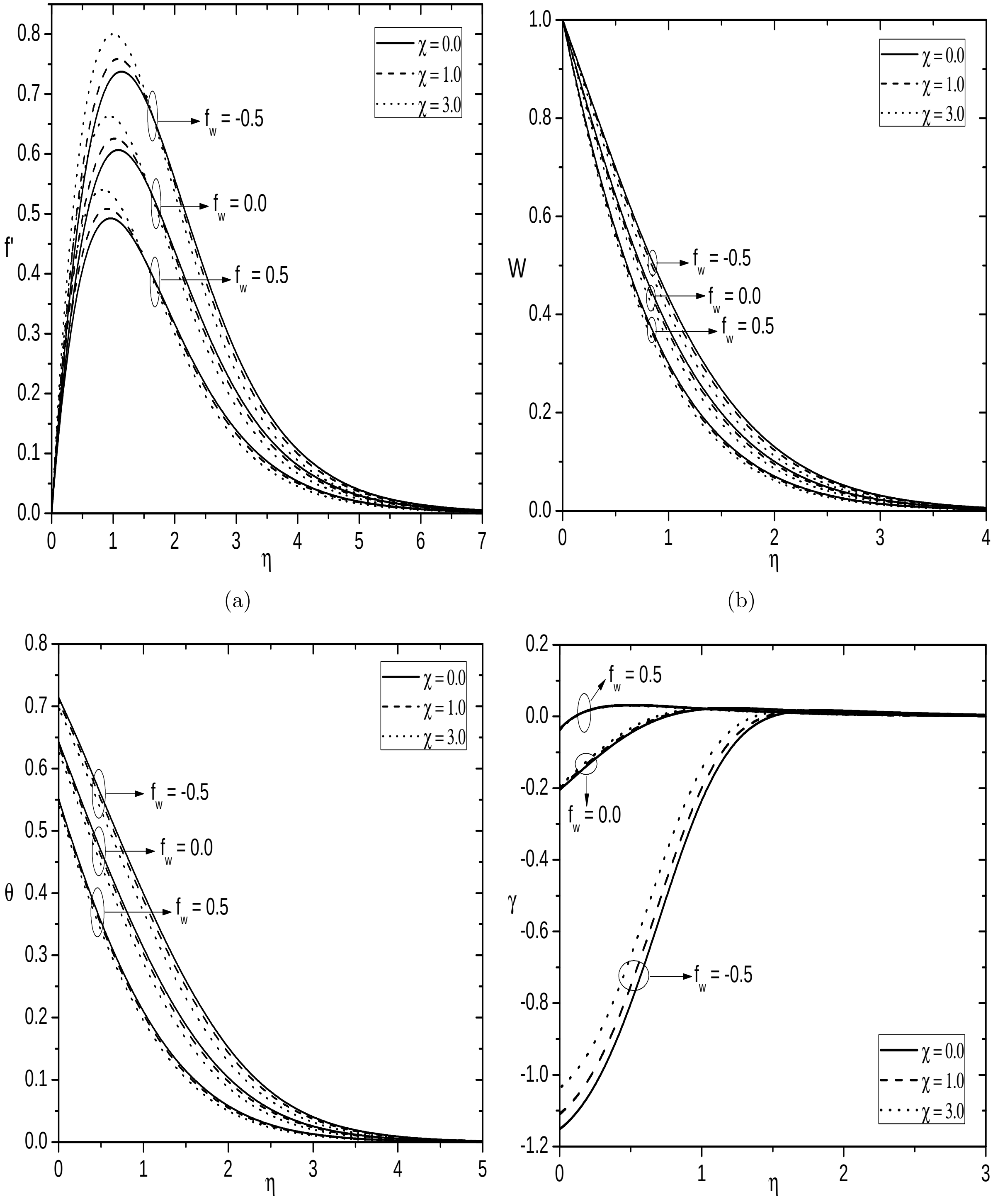

(a)

(b)

(c)

(d)

Figure 6.2: *Effects of* f_w *and* χ *on (a) Tangential velocity, (b) Swirl velocity, (c) Temperature, and (d) Nanoparticle volume fraction for* $Bi = 1.0$*.*

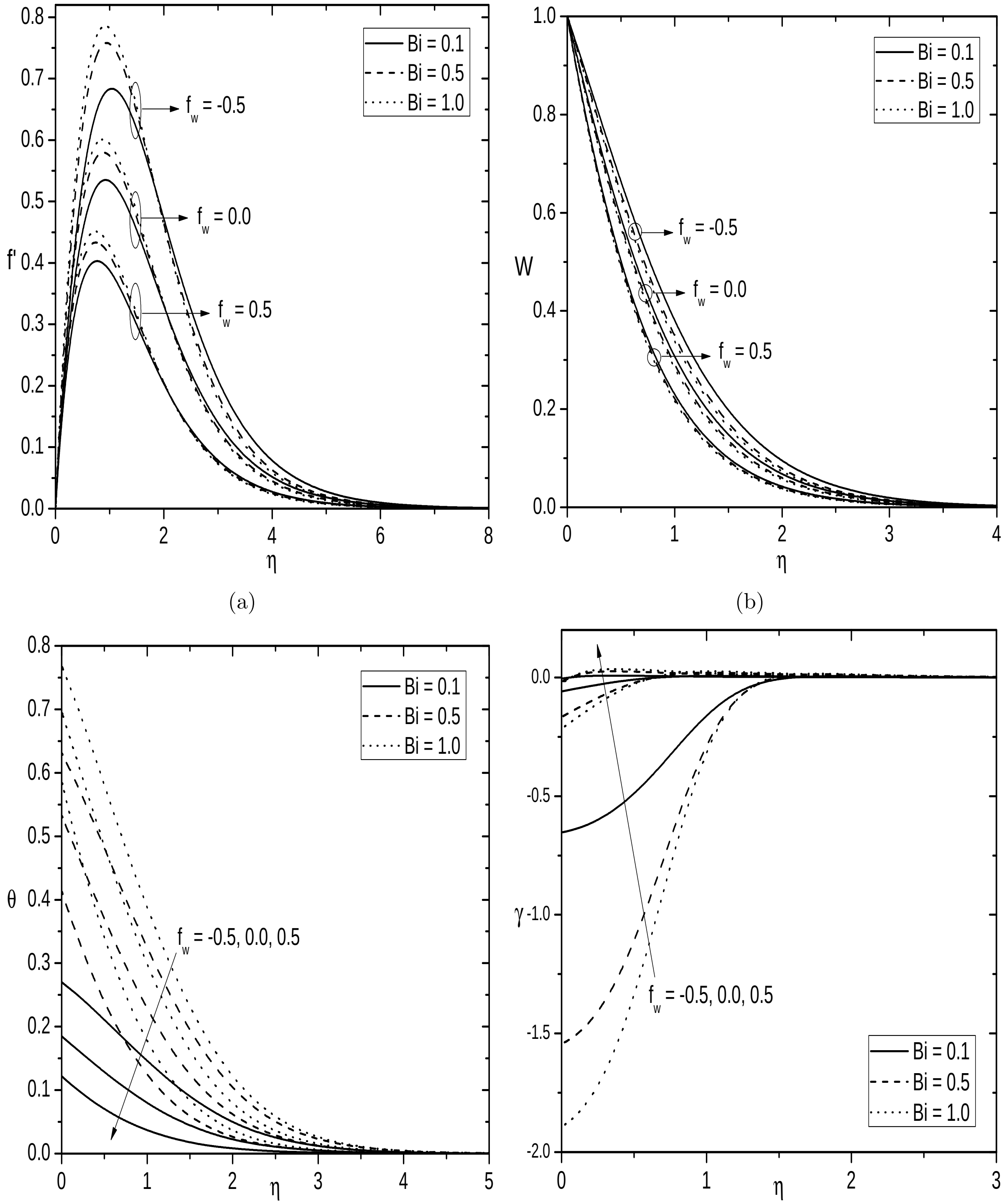

(a) (b) (c) (d)

Figure 6.3: *Effects of f_w and Bi on (a) Tangential velocity, (b) Swirl velocity, (c) Temperature, and (d) Nanoparticle volume fraction for $\chi = 2.0$.*

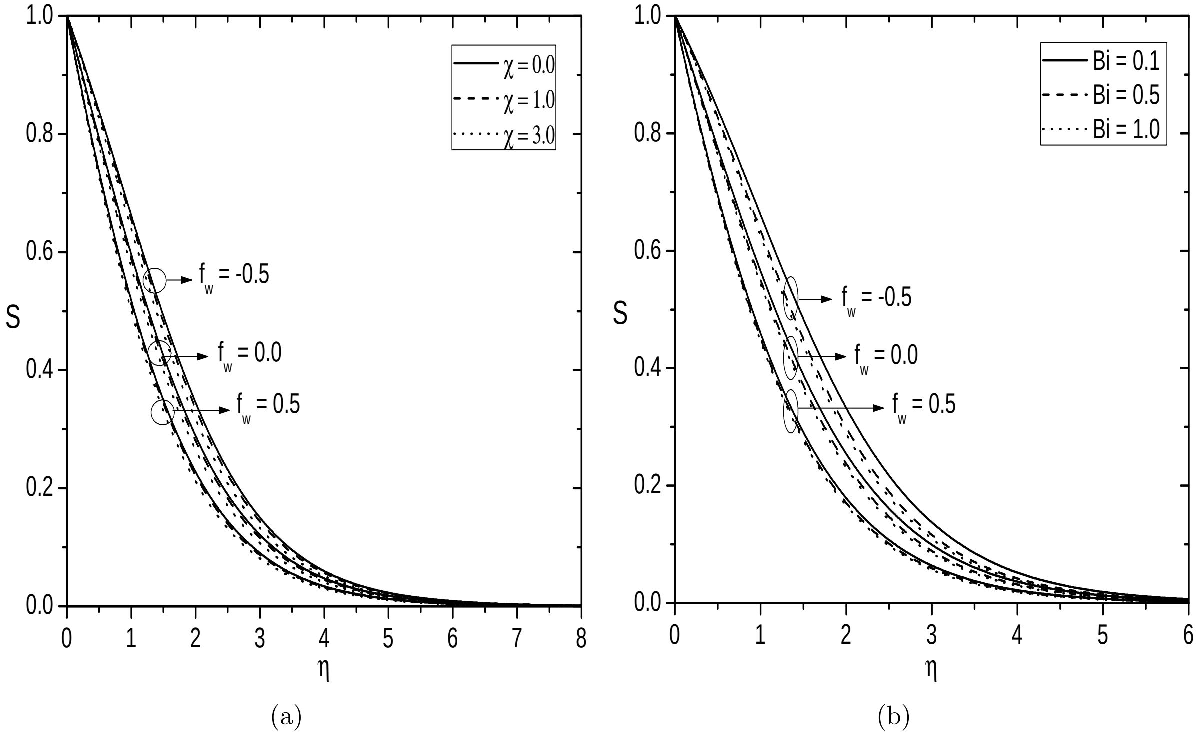

Figure 6.4: *Variations in Regular concentration under the effects of (a)* f_w *and* χ*, and (b)* f_w *and* Bi*.*

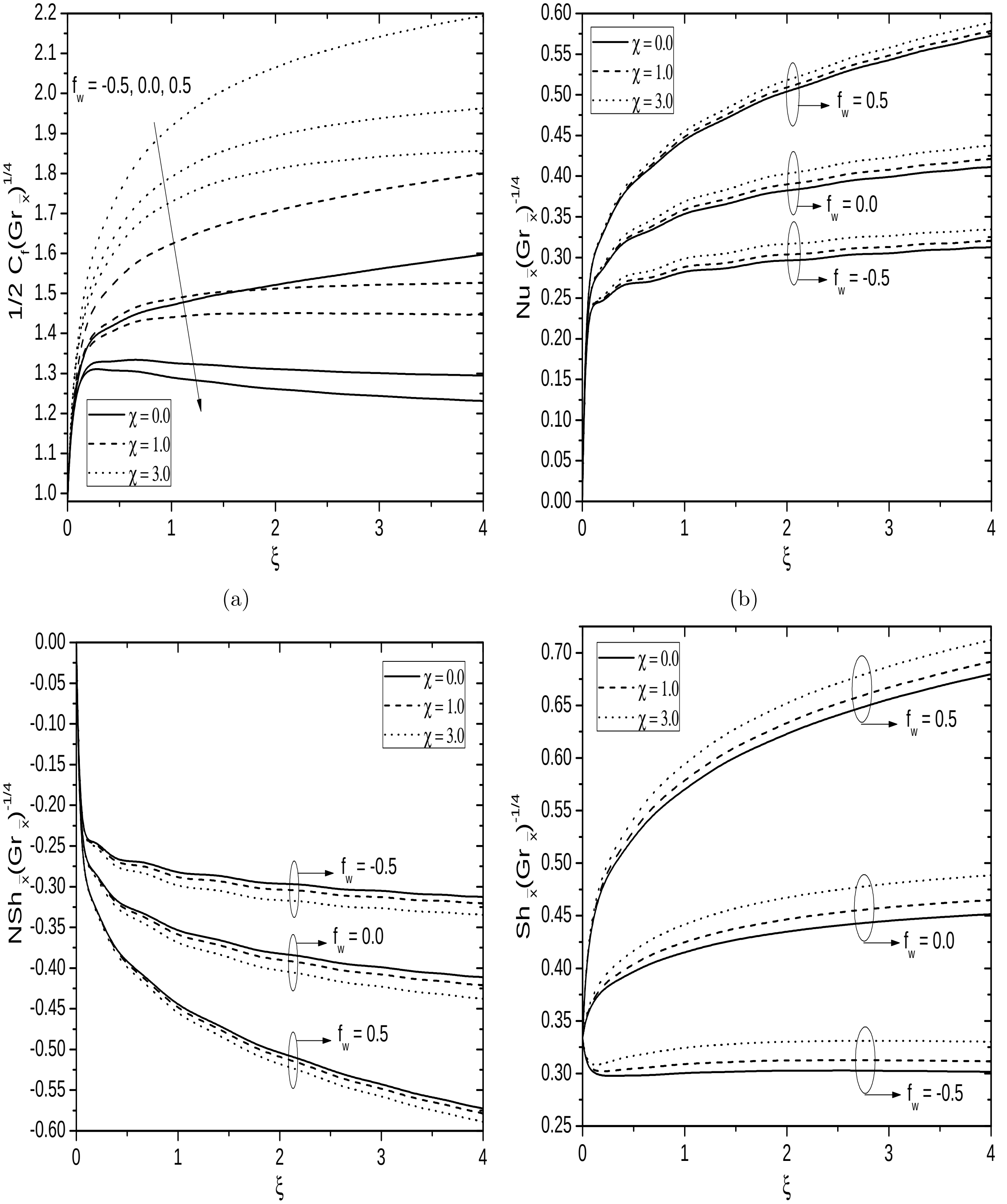

Figure 6.5: *Effects of* f_w *and* χ *on (a) Skin friction, (b) Heat transfer rate, (c) Nanoparticle mass transfer rate, and (d) Regular mass transfer rate for* $Bi = 1.0$.

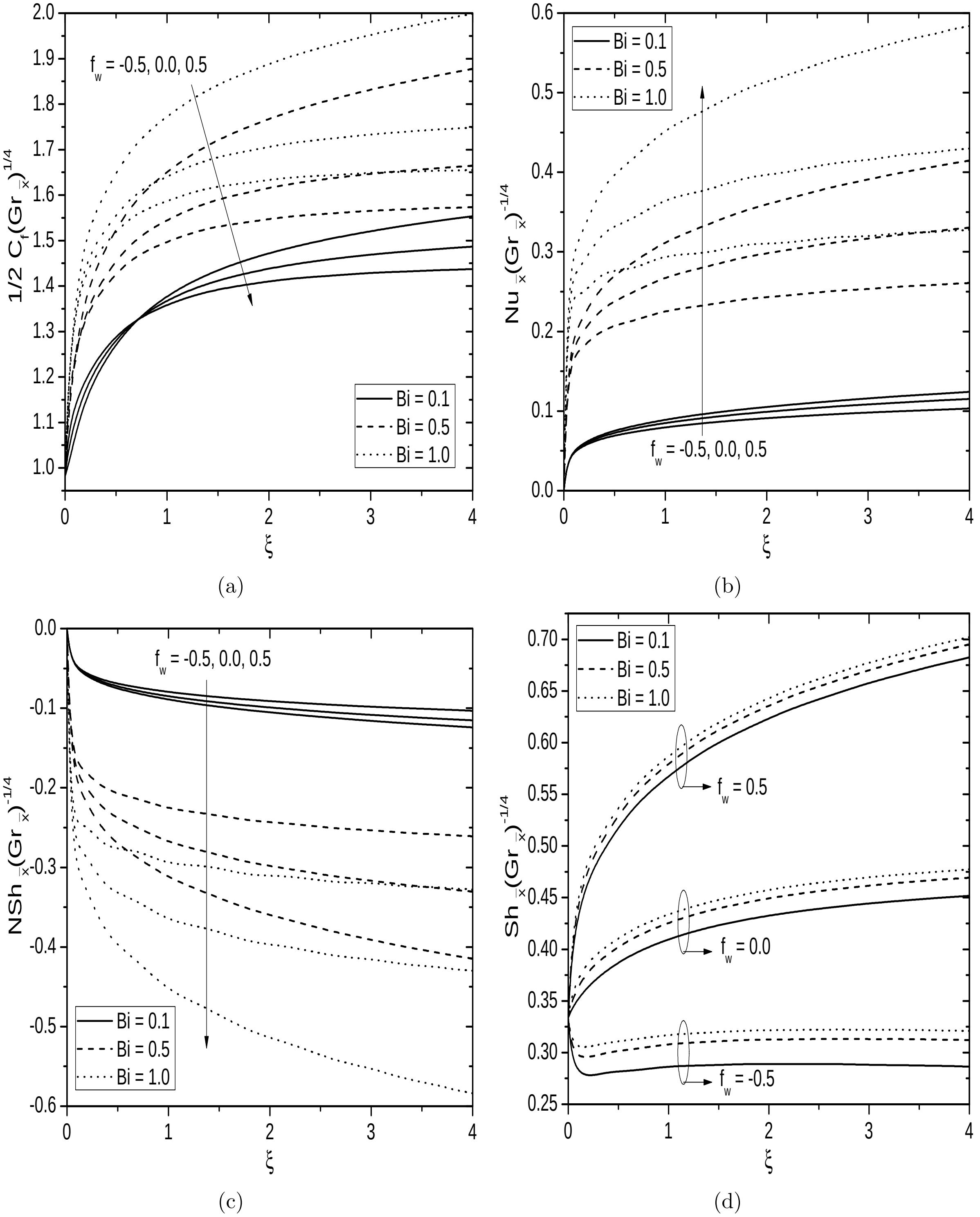

(a)

(b)

(c)

(d)

Figure 6.6: *Effects of* f_w *and* Bi *on (a) Skin friction, (b) Heat transfer rate, (c) Nanoparticle mass transfer rate, and (d) Regular mass transfer rate for* $\chi = 2.0$.

6.2.2 Case(b): Mixed Convection

Consider the flow to be mixed convection arises from buoyancy forces and an external flow with velocity U_∞. Next, introduce the following non-similarity transformations

$$\xi = \frac{x - x_0}{x_0} = \frac{\overline{x}}{x_0},\ \eta = \frac{y}{\overline{x}}\, Re_{\overline{x}}^{1/2},\ \psi = r\,\nu\, Re_{\overline{x}}^{1/2}\, f\left(\xi,\, \eta\right),\ W\left(\xi,\, \eta\right) = \frac{w}{r\,\Omega},$$

$$\theta\left(\xi,\, \eta\right) = \frac{T - T_\infty}{T_f - T_\infty},\ \gamma\left(\xi,\, \eta\right) = \frac{\phi - \phi_\infty}{\phi_\infty},\ S\left(\xi,\, \eta\right) = \frac{C - C_\infty}{C_w - C_\infty} \tag{6.17}$$

where $\overline{x} = x - x_0$ and $Re_x = \frac{U_\infty\, \overline{x}}{\nu}$ is the local Reynolds number.

Substitution of (2.7) and (6.17) into Eqs.(6.2)- (6.6) gives the following system of differential equations:

$$f''' + \left(R + \frac{1}{2}\right) f\, f'' + \chi\, \xi\, (\xi + 1)\, W^2 + \lambda\, \xi\ (\theta + Nc\, S - Nr\, \gamma) = \xi\, \left(f' \frac{\partial f'}{\partial \xi} - \frac{\partial f}{\partial \xi} f''\right) \tag{6.18}$$

$$W'' + \left(R + \frac{1}{2}\right) f\, W' - R\, f'\, W = \xi\, \left(f' \frac{\partial W}{\partial \xi} - \frac{\partial f}{\partial \xi} W'\right) \tag{6.19}$$

$$\frac{1}{Pr}\, \theta'' + \left(R + \frac{1}{2}\right) f\, \theta' + Nb\, \gamma'\, \theta' + Nt\, (\theta')^2 = \xi\, \left(f' \frac{\partial \theta}{\partial \xi} - \frac{\partial f}{\partial \xi} \theta'\right) \tag{6.20}$$

$$\frac{1}{Le}\, \gamma'' + \left(R + \frac{1}{2}\right) f\, \gamma' + \frac{1}{Le}\, \frac{Nt}{Nb}\, \theta'' = \xi\, \left(f' \frac{\partial \gamma}{\partial \xi} - \frac{\partial f}{\partial \xi} \gamma'\right) \tag{6.21}$$

$$\frac{1}{Sc}\, S'' + \left(R + \frac{1}{2}\right) f\, S' = \xi\, \left(f' \frac{\partial S}{\partial \xi} - \frac{\partial f}{\partial \xi} S'\right) \tag{6.22}$$

and the reduced boundary conditions are

$$f'(\xi, \eta) = 0,\ \xi\, \frac{\partial f}{\partial \xi} + \left(R + \frac{1}{2}\right)\ f(\xi, \eta) = \xi^{1/2}\, f_w,\ W(\xi, \eta) = 1,\ \theta'(\xi, \eta) = -Bi\, \xi^{1/2}\ [1 - \theta(\xi, \eta)]\,,$$

$$Nb\, \gamma'(\xi, \eta) + Nt\, \theta'(\xi, \eta) = 0,\ S(\xi, \eta) = 1 \quad \text{at} \quad \eta = 0 \tag{6.23a}$$

$$f'(\xi, \eta) = 1,\ W(\xi, \eta) = 0,\ \theta(\xi, \eta) = 0,\ \gamma(\xi, \eta) = 0,\ S(\xi, \eta) = 0 \quad \text{as} \quad \eta \to \infty \tag{6.23b}$$

where $\lambda = \dfrac{Gr_{x_0}}{Re_{x_0}^2}$ is the mixed convection parameter, $\chi = \dfrac{\Omega^2\, x_0^2\, \sin^2 A}{U_\infty^2}$ is the spinning parameter, $Bi = \dfrac{h_f\, x_0}{k\, Re_{x_0}^{1/2}}$ is the Biot number and $f_w = \dfrac{v_w}{U_\infty}\, Re_{x_0}^{1/2}$ is the suction/injection parameter.

The non-dimensional skin friction $C_f = \dfrac{2\,\mu}{\rho_{f\infty}\, U_\infty^2}\left[\dfrac{\partial u}{\partial y}\right]_{y=0}$, local Nusselt number $Nu_{\overline{x}} = -\dfrac{\overline{x}}{(T_f - T_\infty)}\left[\dfrac{\partial T}{\partial y}\right]_{y=0}$, local nanoparticle Sherwood number $NSh_{\overline{x}} = -\dfrac{\overline{x}}{\phi_\infty}\left[\dfrac{\partial \phi}{\partial y}\right]_{y=0}$ and local regular Sherwood number $Sh_{\overline{x}} = -\dfrac{\overline{x}}{(C_w - C_\infty)}\left[\dfrac{\partial C}{\partial y}\right]_{y=0}$, are given by

$$\left.\begin{aligned} \frac{1}{2}\, C_f\, Re_{\overline{x}}^{1/2} = f''(\xi,\, 0),\ \frac{Nu_{\overline{x}}}{Re_{\overline{x}}^{1/2}} = -\theta'(\xi,\, 0),\\ \frac{NSh_{\overline{x}}}{Re_{\overline{x}}^{1/2}} = -\gamma'(\xi,\, 0),\ \frac{Sh_{\overline{x}}}{Re_{\overline{x}}^{1/2}} = -S'(\xi,\, 0) \end{aligned}\right\} \tag{6.24}$$

Results and Discussion

The reduced non-dimensional partial differential equations (6.18)-(6.22) along with the boundary conditions (6.23) are solved numerically using the Bivariate Pseudo-Spectral Local Linearization Method, as explained in the previous chapters. In order to assess the generated code, for special case of $\chi = 0.0$, $f_w = 0.0$, $Bi \to \infty$ and $\xi = 0$, the present results have been compared with those of Lloyd and Sparrow [56] and the results are in a good agreement [see Tab. 2.2]. To explore the effects of suction/injection parameter (f_w), spinning parameter (χ), Biot number (Bi) and mixed convection parameter (λ), the computations have been carried out for $Pr = 1.0, Nr = 0.5, Nc = 1.0, Nt = 0.2, Nb = 0.2, Sc = 0.6$ and $Le = 10.0$.

The first set of Figs. 6.7(a)-6.7(d) depict the effect of spinning parameter (χ) on the non-dimensional tangential velocity f', swirl velocity W, temperature θ and nanoparticle volume fraction γ, for both aiding and opposing flows. An increase in the spinning parameter, i.e., the higher rotation of the frustum of a cone, significantly increases the tangential velocity, for both opposing and aiding flow cases. This is due to more induced axial flow caused by more rotation of the frustum of a cone. In both opposing and aiding flows, the swirl velocity and temperature decrease with an increase in the spinning parameter. But, the nanoparticle volume fraction increases for both opposing and aiding flows. It is also noted that the tangential velocity and nanoparticle volume fraction are higher in the case of aiding flow, when compared to the case of opposing flow. Whereas, an opposite behavior is observed in the swirl velocity and temperature.

The second set of Figs. 6.8(a)-6.8(d) are prepared to examine the effect of suction/injection parameter (f_w) on the tangential velocity f', swirl velocity W, temperature θ and nanoparticle volume fraction γ, for both the cases of aiding flow ($\lambda = 0.5$) and opposing flow ($\lambda = -0.5$). The higher tangential velocity is observed in the suction case when compared to the impermeability and injection cases, for both aiding and opposing flows, as shown in Fig. 6.8(a). It is seen from Figs. 6.8(b) and 6.8(c) that the swirl velocity and temperature reduces with the enhancement of f_w. It is also noted that the nanoparticle volume fraction shows a reverse trend, as plotted in Fig. 6.8(d). Moreover, it is clear that the higher values of the tangential velocity and nanoparticle volume fraction are observed in the case of aiding flow, whereas the higher values of the swirl velocity and temperature are noticed in the case of opposing flow.

For both the cases of aiding flow ($\lambda = 0.5$) and opposing flow ($\lambda = -0.5$), the influence of Biot number (Bi) on the tangential velocity f', swirl velocity W, temperature θ and nanoparticle volume fraction γ, are depicted in the third set of Figs. 6.9(a)-6.9(d). With an increase in the Biot number, the tangential velocity increases for aiding flow case, and decreases for opposing flow case, as plotted in Fig. 6.9(a). But, opposite results are noticed for the swirl velocity with an increase in the Biot number. The higher values of the Biot number (strong convection) leads to a higher temperature and consequently enhance the temperature for both aiding and opposing flows. When $Bi \gg 1$, the temperature reaches its maximum value as a result of uniform wall temperature condition. It is also noticed that the nanoparticle volume fraction decreases near to the solid surface and increases far away from the surface with an increase of Bi. Further, the values of tangential velocity and nanoparticle volume fraction are more in the aiding flow in comparison with those of the opposing flow, whereas the swirl velocity and temperature show a reverse behavior.

The influence of mixed convection parameter (λ) on the regular concentration for various values of χ, f_w and Bi, is shown in Figs. 6.10(a)-6.10(c). With the increase of χ and f_w, the regular concentration decreases in both the cases of aiding and opposing flows. However, the regular concentration increases for opposing flow, but it decreases for aiding flow, with an increase of Bi. Further, the regular concentration is more in the opposing flow case when compared to that of the aiding flow case.

The next set of Figs. 6.11(a)-6.11(d) are prepared to explore the influence of spinning parameter (χ) on the surface drag $[f''(\xi,0)]$, local Nusselt number $[-\theta'(\xi,0)]$, local nanoparticle Sherwood number $[-\gamma'(\xi,0)]$ and local regular Sherwood number $[-S'(\xi,0)]$, for both aiding and opposing flow situations. Here, $\chi = 0$ represents the stationary surface, whereas $\chi \neq 0$ represents the rotational surface. It is evident from Fig. 6.11(a) that the drag coefficient substantially increases with an increase in the spinning parameter, for both the cases of aiding and opposing flows. But, more surface drag is found in the case of aiding flow. For both the aiding and opposing flows, the local Nusselt and regular Sherwood numbers increase with higher values of the spinning parameter, as depicted in Figs. 6.11(b) and 6.11(d). Also, a rapid increase in the local Nusselt and regular Sherwood numbers are observed in the case of aiding flow. Furthermore, the local nanoparticle Sherwood number diminishes in both the cases of aiding and opposing flows with an increase of the spinning parameter.

The effects of mixed convection parameter (λ) and suction/injection parameter (f_w) on the dimensionless surface drag $[f''(\xi,0)]$, local Nusselt number $[-\theta'(\xi,0)]$, local nanoparticle Sherwood number $[-\gamma'(\xi,0)]$ and local regular Sherwood number $[-S'(\xi,0)]$ over the streamwise coordinate, are shown in Figs. 6.12(a)-6.12(d). It is observed that the surface drag increases in the case of opposing flow, but it decreases in the case of aiding flow with an increase in the suction/injection parameter, as plotted in Fig. 6.12(a). Figure 6.12(b) reveals that the local Nusselt number enhances with the enhancement of suction/injection parameter, and also more heat transfer rate is observed in the case of suction. But, the local nanoparticle Sherwood number diminishes and local regular Sherwood number enhances with enhancing values of the suction/injection parameter. Further, the surface drag, local Nusselt and regular Sherwood numbers are found to be large in the aiding flow case when compared to those of the opposing flow case.

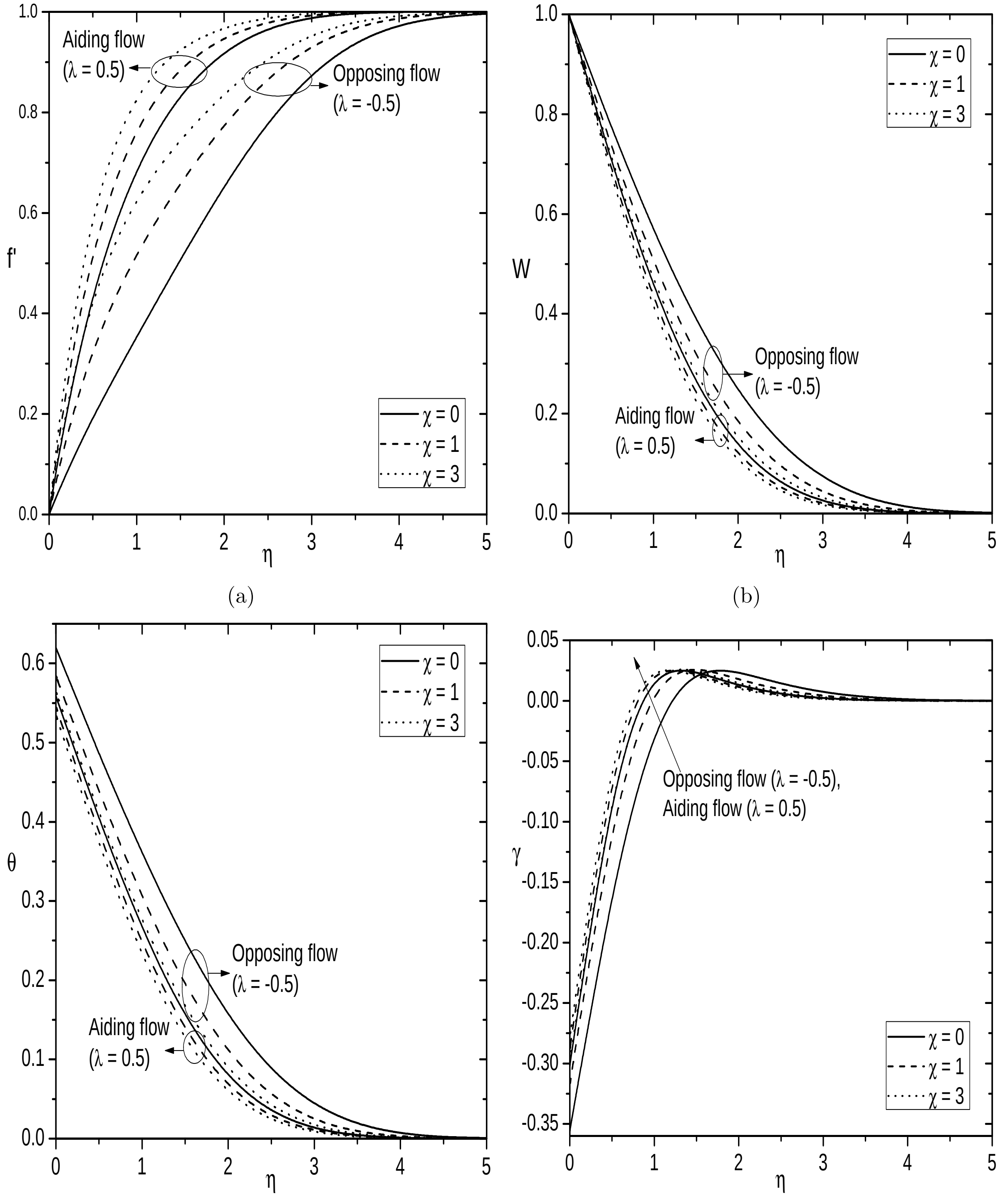

(a) (b) (c) (d)

Figure 6.7: *Effects of* λ *and* χ *on (a) Tangential velocity, (b) Swirl velocity, (c) Temperature, (d) Nanoparticle volume fraction, and (e) Regular concentration for* $f_w = 0.0$ *and* $Bi = 1.0$.

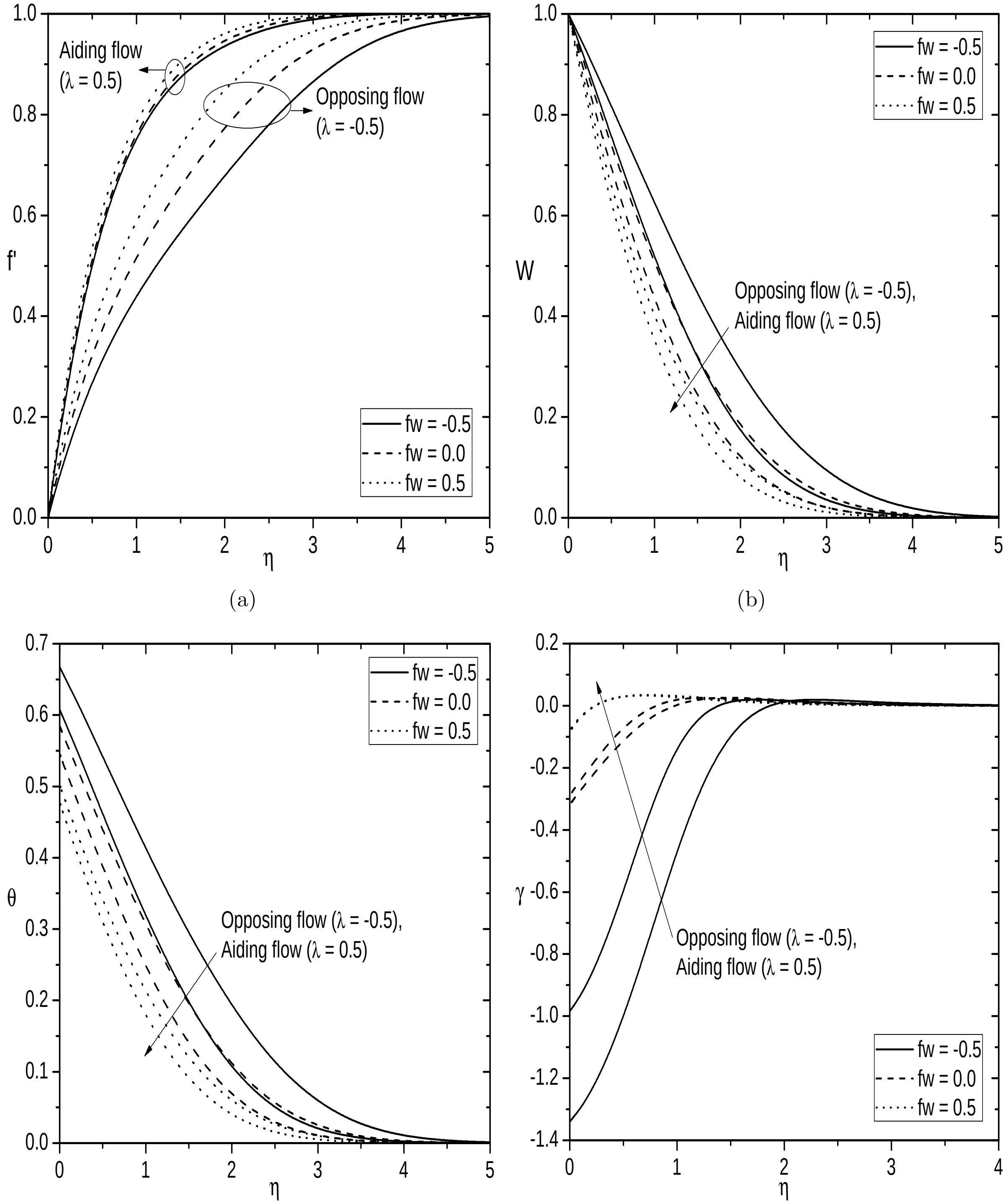

(a) (b)

(c) (d)

Figure 6.8: *Effects of* λ *and* f_w *on (a) Tangential velocity, (b) Swirl velocity, (c) Temperature, (d) Nanoparticle volume fraction, and (e) Regular concentration for* $\chi = 2.0$ *and* $Bi = 1.0$.

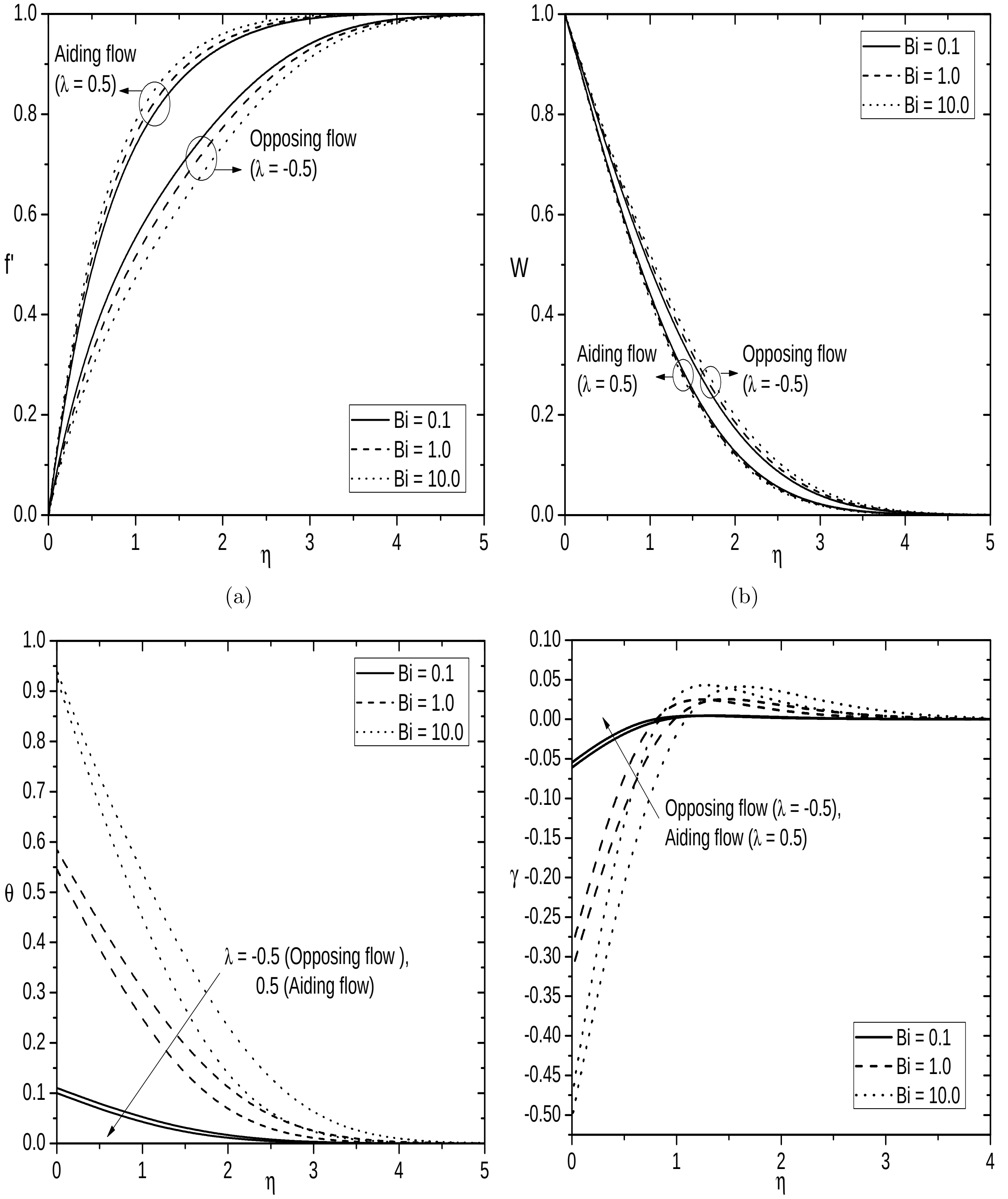

(a)

(b)

(c)

(d)

Figure 6.9: *Effects of* λ *and* Bi *on (a) Tangential velocity, (b) Swirl velocity, (c) Temperature, (d) Nanoparticle volume fraction, and (e) Regular concentration for* $\chi = 2.0$ *and* $f_w = 0.0$.

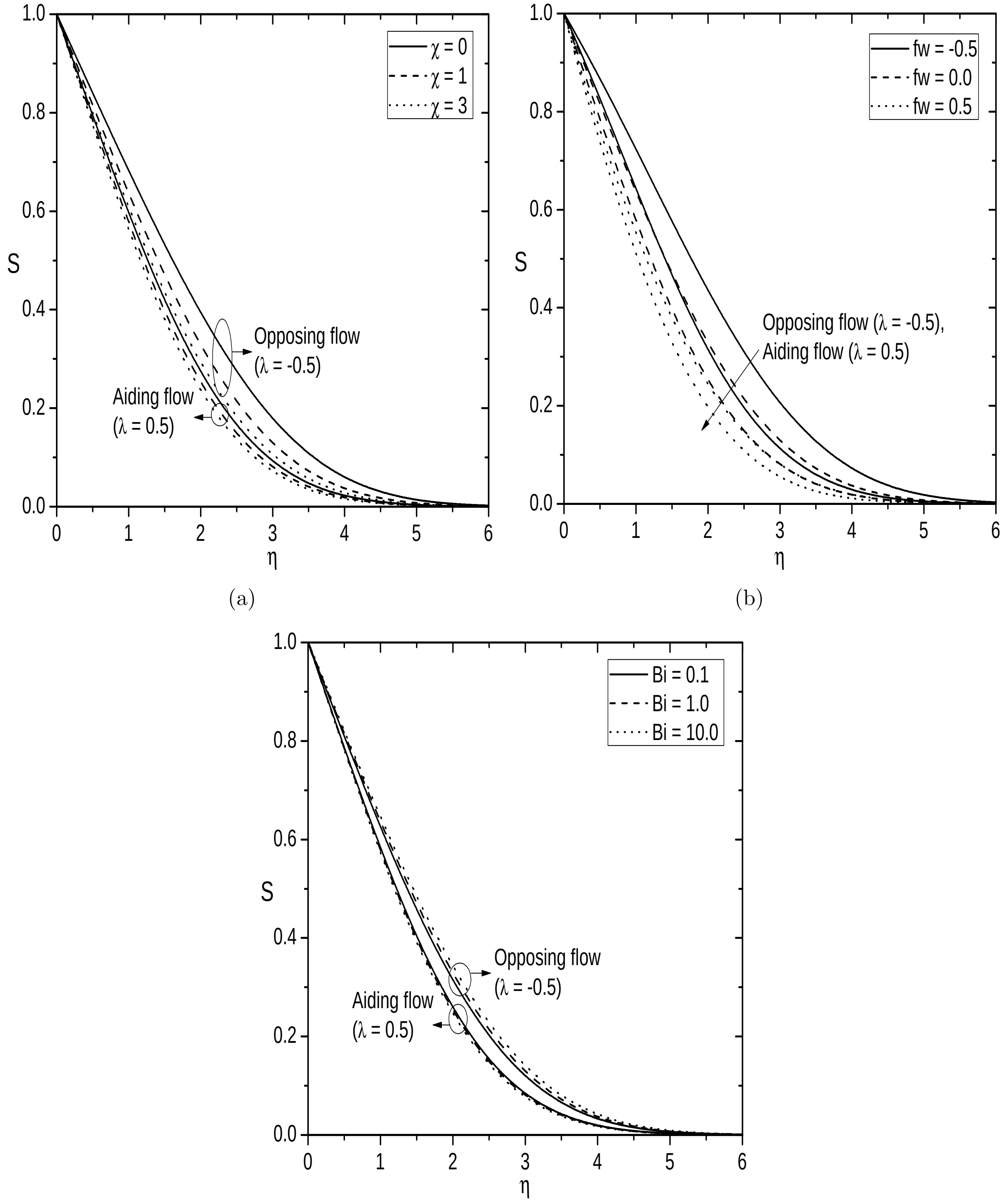

(a)

(b)

(c)

Figure 6.10: *Variations in Regular concentration under the effects of (a) λ and χ, (b) λ and f_w, and (c) λ and Bi.*

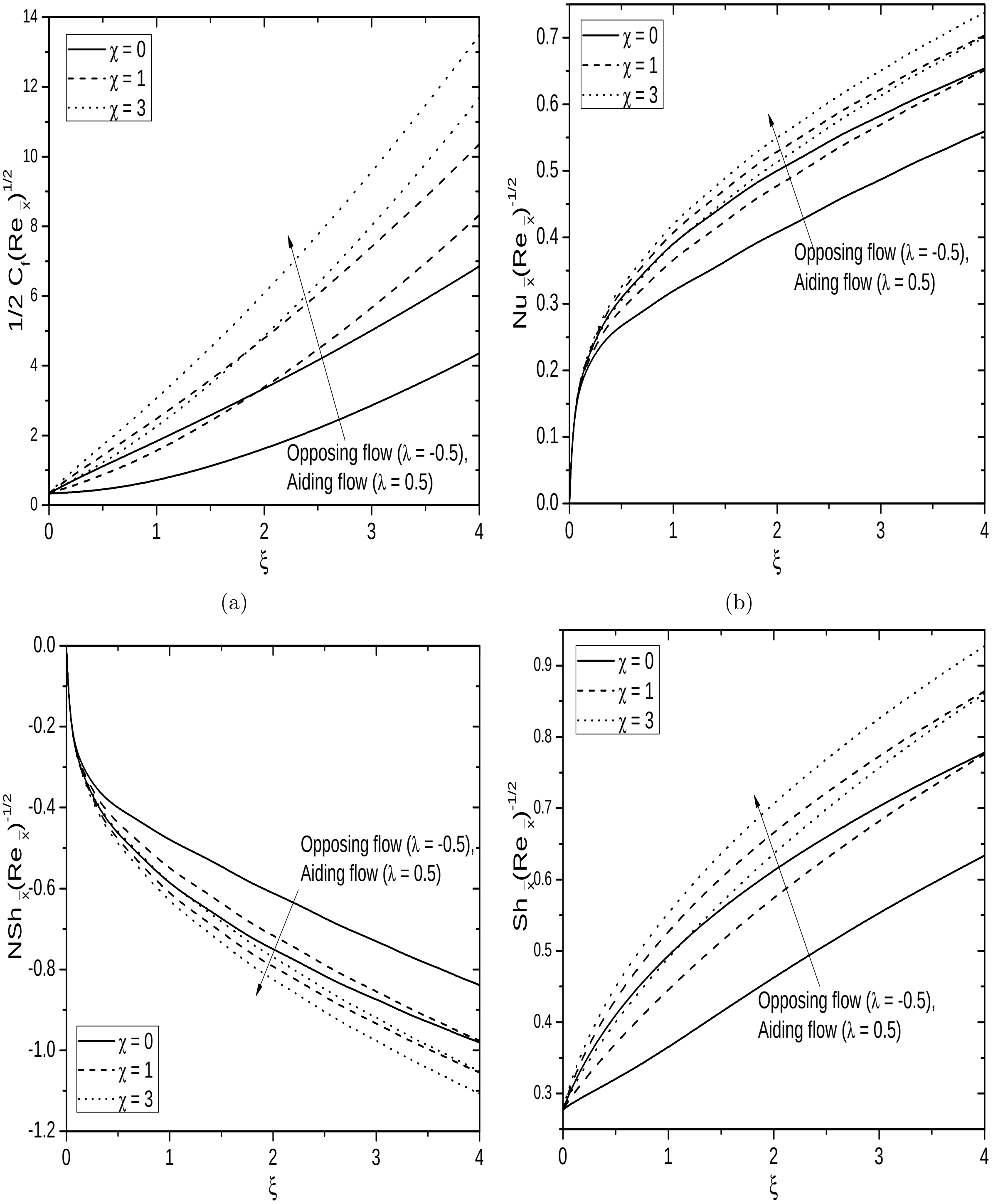

(a)

(b)

(c)

(d)

Figure 6.11: *Effects of* λ *and* χ *on (a) Skin friction, (b) Heat transfer rate, (c) Nanoparticle mass transfer rate, and (d) Regular mass transfer rate for* $f_w = 0.0$ *and* $Bi = 1.0$.

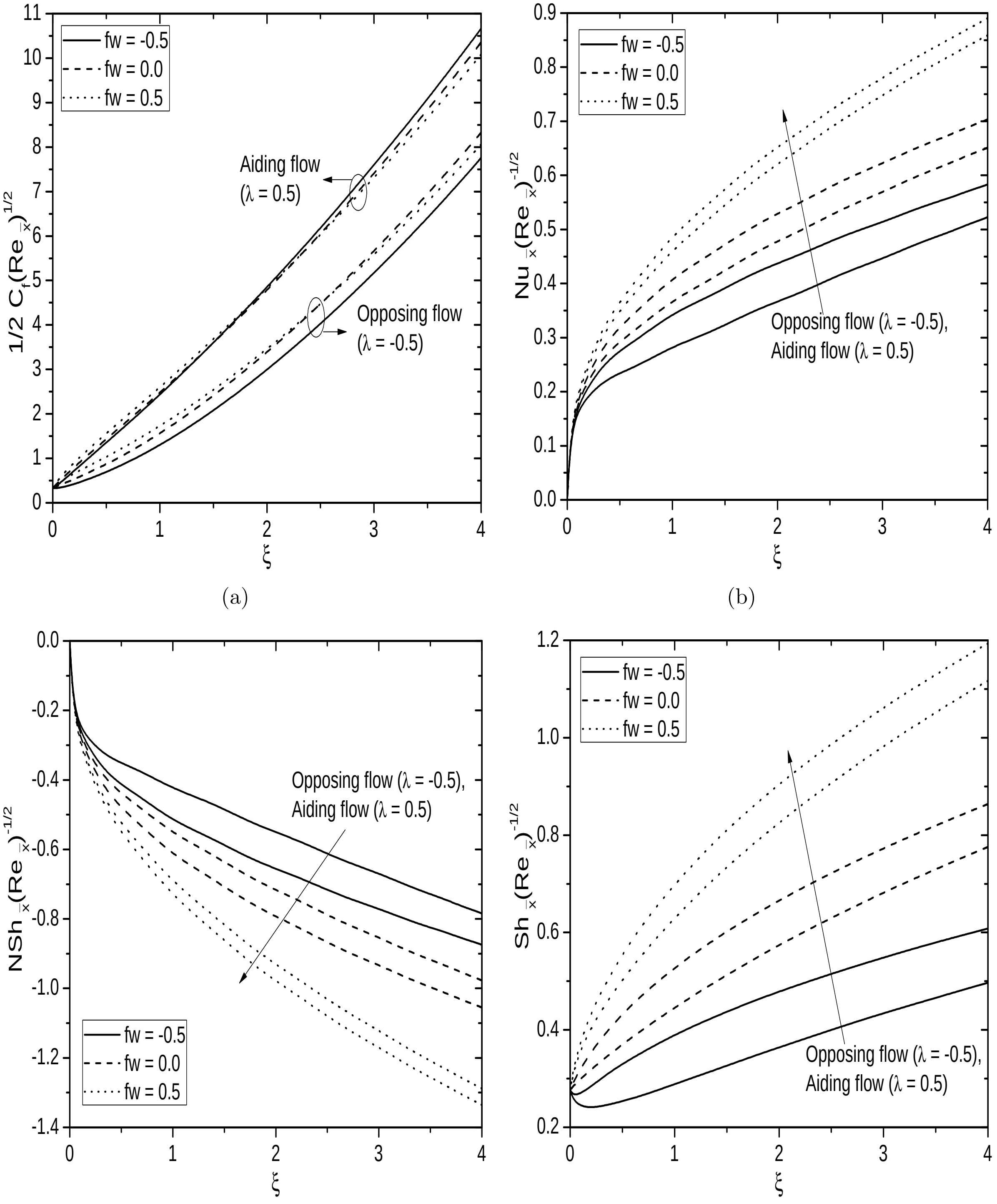

(a) (b)

(c) (d)

Figure 6.12: *Effects of* λ *and* f_w *on (a) Skin friction, (b) Heat transfer rate, (c) Nanoparticle mass transfer rate, and (d) Regular mass transfer rate for* $\chi = 2.0$ *and* $Bi = 1.0$.

6.3 Conclusions

In this chapter, the non-similarity solution is obtained to analyze the effects of suction/injection and convective boundary condition on the convective flow of a nanofluid over the vertically rotating frustum of a cone. From this analysis, the main findings are drawn in both cases (a) and (b) as follows:

An increase in spinning parameter leads to increases the nanoparticle volume fraction, skin friction, local Nusselt and regular Sherwood numbers, but decreases the swirl velocity, temperature, regular concentration and local nanoparticle Sherwood number. Further, the tangential velocity increases in case (a) and case (b), but it shows opposite trend in case (a) far away from the frustum of a cone. With the increase of Biot number, the tangential velocity, temperature, local Nusselt and regular Sherwood numbers enhance, but the swirl velocity, nanoparticle volume fraction, regular concentration, local nanoparticle Sherwood number reduce in case (a). An opposite behavior is noticed in the opposing flow of case (b). As the suction/injection parameter increases, the swirl velocity, temperature, regular concentration and local nanoparticle Sherwood number reduce, but the nanoparticle volume fraction, local Nusselt and regular Sherwood numbers enhance. In addition, the tangential velocity and surface drag decrease in the case (a), while these show a reverse trend in the case (b). Moreover, the higher Nusselt and regular Sherwood numbers are found for the suction case when compared to those of the injection and impermeable cases. Finally, it is noticed that the tangential velocity, nanoparticle volume fraction, surface drag, Nusselt and regular Sherwood numbers are more in the aiding flow when compared to the opposing flow of case (b).

Chapter 7

Nonlinear Convective Flow of a Nanofluid over the Permeable Wavy Frustum of a Cone with Convective Boundary Condition [1]

7.1 Introduction

Most of the theoretical and numerical studies on the convective heat and mass transfer deal with the flat surface and/or uniform surface. Further, the study of convective transport on the irregular wavy surfaces has received significant attention due to its emerging heat and mass transfer applications. In view of the engineering and industrial applications, the effects of temperature dependent viscosity and uniform surface heat flux on natural convective flow over the vertical wavy cone, have been investigated by Rahman *et al.* [97]. Siddiqa *et al.* [112] obtained the numerical solution for the natural convective flow of a two-phase dusty nanofluid over the vertical wavy frustum of a cone.

---

[1] Case(a): Published in "**Journal of Nanofluids**" 7 (2018) 1258–1271, Case(b): Communicated to "**International Journal of Numerical Methods for Heat & Fluid Flow**"

The analysis of nonlinear convection (i.e., may be treated as the nonlinear relationship between the density, temperature and concentration) is of great interest owing to their numerous applications such as cooling of electronic components, pore water convection near salt domes, etc. Very few researchers have aimed at this point and tried to explore various aspects on the fluid flows in this direction. Kameswaran *et al.* [47] analyzed the effects of nonlinear Boussinesq approximation and convective boundary condition on the mixed convective flow of a thermally stratified nanofluid over the vertical wavy surface in a non-Darcy porous medium. The combined effects of radiation and nonlinear convection on a three dimensional thermal boundary layer flow of a nanfluid over the stretching sheet have been addressed by Mahanthesh *et al.* [57] (For more details, see the citations therein).

The objective of this chapter is to examine the influence of nonlinear Boussinesq approximation on convective flow of a nanofluid over the permeable wavy frustum of a cone in the presence of convective boundary condition. As in the previous chapter, here also, the Bivariate Pseudo-Spectral Local Linearization Method is employed to solve the system of reduced non-linear partial differential equations. The effects of various physical parameters on the dimensionless velocity, temperature, nanoparticle volume fraction, regular concentration along with the skin friction, heat and mass transfer rates are displayed through graphs and the salient features are discussed.

7.2 Mathematical Formulation

A steady, laminar and two-dimensional convective flow of an incompressible nanofluid over the wavy frustum of a cone with transverse sinusoidal waves of characteristic length $2L$ and amplitude a, is considered in this chapter. Choose the coordinate system such that the x-axis is taken along the surface of the wavy frustum of a cone and y-axis is measured normal to it, with the origin O at the vertex of a full cone, as shown in Fig. (7.1). The wavy surface profile of the frustum of a cone is characterized by

$$y_w = \sigma(\overline{x}) = a \left(\frac{\pi \left(x - x_0\right)}{L} \right) \tag{7.1}$$

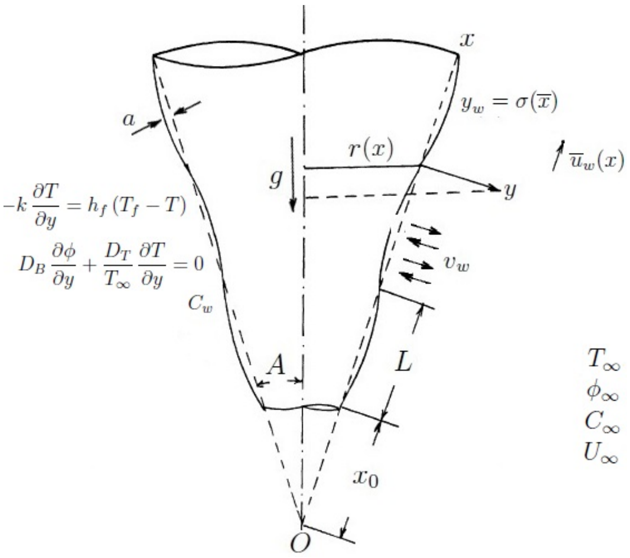

Figure 7.1: *Physical model of the problem*

where x_0 is the height of frustum of a cone. Assume that the regular concentration near to wavy surface is C_w. The temperature, nanoparticle volume fraction and regular concentration at ambient medium are assumed to be T_∞, ϕ_∞ and C_∞, respectively. Due to the convective boundary condition, the wavy surface is to be heated for $T_f > T_\infty$ or cooled for $T_f < T_\infty$ in which T_f is the nanofluid temperature.

Following the above assumptions and nonlinear Oberbeck-Boussinesq approximations, the basic governing equations are given by

$$\frac{\partial(r\,u)}{\partial x} + \frac{\partial(r\,v)}{\partial y} = 0 \tag{7.2}$$

$$\begin{aligned}\rho_{f\infty}\left(u\,\frac{\partial u}{\partial x} + v\,\frac{\partial u}{\partial y}\right) = -\frac{\partial p}{\partial x} + \mu\,\nabla^2 u + \rho_{f\infty}\,g\,(1-\phi_\infty)\Big[\beta_T\,(T-T_\infty) + \beta_{TT}\,(T-T_\infty)^2 \\ + \beta_C\,(C-C_\infty) + \beta_{CC}\,(C-C_\infty)^2\Big]\cos A - (\rho_p - \rho_{f\infty})\,g\,(\phi-\phi_\infty)\cos A\end{aligned} \tag{7.3}$$

$$\rho_{f_\infty}\left(u\,\frac{\partial v}{\partial x}+v\,\frac{\partial v}{\partial y}\right)=-\frac{\partial p}{\partial y}+\mu\,\nabla^2 v-\rho_{f_\infty}\,g\,(1-\phi_\infty)\,\Big[\beta_T\,(T-T_\infty)+\beta_{TT}\,(T-T_\infty)^2 \\ +\beta_C\,(C-C_\infty)+\beta_{CC}\,(C-C_\infty)^2\Big]\sin A \tag{7.4}$$

$$u\,\frac{\partial T}{\partial x}+v\,\frac{\partial T}{\partial y}=\alpha_m\,\nabla^2 T+\mathcal{J}\,\left[D_B\,\nabla\phi\cdot\nabla T+\frac{D_T}{T_\infty}\,\nabla T\cdot\nabla T\right] \tag{7.5}$$

$$u\,\frac{\partial \phi}{\partial x}+v\,\frac{\partial \phi}{\partial y}=D_B\,\nabla^2\phi+\frac{D_T}{T_\infty}\,\nabla^2 T \tag{7.6}$$

$$u\,\frac{\partial C}{\partial x}+v\,\frac{\partial C}{\partial y}=D_S\,\nabla^2 C \tag{7.7}$$

where ∇^2 is the Laplacian operator, p is the pressure, β_T and β_{TT} are the first and second order thermal expansion coefficients, and β_C and β_{CC} are the first and second order solutal expansion coefficients, respectively.

The associated boundary conditions are

$$u=0,\;\; v=v_w,\;\; -k\,\frac{\partial T}{\partial y}=h_f\,(T_f-T),\;\; D_B\,\frac{\partial \phi}{\partial y}+\frac{D_T}{T_\infty}\,\frac{\partial T}{\partial y}=0,\;\; C=C_w\;\;\text{at}\;\; y=0 \tag{7.8a}$$

$$u=u_w(\overline{x}),\;\; T=T_\infty,\;\; \phi=\phi_\infty,\;\; C=C_\infty\;\;\text{as}\;\; y\to\infty \tag{7.8b}$$

In this chapter also, two types (cases) of problems are considered: (a) free/natural convection and (b) mixed convection.

7.2.1 Case(a): Natural Convection

The flow is assumed to be a natural convection which is caused by buoyancy forces only without any external agent and hence, the velocity of the external flow becomes zero. We introduce the following non-similarity transformations

$$\widetilde{x}=\frac{x-x_0}{L}=\frac{\overline{x}}{L},\; \widetilde{y}=\frac{y-\sigma(\overline{x})}{L}\,Gr^{1/4},\; \widetilde{\psi}=\frac{\psi}{u_e\,L^2}\,Gr^{1/4},\; \widetilde{T}=\frac{T-T_\infty}{T_f-T_\infty},\; \widetilde{\phi}=\frac{\phi-\phi_\infty}{\phi_\infty},$$

$$\widetilde{C}=\frac{C-C_\infty}{C_w-C_\infty},\; \widetilde{p}=\frac{p-p_\infty}{\rho\,u_e^2},\; \widetilde{r}=\frac{r}{L},\; \widetilde{a}=\frac{a}{L},\; \widetilde{x}_0=\frac{x_0}{L} \tag{7.9}$$

where $u_e^2 = g\,L\,\beta_T\,(T_f - T_\infty)\,(1-\phi_\infty)\cos A$ and $Gr^{1/2} = \dfrac{u_e\,L}{\nu}$.

Here, we assumed that the width of the boundary layers is very small as a contrast with the local radius of the flat frustum of a cone. Hence, the local radius to a point in the boundary layer is approximated to the radius of a flat cone. Also, it is assumed that the Grashof number (Gr) is very large and hence the natural convection happens only inside the boundary layer whose width is significantly smaller than the amplitude of the wavy frustum of a cone.

Substituting Eq. (2.7) and Eq. (7.9) into Eqs.(7.3)-(7.7) and letting $Gr \to \infty$ (i.e., boundary layer approximation), the flow governing equations reduce to the following form

$$\frac{1}{\widetilde{r}^2}\left[\frac{\partial \widetilde{\psi}}{\partial \widetilde{y}}\,\frac{\partial^2 \widetilde{\psi}}{\partial \widetilde{x}\partial \widetilde{y}} - \frac{\widetilde{r}_{\widetilde{x}}}{\widetilde{r}}\left(\frac{\partial \widetilde{\psi}}{\partial \widetilde{y}}\right)^2 - \frac{\partial \widetilde{\psi}}{\partial \widetilde{x}}\,\frac{\partial^2 \widetilde{\psi}}{\partial \widetilde{y}^2}\right] = -\frac{\partial \widetilde{p}}{\partial \widetilde{x}} + Gr^{1/4}\,\sigma_{\widetilde{x}}\,\frac{\partial \widetilde{p}}{\partial \widetilde{y}} + \frac{1}{\widetilde{r}}\,(1+\sigma_{\widetilde{x}}^2)\,\frac{\partial^3 \widetilde{\psi}}{\partial \widetilde{y}^3}$$
$$+\left[(1+\lambda_1\,\widetilde{T})\widetilde{T} + Nc\,(1+\lambda_2\,\widetilde{C})\widetilde{C}\right] - Nr\,\widetilde{\phi} \quad (7.10)$$

$$\frac{1}{\widetilde{r}^2}\left[\sigma_{\widetilde{x}}\left(\frac{\partial \widetilde{\psi}}{\partial \widetilde{x}}\frac{\partial^2 \widetilde{\psi}}{\partial \widetilde{y}^2} - \frac{\partial \widetilde{\psi}}{\partial \widetilde{y}}\,\frac{\partial^2 \widetilde{\psi}}{\partial \widetilde{x}\partial \widetilde{y}}\right) - \sigma_{\widetilde{x}\widetilde{x}}\left(\frac{\partial \widetilde{\psi}}{\partial \widetilde{y}}\right)^2\right] + \frac{\widetilde{r}_{\widetilde{x}}}{\widetilde{r}^3}\,\sigma_{\widetilde{x}}\left(\frac{\partial \widetilde{\psi}}{\partial \widetilde{y}}\right)^2 = Gr^{1/4}\,\frac{\partial \widetilde{p}}{\partial \widetilde{y}}$$
$$-\frac{\sigma_{\widetilde{x}}}{\widetilde{r}}\,(1+\sigma_{\widetilde{x}}^2)\,\frac{\partial^3 \widetilde{\psi}}{\partial \widetilde{y}^3} + \left[(1+\lambda_1\,\widetilde{T})\widetilde{T} + Nc\,(1+\lambda_2\,\widetilde{C})\widetilde{C}\right]\tan A \qquad (7.11)$$

$$\frac{1}{\widetilde{r}}\left[\frac{\partial \widetilde{\psi}}{\partial \widetilde{y}}\,\frac{\partial \widetilde{T}}{\partial \widetilde{x}} - \frac{\partial \widetilde{\psi}}{\partial \widetilde{x}}\,\frac{\partial \widetilde{T}}{\partial \widetilde{y}}\right] = (1+\sigma_{\widetilde{x}}^2)\left[\frac{1}{Pr}\,\frac{\partial^2 \widetilde{T}}{\partial \widetilde{y}^2} + Nb\,\frac{\partial \widetilde{T}}{\partial \widetilde{y}}\,\frac{\partial \widetilde{\phi}}{\partial \widetilde{y}} + Nt\left(\frac{\partial \widetilde{T}}{\partial \widetilde{y}}\right)^2\right] \qquad (7.12)$$

$$\frac{1}{\widetilde{r}}\left[\frac{\partial \widetilde{\psi}}{\partial \widetilde{y}}\,\frac{\partial \widetilde{\phi}}{\partial \widetilde{x}} - \frac{\partial \widetilde{\psi}}{\partial \widetilde{x}}\,\frac{\partial \widetilde{\phi}}{\partial \widetilde{y}}\right] = (1+\sigma_{\widetilde{x}}^2)\left[\frac{1}{Le}\,\frac{\partial^2 \widetilde{\phi}}{\partial \widetilde{y}^2} + \frac{1}{Le}\,\frac{Nt}{Nb}\,\frac{\partial^2 \widetilde{T}}{\partial \widetilde{y}^2}\right] \qquad (7.13)$$

$$\frac{1}{\widetilde{r}}\left[\frac{\partial \widetilde{\psi}}{\partial \widetilde{y}}\,\frac{\partial \widetilde{C}}{\partial \widetilde{x}} - \frac{\partial \widetilde{\psi}}{\partial \widetilde{x}}\,\frac{\partial \widetilde{C}}{\partial \widetilde{y}}\right] = (1+\sigma_{\widetilde{x}}^2)\left[\frac{1}{Sc}\,\frac{\partial^2\,\widetilde{C}}{\partial \widetilde{y}^2}\right] \qquad (7.14)$$

along with the boundary conditions

$$\frac{\partial \widetilde{\psi}}{\partial \widetilde{y}} = 0,\ \frac{1}{\widetilde{r}}\frac{\partial \widetilde{\psi}}{\partial \widetilde{x}} = f_w,\ \frac{\partial \widetilde{T}}{\partial \widetilde{y}} = -Bi\,(1-\widetilde{T}),\ Nb\,\frac{\partial \widetilde{\phi}}{\partial \widetilde{y}} + Nt\,\frac{\partial \widetilde{T}}{\partial \widetilde{y}} = 0,\ \widetilde{C} = 1 \ \text{ at } \ \widetilde{y} = 0 \quad (7.15a)$$

$$\frac{\partial \widetilde{\psi}}{\partial \widetilde{y}} = 0,\ \widetilde{T} = 0,\ \widetilde{\phi} = 0,\ \widetilde{C} = 0,\ \widetilde{p} = 0 \ \text{ as } \ \widetilde{y} \to \infty \quad (7.15b)$$

where $\lambda_1 = \dfrac{\beta_{TT}\,(T_f - T_\infty)}{\beta_T}$ and $\lambda_2 = \dfrac{\beta_{CC}(\overline{C}_w - \overline{C}_\infty)}{\beta_C}$ are the nonlinear density temperature parameter (NDT) and nonlinear density concentration parameter (NDC), respectively. Further, $f_w = -\frac{v_w}{u_e}\,Gr^{1/4}$ is the suction/injection parameter with $f_w < 0$ for injection, $f_w > 0$ for suction, and $f_w = 0$ for impermeable surface.

From the Eq. (7.11), it is seen that the order of the term $\frac{\partial \widetilde{p}}{\partial \widetilde{y}}$ is $O(Gr^{-1/4})$. Therefore, the least order of $\frac{\partial \widetilde{p}}{\partial \widetilde{x}}$ can be evaluated from the solution of inviscid flow case. But, this pressure gradient is zero for the problem under consideration. On eliminating the term $\frac{\partial \widetilde{p}}{\partial \widetilde{y}}$ from Eqs. (7.10) and (7.11), we get

$$\frac{1}{\widetilde{r}^2}\left[\left(\frac{\partial \widetilde{\psi}}{\partial \widetilde{y}}\frac{\partial^2 \widetilde{\psi}}{\partial \widetilde{x}\partial \widetilde{y}} - \frac{\partial \widetilde{\psi}}{\partial \widetilde{x}}\frac{\partial^2 \widetilde{\psi}}{\partial \widetilde{y}^2}\right) - \frac{\widetilde{r}_{\widetilde{x}}}{\widetilde{r}}\left(\frac{\partial \widetilde{\psi}}{\partial \widetilde{y}}\right)^2 + \frac{\sigma_{\widetilde{x}}\sigma_{\widetilde{x}\widetilde{x}}}{1+\sigma_{\widetilde{x}}^2}\left(\frac{\partial \widetilde{\psi}}{\partial \widetilde{y}}\right)^2\right] = \frac{1}{\widetilde{r}}\,(1+\sigma_{\widetilde{x}}^2)\,\frac{\partial^3 \widetilde{\psi}}{\partial \widetilde{y}^3}$$
$$+\frac{1-\sigma_{\widetilde{x}}\tan A}{1+\sigma_{\widetilde{x}}^2}\left[(1+\lambda_1\widetilde{T})\widetilde{T} + Nc\,(1+\lambda_2\widetilde{C})\widetilde{C}\right] - \frac{Nr}{1+\sigma_{\widetilde{x}}^2}\widetilde{\phi} \quad (7.16)$$

For the numerical purpose, again we introduce the following new variables

$$\xi = \widetilde{x},\ \eta = \frac{\widetilde{y}}{\xi^{1/4}},\ \widetilde{\psi} = \xi^{3/4}\,\widetilde{r}\,f(\xi,\eta),\ \theta = \widetilde{T}(\xi,\eta),\ \gamma = \widetilde{\phi}(\xi,\eta),\ S = \widetilde{C}(\xi,\eta) \quad (7.17)$$

where $\widetilde{r} = (\xi + \xi_0)\,\sin A$.

Substituting Eq. (7.17) into Eq. (7.16) and Eqs. (7.12) - (7.14), we obtain

$$(1+\sigma_\xi^2)\,f''' + \left(R + \frac{3}{4}\right) f\,f'' - \frac{1}{2}\,(f')^2 + \frac{1-\sigma_\xi\tan A}{1+\sigma_\xi^2}\ [(1+\lambda_1\,\theta)\theta + Nc\,(1+\lambda_2\,S)S]$$
$$-\frac{Nr}{1+\sigma_\xi^2}\,\gamma = \xi\ \left(\frac{\sigma_\xi\,\sigma_{\xi\xi}}{1+\sigma_\xi^2}\,f'^2 + f'\frac{\partial f'}{\partial \xi} - \frac{\partial f}{\partial \xi}f''\right) \quad (7.18)$$

$$\frac{1+\sigma_\xi^2}{Pr}\,\theta'' + \left(R+\frac{3}{4}\right) f\,\theta' + (1+\sigma_\xi^2)\,Nb\,\theta'\,\gamma' + Nt\,(1+\sigma_\xi^2)\,(\theta')^2 = \xi\,\left(f'\frac{\partial\theta}{\partial\xi} - \frac{\partial f}{\partial\xi}\theta'\right) \tag{7.19}$$

$$\frac{1+\sigma_\xi^2}{Le}\,\gamma'' + \left(R+\frac{3}{4}\right) f\,\gamma' + \frac{1+\sigma_\xi^2}{Le}\,\frac{Nt}{Nb}\,\theta'' = \xi\,\left(f'\frac{\partial\gamma}{\partial\xi} - \frac{\partial f}{\partial\xi}\gamma'\right) \tag{7.20}$$

$$\frac{1+\sigma_\xi^2}{Sc}\,S'' + \left(R+\frac{3}{4}\right) f\,S' = \xi\,\left(f'\frac{\partial S}{\partial\xi} - \frac{\partial f}{\partial\xi}S'\right) \tag{7.21}$$

and the associated boundary conditions (7.15) reduce to

$$f'(\xi,\eta)=0,\; \xi\,\frac{\partial f}{\partial\xi} + \left(R+\frac{3}{4}\right) f(\xi,\eta) = \xi^{1/4}\,f_w,\; \theta'(\xi,\eta) = -Bi\,\xi^{1/4}\,\left[1-\theta(\xi,\eta)\right],$$

$$Nb\,\gamma'(\xi,\eta) + Nt\,\theta'(\xi,\eta) = 0,\; S(\xi,\eta)=1 \quad \text{at} \quad \eta = 0 \tag{7.22a}$$

$$f'(\xi,\eta)=0,\; \theta(\xi,\eta)=0,\; \gamma(\xi,\eta)=0,\; S(\xi,\eta)=0 \quad \text{as} \quad \eta\to\infty \tag{7.22b}$$

where $R = \dfrac{\xi}{\xi+\xi_0}$.

The non-dimensional skin friction $C_f = \dfrac{2\,\tau_w}{\rho_{f\infty}\,U_*^2}$, local Nusselt number $Nu_{\overline{x}} = \dfrac{q_w\,\overline{x}}{k(T_f - T_\infty)}$, local nanoparticle Sherwood number $NSh_{\overline{x}} = \dfrac{q_n\,\overline{x}}{D_B\,\phi_\infty}$ and local regular Sherwood number $Sh_{\overline{x}} = \dfrac{q_m\,\overline{x}}{D_S\,(C_w - C_\infty)}$, in which

$$\tau_w = \mu\,\left[\mathbf{n}\cdot\nabla u\right]_{y=\sigma(\overline{x})},\; q_w = -k\,\left[\mathbf{n}\cdot\nabla T\right]_{y=\sigma(\overline{x})}, q_n = -D_B\,\left[\mathbf{n}\cdot\nabla\phi\right]_{y=\sigma(\overline{x})},\; q_m = -D_S\,\left[\mathbf{n}\cdot\nabla C\right]_{y=\sigma(\overline{x})}$$

where

$$\mathbf{n} = \left(-\frac{\sigma_\xi}{\sqrt{1+\sigma_\xi^2}}, \frac{1}{\sqrt{1+\sigma_\xi^2}}\right)$$

is the unit normal vector to the surface of the wavy frustum of a cone, are given by

$$\left.\begin{aligned} \frac{1}{2}\,C_f\,Gr_{\overline{x}}^{1/4} = \xi^{-3/4}\,\sqrt{1+\sigma_\xi^2}\,f''(\xi,0),\; \frac{Nu_{\overline{x}}}{Gr_{\overline{x}}^{1/4}} = -\xi^{3/4}\,\sqrt{1+\sigma_\xi^2}\,\theta'(\xi,0),\\ \frac{NSh_{\overline{x}}}{Gr_{\overline{x}}^{1/4}} = -\xi^{3/4}\,\sqrt{1+\sigma_\xi^2}\,\gamma'(\xi,0),\; \frac{Sh_{\overline{x}}}{Gr_{\overline{x}}^{1/4}} = -\xi^{3/4}\,\sqrt{1+\sigma_\xi^2}\,S'(\xi,0) \end{aligned}\right\} \tag{7.23}$$

Results and Discussion

As explained in the previous chapters, here also, the Bivariate Pseudo-Spectral Local Linearization Method is employed to solve the non-homogeneous and non-linear coupled partial differential equations (7.18)-(7.21) along with the boundary conditions (7.22). To validate the generated code, the numerical values of the surface drag $\frac{1}{2}C_f(Gr)^{1/4}$ and heat transfer rate $Nu_{\overline{x}}(Gr)^{-1/4}$ at $\xi = 0$ (i.e., flat vertical plate case) are compared with the existing results (Na and Chiou [75], Na [74], Yih [130] and Cebeci and Bradshaw [15]), as given in Tab. (7.1). Also, the numerical values of the surface drag and heat transfer rate for $\xi \to \infty$ (i.e., flat full cone case) are compared with the results presented by Na and Chiou [75], Roy [107], Alamgir [4] and Yih [130], as given in Tab. (7.2). It is observed that the results are in a good agreement, as exhibited in Tabs. (7.1) and (7.2). To investigate the effects of amplitude (a) and half angle (A) of the wavy frustum of a cone, suction/injection parameter (f_w), Biot number (Bi), nonlinear density temperature parameter (λ_1) and nonlinear density concentration parameter (λ_2), the computations have been carried out for $Nc = 1, Nr = 0.5, Sc = 0.6, Pr = 1, Le = 10, Nt = 0.2$, $Nb = 0.2$ and $\xi_0 = 1$. These values are fixed in this analysis unless otherwise specified.

The influence of nonlinear density temperature parameter (λ_1) and suction/injection parameter (f_w) on the velocity f', temperature θ, nanoparticle volume fraction γ, and regular concentration S, is explored in Figs. 7.2(a)-7.2(d). Figure 7.2(a) reveals that the velocity increases with an increase of the nonlinear density temperature parameter (NDT) for all the cases of injection, impermeability and suction. It is well known that the NDT parameter shows the nonlinear relationship between the fluid density and temperature. Physically, $\lambda_1 > 0$ refers to the heat supplies from the surface of a wavy cone to the fluid region. For $f_w = -0.5$, $f_w = 0.0$ and $f_w = 0.5$, the profiles of the temperature and regular concentration diminish with an enhancement in the NDT parameter, as plotted in Figs. 7.2(b) and 7.2(d). But, the reverse responses are noticed for the nanoparticle volume fraction, as shown in Fig. 7.2(c). Further, the velocity, temperature and regular concentration are found to be high in the case of injection in comparison with those of the suction and impermeable cases.

Table 7.1: *Comparison of* $\frac{1}{2}C_f(Gr)^{1/4}$ *and* $Nu_{\overline{x}}(Gr)^{-1/4}$ *for various values of* Pr, *when* $Nr = Nc = Nt = 0, Sc = Le = 1, Nb \to 0, \overline{a} = \sigma_\xi = 0, A = 0, \lambda_1 = \lambda_2 = 0, f_w = 0,$ $Bi \to \infty$ *and* $\xi = 0$.

	$f''(0,\,0)$			$-\theta'(0,\,0)$				
Pr	[130]	[15]	Present	[74]	[75]	[130]	[15]	Present
0.1	1.2144	1.2104	1.21165028	——	——	0.1629	0.1637	0.16340583
1	0.9084	0.9081	0.90819093	0.4010	0.4011	0.4012	0.4009	0.40103296
10	0.5927	0.5930	0.59282326	0.8269	0.8269	0.8266	0.8266	0.82683087
100	0.3558	0.3564	0.35588101	1.5493	1.5493	1.5493	1.5495	1.54931193
1000	0.2049	——	0.20574685	——	——	2.8035	——	2.80316218

Figures 7.3(a)-7.3(d) explore the effects of wavy surface parameter (a) and NDC parameter (λ_2) on the velocity f', temperature θ, volume fraction γ, and regular concentration S. Here, $a = 0$ and $\lambda_2 = 0$ are used to indicate the flat surface and linear density concentration, respectively. From Figs. 7.3(a), 7.3(b) and 7.3(d), it is seen that the enhancement in the amplitude of wavy surface leads to enhance the thickness of the momentum and solutal boundary layers but reduces the thermal boundary layer thickness. Further, the nanoparticle volume fraction increases in the neighborhood of the surface and gradually decreases towards the outer edge of the boundary layer, as shown in Fig. 7.3(c). The NDC parameter causes to escalate the velocity and nanoparticle volume fraction near to the wavy surface, but an opposite behavior is noticed towards the outer edge of the corresponding boundary layers, as plotted in Figs. 7.3(a) and 7.3(c). The magnitude of temperature and regular concentration diminishes with rising values of the NDC parameter, as given in Figs. 7.3(b) and 7.3(d). Further, it is observed that the influence of NDC parameter λ_2 is more on the temperature and regular concentration profiles as a contrast with that of the NDT parameter λ_1.

The variations of velocity f', temperature θ, nanoparticle volume fraction γ, and regular concentration S for diverse values of Biot number (Bi) and half angle of the wavy cone (A), are shown in Figs. 7.4(a)-7.4(d) . When the wavy surface is non-isothermal (i.e., small values of Bi), the thickness of momentum and regular concentration boundary layers increase, but the thermal boundary layer thickness decreases with an increase in the half angle of wavy cone. With the enhancement of the half angle parameter (A), the nanoparticle volume

Table 7.2: *Comparison of* $\frac{1}{2}C_f(Gr)^{1/4}$ *and* $Nu_{\overline{x}}(Gr)^{-1/4}$ *for various values of* Pr*, when* $Nr = Nc = Nt = 0, Sc = Le = 1, Nb \to 0, \overline{a} = \sigma_\xi = 0, A = 0, \lambda_1 = \lambda_2 = 0, f_w = 0,$ $Bi \to \infty$ *and* $\xi \to \infty$.

	$f''(\infty,\,0)$			$-\theta'(\infty,\,0)$				
Pr	[107]	[130]	Present	[107]	[4]	[75]	[130]	Present
0.1	——	1.0960	1.09464314	——	0.2141	——	0.2116	0.21130560
1	0.8600	0.7699	0.76944922	0.5275	0.5280	0.5104	0.5109	0.51039548
10	0.4899	0.4877	0.48769819	1.0354	1.0159	1.0340	1.0339	1.03398025
100	0.2897	0.2896	0.28960777	1.9229	1.8237	1.9220	1.9226	1.92271470
1000	0.1661	0.1661	0.16168925	3.4700	3.2463	——	3.4696	3.46515335

fraction enhances near to the wavy surface and shown an opposite trend towards the outer edge of the boundary layer, as displayed in Fig. 7.4(c). Additionally, the ratio of the thermal resistance of the boundary layer and the solid surface is characterized by the Biot number (Bi). With an increase in the Biot number, the non-dimensional velocity and temperature enhance rapidly, whereas the nanoparticle volume fraction and regular concentration reduce, as plotted in Figs. 7.4(a)-7.4(d).

The streamwise variations on the surface drag $\frac{1}{2}C_f(Gr)^{1/4}$, local heat transfer rate $Nu_{\overline{x}}(Gr)^{-1/4}$, local nanoparticle mass transfer rate $NSh_{\overline{x}}(Gr)^{-1/4}$, and local regular mass transfer rate $Sh_{\overline{x}}(Gr)^{-1/4}$ under the influence of suction/injection parameter (f_w) and nonlinear density temperature parameter (λ_1), are shown in Figs. 7.5(a)-7.5(d). Figure 7.5(a) reveals that the surface drag enhances with an enhancement in the NDT parameter for the injection, impermeable and suction cases. Figures 7.5(b) and 7.5(d) shown that the local heat and regular mass transfer rates rise with rising values of NDT for all cases of f_w. But, an opposite behavior is noticed on the local nanoparticle mass transfer rate, as given in Fig. 7.5(c). Moreover, the local heat and regular mass transfer rates are found to be high for the suction case in comparison with those of the impermeable and injection cases. But, the surface drag and local nanoparticle mass transfer rate are more in the case of injection when these are compared to other cases.

The influence of wavy surface parameter (a) and NDC parameter (λ_2) on the non-dimensional surface drag $\frac{1}{2}C_f(Gr)^{1/4}$, local heat transfer rate $Nu_{\overline{x}}(Gr)^{-1/4}$, local nanoparticle mass transfer rate $NSh_{\overline{x}}(Gr)^{-1/4}$, and local regular mass transfer rate $Sh_{\overline{x}}(Gr)^{-1/4}$ over ξ, are presented in Figs. 7.6(a)-7.6(d). The range of ξ is taken from 0 to 4, which is proportional to two full cycles of the wavy surface, as displayed in Fig. 7.1. At fixed λ_2, the surface drag and local regular mass transfer rate are observed to be higher for a smooth surface ($a = 0$) compared to the wavy surface ($a \neq 0$). The reason for this behaviour is that the buoyancy force along the wavy frustum of a cone is reduced by the component $\frac{1-\sigma_\xi \tan A}{1+\sigma_\xi^2}$ from its value of the smooth frustum of a cone. Further, we consider one full cycle for ξ from 2 to 4. When a increases, the local heat transfer rate decreases in the first quarter of the cycle ($\xi \approx 2.0$ to $\xi \approx 2.5$) and then increases in the second quarter of the cycle ($\xi \approx 2.5$ to $\xi \approx 3.0$). Again, a decrease in the heat transfer rate is observed for the third quarter of the cycle ($\xi \approx 3.0$ to $\xi \approx 3.5$) and a large increase is noticed in the last quarter of the cycle ($\xi \approx 3.5$ to $\xi \approx 4.0$). But, the nanoparticle mass transfer rate follows an opposite trend in all the cycles from $\xi = 2$ to $\xi = 4$. The same phenomenon is repeated when the range of ξ is promoted by another cycle. For the wavy surface ($a \neq 0$), the surface drag, local heat and regular mass transfer rates enhance but the local nanoparticle mass transfer rate diminishes with an increase of the NDC parameter.

The streamwise distributions of the surface drag $\frac{1}{2}C_f(Gr)^{1/4}$, local heat transfer rate $Nu_{\overline{x}}(Gr)^{-1/4}$, nanoparticle mass transfer rate $NSh_{\overline{x}}(Gr)^{-1/4}$ and regular mass transfer rate $Sh_{\overline{x}}(Gr)^{-1/4}$ for different values of Biot number (Bi) and half angle of the wavy cone (A), are presented in Figs. 7.7(a)-7.7(d). Here also, one full cycle for ξ from 2 to 4 is considered to explore the influence of half angle parameter. It is seen that the surface drag, local heat and regular mass transfer rates increase in the first half of the cycle ($\xi \approx 2.0$ to $\xi \approx 3.0$) and then it shows a reverse trend in the second half of the cycle ($\xi \approx 3.0$ to $\xi \approx 4.0$) with an increase in the half angle of a cone. But, the opposite results are noticed for nanoparticle mass transfer rate with half angle of a cone. These trends are repeated when the range of ξ is extended by one more cycle. For a fixed A, the surface drag, local heat and regular mass transfer rates enhance, but the local nanoparticle mass transfer rate diminishes with an increase in the Biot number, as plotted in Figs. 7.7(a)-7.7(d).

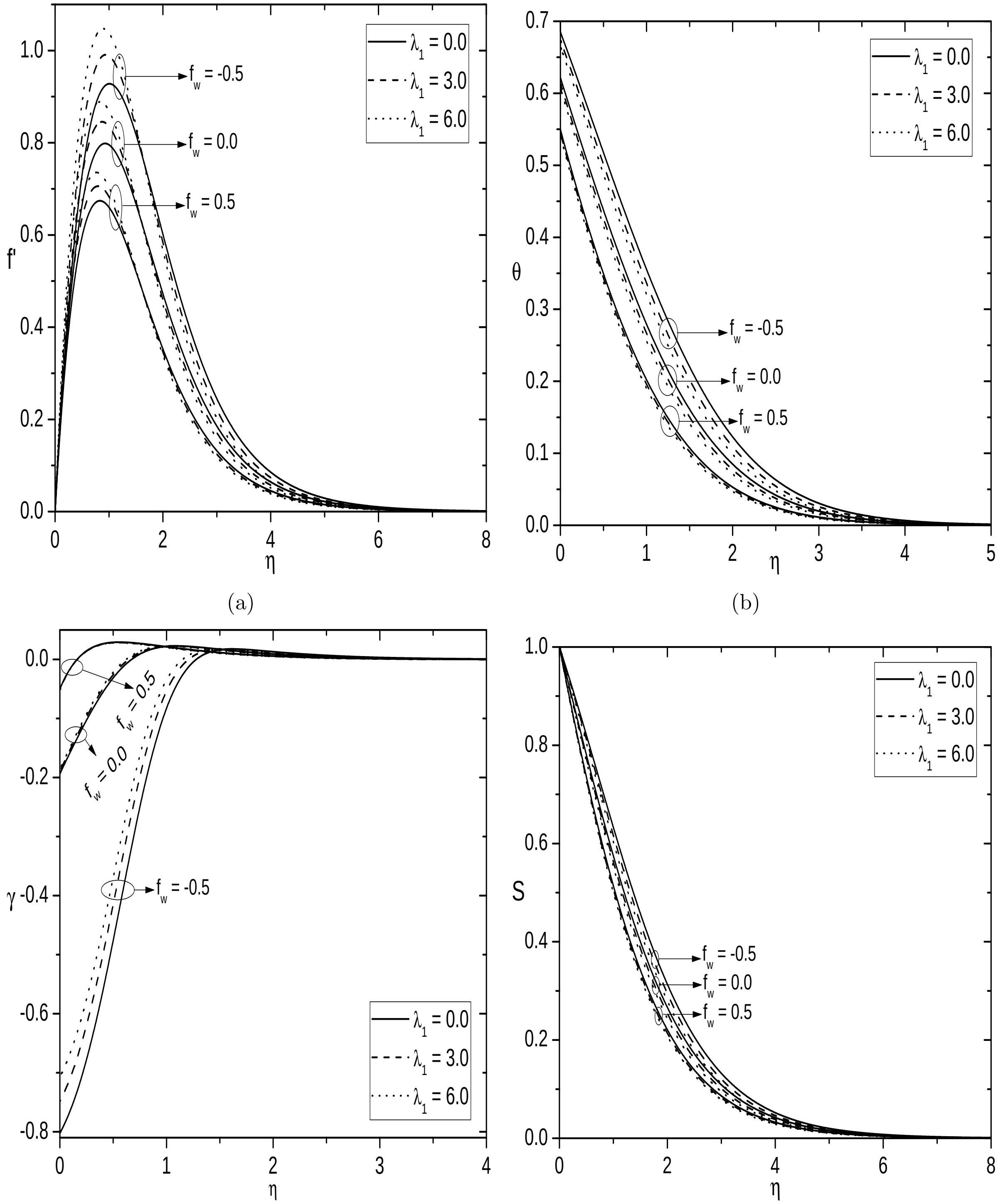

(a)

(b)

(c)

(d)

Figure 7.2: *Effects of* f_w *and* λ_1 *on (a) Velocity, (b) Temperature, (c) Nanoparticle volume fraction, and (d) Regular concentration for* $a = 0.15, \lambda_2 = 3, A = 10^0$ *and* $Bi = 1$.

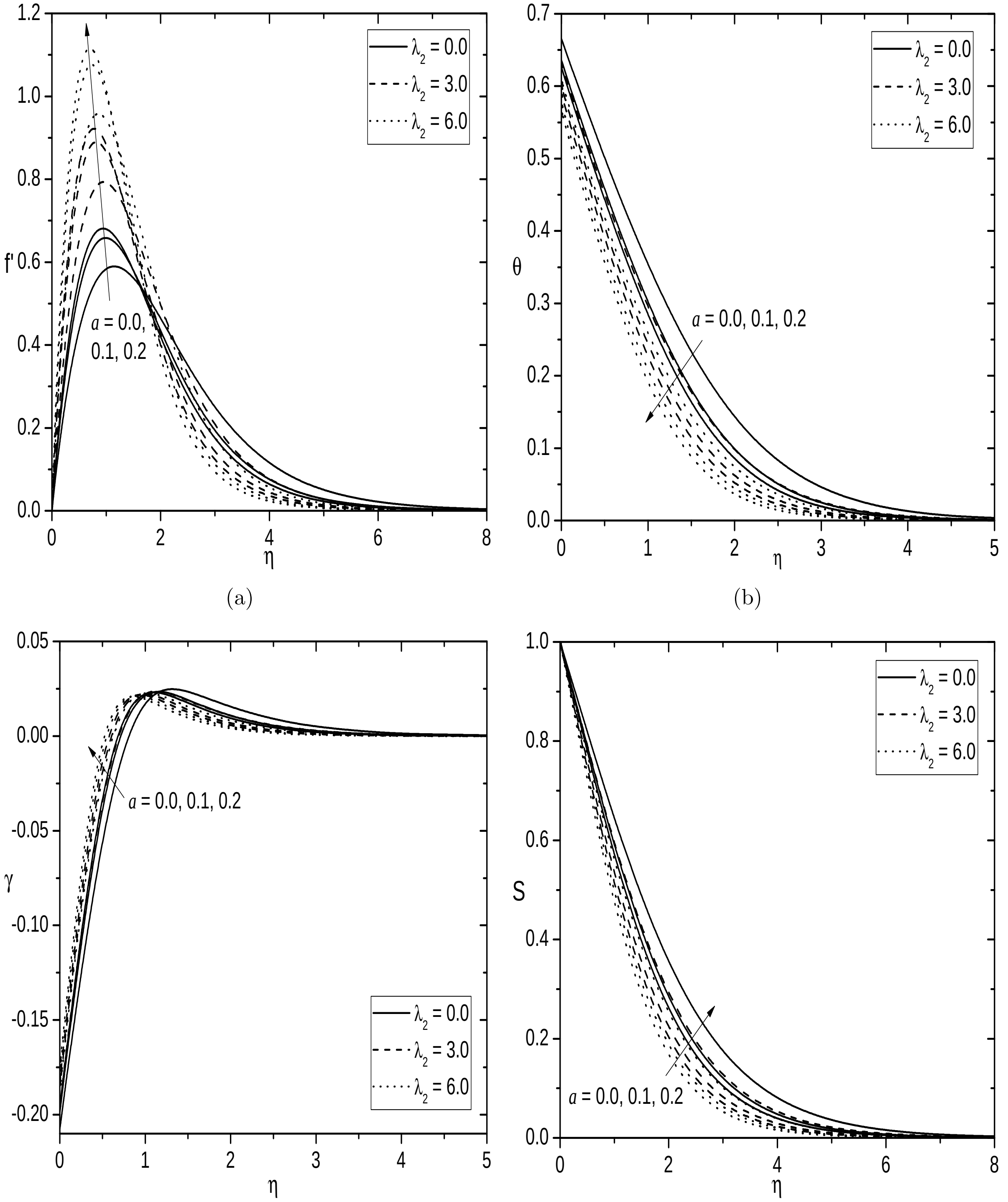

(a) (b)

(c) (d)

Figure 7.3: *Effects of* a *and* λ_2 *on (a) Velocity, (b) Temperature, (c) Nanoparticle volume fraction, and (d) Regular concentration for* $f_w = 0, \lambda_1 = 3, A = 10^0$ *and* $Bi = 1$.

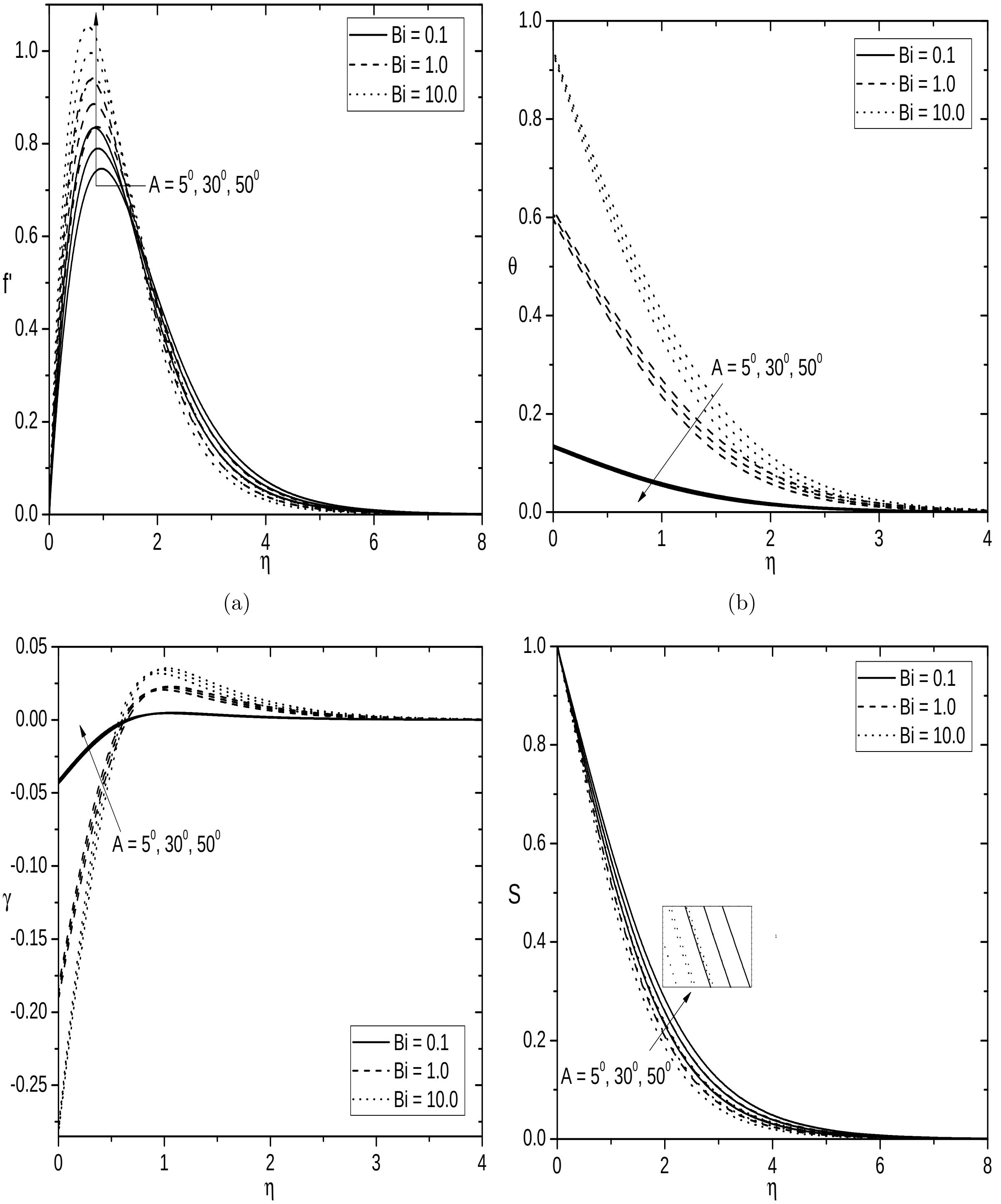

(a) (b)

(c) (d)

Figure 7.4: *Effects of A and Bi on (a) Velocity, (b) Temperature, (c) Nanoparticle volume fraction, and (d) Regular concentration for* $f_w = 0, \lambda_1 = 3, \lambda_2 = 3$ *and* $a = 0.15$.

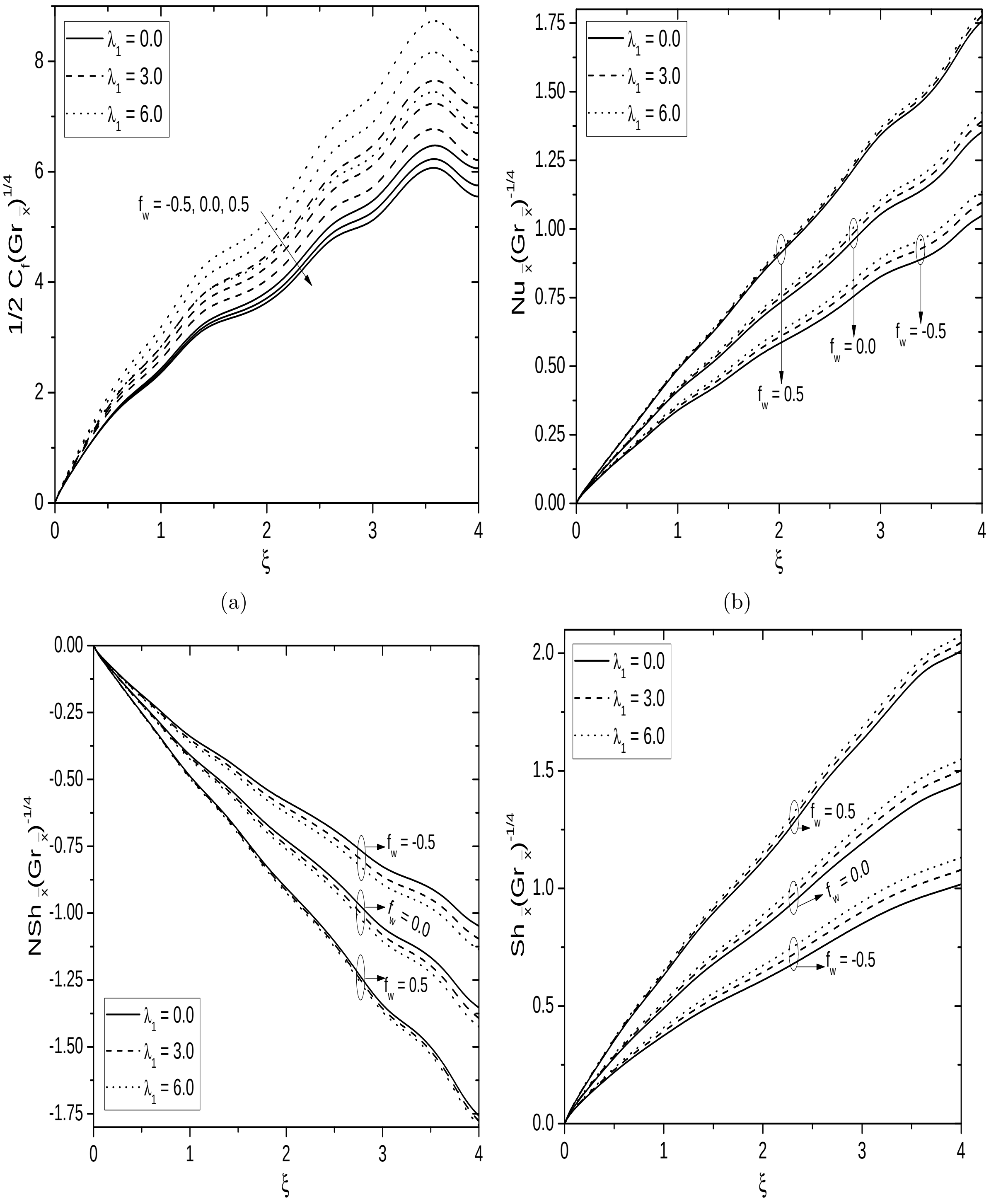

(a) (b)

(c) (d)

Figure 7.5: *Effects of* f_w *and* λ_1 *on (a) Skin friction, (b) Heat transfer rate, (c) Nanoparticle mass transfer rate, and (d) Regular mass transfer rate for* $a = 0.15, \lambda_2 = 3, A = 10^0$ *and* $Bi = 1$.

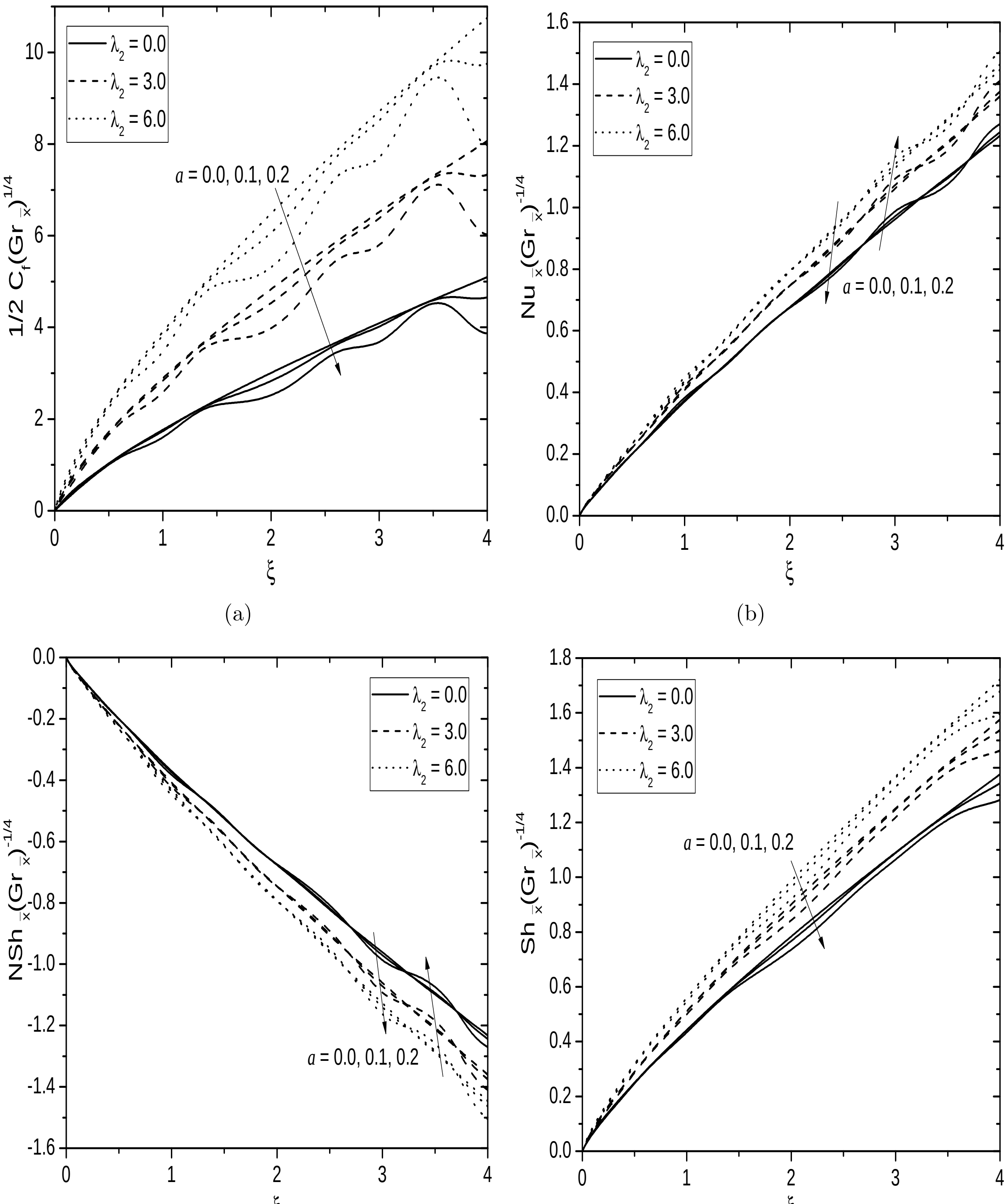

(a) (b)

(c) (d)

Figure 7.6: *Effects of* a *and* λ_2 *on (a) Skin friction, (b) Heat transfer rate, (c) Nanoparticle mass transfer rate, and (d) Regular mass transfer rate for* $f_w = 0, \lambda_1 = 3, A = 10^0$ *and* $Bi = 1$.

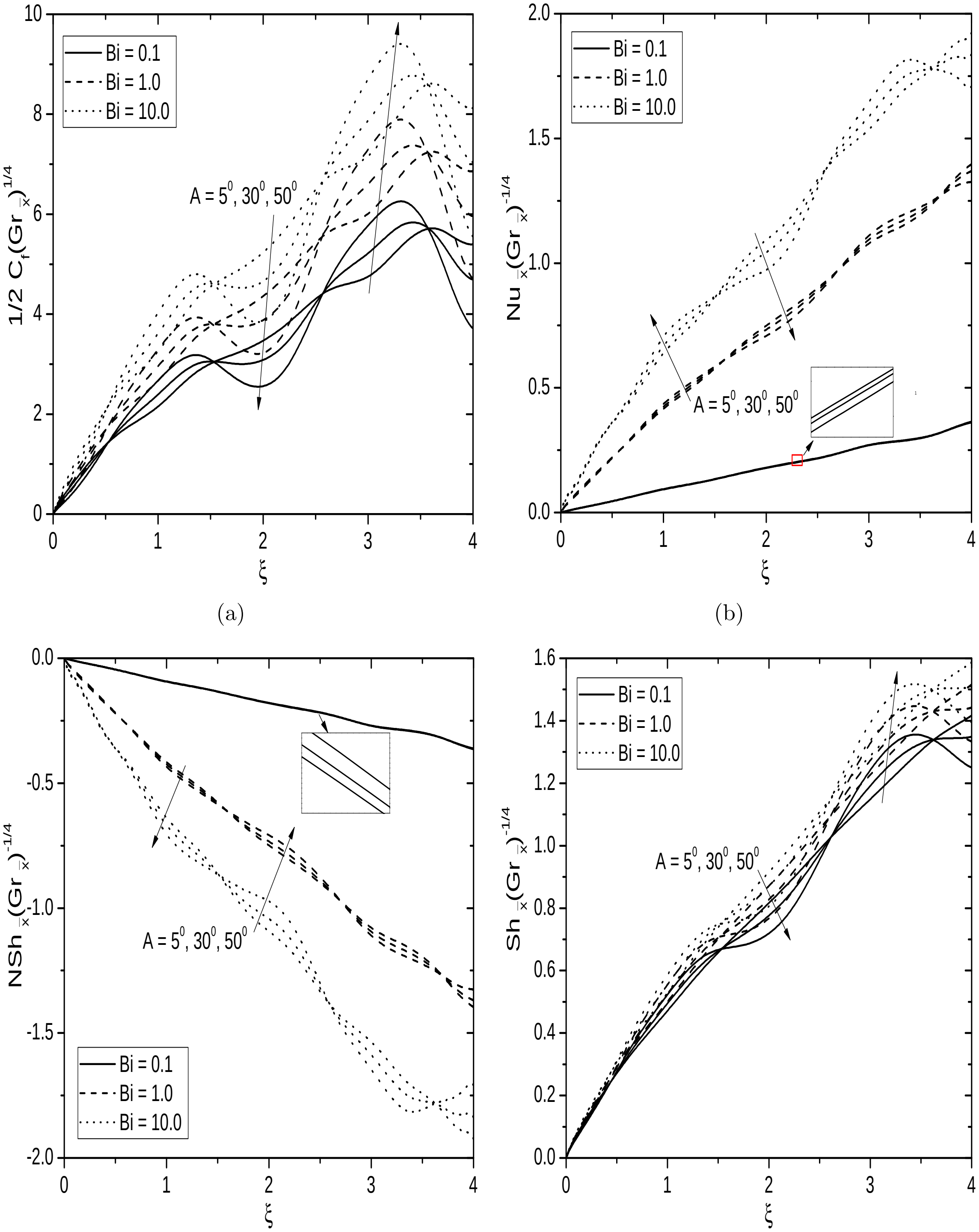

(a) (b)

(c) (d)

Figure 7.7: *Effects of A and Bi on (a) Skin friction, (b) Heat transfer rate, (c) Nanoparticle mass transfer rate, and (d) Regular mass transfer rate for $f_w = 0, \lambda_1 = 3, \lambda_2 = 3$ and $a = 0.15$.*

7.2.2 Case(b): Mixed Convection

Consider the mixed convective flow arises from an external flow with velocity U_∞ and buoyancy forces. We introduce the non-similarity transformations in the following form

$$\widetilde{x} = \frac{x - x_0}{L} = \frac{\overline{x}}{L},\ \widetilde{y} = \frac{y - \sigma(\overline{x})}{L}\, Re^{1/2},\ \widetilde{\psi} = \frac{\psi}{U_\infty\, L^2}\, Re^{1/2},\ \widetilde{T} = \frac{T - T_\infty}{T_f - T_\infty},\ \widetilde{\phi} = \frac{\phi - \phi_\infty}{\phi_\infty},$$

$$\widetilde{C} = \frac{C - C_\infty}{C_w - C_\infty},\ \widetilde{p} = \frac{p - p_\infty}{\rho\, U_\infty^2},\ \widetilde{r} = \frac{r}{L},\ \widetilde{\sigma} = \frac{\sigma}{L},\ \widetilde{a} = \frac{a}{L},\ \widetilde{x}_0 = \frac{x_0}{L},\ u_w = \frac{\overline{u}_w}{U_\infty} \tag{7.24}$$

where $Re = \dfrac{U_\infty\, L}{\nu}$ is the Reynolds number and U_∞ is the reference free stream velocity.

Substituting Eq. (2.7) and Eq. (7.24) into Eqs. (7.3)-(7.7) and letting ($Re \to \infty$) (i.e., boundary layer approximation), the dimensionless boundary layer equations can be written as

$$\begin{aligned}\frac{1}{\widetilde{r}^2}\left[\frac{\partial \widetilde{\psi}}{\partial \widetilde{y}}\,\frac{\partial^2 \widetilde{\psi}}{\partial \widetilde{x}\partial \widetilde{y}} - \frac{\widetilde{r}_{\widetilde{x}}}{\widetilde{r}}\left(\frac{\partial \widetilde{\psi}}{\partial \widetilde{y}}\right)^2 - \frac{\partial \widetilde{\psi}}{\partial \widetilde{x}}\,\frac{\partial^2 \widetilde{\psi}}{\partial \widetilde{y}^2}\right] &= -\frac{\partial \widetilde{p}}{\partial \widetilde{x}} + \sigma_{\widetilde{x}}\, Re^{1/2}\frac{\partial \widetilde{p}}{\partial \widetilde{y}} + \frac{1}{\widetilde{r}}\,(1 + \sigma_{\widetilde{x}}^2)\,\frac{\partial^3 \widetilde{\psi}}{\partial \widetilde{y}^3}\\ &\quad + \lambda\,\left[(1 + \lambda_1\,\widetilde{T})\widetilde{T} + Nc\,(1 + \lambda_2\,\widetilde{C})\widetilde{C} - Nr\,\widetilde{\phi}\right]\end{aligned} \tag{7.25}$$

$$\begin{aligned}\frac{1}{\widetilde{r}^2}\left[\sigma_{\widetilde{x}}\left(\frac{\partial \widetilde{\psi}}{\partial \widetilde{x}}\,\frac{\partial^2 \widetilde{\psi}}{\partial \widetilde{y}^2} - \frac{\partial \widetilde{\psi}}{\partial \widetilde{y}}\,\frac{\partial^2 \widetilde{\psi}}{\partial \widetilde{x}\partial \widetilde{y}}\right) - \sigma_{\widetilde{x}\widetilde{x}}\left(\frac{\partial \widetilde{\psi}}{\partial \widetilde{y}}\right)^2\right] + \frac{\widetilde{r}_{\widetilde{x}}}{\widetilde{r}^3}\,\sigma_{\widetilde{x}}\left(\frac{\partial \widetilde{\psi}}{\partial \widetilde{y}}\right)^2 &= Re^{1/2}\,\frac{\partial p}{\partial \widetilde{y}} - \frac{\sigma_{\widetilde{x}}}{\widetilde{r}}\,(1 + \sigma_{\widetilde{x}}^2)\,\frac{\partial^3 \widetilde{\psi}}{\partial \widetilde{y}^3}\\ &\quad + \lambda\,\left[(1 + \lambda_1\,\widetilde{T})T + Nc\,(1 + \lambda_2\,\widetilde{C})C\right]\tan A\end{aligned} \tag{7.26}$$

$$\frac{1}{\widetilde{r}}\left[\frac{\partial \widetilde{\psi}}{\partial \widetilde{y}}\,\frac{\partial \widetilde{T}}{\partial \widetilde{x}} - \frac{\partial \widetilde{\psi}}{\partial \widetilde{x}}\,\frac{\partial \widetilde{T}}{\partial \widetilde{y}}\right] = \frac{(1 + \sigma_{\widetilde{x}}^2)}{Pr}\,\frac{\partial^2 \widetilde{T}}{\partial \widetilde{y}^2} + Nb\,(1 + \sigma_{\widetilde{x}}^2)\,\frac{\partial \widetilde{T}}{\partial \widetilde{y}}\,\frac{\partial \widetilde{\phi}}{\partial \widetilde{y}} + Nt\,(1 + \sigma_{\widetilde{x}}^2)\,\left(\frac{\partial \widetilde{T}}{\partial \widetilde{y}}\right)^2 \tag{7.27}$$

$$\frac{1}{\widetilde{r}}\left[\frac{\partial \widetilde{\psi}}{\partial \widetilde{y}}\,\frac{\partial \widetilde{\phi}}{\partial \widetilde{x}} - \frac{\partial \widetilde{\psi}}{\partial \widetilde{x}}\,\frac{\partial \widetilde{\phi}}{\partial \widetilde{y}}\right] = \frac{(1 + \sigma_{\widetilde{x}}^2)}{Le}\,\frac{\partial^2 \widetilde{\phi}}{\partial \widetilde{y}^2} + \frac{(1 + \sigma_{\widetilde{x}}^2)}{Le}\,\frac{Nt}{Nb}\,\frac{\partial^2 \widetilde{T}}{\partial \widetilde{y}^2} \tag{7.28}$$

$$\frac{1}{\widetilde{r}}\left[\frac{\partial\widetilde{\psi}}{\partial\widetilde{y}}\,\frac{\partial\widetilde{C}}{\partial\widetilde{x}}-\frac{\partial\widetilde{\psi}}{\partial\widetilde{x}}\,\frac{\partial\widetilde{C}}{\partial\widetilde{y}}\right]=\frac{(1+\sigma_{\widetilde{x}}^2)}{Sc}\,\frac{\partial^2\widetilde{C}}{\partial\widetilde{y}^2} \tag{7.29}$$

along with the boundary conditions

$$\frac{\partial\widetilde{\psi}}{\partial\widetilde{y}}=0,\ \frac{1}{\widetilde{r}}\,\frac{\partial\widetilde{\psi}}{\partial\widetilde{x}}=f_w,\ \frac{\partial\widetilde{T}}{\partial\widetilde{y}}=-Bi\,(1-T),\ Nb\,\frac{\partial\widetilde{\phi}}{\partial\widetilde{y}}+Nt\,\frac{\partial\widetilde{T}}{\partial\widetilde{y}}=0,\ \widetilde{C}=1\ \text{ at }\ \widetilde{y}=0 \tag{7.30a}$$

$$\frac{\partial\widetilde{\psi}}{\partial\widetilde{y}}=\widetilde{r}\,u_w,\ \widetilde{T}=0,\ \widetilde{\phi}=0,\ \widetilde{C}=0,\ \widetilde{p}=0\ \text{ as }\ \widetilde{y}\to\infty \tag{7.30b}$$

where $f_w=-\dfrac{v_w}{U_\infty\,Re^{1/2}}$ is the suction/injection parameter.

It is seen from Eq. (7.26) that the order of the term $\frac{\partial\widetilde{p}}{\partial\widetilde{y}}$ is $O(Re^{-1/2})$. Therefore, the least order of pressure gradient in the $\widetilde{x}$ - direction can be evaluated from the solution of inviscid flow case and it is given by (see [67], [62] and [111])

$$\frac{\partial\widetilde{p}}{\partial\widetilde{x}}=-\big[\big(1+\sigma_{\widetilde{x}}^2\big)\,u_w\,u_w'+\sigma_{\widetilde{x}}\,\sigma_{\widetilde{x}\,\widetilde{x}}\,u_w^2\big] \tag{7.31}$$

Now, the elimination of the term $\frac{\partial\widetilde{p}}{\partial\widetilde{y}}$ from Eqs. (7.25) and (7.26) gives

$$\begin{aligned}&\frac{1}{\widetilde{r}^2}\left[\left(\frac{\partial\widetilde{\psi}}{\partial\widetilde{y}}\,\frac{\partial^2\widetilde{\psi}}{\partial\widetilde{x}\partial\widetilde{y}}-\frac{\partial\widetilde{\psi}}{\partial\widetilde{x}}\,\frac{\partial^2\widetilde{\psi}}{\partial\widetilde{y}^2}\right)-\frac{\widetilde{r}_{\widetilde{x}}}{\widetilde{r}}\left(\frac{\partial\widetilde{\psi}}{\partial\widetilde{y}}\right)^2+\frac{\sigma_{\widetilde{x}}\,\sigma_{\widetilde{x}\widetilde{x}}}{1+\sigma_{\widetilde{x}}^2}\left(\frac{\partial\widetilde{\psi}}{\partial\widetilde{y}}\right)^2\right]=-\frac{1}{(1+\sigma_{\widetilde{x}}^2)}\,\frac{\partial\widetilde{p}}{\partial\widetilde{x}}\\&+\frac{1}{\widetilde{r}}\,(1+\sigma_{\widetilde{x}}^2)\,\frac{\partial^3\widetilde{\psi}}{\partial\widetilde{y}^3}+\lambda\,\frac{1-\sigma_{\widetilde{x}}\,\tan A}{1+\sigma_{\widetilde{x}}^2}\,\left[(1+\lambda_1\,\widetilde{T})\widetilde{T}+Nc\,(1+\lambda_2\,\widetilde{C})\widetilde{C}\right]-\lambda\,\frac{Nr}{1+\sigma_{\widetilde{x}}^2}\,\widetilde{\phi}\end{aligned} \tag{7.32}$$

For the numerical purpose, we introduce the following new variables

$$\xi=\widetilde{x},\ \eta=u_w^{1/2}\,\xi^{-1/2}\,\widetilde{y},\ \widetilde{\psi}=\widetilde{r}\,u_w^{1/2}\,\xi^{1/2}\,f(\xi,\eta),\ \theta=\widetilde{T}(\xi,\eta),\ \gamma=\widetilde{\phi}(\xi,\eta),\ S=\widetilde{C}(\xi,\eta) \tag{7.33}$$

Substituting Eq. (7.33) into Eq. (7.32) and Eqs. (7.27) - (7.29), we obtain

$$\begin{aligned}(1+\sigma_\xi^2)\, f''' + \left(R+\frac{1}{2}+\frac{1}{2}\,\xi\,\frac{u_w'}{u_w}\right) f\, f'' - \xi\,\left(\frac{\sigma_\xi\,\sigma_{\xi\xi}}{1+\sigma_\xi^2}+\frac{u_w'}{u_w}\right)(f')^2 - \lambda\,\frac{\xi}{u_w^2}\,\frac{Nr}{1+\sigma_\xi^2}\,\gamma \\ +\lambda\,\frac{\xi}{u_w^2}\,\frac{1-\sigma_\xi\,\tan A}{1+\sigma_\xi^2}\,\left[(1+\lambda_1\,\theta)\,\theta + Nc\,(1+\lambda_2\,S)\,S\right] = \xi\,\left(f'\frac{\partial f'}{\partial \xi}-\frac{\partial f}{\partial \xi}f''\right)\end{aligned} \tag{7.34}$$

$$\frac{(1+\sigma_\xi^2)}{Pr}\,\theta'' + \left(R+\frac{1}{2}+\frac{1}{2}\,\xi\,\frac{u_w'}{u_w}\right) f\,\theta' + Nb\,(1+\sigma_\xi^2)\,\theta'\,\gamma' + Nt\,(1+\sigma_\xi^2)\,(\theta')^2 = \xi\,\left(f'\frac{\partial \theta}{\partial \xi}-\frac{\partial f}{\partial \xi}\theta'\right) \tag{7.35}$$

$$\frac{(1+\sigma_\xi^2)}{Le}\,\gamma'' + \left(R+\frac{1}{2}+\frac{1}{2}\,\xi\,\frac{u_w'}{u_w}\right) f\,\gamma' + \frac{(1+\sigma_\xi^2)}{Le}\,\frac{Nt}{Nb}\,\theta'' = \xi\,\left(f'\frac{\partial \gamma}{\partial \xi}-\frac{\partial f}{\partial \xi}\gamma'\right) \tag{7.36}$$

$$\frac{(1+\sigma_\xi^2)}{Sc}\,S'' + \left(R+\frac{1}{2}+\frac{1}{2}\,\xi\,\frac{u_w'}{u_w}\right) f\,S' = \xi\,\left(f'\frac{\partial S}{\partial \xi}-\frac{\partial f}{\partial \xi}S'\right) \tag{7.37}$$

and the associated boundary conditions reduce to

$$\begin{gathered}f'(\xi,\eta)=0,\ \xi\,\frac{\partial f}{\partial \xi} + \left(R+\frac{1}{2}+\frac{1}{2}\,\xi\,\frac{u_w'}{u_w}\right) f(\xi,\eta) = u_w^{-1/2}\,\xi^{1/2}\,f_w, \\ \theta'(\xi,\eta) = -u_w^{-1/2}\,\xi^{1/2}\,Bi\,\left[1-\theta(\xi,\eta)\right], Nb\,\gamma'(\xi,\eta)+Nt\,\theta'(\xi,\eta)=0,\ S(\xi,\eta)=1 \quad \text{at} \quad \eta=0\end{gathered} \tag{7.38a}$$

$$f'(\xi,\eta)=1,\ \theta(\xi,\eta)=0,\ \gamma(\xi,\eta)=0,\ S(\xi,\eta)=0 \quad \text{as} \quad \eta\to\infty \tag{7.38b}$$

The terms u_w' and u_w appeared in the above system of equations (7.34)-(7.37) can be obtained from the solution of an inviscid fluid flow problem. But, this solution is valid only for small values of the amplitude-wave length ratio. Therefore, the solution $u_w(\widetilde{x})$ of the potential flow for small values of $\widetilde{a}(<< 1)$ is given by (For more details, see [67], [62] and [111])

$$u_w(\widetilde{x}) = 1 + \widetilde{a}\,\left[\frac{1}{\pi}\int_0^\infty \frac{\sigma'(t)}{\widetilde{x}-t}dt\right] + O(\widetilde{a}^2) \tag{7.39}$$

The non-dimensional skin friction $C_f = \dfrac{2\,\tau_w}{\rho_{f\infty}\,U_\infty^2}$, local Nusselt number $Nu_{\overline{x}} = \dfrac{q_w\,\overline{x}}{k\,(T_f - T_\infty)}$, local nanoparticle Sherwood number $NSh_{\overline{x}} = \dfrac{q_n\,\overline{x}}{D_B\,\phi_\infty}$ and local regular Sherwood number

$Sh_{\overline{x}} = \dfrac{q_m\,\overline{x}}{D_S\,(C_w - C_\infty)}$, are given by

$$\left.\begin{aligned} \frac{1}{2}\,C_f\,Re^{1/2} &= u_w^{3/2}\,\xi^{-1/2}\,\sqrt{1+\sigma_\xi^2}\,f''(\xi,0), & \frac{Nu_{\overline{x}}}{Re^{1/2}} &= -u_w^{1/2}\,\xi^{1/2}\,\sqrt{1+\sigma_\xi^2}\,\theta'(\xi,0), \\ \frac{NSh_{\overline{x}}}{Re^{1/2}} &= -u_w^{1/2}\,\xi^{1/2}\,\sqrt{1+\sigma_\xi^2}\,\gamma'(\xi,0), & \frac{Sh_{\overline{x}}}{Re^{1/2}} &= -u_w^{1/2}\,\xi^{1/2}\,\sqrt{1+\sigma_\xi^2}\,S'(\xi,\,0) \end{aligned}\right\} \tag{7.40}$$

Results and Discussion

The resultant system of partial differential Eqs. (7.34)-(7.37) along with the boundary conditions (7.38) are solved numerically using the Bivariate Pseudo-Spectral Local Linearization Method. In order to assess the generated code, for special case of $a = 0$, $\lambda_1 = 0$, $\lambda_2 = 0$, $f_w = 0$ and $Bi \to \infty$, the present results of the local Nusselt number at $\xi = 0$ (Vertical flat plate case) have been compared with those of Lloyd and Sparrow [56] and an excellent agreement is noticed, as shown in Tab. (2.2). To study the influence of various physical parameters, the computations have been carried out for $Nc = 1, Nr = 0.5, Sc = 0.6, Pr = 1, Le = 10, Nt = 0.2, Nb = 0.2,\ A = 10^0$ and $\xi_0 = 1$.

Figures 7.8(a)-7.8(d) are plotted to explore the effects of NDT parameter (λ_1) and suction/injection parameter (f_w) on the dimensionless velocity f', temperature θ, nanoparticle volume fraction γ, and solutal concentration S at $\lambda = 1$. Physically, the nonlinear density temperature parameter (NDT) shows a nonlinear relationship between the fluid density and temperature. Therefore, $\lambda_1 > 0\,(i.e., T_f > T_\infty)$ refers to the heat supplies from the surface of a wavy cone to the nanofluid region. As expected, the velocity and nanoparticle volume fraction increase with an increase in the NDT parameter, as displayed in Fig. 7.8(a) and 7.8(c). But, the temperature and regular concentration decrease with increasing values of λ_1, as shown in Figs. 7.8(b) and 7.8(d). These observations are also true for the suction, injection and impermeability cases. Moreover, the permeable surface is characterized by suction/injection parameter f_w. The values $f_w = -0.5, 0$ and 0.5 indicate the injection, impermeable surface and suction cases, respectively. For a fixed λ_1, the velocity increases when suction/injection parameter increases, as given in Fig. 7.8(a). With the increasing values of f_w, the non-dimensional temperature decreases at a fixed λ_1, as plotted in 7.8(b).

From Figs. 7.8(c) and 7.8(d), it is also noted that the nanoparticle volume fraction enhances and regular concentration diminishes with enhancing values of f_w. Further, the temperature and regular concentration of the nanofluid are more in the case of injection in comparison with those of fluid suction and impermeable surface cases.

For various values of the NDC parameter (λ_2) and Biot number (Bi), the distributions of velocity f', temperature θ, nanoparticle volume fraction γ, and regular concentration S, are demonstrated in Figs. 7.9(a)-7.9(d). Physically, the NDC describes a nonlinear relationship between the fluid density and concentration. Therefore, $\lambda_2 > 0\,(i.e., C_w > C_\infty)$ refers to the mass supplied from the surface of a wavy cone to the nanofluid region. For small values of Bi, the NDC parameter escalate the velocity and nanoparticle volume fraction near to the wavy surface, but an opposite behavior is noticed towards the outer edge of the corresponding boundary layers, as shown in Figs. 7.9(a) and 7.9(c). It is seen from Figs. 7.9(b) and 7.9(d) that the magnitude of temperature and regular concentration diminish as the NDC parameter raises. This effect is due to the additional mass supplied from the mass near to the surface. It is interesting to note that the influence of λ_2 is more prominent on the temperature and regular concentration profiles, as a contrast with that of λ_1. With an increase in the Biot number, the magnitude of the velocity increases as given in Fig. 7.9(a). Figure 7.9(b) explores that an increase in the Biot number (Bi) rapidly increases the dimensionless temperature. Further, it is found that the magnitude of nanoparticle volume fraction diminish near to the surface and show a reverse trend towards the outer edge of the corresponding boundary layer, whereas the regular concentration fall down with the rise of Biot number, as plotted in Figs. 7.9(c)-7.9(d).

The influence of mixed convection parameter (λ) on the velocity f', temperature θ, nanoparticle volume fraction γ, and regular concentration S, is demonstrated in Figs. 7.10(a)-7.10(d). The mixed convection parameter characterizes the fluid flow behavior such as the opposing flow for $\lambda < 0$, forced convective flow for $\lambda = 0$ and aiding flow for $\lambda > 0$. For large values of the mixed convection parameter $(i.e., \lambda \to \infty)$, the flow becomes the free convection. From Fig. 7.10(a), it is clear that the velocity in aiding flow is found to be more when compared with the opposing, forced and free convective flows. The higher temperature is noticed for opposing flow when compared to the aiding, free convective and forced convective flows, as plotted in Fig. 7.10(b). From Fig. 7.10(c), it is clear that the nanoparticle volume fraction reaches its maximum value for free convective flow, as compared to the mixed convective flows. This is due to the large buoyancy forces occurred in the presence of the mixed convection parameter. The regular concentration for aiding flow is very less in comparison with the opposing, forced and free convective flows, as depicted in Fig. 7.10(d).

Figures 7.11(a)-7.11(d) exhibit the effects of NDT (λ_1) and NDC (λ_2) parameters on the streamwise distributions of surface drag, local heat transfer rate, local nanoparticle and regular mass transfer rates for $Bi = 1$ (non-isothermal case) and $Bi >> 1$ (isothermal case). For a fixed value of NDC parameter, the surface drag, local heat and regular mass transfer rates rise with the rising values of NDT parameter, as plotted in Figs. 7.11(a), 7.11(b) and 7.11(d). The similar observation is drawn with the rising values of NDC parameter for a fixed value of NDT parameter. Also, a huge increment is noticed in the drag coefficient, and local heat and regular mass transfer rates in the presence of both NDT and NDC parameters. But, the opposite results are noticed for the local nanoparticle mass transfer rate, as shown in Fig. 7.11(c). From the obtained results, it is clear that the influence of NDC parameter is more significant on both heat and regular mass transfer rates when compared to that of NDT parameter. Further, the presence of convective thermal boundary condition at the surface controls the drag coefficient and also the heat and regular mass transfer rates. That is, the higher heat and regular mass transfer rates are noticed when $Bi \to \infty$ (i.e., for isothermal surface).

The influence of suction/injection parameter (f_w) on the surface drag, local heat transfer rate, local nanoparticle and regular mass transfer rates versus the streamwise coordinate (ξ), for smooth surface ($a = 0.0$) and wavy surface ($a = 0.2$), is displayed in Figs. 7.12(a)-7.12(d). The range of ξ is taken from 0 to 4, which is proportional to two full cycles of the wavy surface. At a constant f_w, the surface drag, local nanoparticle and regular mass transfer rates are observed to be higher for smooth surface ($a = 0$) than that of the corresponding wavy surface ($a = 0.2$). From Fig. 7.12(a), it is clear that the surface drag coefficient increases with the increase of suction/injection parameter, for both $a = 0.0$ and $a = 0.2$. The same behavior is noticed for both local heat and regular mass transfer rates, as depicted in Figs. 7.12(b) and 7.12(d). But, the local nanoparticle mass transfer rate follows an opposite trend with suction/injection parameter, as shown in Fig. 7.12(c). Particularly, the higher values of heat and regular mass transfer rates are found in the suction case when compared to the injection and impermeability cases.

Figures 7.13(a)-7.13(d) illustrate the streamwise distribution of surface drag, local heat transfer rate, local nanoparticle and regular mass transfer rates under the influence of mixed convection parameter (λ). The magnitude of surface drag in the opposing flow is very less in comparison to the aiding, free and forced convective flows as portrayed in Fig. 7.13(a). Figures 7.13(b) and 7.13(d) reveal that the heat and regular mass transfer rates for aiding flow are noted to be substantial than those of for opposing, free and forced convective flows. But, the mixed convection parameter is shown an opposite behaviour on the nanoparticle mass transfer rate, as depicted in 7.13(c).

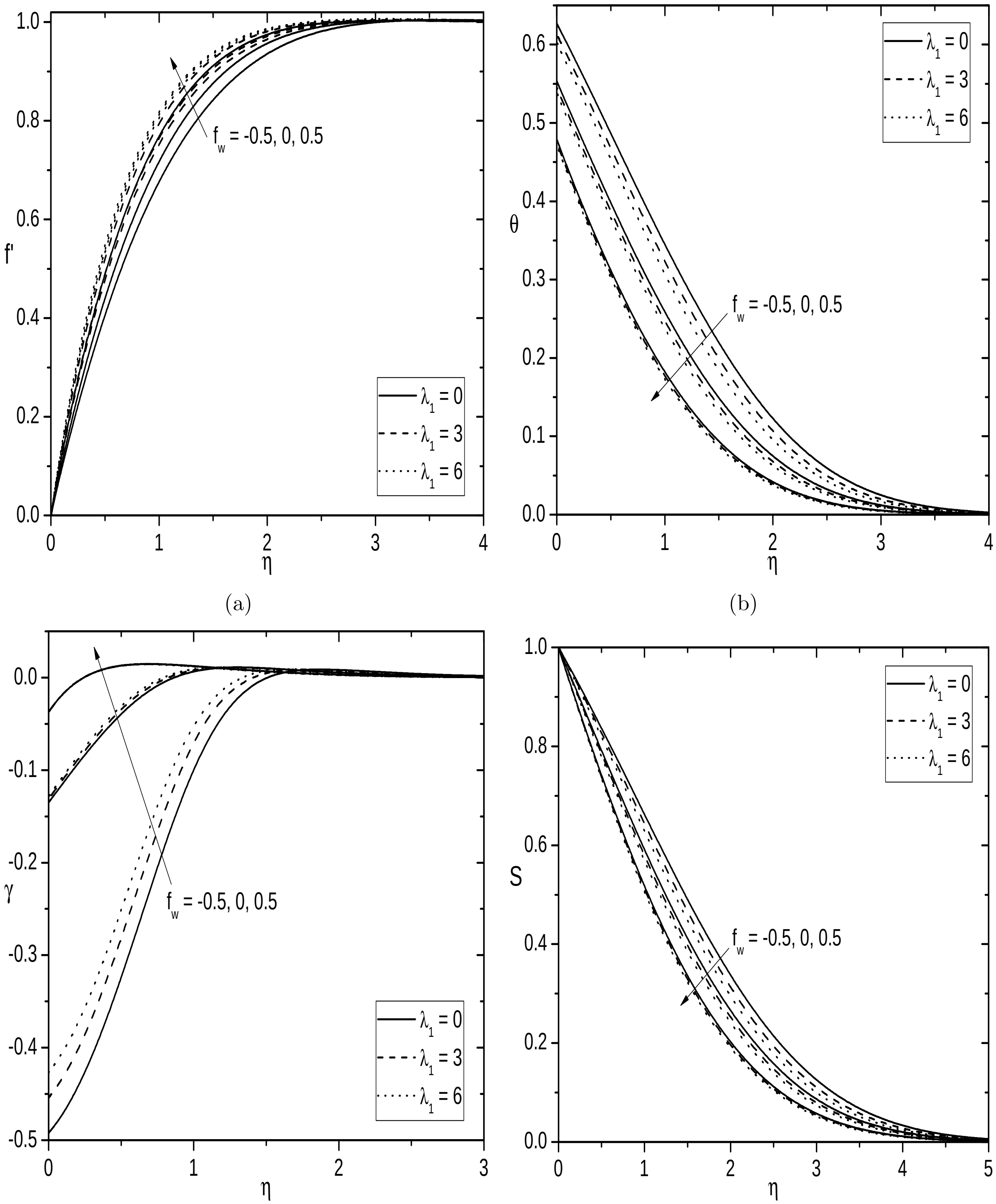

(a)

(b)

(c)

(d)

Figure 7.8: *Effects of* f_w *and* λ_1 *on (a) Velocity, (b) Temperature, (c) Nanoparticle volume fraction, and (d) Regular concentration for* $Bi = 1.0, \lambda_2 = 0.1, a = 0.1$ *and* $A = 10^0$.

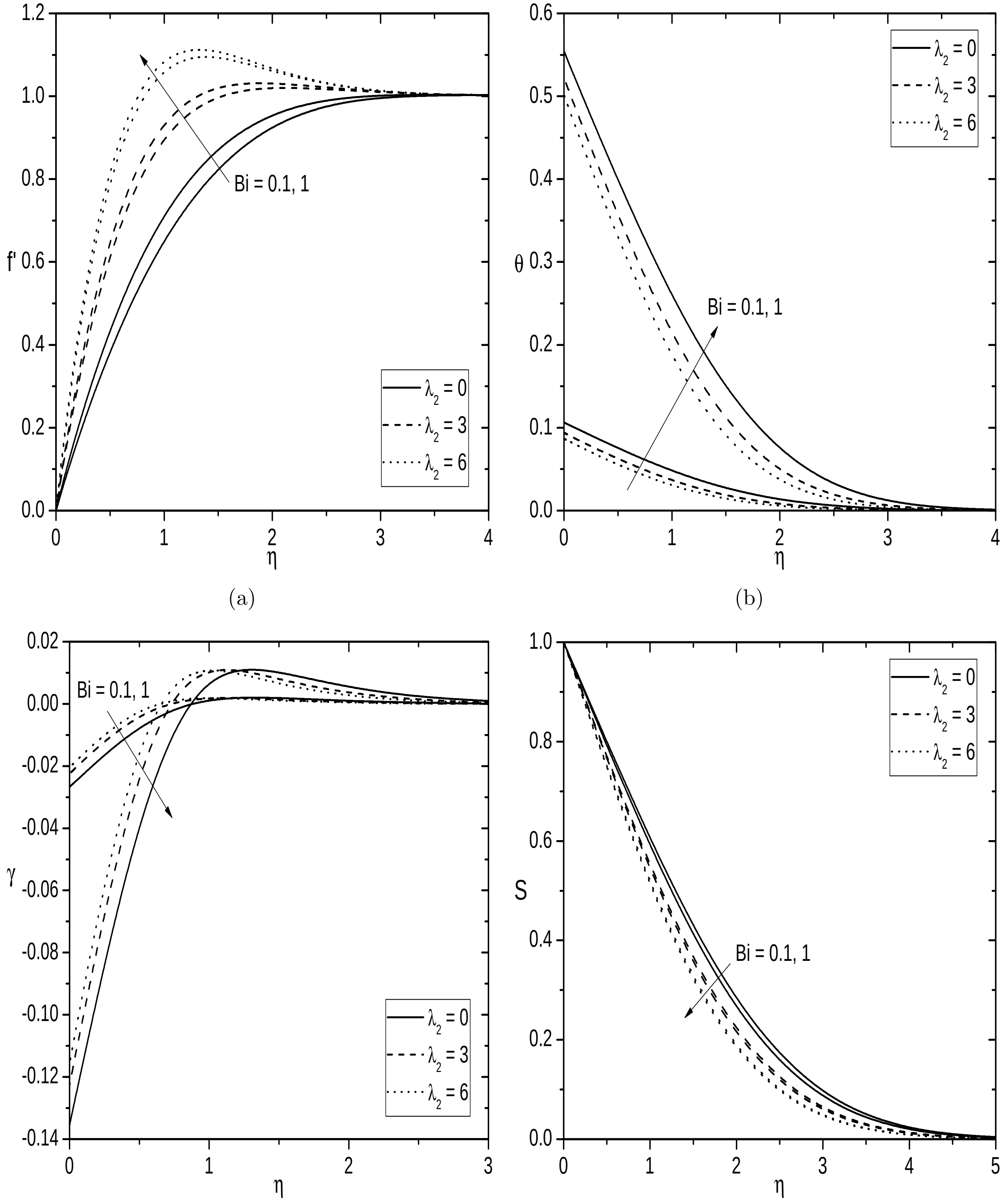

(a)

(b)

(c)

(d)

Figure 7.9: *Effect of Bi and* λ_2 *on (a) Velocity, (b) Temperature, (c) Nanoparticle volume fraction, and (d) Regular concentration for for* $f_w = 0.0, \lambda_1 = 0.1, a = 0.1$ *and* $A = 10^0$.

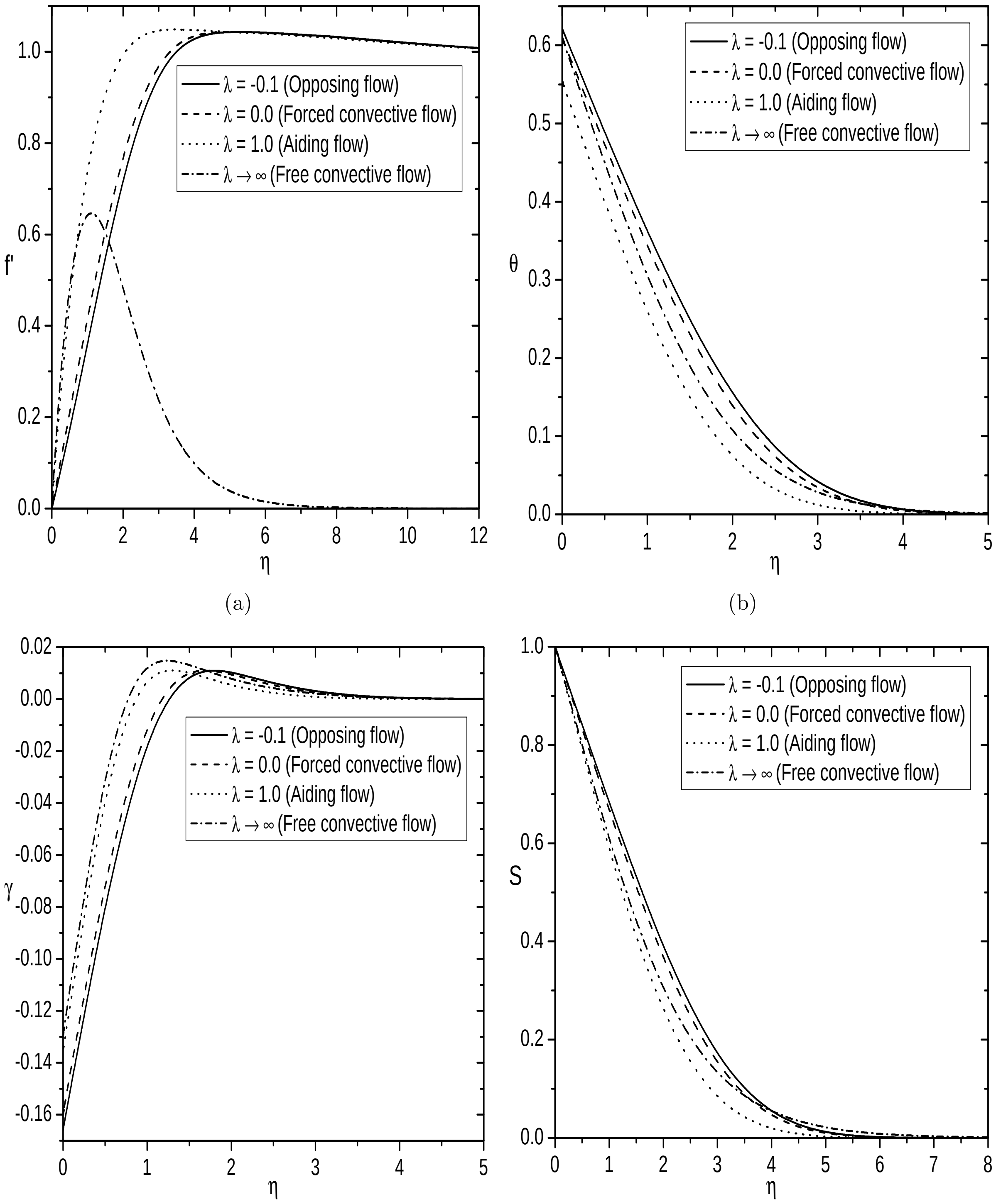

(a)

(b)

(c)

(d)

Figure 7.10: *Effect of* λ *on (a) Velocity, (b) Temperature, (c) Nanoparticle volume fraction, and (d) Regular concentration for* $f_w = 0.0, \lambda_1 = 0.1, \lambda_2 = 0.1, a = 0.1, Bi = 1.0$ *and* $A = 10^0$.

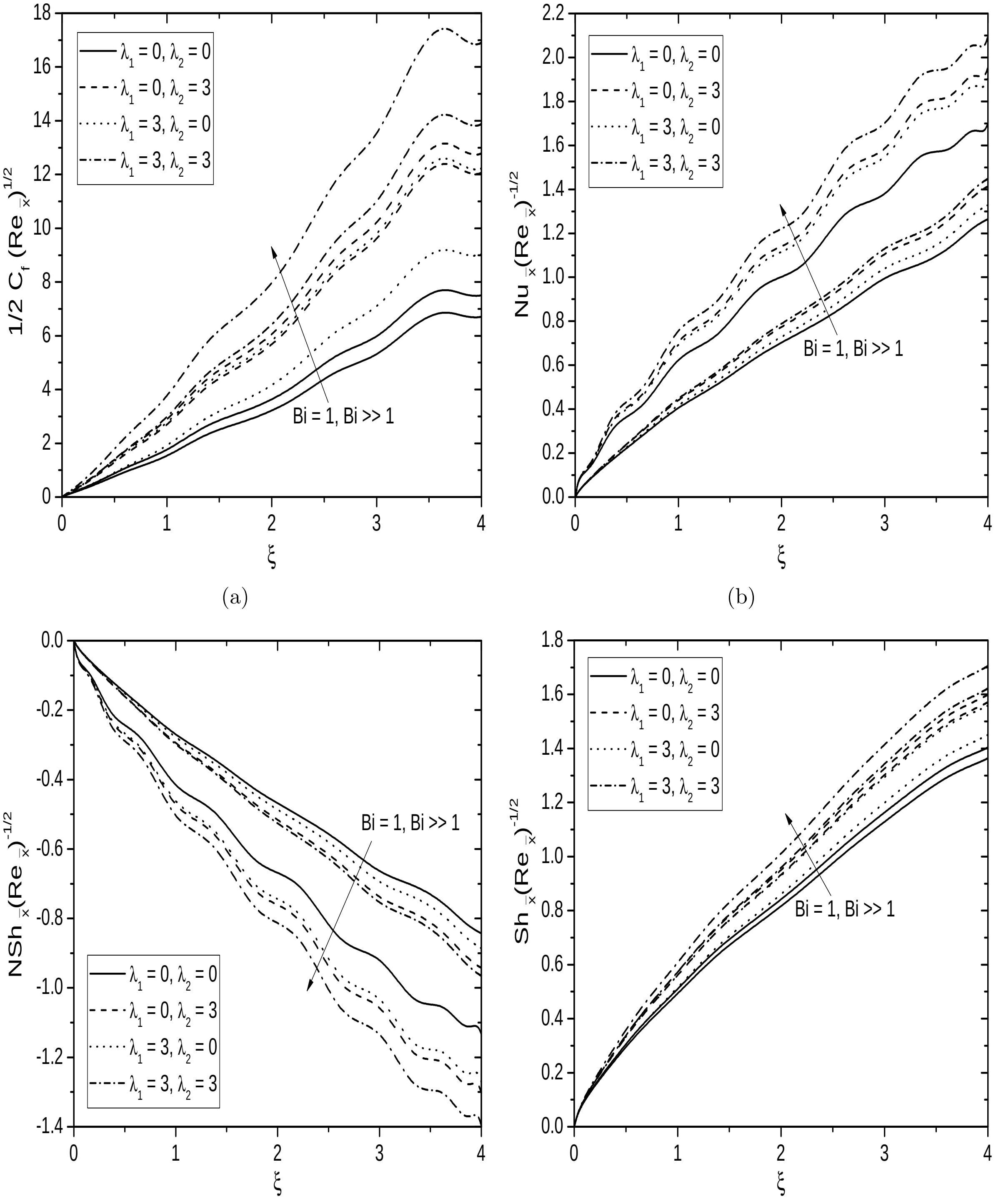

(a) (b)

(c) (d)

Figure 7.11: *Effects of* Bi, λ_1 *and* λ_2 *on (a) Skin friction, (b) Heat transfer rate, (c) Nanoparticle mass transfer rate, and (d) Regular mass transfer rate for* $f_w = 0.0, a = 0.1, \lambda = 1.0$ *and* $A = 10^0$.

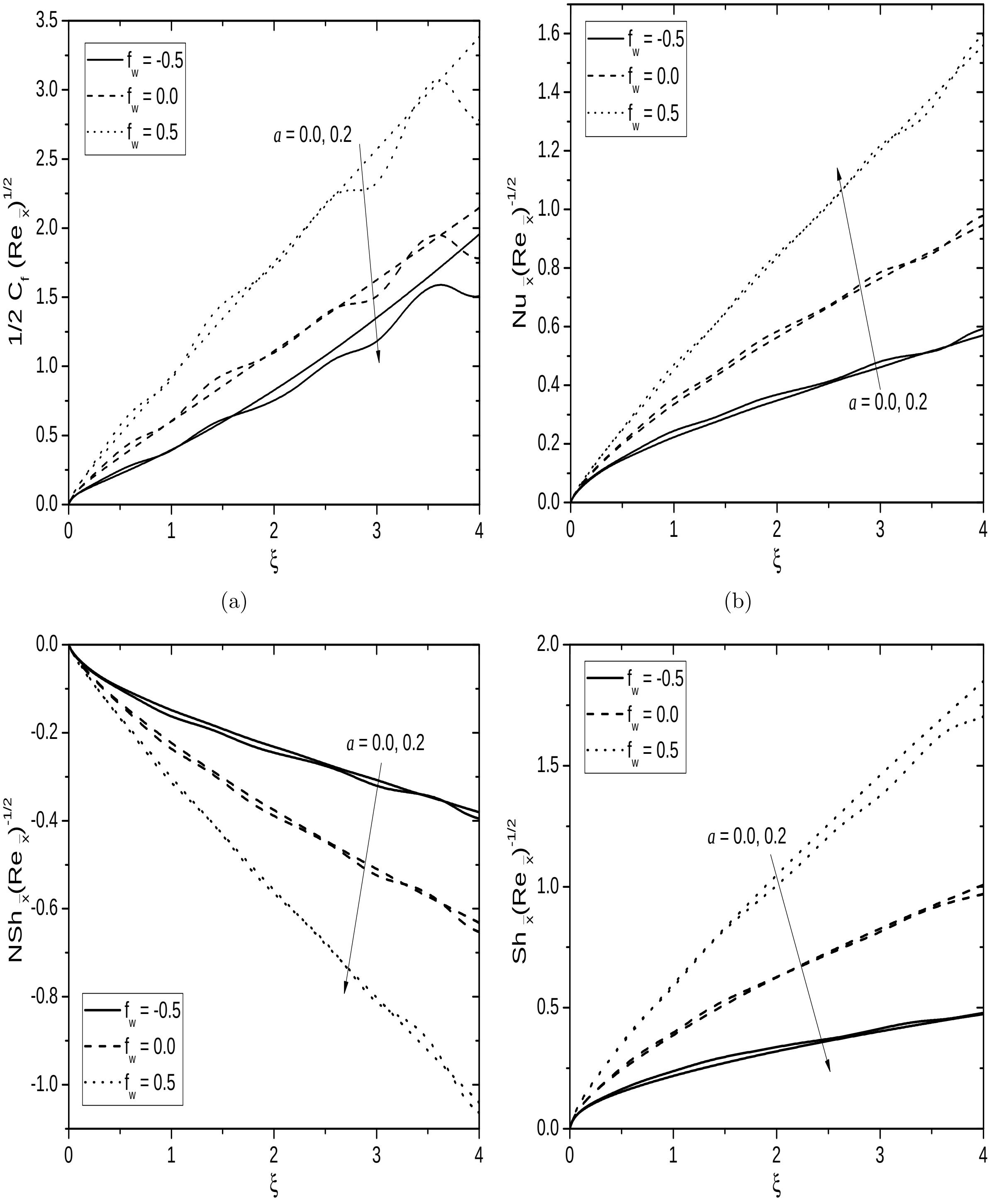

(a) (b)

(c) (d)

Figure 7.12: *Effects of* a *and* f_w *on (a) Skin friction, (b) Heat transfer rate, (c) Nanoparticle mass transfer rate, and (d) Regular mass transfer rate for* $\lambda = 1.0, \lambda_1 = 0.1, \lambda_2 = 0.1, Bi = 1.0$ *and* $A = 10^0$.

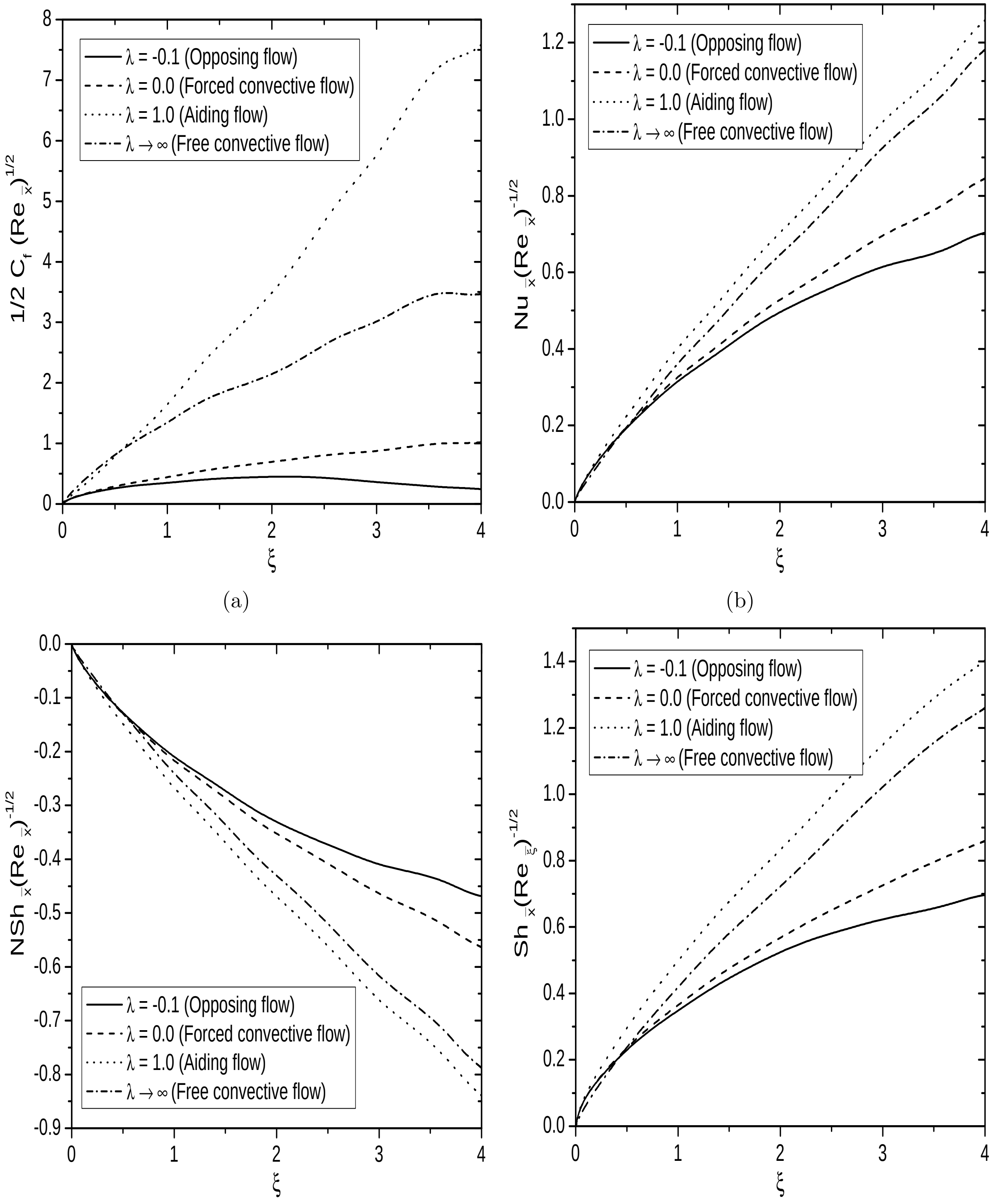

(a) (b) (c) (d)

Figure 7.13: *Effect of* λ *on (a) Skin friction, (b) Heat transfer rate, (c) Nanoparticle mass transfer rate, and (d) Regular mass transfer rate for* $f_w = 0.0, \lambda_1 = 0.1, \lambda_2 = 0.1, a = 0.1, Bi = 1.0$ *and* $A = 10^0$.

7.3 Conclusions

The nonlinear convective flow of an incompressible nanofluid over the permeable wavy frustum of a cone subject to the convective boundary condition, is investigated in this chapter. The resultant non-similarity equations are solved using the Bivariate Pseudo-Spectral Local Linearization Method. Based on the analysis carried out, the main conclusions are drawn for both case (a) and case (b) as given below:

With the increase of both NDT and NDC parameters, the velocity and nanoparticle volume fraction increase, whereas the temperature and regular concentration decrease in both case (a) and case (b). Also, the drag coefficient, local heat and regular mass transfer rates increase in both the cases (a) and (b). For both the cases (a) and (b), the surface drag and regular mass transfer rate reduce, but the sinusoidal oscillations are noticed with an increase of the amplitude of wavy surface. As Biot number enhances, the velocity and temperature profiles along with the heat and regular mass transfer rates enhance, whereas the nanoparticle mass transfer rate diminishes for both the cases (a) and (b). The temperature, regular concentration, and nanoparticle mass transfer rate decrease, but the nanoparticle volume fraction, heat and regular mass transfer rates increase, with an increase of suction/injection parameter in both the cases (a) and (b). However, the velocity and drag coefficient decrease for case (a) but an opposite behaviour is noticed for case (b). Moreover, the heat and regular mass transfer rates are high in the case of opposing flow when compared to the cases of aiding flow, free and forced convective flows.

Chapter 8

Summary and Conclusions

In this thesis, an analysis of convective heat and mass transport over the vertical frustum of a cone in a nanofluid, subject to the uniform wall temperature/convective boundary condition, is discussed.

The steady, two-dimensional natural/mixed convective flow of a nanofluid over the vertical frustum of a cone has been investigated. The main aim of chapters is to present the non-similarity solution for the considered problems and also to investigate the effects of Soret and viscous dissipation, double stratification, non-Darcy porous medium, Arrhenius activation energy, thermal radiation, double dispersion, spinning parameter, nonlinear convection, amplitude and angle of wavy frustum of a cone on the various profiles and physical quantities. Using a suitable set of non-similarity variables, the governing equations are transformed into a system of non-linear partial differential equations and then solved by using the *Bivariate Pseudo-Spectral Local Linearization Method*. The important observations, in both (a) free convection and (b) mixed convection, are as follows:

- An increase in the Eckert number, increases the temperature, nanoparticle volume fraction, local nanoparticle and regular mass transfer rates, but decreases the regular concentration and local heat transfer rate. Moreover, the velocity increases in case (a) and aiding flow of case (b), whereas it decreases in the opposing flow of case (b).

- The velocity, regular concentration, surface drag and local heat transfer rate enhance, whereas the temperature, local nanoparticle and regular mass transfer rates reduce with the increase of Soret number in case (a) and aiding flow of case (b). But, the velocity, temperature, surface drag, local heat and nanoparticle mass transfer rates show a reverse trend in the opposing flow of case (b).

- With the increase of both Brownian motion and thermophoresis parameters, the velocity, temperature, local heat and nanoparticle mass transfer rates increase, but the regular concentration, surface drag and local regular mass transfer rate decrease in case (a) and aiding flow of case (b). Moreover, the velocity, surface drag, and local regular mass transfer rate show a reverse trend in the opposing flow of case (b).

- In case (a) and aiding flow of case (b): the velocity, temperature, local heat and regular mass transfer rates reduce, but the regular concentration and local nanoparticle mass transfer rate enhance with the enhancement of thermal stratification parameter. Moreover, the velocity, regular concentration, local heat and regular mass transfer rates decrease, whereas the local nanoparticle mass transfer rate increases with the increase of solutal stratification parameter. However, the velocity, local heat and regular mass transfer rates show an opposite trend in the opposing flow of case (b).

- As the Forchheimer number increases (i.e., in chapters 3 and 5), the velocity, surface drag, local heat and regular mass transfer rates decrease, but the temperature, regular concentration and local nanoparticle mass transfer rate increase in case (a). The behavior of physical quantities of the flow in case (b) show an opposite nature.

- The higher values of activation energy parameter results in higher velocity and regular concentration, but lower temperature and regular Sherwood number in both case (a) and case (b). However, the drag coefficient increases in case (a) and aiding flow of case (b), whereas it decreases in the opposing flow of case (b).

- The velocity, temperature, local heat and regular mass transfer rate increase, but the regular concentration decreases with the increase of thermal radiation parameter in both free and mixed convective flows.

- In the free convective and aiding flows: the velocity, nanoparticle volume fraction and local heat transfer rate increase, whereas the regular concentration, surface drag and local nanoparticle mass transfer rate decrease with the increase of thermal dispersion parameter.

- As the solutal dispersion parameter enhances, the regular concentration and local regular mass transfer rate enhance in both free and mixed convective flows. But, the velocity, surface drag and local heat transfer rate increase, whereas the local nanoparticle mass transfer rate decreases in case (a) and aiding flow of case (b).

- In both the cases (a) and (b): the nanoparticle volume fraction, skin friction, local heat and regular mass transfer rates increase, but the swirl velocity, temperature, regular concentration and local nanoparticle mass transfer rate decrease with the increase of spinning parameter. Further, the tangential velocity increases in case (a) and case (b), but it shows opposite trend in case (a) far away from the frustum of a cone.

- The higher values of both NDT and NDC parameters results in higher velocity and nanoparticle volume fraction, but lower temperature and regular concentration in both the cases (a) and (b). Also, the surface drag, local heat transfer rate, local nanoparticle and regular mass transfer rates increase in both the cases (a) and (b).

- With an increase of the amplitude of wavy surface, the surface drag and local regular mass transfer rate decrease, whereas the local heat and nanoparticle mass transfer rates show the sinusoidal oscillations in both the cases (a) and (b).

- As the Biot number increases, the temperature, local heat and regular mass transfer rates (i.e., in chapters 4-7) increase, whereas the nanoparticle volume fraction and local nanoparticle mass transfer rate decrease in both free and mixed convective flows. But, the velocity and surface drag increase, and regular concentration decreases in free convective and aiding flows whereas they show reverse trend in the opposing flow situation.

- The temperature, regular concentration and local nanoparticle mass transfer rate reduce, but the nanoparticle volume fraction, local heat and regular mass transfer rates (i.e., chapters 6 and 7) enhance with the enhancement of suction/injection parameter in both the cases (a) and (b). But, the velocity and surface drag show an opposite behavior.

- As compared to the opposing flow, the velocity, nanoparticle volume fraction, surface drag, local heat and regular mass transfer rates are more, but the temperature, regular concentration and local nanoparticle mass transfer rate are less in the case of aiding flow.

The work presented in the thesis can be extended to investigate the effects of Joule heating, MHD, Hall and Ion slip, heat source/sink, first and second order slip, etc. Further, this work can be extended by studying the analysis for various non-Newtonian fluids like micropolar fluids, Casson fluids, Couple stress fluids, etc. Such an exhaustive study can be a rewarding experience though it is challenging as well as time consuming.

Bibliography

[1] A. A. Afify. The influence of slip boundary condition on Casson nanofluid flow over a stretching sheet in the presence of viscous dissipation and chemical reaction. *Mathematical Problems in Engineering*, 2017(3804751):12 pages, 2017.

[2] A. A. Afify and N.S. Elgazery. Effect of double dispersion on non-Darcy mixed convective flow over vertical surface embedded in porous medium. *Applied Mathematics and Mechanics*, 34(10):1247–1262, 2013.

[3] S. E. Ahmed and A. Mahdy. Natural convection flow and heat transfer enhancement of a nanofluid past a truncated cone with magnetic field effect. *World Journal of Mechanics*, 2(5):272, 2012.

[4] M. Alamgir. Overall heat transfer from vertical cones in laminar free convection: An approximate method. *ASME Journal of Heat Transfer*, 101:174–176, 1979.

[5] D. Anilkumar and S. Roy. Unsteady mixed convection flow on a rotating cone in a rotating fluid. *Applied Mathematics and Computation*, 155(2):545–561, 2004.

[6] F. G. Awad, S. S. Motsa, and M. Khumalo. Heat and mass transfer in unsteady rotating fluid flow with binary chemical reaction and activation energy. *PLOS ONE*, 9:e107622, 2014.

[7] F. G. Awad, P. Sibanda, S. S. Motsa, and O. D. Makinde. Convection from an inverted cone in a porous medium with cross - diffusion effects. *Computers and Mathematics with Applications*, 61:1431–1441, 2011.

[8] A. Aziz. A similarity solution for laminar thermal boundary layer over a flat plate with a convective surface boundary condition. *Communications in Nonlinear Sciences and Numerical Simulations*, 14:1064–1068, 2009.

[9] O. A. Beg, V. R. Prasad, B. Vasu, and R. S. R. Gorla. Computational modeling of magneto hydrodynamic convection from a rotating cone in orthotropic Darcian porous media. *Journal of the Brazilian Society of Mechanical Sciences and Engineering*, 39:2035–2054, 2017.

[10] R. E. Bellman and R. E. Kalaba. *Quasilinearisation and Non-Linear Boundary Value Problems.* Elsevier, New York, 1965.

[11] A. R. Bestman. Natural convection boundary layer with suction and mass transfer in a porous medium. *International Journal of Energy Research*, 14:389–396, 1990.

[12] A. R. Bestman. Radiative heat transfer to flow of a combustible mixture in a vertical pipe. *International Journal of Energy Research*, 15:179–184, 1991.

[13] J. Buongiorno. Convective transport in nanofluids. *ASME Journal of Heat Transfer*, 128:240–250, 2006.

[14] C. Canuto, M. Y. Hussaini, A. Quarteroni, and T. A. Zang. *Spectral Methods Fundamentals in Single Domains.* Springer, Berlin, 2006.

[15] T. Cebeci and P. Bradshaw. *Physical and Computational Aspects of Convective Heat Transfer, 1st Ed.* Springer, New York, 1984.

[16] A. J. Chamkha. Combined convection heat transfer from a rotating cone embedded in a power- law fluid saturated porous medium. *Fluid Particle Separation Journal*, 13(1):12–29, 2000.

[17] C. Y. Cheng. Free convection of non-Newtonian nanofluids about a vertical truncated cone in a porous medium. *International Communications in Heat and Mass Transfer*, 39(9):1348–1353, 2012.

[18] C. Y. Cheng. Soret and Dufour effects on double diffusive free convection over a vertical truncated cone in porous media with variable wall heat and mass fluxes. *Transport in Porous Media*, 91:877–888, 2012.

[19] C.Y. Cheng. Natural convection heat and mass transfer near a wavy cone with constant wall temperature and concentration in a porous medium. *Mechanics Research Communications*, 27(5):613–620, 2000.

[20] C.Y. Cheng. Double-diffusive natural convection along a vertical wavy truncated cone in non-Newtonian fluid saturated porous media with thermal and mass stratification. *International Communications in Heat and Mass Transfer*, 35:985–990, 2008.

[21] S. U. S. Choi. Enhancing thermal conductivity of fluids with nanoparticles, developments and applications of non-Newtonian flows. *ASME FED*, 231:99–103, 1995.

[22] S. U. S. Choi, Z. G. Zhang, W. Yu, F. E. Lockwood, and E.A. Grulke. Anomalously thermal conductivity enhancement in nanotube suspension. *Applied Physics Letters*, 79:2252–2254, 2001.

[23] H. Darcy. *The Flow of Homogeneous Fluids Through Porous Media.* Victor Dalmont, Paris, 1856.

[24] S. K. Das, S. U. S. Choi, W. Yu, and T. Pradeep. *Nanofluids: Science and Technology.* Wiley Interscience, New Jersey, 2007.

[25] W. Daungthongsuk and S. Wongwises. A critical review of convective heat transfer nanofluids. *Renewable and Sustainable Energy Reviews*, 11:797–817, 2007.

[26] Z. Dursunkaya and W. M Worek. Diffusion thermo and thermal diffusion effects in transient and steady natural convection from a vertical surface. *International Journal of Heat and Mass Transfer*, 35:2060–2065, 1972.

[27] J. A. Eastman, S. R. Phillpot, S. U. S. Choi, and P. Keblinski. Thermal transport in nanofluids. *Annual Review of Materials Research*, 34:219–246, 2004.

[28] E. R. G. Eckert and R. M. Drake. *Analysis of Heat and Mass Transfer*. McGraw Hill, New York, 1972.

[29] E. M. A. Elbashbeshy, T. G. Emam, and E. A. Sayed. Effect of thermal radiation on free convection flow and heat transfer over a truncated cone in presence of pressure work and heat generation/absorption. *Thermal Science*, 20(2):555–565, 2016.

[30] B. Gebhart. Effects of viscous dissipation in natural convection. *Journal of Fluid Mechanics*, 14:225–232, 1962.

[31] P. Gianluca, P. Samuel, and M. Sen. Nanofluids and their properties. *Applied Mechanics Reviews*, 64:030803, 2011.

[32] D. Gottlieb and S. A. Orszag. *Numerical analysis of spectral methods: theory and applications*. SIAM, United States, 1977.

[33] F. M. Hady, M. R. Eid, M. R. Abd-Elsalam, and M. A. Ahmed. Soret effect on natural convection boundary-layer flow of a non-Newtonian nanofluid over a vertical cone embedded in a porous medium. *IOSR Journal of Mathematics*, 8:51–61, 2013.

[34] T. Hayat, A. Nassem, M. I. Khan, M. Farooq, and A. Al-Saedi. Magnetohydrodynamic (MHD) flow of nanofluid with double stratification and slip conditions. *Physics and Chemistry of Liquids*, 56(2):189–208, 2018.

[35] R. G. Hering. Laminar free convection for a non-isothermal cone at low Prandtl numbers. *International Journal of Heat and Mass Transfer*, 8:1333–1337, 1965.

[36] R. G. Hering and R. J. Grosh. Laminar combined convection from a rotating cone. *Journal of Heat Transfer*, 85(1):29–34, 1963.

[37] M. A. Hossain and H. S. Takhar. Radiation effect on mixed convection along a vertical plate with uniform surface temperature. *Heat and Mass Transfer*, 31(4):243–248, 1996.

[38] M.A. Hossain, M.S. Munir, and I. Pop. Natural convection flow of a viscous fluid with viscosity inversely proportional to linear function of temperature from a vertical wavy cone. *International Journal of Thermal Sciences*, 40(4):366–371, 2001.

[39] D. B. Ingham and I. Pop. *Transport Phenomenon in Porous Media: Vol-II.* Elsevier, Oxford, 2005.

[40] A. Ishak. Similarity solutions for flow and heat transfer over a permeable surface with convective boundary condition. *Applied Mathematics and Computation*, 217:837–842, 2010.

[41] Y. Jaluria and K. Himasekhar. Buoyancy-induced two-dimensional vertical flows in a thermally stratified environment. *Computers and Fluids*, 11(1):39–49, 1983.

[42] N. G. Kafoussias. Local similarity solution for combined free-forced convective and mass transfer flow past a semi-infinite vertical plate. *International Journal of Energy Research*, 14:305–309, 1990.

[43] N. G. Kafoussias and N. G. Williams. Thermal-diffusion and diffusion-thermo effects on mixed free-forced convective and mass transfer boundary layer flow with temperature dependent viscosity. *International Jornal of Engineering Sciences*, 33:1369–1384, 1995.

[44] R.R. Kairi. Viscosity and dispersion effects on natural convection from a vertical cone in a non-Newtonian fluid saturated porous medium. *Thermal Sciences*, 15:S307–S316, 2001.

[45] S. Kakac and A. Pramuanjaroenkij. Review of convective heat transfer enhancement with nanofluids. *International Journal of Heat and Mass Transfer*, 52:3187–3196, 2009.

[46] P. K. Kameswaran, M. Narayana, P. Sibanda, and P. V. S. N. Murthy. Hydromagnetic nanofluid flow due to a stretching or shrinking sheet with viscous dissipation and chemical reaction effects. *International Journal of Heat and Mass Transfer*, 55(25):7587–7595, 2012.

[47] P. K. Kameswaran, B. Vasu, P. V. S. N. Murthy, and R. S. R. Gorla. Mixed convection from a wavy surface embedded in a thermally stratified nanofluid saturated porous medium with non-linear Boussinesq approximation. *International Communications in Heat and Mass Transfer*, 77:78–86, 2016.

[48] R. Kandaswamy, I. Muhaimin, and R. Mohammad. Thermophoresis and Brownian motion effects on MHD boundary layer flow of a nanofluid in the presence of thermal stratification due to solar radiation. *International Journal of Mechanical Sciences*, 70:146–154, 2013.

[49] W. M. Kays and M. E. Crawford. *Convective Heat and Mass transfer, 3rd Ed., P. 402*. McGraw-Hill, New York, 1980.

[50] W. A. Khan and A. Aziz. Natural convection flow of a nanofluid over a vertical plate with uniform surface heat flux. *International Journal of Thermal Sciences*, 50:1207–1214, 2011.

[51] M. R. Krishnamurthy, B. C. Prasannakumara, B. J. Gireesha, and R. S. Gorla. Effect of viscous dissipation on hydromagnetic fluid flow and heat transfer of nanofluid over an exponentially stretching sheet with fluid particle suspension. *Cogent Mathematics*, 2(1):1050973, 2015.

[52] A. V. Kuznetsov and D. A. Nield. Natural convective boundary-layer flow of a nanofluid past a vertical plate. *International Journal of Thermal Sciences*, 49:243–247, 2010.

[53] A. V. Kuznetsov and D. A. Nield. Double-diffusive natural convective boundary-layer flow of a nanofluid past a vertical plate. *International Journal of Thermal Sciences*, 50:712–717, 2011.

[54] A. V. Kuznetsov and D. A. Nield. Natural convective boundary-layer flow of a nanofluid past a vertical plate: A revised model. *International Journal of Thermal Sciences*, 77:126–129, 2014.

[55] H. T. Lin and C. C. Chen. Mixed convection on vertical plate for fluids of any Prandtl number. *Wrme-und Stoffbertragung*, 22:159–168, 1988.

[56] J. R. Lloyd and E. M. Sparrow. Combined forced and free convection flow on vertical surfaces. *International Journal of Heat and Mass Transfer*, 13:434–438, 1970.

[57] B. Mahanthesh, B. J. Gireesha, G. T. Thammanna, S. A. Shehzad, F. M. Abbasi, and R. S. R. Gorla. Nonlinear convection in nano Maxwell fluid with nonlinear thermal radiation: A three-dimensional study. *Alexandria Engineering Journal*, page DOI: 10.1016/j.aej.2017.03.037, 2017.

[58] A. Mahdy, M. A. Mansour, S. E. Ahmed, and S. S. Mohamed. Entropy generation of Cu water nanofluids through non-Darcy porous medium over a cone with convective boundary condition and viscous dissipation effects. *Special Topics and Reviews in Porous Media: An International Journal*, 8(1), 2017.

[59] G. Makanda and P. Sibanda. Numerical analysis of free convection Casson fluid flow from a spinning cone in non-Darcy porous medium with partial slip and viscous dissipation effects. *International Journal of Computer Mathematics*, 1:221–230, 2016.

[60] O. D. Makinde and A. Aziz. MHD mixed convection from a vertical plate embedded in a porous medium with a convective boundary condition. *International Journal of Thermal Sciences*, 49(9):1813–1820, 2010.

[61] O.D. Makinde, W. A. Khan, and Z. H. Khan. Stagnation point flow of MHD chemically reacting nanofluid over a stretching convective surface with slip and radiative heat. *Journal of Process Mechanical Engineering*, page DOI: 10.1177/0954408916629506, 2016.

[62] M. M. Molla and M. A. Hossain. Radiation effect on mixed convection laminar flow along a vertical wavy surface. *International Journal of Thermal Sciences*, 46(9):926–935, 2007.

[63] S. S. Motsa. A new spectral local linearization method for nonlinear boundary layer flow problems. *Journal of Applied Mathematics*, 2013:423628, 2013.

[64] S. S. Motsa and I. L. Animasaun. A new numerical investigation of some thermo-physical properties on unsteady MHD non-Darcian flow past an impulsively started vertical surface. *Thermal Science*, 9(1):249–258, 2015.

[65] S. S. Motsa, F.G. Awad, Z.G. Makukula, and P. Sibanda. The spectral homotopy analysis method extended to systems of partial differential equations. *Abstract and Applied Analysis*, 2014:1–11, 2014.

[66] S. S. Motsa, C. RamReddy, and C. V. Rao. Non-similarity solution for Soret effect on natural convection over the vertical frustum of a cone in a nanofluid using new bivariate pseudo-spectral local linearisation method. *Applied Mathematics and Computation*, 314:439–455, 2017.

[67] S.G. Moulic and L.S. Yao. Mixed convection along a wavy surface. *Journal of Heat Transfer*, 111(4):974–979, 1989.

[68] P. V. S. N. Murthy. Effect of double dispersion on mixed convection heat and mass transfer in non-Darcy porous medium. *Journal of Heat Transfer*, 122(3):476–484, 2000.

[69] P. V. S. N. Murthy, S. Mukherjee, P. V. S. S. S. R. Krishna, and D. Srinivasacharya. Mixed convection heat and mass transfer in a doubly stratified non-Darcy porous medium. *International Journal of Applied Mechanics and Engineering*, 12(1):109–123, 2007.

[70] P. V. S. N. Murthy, C. RamReddy, A. J. Chamkha, and A. M. Rashad. Magnetic effect on thermally stratified nanofluid saturated non-Darcy porous medium under convective boundary condition. *International Communications in Heat and Mass Transfer*, 47:41–48, 2013.

[71] P. V. S. N. Murthy and P. Singh. Effect of viscous dissipation on a non-Darcy natural convection regime. *International Journal of Heat and Mass Transfer*, 40:1251–1260, 1997.

[72] P. V. S. N. Murthy and P. Singh. Thermal dispersion effects on non-Darcy convection over a cone. *Computera and Mathematics with Applications*, 40(12):1433–1444, 2000.

[73] M. Mustafa, A. Mushtaq, T. Hayat, and A. Alsaedi. Numerical study of MHD viscoelastic fluid flow with binary chemical reaction and Arrhenius activation energy. *International Journal of Chemical Reactor Engineering*, 15(1), 2016.

[74] T. Y. Na. Numerical solution of natural convection flow past a non-isothermal vertical flat plate. *Applied Scientific Research*, 33:519–543, 1978.

[75] T. Y. Na and J. P. Chiou. Laminar natural convection over a frustum of a cone. *Applied Scientific Research*, 35(5):409–421, 1979.

[76] J. Nakamura, K. Kusunoki, M. Matsushita, M. Watanabe, I. Sawada, H. Fukada, and S. Tohi. *Plate heat exchanger used as evaporator or condenser*. W02010013608, 2010.

[77] M. Narayana, F. G. Awad, and P. Sibanda. Free magneto hydrodynamic flow and convection from a vertical spinning cone with cross - diffusion effects. *Applied Mathematical Modeling*, 37(5):2662–2678, 2013.

[78] M. Narayana, A. A. Khidir, P. Sibanda, and P. V. S. N. Murthy. Soret effect on the natural convection from a vertical plate in a thermally stratified porous medium saturated with a non-Newtonian liquid. *ASME Journal of Heat Transfer*, 135:1–10, 2013.

[79] P. A. L. Narayana and P. V. S. N. Murthy. Free convective heat and mass transfer in a doubly stratified non-Darcy porous medium. *Journal of Heat transfer*, 128(11):1204–1212, 2006.

[80] P. L. Narayana and P. Sibanda. Influence of the Soret effect and double dispersion on MHD mixed convection along a vertical at plate in non-Darcy porous medium. *International Journal of Nonlinear Science*, 12:352–364, 2011.

[81] D. A. Nield and A. V. Kuznetsov. The Cheng-Minkowycz problem for natural convective boundary-layer flow in a porous medium saturated by a nanofluid. *International Journal of Heat Mass Transfer*, 52:5792–5795, 2009.

[82] D. A. Nield and A. V. Kuznetsov. Thermal instability in a porous medium layer saturated by a nanofluid. *International Journal of Heat Mass Transfer*, 52:5796–5801, 2009.

[83] D. A. Nield and A. V. Kuznetsov. The Cheng Minkowycz problem for the double-diffusive natural convective boundary layer flow in a porous medium saturated by a nanofluid. *International Journal of Heat and Mass Transfer*, 54(1):374–378, 2011.

[84] D.A. Nield and A. Bejan. *Convection in Porous Media, 4th Ed.* Springer-Verlag, New York, 2013.

[85] A. Noghrehabadi, A. Behseresht, and M. Ghalambaz. Natural convection of nanofluid over vertical plate embedded in porous medium: prescribed surface heat flux. *Applied Mathematics and Mechanics*, 34:669–686, 2013.

[86] A. Noghrehabadi, R. Pourrajab, and M. Ghalambaz. Flow and heat transfer of nanofluids over stretching sheet taking into account partial slip and thermal convective boundary conditions. *Heat and Mass Transfer*, 49(9):1357–1366, 2013.

[87] M.K. Partha. Nonlinear convection in a non-Darcy porous medium. *Applied Mathematics and Mechanics*, 31(5):565574, 2010.

[88] F. O. Patrulescu, T. Groan, and I. Pop. Mixed convection boundary layer flow from a vertical truncated cone in a nanofluid. *International Journal of Numerical Methods for Heat and Fluid Flow*, 24(5):1175–1190, 2014.

[89] N. C. Peddisetty. Effects of thermal stratification on transient free convective flow of a nanofluid past a vertical plate. *Pramana*, 87(4):62, 2016.

[90] I. Pop and T. Y. Na. Naturnal convection of a Darcian fluid about a wavy cone. *International Communications in Heat and Mass Transfer*, 21(6):891–899, 1994.

[91] I. Pop and T. Y. Na. Natural convection from a wavy cone. *Applied Scientific Research*, 54(2):125–136, 1995.

[92] I. Pop and T. Y. Na. Natural convection over a frustum of a wavy cone in a porous medium. *Mechanics Research Communications*, 22(2):181–190, 1995.

[93] I. Pop and T. Y. Na. Laminar flow due to a rotating frustum of a cone. *Applied Mechanics and Engineering*, 4(1):113–120, 1999.

[94] I. Pop and T. Y. Na. Natural convection over a frustum of a wavy cone in a porous medium. *International Journal of Non-linear Mechanics*, 34(5):925–934, 1999.

[95] L. Prandtl. *Essentials of Fluid Dynamics*. Blackie and Son Ltd., London and Glasgow, 1952.

[96] K. V. Prasad, K. Vajravelu, and R.A. Van Gorder. Non-Darcian flow and heat transfer along a permeable vertical surface with nonlinear density temperature variation. *Acta Mechanica*, 220:139–154, 2011.

[97] A. Rahman, M. M. Molla, and M. M. A. Sarker. Natural convection flow along the vertical wavy cone in case of uniform surface heat flux where viscosity is an exponential function of temperature. *International Communications in Heat and Mass Transfer*, 38(6):774–780, 2011.

[98] M. M. Rahman and I. A. Eltayeb. Radiative heat transfer in a hydromagnetic nanofluid past a non-linear stretching surface with convective boundary condition. *Meccanica*, 48:601–615, 2013.

[99] M. M. Rahman, J. H. Merkin, and I. Pop. Mixed convection boundary layer flow past a vertical at plate with a convective boundary condition. *Acta Mechanica*, 226(8):2441–2460, 2015.

[100] C. RamReddy. Effect of double dispersion on convective flow over a cone. *International Journal of Non-linear Science*, 15(4):309–321, 2013.

[101] C. RamReddy, P. V. S. N. Murthy, A. M. Rashad, and A. J. Chamkha. Numerical study of thermally stratified nanofluid flow in a saturated non-Darcy porous medium. *The European Physical Journal Plus*, 129(2):25, 2014.

[102] C. RamReddy, P. V. S. N. Murthy, A. M. Rashad, and A. J. Chamkha. Soret effect on stagnation-point flow past a stretching/shrinking sheet in a nanofluid-saturated non-Darcy porous medium. *Special Topics and Reviews in Porous Media: An International Journal*, 7(3), 2016.

[103] C. RamReddy and T. Pradeepa. Non-similarity solutions for viscous dissipation and Soret effects in micropolar fluid over a truncated cone with convective boundary condition: Spectral quasilinearization approach. *International Journal of Nonlinear Sciences and Numerical Simulation*, 18(5):327–342, 2017.

[104] M. Ramzan, N. Ullah, J. D. Chung, D. Lu, and U. Farooq. Buoyancy effects on the radiative magneto micropolar nanofluid flow with double stratification, activation energy and binary chemical reaction. *Scientific Reports*, 7(1):12901, 2017.

[105] A. M. Rashad, S. Abbasbandy, and A. J. Chamkha. Non-Darcy natural convection from a vertical cylinder embedded in a thermally stratified and nanofluid saturated porous media. *ASME Journal of Heat Transfer*, 136:1–9, 2014.

[106] A. B. Rosmila, R. Kandaswamy, and J. Muhaimin. Lie symmetry group transformation for MHD natural convection flow of nanofluid over linearly porous stretching sheet in the presence of thermal stratification. *Applied Mathematics and Computation*, 33:593–694, 2012.

[107] S. Roy. Free convection from a vertical cone at high Prandtl numbers. *ASME Journal of Heat Transfer*, 96:115–117, 1974.

[108] Z. Shafique, M. Mustafa, and A. Mushtaq. Boundary layer flow of Maxwell fluid in rotating frame with binary chemical reaction and activation energy. *Results in Physics*, 6:627–633, 2016.

[109] S. Shaw, P.K. Kameswaran, and P. Sibanda. Effects of slip on nonlinear convection in nanofluid flow on stretching surfaces. *Boundary Value Problems*, 2016(2):11, 2016.

[110] S. Shaw, P. Sibanda, A. Sutradhar, and P. V. S. N. Murthy. Magnetohydrodynamics and Soret effects on bioconvection in a porous medium saturated with a nanofluid containing gyrotactic microorganisms. *Journal of Heat Transfer*, 136(5):052601, 2014.

[111] A. Shenoy, M. Sheremet, and I. Pop. *Convective Flow and Heat Transfer from Wavy Surfaces: Viscous Fluids, Porous Media, and Nanouids.* CRC Press, Taylor and Francis Group, 2016.

[112] S. Siddiqa, N. Begum, M. A. Hossain, and R. S. R. Gorla. Numerical solutions of natural convection flow of a dusty nanofluid about a vertical wavy truncated cone. *Journal of Heat Transfer*, 139(2):022503, 2017.

[113] S. Siddiqa, N. Begum, and M.A. Hossain. Radiation effects from an isothermal vertical wavy cone with variable fluid properties. *Applied Mathematics and Computation*, 289:149–158, 2016.

[114] P. Singh, V. Radhakrishnan, and K. A. Narayan. Non-similar solutions of free convection flow over a vertical frustum of a cone for constant wall temperature. *Ingenieur-Archiv*, 59(5):382–389, 1989.

[115] D. Srinivasacharya and O. Surender. Non-similar solution for natural convective boundary layer flow of a nanofluid past a vertical plate embedded in a doubly stratified porous medium. *International Journal of Heat and Mass Transfer*, 71:431–438, 2014.

[116] R. S. Telles and O. V. Trevisan. Dispersion in heat and mass transfer natural convection along vertical boundaries in porous media. *International Journal of Heat and Mass Transfer*, 36:1357–1365, 1993.

[117] K. Tewari and P. Singh. Natural convection in a thermally stratified porous medium. *International Journal of Engineering Sciences*, 30:1003–1007, 1992.

[118] R. K. Tiwari and M. K. Das. Heat transfer augmentation in a two-sided lid-driven differentially heated square cavity utilizing nanofluids. *International Journal of Heat and Mass Transfer*, 50:2002–2018, 2007.

[119] L. N. Trefethen. *Spectral methods in MATLAB*. SIAM, United States, 2000.

[120] V. Trisaksri and S. Wongwises. Critical review of heat transfer characteristics of nanofluids. *Renewable and Sustainable Energy Reviews*, 11:512–523, 2007.

[121] M. J. Uddin, B. Rostami, M. M. Rashid, and P. Rostami. Similarity and analytical solutions of free convective flow of dilatant nanofluid in a Darcian porous medium with

multiple convective boundary conditions. *Alexandria Engineering Journal*, 55(1):263–274, 2016.

[122] K. Vafai. *Handbook of Porous Media. 3rd Ed.* CRC Press, Taylor and Francis Group, 2015.

[123] K. Vajravelu and K. S. Sastri. Fully developed laminar free convection flow between two parallel vertical walls - I. *International Journal of Heat and Mass Transfer*, 20(6):655–660, 1977.

[124] R. Vasantha, I. Pop, and G. Nath. Non-Darcy natural convection over a slender vertical frustum of a cone in a saturated porous medium. *International Journal of Heat and Mass Transfer*, 29(1):153–156, 1986.

[125] T. Y. Wang, C. Kleinstreuer, and H. Chiang. Mixed convection from a rotating cone with variable surface temperature. *Numerical Heat Transfer: Part-A Applications*, 25(1):75–83, 1994.

[126] X. Q. Wang and A. S. Mujumdar. Heat transfer characteristics of nanofluids: A review. *International Journal of Thermal Sciences*, 46:1–19, 2007.

[127] X. Q. Wang and A. S. Mujumdar. A review on nanofluids - Part I: theoretical and numerical investigations. *Brazilian Journal of Chememical Engineering*, 25:613–630, 2007.

[128] X. Q. Wang and A. S. Mujumdar. A review on nanofluids - Part II: theoretical and numerical investigations. *Brazilian Journal of Chememical Engineering*, 25:631–648, 2007.

[129] K. A. Yih. Coupled heat and mass transfer by free convection over a truncated cone in porous media: VWT/VWC or VHF/VMF. *Acta Mechanica*, 137(1):83–87, 1999.

[130] K. A. Yih. Effect of radiation on natural convection about a truncated cone. *International Journal of Heat and Mass Transfer*, 42:4299–4305, 1999.